



Solution Growth and Functional Properties of Vertically Aligned ZnO Nanowires

Jiandong Fan

ADVERTIMENT. La consulta d'aquesta tesi queda condicionada a l'acceptació de les següents condicions d'ús: La difusió d'aquesta tesi per mitjà del servei TDX (www.tdx.cat) i a través del Dipòsit Digital de la UB (diposit.ub.edu) ha estat autoritzada pels titulars dels drets de propietat intel·lectual únicament per a usos privats emmarcats en activitats d'investigació i docència. No s'autoritza la seva reproducció amb finalitats de lucre ni la seva difusió i posada a disposició des d'un lloc aliè al servei TDX ni al Dipòsit Digital de la UB. No s'autoritza la presentació del seu contingut en una finestra o marc aliè a TDX o al Dipòsit Digital de la UB (framing). Aquesta reserva de drets afecta tant al resum de presentació de la tesi com als seus continguts. En la utilització o cita de parts de la tesi és obligat indicar el nom de la persona autora.

ADVERTENCIA. La consulta de esta tesis queda condicionada a la aceptación de las siguientes condiciones de uso: La difusión de esta tesis por medio del servicio TDR (www.tdx.cat) y a través del Repositorio Digital de la UB (diposit.ub.edu) ha sido autorizada por los titulares de los derechos de propiedad intelectual únicamente para usos privados enmarcados en actividades de investigación y docencia. No se autoriza su reproducción con finalidades de lucro ni su difusión y puesta a disposición desde un sitio ajeno al servicio TDR o al Repositorio Digital de la UB. No se autoriza la presentación de su contenido en una ventana o marco ajeno a TDR o al Repositorio Digital de la UB (framing). Esta reserva de derechos afecta tanto al resumen de presentación de la tesis como a sus contenidos. En la utilización o cita de partes de la tesis es obligado indicar el nombre de la persona autora.

WARNING. On having consulted this thesis you're accepting the following use conditions: Spreading this thesis by the TDX (www.tdx.cat) service and by the UB Digital Repository (diposit.ub.edu) has been authorized by the titular of the intellectual property rights only for private uses placed in investigation and teaching activities. Reproduction with lucrative aims is not authorized nor its spreading and availability from a site foreign to the TDX service or to the UB Digital Repository. Introducing its content in a window or frame foreign to the TDX service or to the UB Digital Repository is not authorized (framing). Those rights affect to the presentation summary of the thesis as well as to its contents. In the using or citation of parts of the thesis it's obliged to indicate the name of the author.

Programa de Doctorat en Física

Solution Growth and Functional Properties of Vertically Aligned ZnO Nanowires

Tesis que presenta Jiandong Fan

per obtenir el títol de Doctor per la Universitat de Barcelona

Director de la tesis:

Dr. Andreu Cabot Codina

Professor agregat

Departament d'Electrònica
Grup Materials Electrònics i Energia (M-2E)
Institut de Recerca en Energia de Catalunya (IREC)



Contents

Acknowledgements	7
List of Publications	9
Authors' contributions	11
Preface	15
Summary of Results	17
Resumen de los resultados.....	21
Chapter 1 Introduction.....	25
Introduction to block 1: Synthesis and characterization of ZnO:Cl nanowires	25
1.1.1 Structure and morphology of ZnO NWs	26
1.1.2 Electrochemical deposition of vertically aligned ZnO NWs	28
1.1.3 Hydrothermal deposition of vertically aligned ZnO NWs	28
1.1.4 Successive ionic layer adsorption and reaction (SILAR).....	29
1.1.5 Extrinsic Doping of ZnO NWs.....	30
1.1.6 Scanning Probe Microscope (SPM) Characterization.....	31
1.1.7 Mott-Schottky Measurement.....	32
1.1.8 Photoluminescence (PL) Measurement	33
1.1.9 Electrochemical impedance spectroscopy (EIS)	33
Introduction to block 2: Hetero/homo nanostructures based on ZnO:Cl nanowires for efficient photoelectrochemical cells	35
1.2.1 Photoelectrochemical (PEC) cells	35
1.2.2 ZnO NWs-based PEC cells	38
1.2.3 Characterization of PEC cells	39
Introduction to block 3: Photovoltaic performance of dye-sensitized solar cells based on ZnO nanowires.....	40
1.3.1 Dye-sensitized solar cells (DSCs).....	40
1.3.2 ZnO NWs-based DSCs.....	42
1.3.3 Characterization techniques of DSCs.....	43
1.4 References	45
Chapter 2 Control of the Doping Concentration, Morphology and Optoelectronic Properties of Vertically Aligned Chlorine-Doped ZnO Nanowires	51
2.1 Abstract.....	51
2.2 Introduction.....	52

2.3 Experimental section.....	54
2.3.1 NWs growth	54
2.3.2 Characterization	54
2.4 Results and Discussion	56
2.5 Conclusions.....	72
2.6 References.....	73
Chapter 3 Visible Photoluminescence Components of Solution-Grown ZnO Nanowires: Influence of the Surface Depletion Layer.....	
3.1 Abstract.....	79
3.2 Introduction.....	80
3.3 Experimental section.....	81
3.3.1 NWs growth.	81
3.3.2 Characterization	82
3.4 Results and Discussion	83
3.5 Conclusions.....	95
3.6 References.....	95
Chapter 4 Enhancement of the Photoelectrochemical Properties of Cl-Doped ZnO Nanowires by Tuning Their Coaxial Doping Profile	
4.1 Abstract.....	99
4.2 Introduction.....	100
4.3 Experimental section.....	101
4.3.1 NWs growth	101
4.3.2 Characterization	102
4.4 Results and discussion	103
4.5 Conclusions.....	111
4.6 References.....	111
Chapter 5 Solution-Growth and Optoelectronic Properties of ZnO:Cl@ZnS Core-Shell Nanowires with Tunable Shell Thickness	
5.1 Abstract.....	115
5.2 Introduction.....	116
5.3 Experimental section.....	117
5.3.1 ZnO:Cl NWs growth	117
5.3.2 ZnS shell growth	118
5.3.3 Characterization techniques	118

5.4 Results and Discussion	120
5.5 Conclusions.....	130
5.6 References.....	130
Chapter 6 Solution-Growth and Optoelectronic Performance of ZnO:Cl@TiO ₂ and ZnO:Cl@Zn _x TiO _y @TiO ₂ Core-Shell Nanowires with Tunable Shell Thickness	133
6.1 Abstract.....	133
6.2 Introduction.....	134
6.3 Experimental details	136
6.3.1 ZnO NWs growth	136
6.3.2 TiO ₂ shell growth	137
6.3.3 Materials characterization	138
6.3.4 Photoelectrochemical characterization.....	139
6.3.5 DSCs fabrication and characterization.....	139
6.3.6 Electrochemical impedance spectroscopy.....	140
6.4 Results and Discussion	140
6.5 Conclusions.....	151
6.6 References.....	152
Chapter 7 Cobalt (II/III) Redox Electrolyte in ZnO Nanowire-Based Dye-Sensitized Solar Cells	157
7.1 Abstract.....	157
7.2 Introduction.....	158
7.3 Experimental section.....	160
7.3.1 Synthesis of ZnO NWs.....	160
7.3.2 DSCs fabrication	161
7.3.3 Characterization	162
7.4 Results and discussion	163
7.5 Conclusions.....	169
7.6 References.....	169
Chapter 8 Influence of the Annealing Atmosphere on the Performance of ZnO Nanowires-Based Dye-Sensitized Solar Cells.....	173
8.1 Abstract.....	173
8.2 Introduction.....	174
8.3 Experimental section.....	176
8.3.1 Synthesis of ZnO NWs.....	176

8.3.2 DSCs fabrication	176
8.3.3 Characterization	177
8.4 Results and Discussion	178
8.5 Conslusions	190
8.6 References.....	190
Conclusions	195
Future work	197
Abbreviations	199
Curriculum Vitae	201
Annex	205

Acknowledgements

Four years ago, I made a decision to come here for starting my PhD study. Today I would say it is the people around me that make the journey worth taking.

First of all, I would like to thank my supervisor: Andreu Cabot, thank you for having me in your group. You open the scientific door for me and gave me so much freedom in which direction to go with my research. Importantly, let me know “interest is the largest motivation”. Your rigorous and responsible style in science has deeply impressed me, which will definitely affect me in my scientific carrer. I wish to thank you for providing me the financial support for my PhD and attending international conferences. Besides, I really appreciate you for your “tons of gifts” to my daughter.

I am very thankful to Prof. J. R. Morante for giving me constructive suggestions in my research. Also, I would like to say thank to Cristian and Teresa for interesting discussion in photoelectrochemical cells.

I have to thank the people from the Functional Nanomaterials group. I still clearly remember Pablo helped me to register in university with many twists and turns. Alexey, you gave me the idea to grow the first nanowire in my life, thank you for your always helpful and kind discussions. Maria, many thanks for your thousands of translations and always kind help in life and academic issues. Doris and Alex, thank you for buying the lab stuff, “yes, we can!”. I also want to thank Raquel, Ariadna, Silvia, Joost and Joana for the help in lab. Also, I would like to thank the “Chinese group”, Zhiguo, Wenhua, Shaofeng, Weijie, Zhishan, Haibing, Xianyun and Xuelian. I could not forget the interesting “lunch talking”.

A special thank should be given to Jordi and Reza, many nice HRTEM characterizations were done timely and carefully for me. I really appreciate you for your nice job.

I would like to thank Frank who helped me to measure and process the photoluminescence spectra being important part in my thesis, and Lorenzo who trained me in XPS measurement. I also want to thank Diouldé for helpful discussions in electrochemical depsoition, and Edgardo for the characterizations of solar cells.

I wish to express my acknowledgment to Prof. Anders Hagfeldt who received me for short-visting in Uppsala Univerisity. I would like to thank Gerrit and Eric for academic discussion in solid and liquid dye-sensitized solar cells. I also want to thank Yan hao for helping me to fabricate and characterize the dye-sensitized solar cells.

I want to express my gratitude to Jean and Servane from Institute for Research and Development of Photovoltaic Energy (IRDEP), France, for the characterization of Mott-Schottky.

I would like to thank Carmen and Mar from Instituto de Ciencia de Materiales de Madrid (ICMM) for SPM characterization.

I want to thank the fellowship (FI-DGR and BE-DGR) from Catalan government and Chinese government award for outstanding self-financed students abroad for providing me the financial support for my PhD and academic visit.

Finally, I wish to express my gratitude to my parents, thank you for your encouragement and support, which drive me to go ahead. I also want to give my special thank to my wife and my daughter, you provid me inspiration and driving force. Things are going well with you, thank you!

List of Publications

The publications contained in the list below are the ones to be considered for the evaluation of this PhD dissertation. A copy of the published manuscripts with the integrated supporting information is presented as chapters 2 to 8 in the thesis. The published version can be found in the Annex. Additionally the impact factor and quartile in category of the journal were confirmed by *ISI web of knowledge*. None of these publications has been previously presented in any other PhD dissertation.

1. **Jiandong Fan**, Alexey Shavel, Reza Zamani, Cristian Fábrega, Jean Rousset, Servane Haller, Frank Güell, Alex Carrete, Teresa Andreu, Jordi Arbiol, Joan Ramon Morante, and Andreu Cabot. “Control of the Doping Concentration, Morphology and Optoelectronic Properties of Vertically Aligned Chlorine-doped ZnO Nanowires”, *Acta Materialia*, 2011, 59, 6790-6800.
Impact factor 2011: **3.755** (Q1 in Material Science)
2. **Jiandong Fan**, Frank Güell, Cristian Fábrega, Alexey Shavel, Alex Carrete, Teresa Andreu, Joan Ramón Morante, and Andreu Cabot. “Enhancement of the Photoelectrochemical Properties of ZnO Nanowires by Tuning Their Coaxial Doping Profile”, *Appl. Phys. Lett.* 2011, 99, 262102.
Impact factor 2011: **3.844** (Q1 in Applied Physics)
3. **Jiandong Fan**, Reza Zamani, Cristian Fábrega, Alexey Shavel, Cristina Flox, Maria Ibáñez, Teresa Andreu, Antonio M. López, Jordi Arbiol, Joan Ramón Morante, and Andreu Cabot. “Solution-Growth and Optoelectronic Performance of ZnO:Cl/TiO₂ and ZnO:Cl/Zn_xTiO_y/TiO₂ Core-Shell Nanowires with Tunable Shell Thickness”, *J. Phys. D: Appl. Phys.* 2012, 45, 415301.
Impact factor 2011: **2.544** (Q1 in Applied Physics)
4. **Jiandong Fan**, Frank Güell, Cristian Fábrega, Andrew Fairbrother, Teresa Andreu, Antonio M. López, Joan Ramón Morante, and Andreu Cabot. “Visible

Photoluminescence Components of Solution-Grown ZnO Nanowires: Influence of the Surface Depletion Layer”, *J. Phys. Chem. C* 2012, 116, 19496–19502.

Impact factor 2011: **4.805** (Q1 in Material Science)

5. **Jiandong Fan**, Cristian Fábrega, Reza Zamani, Alexey Shavel, Frank Güell, Alex Carrete, Teresa Andreu, Antonio M. López, Joan Ramón Morante, Jordi Arbiol, and Andreu Cabot, “Solution-Growth and Optoelectronic Properties of ZnO:Cl@ZnS Core-Shell Nanowires with Tunable Shell Thickness”, *J. Alloy. Compd.* 2013, 555, 213–218.

Impact factor 2011: **2.289** (Q1 in Material Science)

6. **Jiandong Fan**, Yan Hao, Andreu Cabot, Erik M. J. Johansson, Gerrit Boschloo, and Anders Hagfeldt. “Cobalt (II/III) Redox Electrolyte in ZnO Nanowire-Based Dye-Sensitized Solar Cells”, *ACS Appl. Mater. Interfaces* 2013, 5, 1902–1906.

Impact factor 2011: **4.525** (Q1 in Material Science)

7. **Jiandong Fan**, Yan Hao, Mar García Hernández, Carmen Munuera, Frank Güell, Erik M. J. Johansson, Gerrit Boschloo, Anders Hagfeldt, and Andreu Cabot. “Influence of the Annealing Atmosphere on the Performance of ZnO Nanowires-Based Dye-Sensitized Solar Cells”. Submitted.

Authors' contributions

The work presented in this dissertation has been carried out at the Electronics Department of the Physics Faculty at the University of Barcelona (UB) and at the Advanced Material Research Department of the Catalonia Institute for Energy Research (IREC). The PhD student, Jiandong Fan, has had primary responsibility for all the experimental work, data analysis, and manuscript writing and design in all the publications presented. Andreu Cabot coordinated and strongly participated in the designing and writing of all the papers. The co-authors contributions for each paper are specified below these lines.

Paper 1 (Chapter 2): *Jiandong Fan*, Alexey Shavel, Reza Zamani, Cristian Fábrega, Jean Rousset, Servane Haller, Frank Güell, Alex Carrete, Teresa Andreu, Jordi Arbiol, Joan Ramon Morante, and Andreu Cabot. “Control of the Doping Concentration, Morphology and Optoelectronic Properties of Vertically Aligned Chlorine-doped ZnO Nanowires”, *Acta Materialia*, 2011, 59, 6790-6800.

Alexey Shavel and Alex Carrete participated in the materials synthesis. Reza Zamani and Jordi Arbiol performed the HRTEM. Cristian Fábrega and Teresa Andreu participated in the characterization and discussion. Frank Güell participated in the PL measurement. Jean Rousset and Servane Haller participated in the mott-schottky measurement. Joan Ramon Morante revised the manuscript critically.

Paper 2 (Chapter 3): *Jiandong Fan*, Frank Güell, Cristian Fábrega, Andrew Fairbrother, Teresa Andreu, Antonio M. López, Joan Ramón Morante, and Andreu Cabot. “Visible Photoluminescence Components of Solution-Grown ZnO Nanowires: Influence of the Surface Depletion Layer”, *J. Phys. Chem. C*. 2012, 116, 19496–19502.

Frank Güell participated in the PL measurement. Cristian Fábrega and Teresa Andreu participated in the characterization and discussion. Andrew Fairbrother, Antonio M. López and Joan Ramón Morante revised the manuscript critically.

Paper 3 (Chapter 4): **Jiandong Fan**, Frank Güell, Cristian Fábrega, Alexey Shavel, Alex Carrete, Teresa Andreu, Joan Ramón Morante, and Andreu Cabot. “Enhancement of the Photoelectrochemical Properties of ZnO Nanowires by Tuning Their Coaxial Doping Profile”, *Appl.Phys.Lett.* 2011, 99, 262102.

Frank Güell participated in the PL measurement. Alexey Shavel and Alex Carrete participated in the materials synthesis. Cristian Fábrega and Teresa Andreu participated in the characterization and discussion. Joan Ramón Morante revised the manuscript critically.

Paper 4 (Chapter 5): **Jiandong Fan**, Cristian Fábrega, Reza Zamani, Alexey Shavel, Frank Güell, Alex Carrete, Teresa Andreu, Antonio M. López, Joan Ramón Morante, Jordi Arbiol, and Andreu Cabot. “Solution-Growth and Optoelectronic Properties of ZnO:Cl@ZnS Core-Shell Nanowires with Tunable Shell Thickness”, *J. Alloy. Compd.* 2013, 555, 213–218.

Cristian Fábrega and Teresa Andreu participated in the photoelectrochemical characterization. Reza Zamani and Jordi Arbiol performed the HRTEM. Alexey Shavel and Alex Carrete participated in the materials synthesis. Frank Güell participated in the PL measurement. Antonio M. López and Joan Ramón Morante revised the manuscript critically.

Paper 5 (Chapter 6): **Jiandong Fan**, Reza Zamani, Cristian Fábrega, Alexey Shavel, Cristina Flox, Maria Ibáñez, Teresa Andreu, Antonio M. López, Jordi Arbiol, Joan Ramón Morante, and Andreu Cabot. “Solution-Growth and Optoelectronic Performance of ZnO:Cl/TiO₂ and ZnO:Cl/Zn_xTiO_y/TiO₂ Core-Shell Nanowires with Tunable Shell Thickness”, *J. Phys. D: Appl. Phy.* 2012, 45, 415301.

Reza Zamani, Maria Ibáñez and Jordi Arbiol performed the TEM. Cristian Fábrega and Teresa Andreu participated in the photoelectrochemical characterization. Cristina Flox participated in the impedance measurement. Antonio M. López and Joan Ramón Morante revised the manuscript critically.

Paper 6 (Chapter 7): **Jiandong Fan**, Yan Hao, Andreu Cabot, Erik M. J. Johansson, Gerrit Boschloo, and Anders Hagfeldt. “Cobalt (II/III) Redox Electrolyte in ZnO

Nanowire-Based Dye-Sensitized Solar Cells”, *ACS Appl. Mater. Interfaces* 2013, 5, 1902–1906.

Yan Hao participated in the fabrication and characterization of DSCs. Erik M. J. Johansson, Gerrit Boschloo and Anders Hagfeldt participated in the discussion and revised the manuscript critically.

Paper 7 (Chapter 8): **Jiandong Fan**, Yan Hao, Mar García Hernández, Carmen Munuera, Frank Güell, Erik M. J. Johansson, Gerrit Boschloo, Anders Hagfeldt, and Andreu Cabot. “Influence of the Annealing Atmosphere on the Performance of ZnO Nanowires-Based Dye-Sensitized Solar Cells”, Submitted.

Yan Hao participated in the fabrication and characterization of DSCs. Mar García Hernández, Carmen Munuera performed the SPM characterization. Frank participated in the PL measurement. Erik M. J. Johansson, Gerrit Boschloo and Anders Hagfeldt participated in the discussion and revised the manuscript critically.

Dr. Andreu Cabot

Certify the information provided above is true

Barcelona, 20th of May 2013

Preface

As a wide band gap semiconductor material with unique properties, ZnO nanowires have been widely studied in recent years. In the present dissertation, I have focused my study on the synthesis and properties of vertically aligned ZnO nanowires, as well as the applications in photoelectrochemical cells for water splitting and dye-sensitized solar cells. I divide the work into three blocks. The first block corresponds to the synthesis and properties of ZnO:Cl nanowires (chapter 2 and 3). In the second block hetero and homo nanostructures based on ZnO:Cl nanowires for efficient photoelectrochemical cells will be demonstrated (chapter 4, 5 and 6). In the last block, photovoltaic performance of dye-sensitized solar cell based on ZnO nanowires will be carefully studied. I will present a direct comparison of the performance of $[\text{Co}(\text{bpy})_3]^{2+/3+}$ and Γ/I_3^- redox couples as electrolytes (chapter 7). A further study concerning the annealing effect on the functional properties of ZnO nanowires-based devices will also be carried out in this block (chapter 8).

Summary of Results

Block 1: Synthesis and characterization of ZnO:Cl nanowires (NWs)

Vertically aligned single-crystal and chlorine-doped ZnO NWs were grown by a low-cost, high-yield and seed-free electrochemical route. The effects of the applied potential and the concentration of ammonium chloride on the morphology, structural and optoelectronic properties of the ZnO:Cl NWs were comprehensively investigated (chapter 2). Detailed morphology, optical and electronic parameters of the ZnO:Cl NWs with different concentration of Cl doping were calculated. The results demonstrated that the carrier concentration of such ZnO:Cl NWs with controllable morphology could be tuned in the range between 5×10^{17} and $4 \times 10^{20} \text{ cm}^{-3}$. Besides, intrinsic ZnO NWs with various lengths from 6 μm to 12 μm can also be obtained by hydrothermal deposition for the application in DSCs.

In chapter 3, arrays of electrodeposited ZnO NWs were used to illustrate the dependence of the ZnO visible photoluminescence emission on the extension of the surface depletion layer and to obtain further insight into the localization of the related states. Results evidenced that the yellow and orange emissions from electrodeposited ZnO NWs are correlated with the extension of the NWs surface depletion region. On the other hand, the green emission that dominates the visible part of the PL spectra in annealed ZnO NWs showed no dependence on the surface band bending, thus pointing toward its origin in the bulk.

The results shown in chapter 2 were published in *Acta Materialia*. The results presented in chapter 3 were published in *Journal of Physical Chemistry C*.

Block 2: Hetero and homo nanostructures based on ZnO:Cl NWs for efficient photoelectrochemical cells

In this block, we demonstrated that the ZnO:Cl NWs can be coated with selected shell materials having controlled thickness to produce homo and hetero structures with modified surface properties and varied electrical field values at the surface. In particular, ZnO:Cl@ZnO homo structures were grown by a facile and low cost electrodeposition two-step process (chapter 4). ZnO:Cl@ZnS hetero structures were prepared by the successive ionic layer adsorption and reaction (chapter 5). ZnO:Cl NWs were coated by a titanium oxide shells of tunable thickness mediating successive adsorption-hydrolysis-condensation steps (chapter 6). In general, due to the controlled surface electrical field, the photoelectrochemical properties of these NWs were highly enhanced up to a factor 5 with the presence of these shell layers. An experimental study as function of their thicknesses was presented and modeled to explain the promotion of the surface-related radiative recombination processes. The enhancement factor was proved to depend on the shell thickness. These performances are associated with the improvement of the photogenerated charge carrier separation and transfer from the surface to neutral inner part achieved when increasing the space charge area within the nanowires with a built-in electric field introduced by the doping profile. These features allowed the deduction of practical rules for the design and optimization of these three dimensional photoelectrodes for the production of fuels, among others.

The results shown in chapter 4 were published in *Applied Physics Letters*. The results presented in chapter 5 were published in *Journal of Alloys and Compounds*. The results shown in chapter 6 were published in *Journal of Physics D: Applied Physics*.

Block 3: Photovoltaic performance of dye-sensitized solar cells (DSCs) based on ZnO NWs

ZnO is the main alternative wide band gap semiconductor to replace TiO₂ as an electron conductor in DSCs. In this block, we explored the performance of the [Co(bpy)₃]^{2+/3+} redox couple in ZnO NWs-based DSCs (chapter 7). We first tested the new redox electrolyte using ZnO NW arrays prepared by hydrothermal deposition with different lengths. Then, using the exact same NW arrays and LEG4 dye as sensitizer, we performed a direct comparison of the performance of [Co(bpy)₃]^{2+/3+} and Γ/I_3^- redox couples as electrolytes in ZnO NW DSCs. The results demonstrated the higher suitability of the cobalt complex, both in terms of a larger open circuit voltage (V_{OC}) and a higher photocurrent. The [Co(bpy)₃]^{2+/3+} electrolyte resulted in V_{OC} enhancements of above 200 mV. This V_{OC} increase is associated with the better match between the cobalt complex redox potential and the oxidation potential of the dye. The incident photon-to-current efficiency enhancement is attributed to a less competitive visible light absorption of the cobalt redox couple. Thus the present study opens new opportunities to improve energy conversion efficiency in ZnO-based DSCs.

Subsequently, the effects of post-annealing atmosphere on the functional properties of ZnO NWs-based devices were carefully studied in the present block (chapter 8). The $I-V$ characteristic of individual NWs was assessed by conducting scanning probe microscopy showing that the post-annealing process under argon atmosphere can effectively boost the conductivity of NWs compared to those annealed in air. A direct comparison of the photovoltaic performance of DSCs demonstrated that a higher photocurrent for the NWs annealed in argon can be obtained, but a lower V_{oc} compared to the NWs annealed in air. The post-annealing of the NWs in argon allowed further improving the power conversion efficiency with a value of 30% compared to air. The

improved efficiency was dominated by significantly higher photocurrents (~50%) measured from Ar-DSCs when compared with Air-DSCs. The improved functional properties can be attributed to the built-in oxygen vacancies when annealing the NWs in argon. The multi trap distribution inside ZnO NWs by means of fitting the characteristics of charge extraction and lifetime gives a reasonable explanation on the different functional properties.

The results presented in chapter 7 were published in *ACS Applied Materials & Interfaces*. The results shown in chapter 8 were recently submitted for publication and are now under review.

Resumen de los resultados

Bloque 1: Síntesis y caracterización de nanohilos de ZnO:Cl (NHs)

NHs monocristalinos de ZnO, alineados verticalmente y dopados con cloro fueron sintetizados mediante un método electroquímico de bajo costo, alto rendimiento y sin necesidad de semillas. Los efectos del potencial aplicado y de la concentración de cloruro de amonio en la morfología, estructura y propiedades optoelectrónicas de los NHs de ZnO:Cl fueron exhaustivamente investigados (capítulo 2). La morfología, parámetros ópticos y electrónicos de los NHs de ZnO:Cl con diferentes concentraciones de Cl fueron caracterizados. Los resultados demuestran que la concentración de portadores de carga en estos NHs de ZnO:Cl pueden ser modificados en un rango entre 5×10^{17} y $4 \times 10^{20} \text{ cm}^{-3}$. Además, NHs de ZnO intrínsecos de varias longitudes de entre 6 μm y 12 μm pueden ser obtenidos por deposición hidrotérmica para aplicación en Celdas Solares Sensibilizadas por Colorante.

En el capítulo 3, matrices de NHs de ZnO electrodepositados fueron usados para ilustrar la dependencia de la emisión fotoluminiscente (PL) en el rango visible del ZnO en la extensión de la capa de depleción superficial y obtener una mayor comprensión de la localización superficial de estos estados. Estos resultados muestran la localización superficial de los estados origen de las transiciones amarilla y naranja. Por otro lado, la emisión en el verde, que domina la parte visible del espectro PL en NHs de ZnO sinterizados mostró que no hay dependencia en el doblamiento de la banda superficial, probando por tanto que su origen no está en la superficie de los NHs.

Los resultados obtenidos en el capítulo 2 se publicaron en *Acta Materialia*. Los resultados presentados en el capítulo 3 se publicaron en *Journal of Physical Chemistry C*.

Bloque 2: Hetero y homo nanoestructuras basada en NHs de ZnO:Cl para celdas fotoelectroquímicas eficientes

En este bloque, demostramos que los NHs de ZnO:Cl se pueden recubrir por otro material con un grosor controlado para tener homo y hetero-estructuras con propiedades superficiales modificadas así como diferentes valores del campo eléctrico en su superficie. En particular, ZnO:Cl@ZnO homo-estructuras fueron sintetizadas por medio de un proceso fácil y barato de electroposición en dos pasos (capítulo 4). ZnO:Cl@ZnS hetero-estructuras fueron preparadas por la sucesiva adsorción y reacción de iones (SILAR) (capítulo 5). NHs de ZnO:Cl fueron recubiertos por una capa de óxido de titanio con un espesor modificable por medio de sucesivos pasos de adsorción-hidrólisis-condensación (capítulo 6). En general, debido al control del campo eléctrico superficial, las propiedades fotoelectroquímicas de estos NHs fueron altamente mejoradas con la presencia de estas capas. Un estudio experimental en función de su grosor fue presentado y modelizado para explicar los procesos de recombinación radiactiva en la superficie. Se probó que el factor de aumento depende del grosor de la capa superficial. Estos rendimientos están asociados con una mejora de la separación de los portadores de carga fotogenerados y la mejorada capacidad de transferencia entre la superficie y la zona central neutra. Esto se consigue al incrementar la zona de carga espacial dentro de los NHs con un campo eléctrico introducido mediante el perfil dopante.

Los resultados obtenidos en el capítulo 4 se publicaron en *Applied Physics Letters*. Los resultados presentados en el capítulo 5 se publicaron en *Journal of Alloys and Compounds*. Los resultados que se muestran en el capítulo 6 se publicaron en *Journal of Physics D: Applied Physics*.

Bloque 3: El rendimiento fotovoltaico de células solares sensibilizadas por colorante (DSCs), basadas en NHs de ZnO.

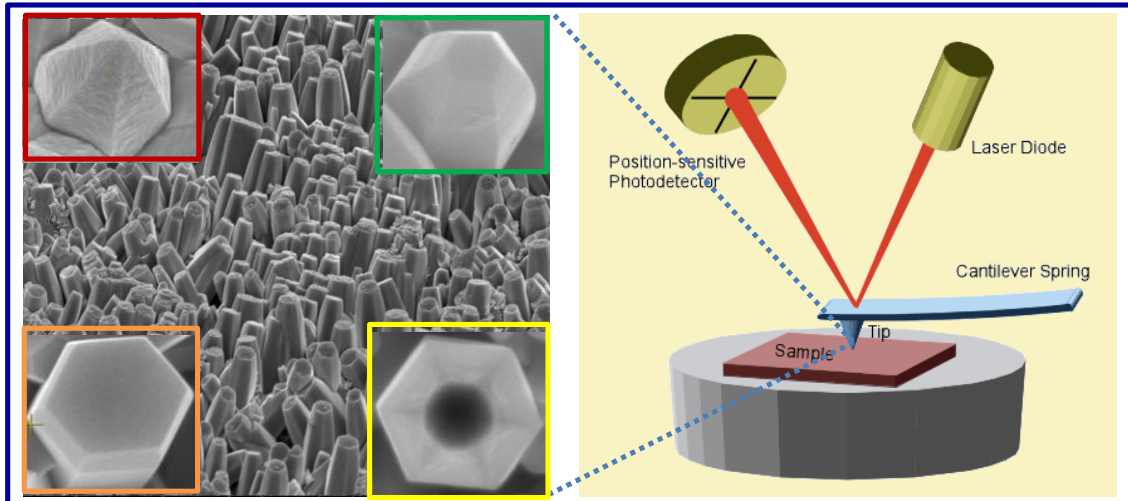
El ZnO es la principal alternativa para remplazar al TiO₂ como conductor de electrones en DSCs. En este bloque, exploramos el rendimiento de la pareja redox [Co(bpy)₃]^{2+/3+} en DSCs basadas en NHs de ZnO (capítulo 7). Primero probamos el nuevo electrolito usando matrices de NHs de ZnO preparadas mediante deposición hidrotérmica con diferentes longitudes. Entonces, usando los mismos NHs y LEG4 como colorante sensibilizador, desarrollamos una comparación directa del rendimiento del [Co(bpy)₃]^{2+/3+} y I⁻/I₃⁻ parejas redox como electrolitos en DSCs de NHs de ZnO. Los resultados demuestran que el complejo de cobalto es más adecuado, tanto en términos de un mayor voltaje en circuito abierto (V_{OC}) como en una mayor fotocorriente. El electrolito [Co(bpy)₃]^{2+/3+} resulta en un aumento por encima de 200 mV en el V_{OC} . Esta mejora en el V_{OC} está asociada a una mejor conexión entre el potencial redox del complejo de cobalto y el potencial de oxidación del colorante. La mejora de la eficiencia de conversión de fotones incidentes a corriente se debe a una absorción menos competitiva del espectro visible por parte del par redox de cobalto. Por lo tanto, el presente estudio abre una nueva oportunidad para mejorar la eficiencia de conversión energética en las DSCs basadas en ZnO.

Posteriormente, los efectos de la atmósfera del proceso térmico de sinterizado en el rendimiento de los dispositivos basados en NHs de ZnO fueron cuidadosamente estudiados en el presente bloque (capítulo 8). Las características $I-V$ de NHs individuales fueron evaluadas por medio de un microscopio de fuerza atómica mostrando que el proceso de sinterizado en atmósfera de argón puede aumentar de manera efectiva la conductividad de los NHs en comparación con los sinterizados en aire. Una comparación directa del rendimiento fotovoltaico de las DSCs demuestra que se puede obtener un mayor fotocorriente en los NHs sinterizados en argón, pero un V_{OC} menor comparado con los sinterizados en aire. El mecanismo de múltiples capturas con una distribución de capturas exponencial dentro de los NHs de ZnO por medio del ajuste de las características de extracción y tiempo de vida da una explicación razonable del diferente rendimiento.

Los resultados presentados en el capítulo 7 se publicaron en *ACS Applied Materials & Interfaces*. Los resultados obtenidos en el capítulo 8 se han enviado y están ahora bajo revisión.

Chapter 1

Introduction to block 1: Synthesis and characterization of ZnO:Cl nanowires



ZnO nanowires (NWs) have been widely studied in the past decade,¹⁻³ not only because of their range of morphologies produced by various methods, but also because of their broad applications in electronic, optoelectronic, piezoelectronics, etc. Among others, as an environmental friendly material, ZnO NWs have intensively been studied for clean and sustainable solar energy devices.^{4,5} In particular, vertically aligned ZnO NWs offer various advantages for the application in solar energy conversion: (i) Increasing the interface/surface areas; (ii) Improving the electron transport properties, increasing the electron diffusion length up to the order of 100 μm ;⁶ (iii) Minimizing recombination during charge carrier transport to the external circuit.

1.1.1 Structure and morphology of ZnO NWs

Wurtzite ZnO has a hexagonal structure with the space group $C6_{3mc}$ and lattice parameters $a = 0.3296$ and $c = 0.52065$ nm.³ The structure of ZnO can be simply described as a number of alternating planes composed of tetrahedrally coordinated O^{2-} and Zn^{2+} ions, stacked alternately along the c -axis (Figure 1a). Structurally, ZnO has three types of fast growth directions: $\langle 2\bar{1}10 \rangle$ ($\pm[2\bar{1}10]$, $\pm[-12\bar{1}0]$, $\pm[-1\bar{1}20]$); $\langle 01\bar{1}0 \rangle$ ($\pm[01\bar{1}0]$, $\pm[10\bar{1}0]$, $\pm[1\bar{1}00]$); and $\pm[0001]$. Meanwhile, polar surfaces of ZnO are also important characteristic to decide the morphology of ZnO NWs.³ Under the interplay of these two factors, ZnO NWs exhibit a wide range of novel structures that can be grown by tuning the growth rates along these directions (Figure 1b).

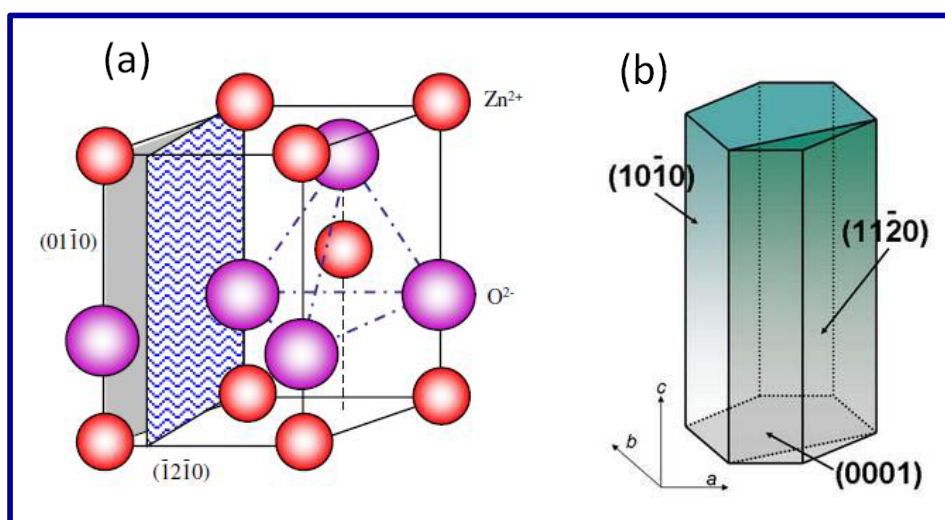


Figure 1. (a) The wurtzite structure model of ZnO, the tetrahedral coordination of Zn–O is shown in the unit cell. (b) Schematic diagram of wurtzite structure in crystallographic coordinates.³

ZnO NWs can be synthesized by various techniques including pulsed laser deposition,⁷ chemical vapor deposition,⁸ physical vapor deposition,^{9,10} thermal decomposition.¹¹ However, these technologies are either high-cost or non-versatile for

the application of large area devices, because they require relatively high energies and controlled atmospheres and they provide low growth rates and yields. Alternatively, hydrothermal deposition¹² and electrochemical deposition¹³ allow the preparation of large areas of vertically aligned NWs arrays at low temperatures and at high production rates and yields. It should be noted that the deposition technique affects the morphology of ZnO NWs as well. Figure 2 shows the different morphology of ZnO NWs by different techniques.

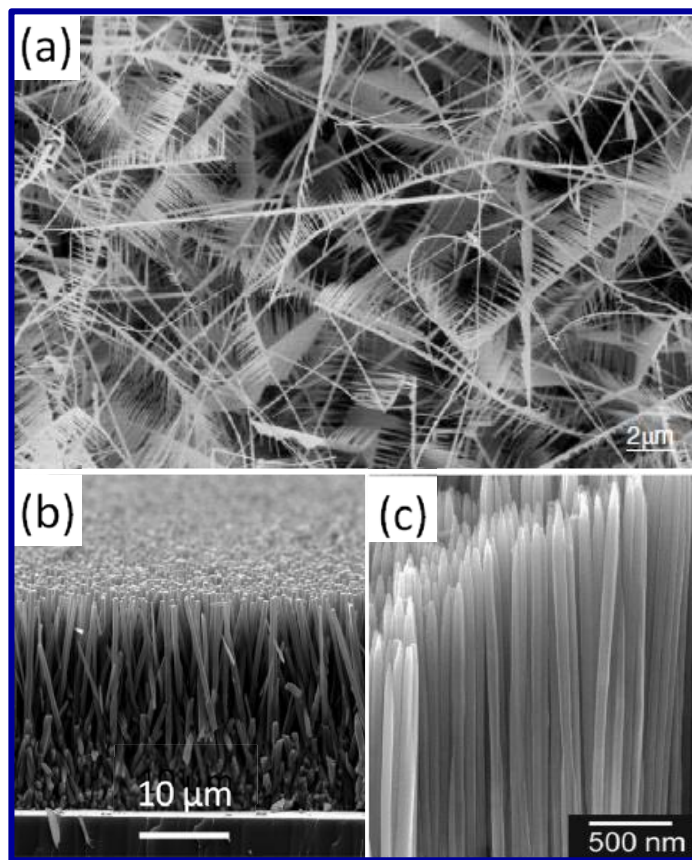


Figure 2. ZnO NWs grown by (a) Physical vapor deposition,¹⁰ (b) Hydrothermal deposition,¹² (c) Chemical vapor deposition.⁸

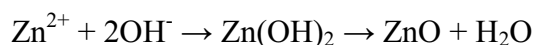
1.1.2 Electrochemical deposition of vertically aligned ZnO NWs

The electrochemical deposition of ZnO NW arrays, from a single source of Zn and oxygen, such as $\text{Zn}(\text{NO}_3)_2 \cdot 4\text{H}_2\text{O}$, is based on the generation of OH^- ions by the electroreduction of nitrate to nitrite and their posterior combination with Zn^{2+} to form $\text{Zn}(\text{OH})_2$. ZnO NWs grow at the cathode from the preferential $\text{Zn}(\text{OH})_2$ decomposition at the polar $\{0001\}$ surfaces of the ZnO structure.^{14,15}

Beside the fact that the electrochemical route allows the preparation of large areas of aligned NWs arrays at low temperatures (90 °C), additional advantages of the electrochemical deposition are that it does not require the seeds and provides faster growth rates and higher deposition yields.¹⁶ Importantly, the electrochemical deposition allows the extrinsic doping insided ZnO nanostructures by either cation¹⁷ or anion.^{13,18,19} However, the thicker diameter and shorter length of ZnO NWs grown by electrochemical deposition block its potential applications in a manner.

1.1.3 Hydrothermal deposition of vertically aligned ZnO NWs

In a typical hydrothermal deposition, ZnO NWs are synthesized based on the following reaction:



where hexamethylenetetramine (HMTA), NaOH, or NH_4OH may be used as the hydroxide source. In the reaction mixture, there is a high degree of supersaturation with respect to ZnO or $\text{Zn}(\text{OH})_2$, which consequently induces the formation of ZnO solid in the bulk solution through homogeneous nucleation as well as on the surface of pre-existing nuclei.¹²

The low-temperature hydrothermal method offers the potential for much lower cost because of eliminating the expense associated with high-temperature manufacturing and vacuum processing. In addition, hydrothermal synthesis is easily scalable to large areas and is compatible with roll-to-roll processing of soft plastic substrates. At the same time, the hydrothermal-route-synthesized NWs were found to be longer and thinner compared to the NWs fabricated by the other methods,^{12,20} which facilitates to improve the efficiency of ZnO NWs-based device. However, there are some disadvantages for hydrothermal deposition. One main disadvantage is that ZnO NWs can only grow at a pre-existing nucleus on seeded substrates. Also, it is difficult to introduce impurity ions into ZnO nanostructures for improving the carrier concentration.

1.1.4 Successive ionic layer adsorption and reaction (SILAR)

SILAR method is relatively a new method to produce thin film, first reported in 1985 by Ristov et al.²¹ The name SILAR was ascribed to this method by Nicolau²² and discussed in subsequent papers of Nicolau and coworkers,²³ which deals with ZnS, CdZnS and CdS thin films. The SILAR method is useful for the deposition of thin films of chalcogenide groups I–VI, II–VI, III–VI, V–VI, VIII–VI binary and I–III–VI, II–II–VI, II–III–VI, II–VI–VI and II–V–VI ternary chalcogenides and composite films.²⁴

It is relatively inexpensive, simple and convenient for large area deposition. It can be carried out in glass beakers. The starting materials are commonly available and low-cost. Figure 3 demonstrates the scheme of SILAR reaction steps.

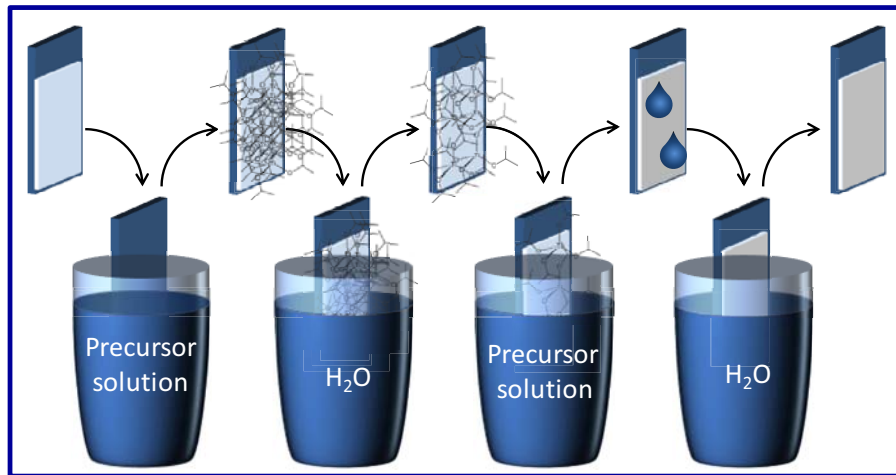


Figure 3. Scheme of SILAR reaction steps

In spite of its simplicity, SILAR has a number of advantages:²⁴ (i) It offers extremely easy way to dope film with virtually any element in any proportion by merely adding it in some form of the cationic solution; (ii) SILAR does not require high quality target and/or substrates nor does it require vacuum at any stage; (iii) The deposition rate and the thickness of the film can be easily controlled over a wide range by changing the deposition cycles; (iv) Operating at room temperature can produce films on less robust materials.

1.1.5 Extrinsic Doping of ZnO NWs

Extrinsic doping is an effective way to control the band gap and electrical conductivity of ZnO NWs. Many metals and nonmetals have been successfully used to dope ZnO NWs by various synthesis methods for improving the charge carrier concentration, such as: Co,²⁵ Cu,²⁶ Al,²⁷ Eu,²⁸ Sb,²⁹ F,³⁰ Cl,³¹ S,³² N.³³ It is also possible to convert ZnO NWs from n-type to p-type by using N₂O as a dopant source via vapor-liquid-solid growth.³⁴ Moreover, co-doping ZnO NWs such as: Mn + Li,³⁵ Mn + Co,³⁶ have also been studied recently. Among them, cationic-doping obtained by the

replacement of Zn has been commonly targeted. While anionic-doping offers the potential advantage of a higher processing simplicity, the replacement of oxygen by anions inside the ZnO structure has not been widely studied.

1.1.6 Scanning Probe Microscope (SPM) Characterization

SPM is a branch of microscopy that forms images of surfaces using a physical probe that scans the specimen. An image of the surface is obtained by mechanically moving the probe in a raster scan of the specimen, line by line, and recording the probe-surface interaction as a function of position. An applied potential on the Pt electrode allows obtaining the I - V characterization of single NW (Figure 4). It is a novel technique to study the conductivity of single NW.¹³

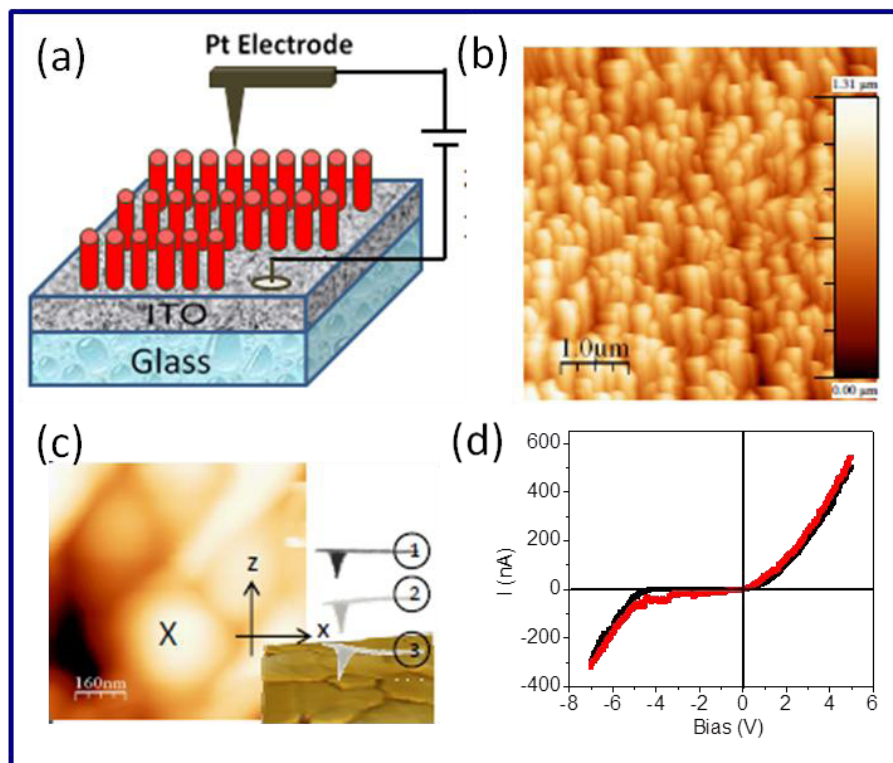


Figure 4. (a) Cartoon of the experimental set-up showing the ZnO NWs deposited on ITO substrate and measured by conducting SPM using a Pt tip, (b) Topographic image of ZnO NWs by SPM, (c) Scheme of Pt tip and surface of ZnO NW, (d) I - V characteristics of the ZnO NW measured by SPM.

1.1.7 Mott-Schottky Measurement

Mott-Schottky measurement is a standard technique, commonly used to determine both dopant density and flatband potential at semiconductor/liquid contacts.³⁷⁻³⁹ The depletion zone created in the semiconductor material is characterized by a capacitance measurement. The variation of the differential capacitance of the space charge layer, C_{sc} , is measured as a function of the applied potential. The theory predicts a linear dependence of C_{sc}^{-2} with the applied potential, as described by the following equation for an n-type semiconductor:

$$\frac{1}{C_{sc}^2} = \frac{2}{\epsilon\epsilon_0 e_0 N_d A^2} \left(E - E_{FB} - \frac{kT}{e_0} \right)$$

Where C_{sc} is the capacitance of the space charge region, ϵ_0 is the permittivity of the free space, ϵ is the relative dielectric constant of the semiconductor, e_0 is the electron charge, N_d is the free carrier concentration of the semiconductor, A is the area in contact with the electrolyte, E is the applied potential, E_{FB} is the flatband potential, k is the Boltzmann constant and T is the absolute temperature.

Two assumptions should be satisfied to apply the above relationships.⁴⁰ The first one is that the capacitance is assumed to be the space charge capacitance. The contribution of the double layer capacitance to the total capacitance is negligible because the space charge capacitance is much smaller than the double layer capacitance. The second one is that the equivalent circuit is a series combination of a resistor and a capacitance.

1.1.8 Photoluminescence (PL) Measurement

PL studies are a useful tool to examine the quality of ZnO nanostructures. In room temperature PL spectra of ZnO nanostructures, besides the typical UV emission, there are also one or more emission bands in the visible spectral region which originate from defect emissions. The origin of these emissions has not been conclusively established, and there have been a number of hypotheses proposed for each emission band.⁴¹⁻⁴³ It should be noted that most of the PL studies of ZnO nanostructures focus on the origin of defect emission or the ratio of UV-to-visible emission. The various contributions to the visible emission has been associated to oxygen vacancies,⁴⁴⁻⁴⁶ oxygen antisites, oxygen interstitial,^{47,48} zinc vacancy,^{49,50} zinc interstitials,^{51,52} and trapped OH⁻ groups.⁵³ On the other hand, evidences exist that the intensity of some contributions to the visible emission band depend on the material surface-to-bulk ratio.^{42,54,55} It should be mentioned that the controversy on the association of the transitions behind the visible PL emission is in part originated from the strong dependence of the PL emission on the ZnO preparation techniques, the specific growth parameters used and the applied post-growth treatments.⁵⁶

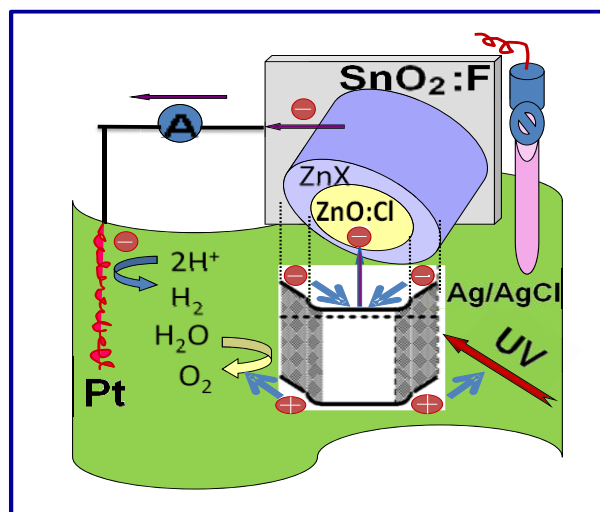
1.1.9 Electrochemical impedance spectroscopy (EIS)

The history of EIS begins with the introduction of impedance into electrical engineering by Oliver Heaviside in the 1880s.⁵⁷ EIS has been widely employed to study the kinetics of electrochemical and photoelectrochemical processes including the elucidation of electronic and ionic processes occurring in the dye-sensitized solar cells.⁵⁸⁻⁶²

EIS is a steady-state method measuring the current response to the application of an AC voltage as a function of the frequency.^{57,63} It is usually measured by applying an AC potential to an electrochemical cell and then measuring the current through the cell. The Nyquist diagram features typically three semicircles that in the order of increasing frequency are attributed to the Nernst diffusion within the electrolyte, the electron transfer at the oxide/electrolyte interface, and the redox reaction.⁶⁴ EIS data is commonly analyzed by fitting it to an equivalent electrical circuit model. Most of the circuit elements in the model are common electrical elements such as resistors, capacitors, and inductors. To be useful, the elements in the model should have a basis in the physical electrochemistry of the system.

An important advantage of EIS over other techniques is the possibility of using tiny AC voltage amplitudes exerting a very small perturbation on the system. It should be stressed that EIS cannot give all the answers. It is a complementary technique and other methods must also be used to elucidate the interfacial processes.

Introduction to block 2: Hetero/homo nanostructures based on ZnO:Cl nanowires for efficient photoelectrochemical cells



1.2.1 Photoelectrochemical (PEC) cells

Hydrogen represents a potentially high-efficiency and environmentally clean fuel. PEC water decomposition is the most promising method for hydrogen generation using a source of renewable energy.^{65,66} The generation of hydrogen from PEC water splitting was first demonstrated by Honda and Fujishima in 1972.⁶⁷ A typical photoelectrochemical cell consists of a photoactive semiconductor working electrode (either n- or p-type) and counter electrode made of either metal (e.g. Pt) or semiconductors. Both electrodes are immersed in the electrolyte containing suitable redox couples (Figure 5a).

A working principle is elucidated here by taking an n-type semiconductor as the photoanode (Figure 5b). Under irradiation with the photon energy equal to or exceeding the band-gap energy of the semiconductor photoanode, the electrons are excited and

promoted from the valence band (VB) to the unoccupied conduction band (CB). The electrons transport to the cathode and react with protons to generate hydrogen ($2\text{H}^+ + 2\text{e}^- \rightarrow \text{H}_2$), while the holes accumulate on the surface of the photoanode and react with water molecules to produce oxygen ($\text{H}_2\text{O} + 2\text{h}^+ \rightarrow 2\text{H}^+ + 1/2\text{O}_2$).

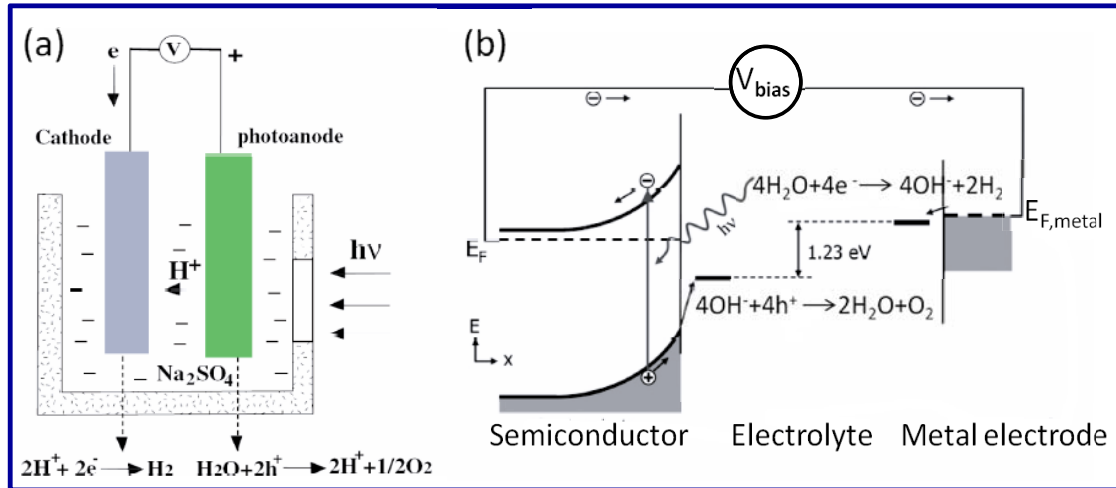


Figure 5. (a) Schematic of a typical PEC device and its basic operation mechanism for hydrogen generation from water splitting. (b) Energy diagram of a PEC cell consisting of an n-type semiconductor photoanode and metal cathode for water splitting.⁶⁵

At the interface between the semiconductor and electrolyte, changing the potential applied to the electrode results in a change of the band bending of the semiconductor. The charge transfer abilities of a semiconductor electrode depend on whether there is an accumulation layer or a depletion layer (Figure 6). If there is an accumulation layer, the behavior of a semiconductor electrode is similar to that of a metallic electrode, since there is an excess of the majority charge carriers available for charge transfer. In contrast, if there is a depletion layer, then there are few charge carriers available for charge transfer, and electron transfer reactions occur slowly. For an n-type semiconductor at positive potentials, the band edges curve upwards, and hence the hole

moves towards the interface, and the electron moves to the interior of the semiconductor. In this case, the n-type semiconductor electrode acts as a photoanode. At potentials positive of the flatband potential, a depletion layer exists, so there can be no oxidative current in the dark. However, a photocurrent can be observed upon irradiation. At potentials negative of the flatband potential, there can be always current both in the dark and under illumination since there is an accumulation layer in this case (Figure 6).

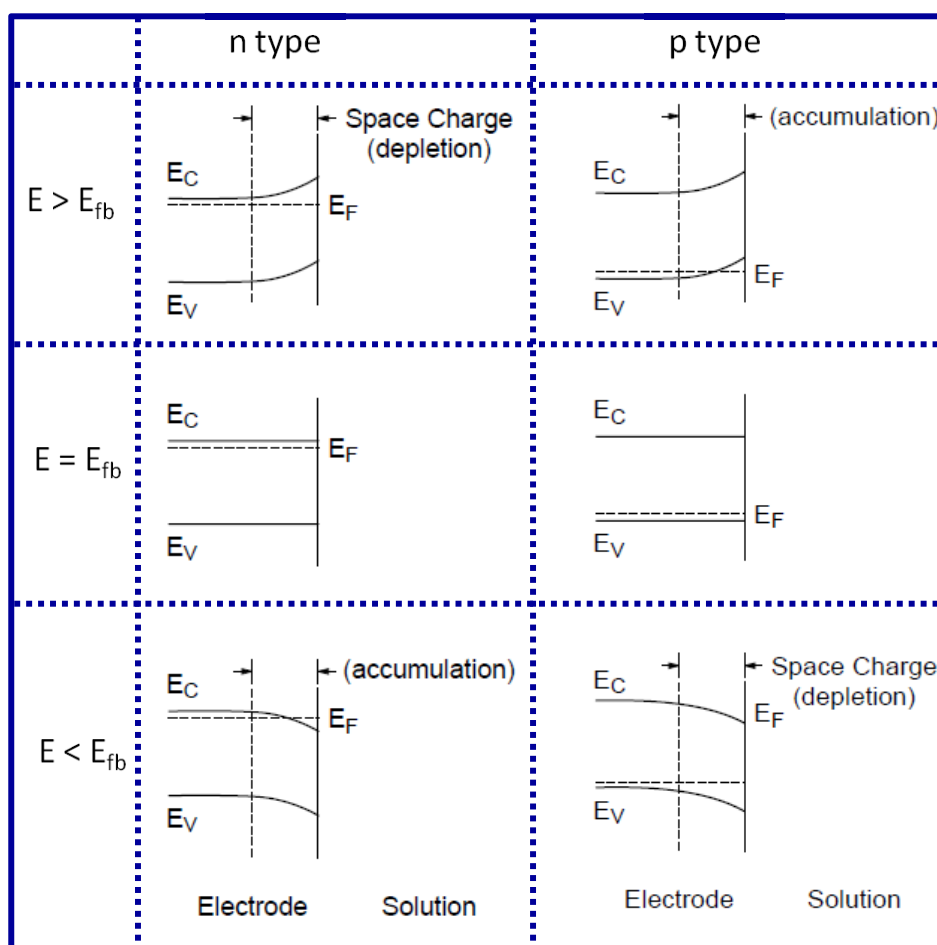


Figure 6. Effect of varying the applied potential on the band edges in the interior of n-type and p-type semiconductor.

In order to obtain efficient PEC cells, the semiconductor photoanode should meet several criteria:^{66,68} (i) With a conduction band edge more negative than the H_2

evolution potential and a valence band edge more positive than the O₂ evolution potential; (ii) Photochemically stable with good corrosion resistance in aqueous solution; (iii) Strong absorption in the solar spectrum region.

1.2.2 ZnO NWs-based PEC cells

ZnO NWs electrode offers some potential advantages over their bulk counterparts for photoelectrodes in PEC:⁶⁵ (i) It provides a larger surface area for the redox reactions to take place; (ii) The small sizes of NWs reduce the distance for photogenerated holes to diffuse to the photoanode/electrolyte interface for the oxidation of water. (iii) The optical and electronic properties can be designed and modified by varying the nanomaterial structure. (iv) The unique synthetic strategy avoids the formation of dislocations due to the lattice mismatch between growth substrate and semiconductor.

Various approaches have been used to improve the efficiency of ZnO NWs-based PEC cells: (i) The enhanced PEC responses were obtained by annealing intrinsic ZnO NWs in mixed Ar/N₂ gas ambient;⁶⁹ (ii) N doped ZnO NW arrays as photoanodes displayed an enhancement of photoresponse in the visible region and an order of magnitude increase in photocurrent density compared to undoped ZnO NWs;³³ (iii) The presence of a ZnO shell enhances the photoelectrochemical properties of ZnO:Cl nanowires up to a factor 5.⁷⁰ (iv) Heterogeneous nanostructures, such as: ZnO/ZnS,⁷¹ ZnO/CdS,⁷² ZnO/ZnSe,⁷³ ZnO/CdTe,^{74,75} ZnO/ Zn_xCd_{1-x}Se,⁷⁶ have also demonstrated improved PEC photocurrent density because of the extended absorption bands in the visible spectrum.

1.2.3 Characterization of PEC cells

The efficiency of photon-to-hydrogen generation (η) should be the ratio of the power used in water splitting to the input light power. Assuming that all the electrons and holes are consumed in the redox reaction, η can be calculated using the equation:⁶⁶

$$\eta = \frac{I(1.23 - V_{bias})}{J_{light} \times A}$$

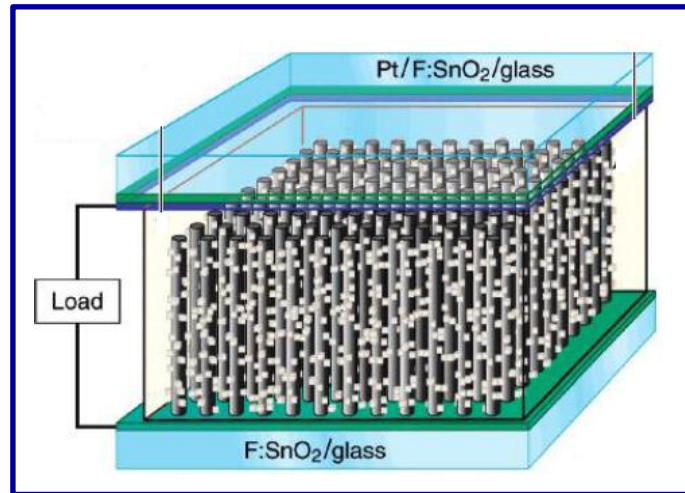
where I is the photocurrent, 1.23V is the theoretical potential required for water splitting, The J_{light} (W/m^2) is the light irradiance, and A is the irradiated area (m^2). V_{bias} (V) is the applied external potential, $V_{bias} = V_{meas} - V_{aoc}$, where V_{meas} is the electrode potential (versus Ag/AgCl) of the working electrode at which photocurrent was measured under illumination (I in W/m^2) and V_{aoc} is the electrode potential (versus Ag/AgCl) of the same working electrode under open circuit conditions, under the same illumination and in the same electrolyte.

The efficiency of a PEC device may also be evaluated by the incident photon-to-current conversion efficiency (IPCE), which is defined by the number of electrons generated by light in the external circuit divided by the number of incident photons:⁶⁶

$$IPCE = \frac{1240 \times I_{PH}}{\lambda \times P_{light}}$$

where I_{PH} is the generated photocurrent density (A/m^2), λ is the incident light wavelength (nm), P_{light} is the photon flux (W/m^2), and 1240 is the unit correction factor. IPCE reveals the photoresponse of the semiconductor photoanode as a function of incident wavelength.

Introduction to block 3: Photovoltaic performance of dye-sensitized solar cells based on ZnO nanowires



1.3.1 Dye-sensitized solar cells (DSCs)

Since the breakthrough in 1991,⁷⁷ DSCs have attracted a lot of attention because of their exciting possibility of application in solar energy conversion.⁷⁸ Compared with other solar cell technologies, DSCs have some outstanding features: low-cost investments and fabrication, better performance under diffuse light conditions and at higher temperatures. DSCs also offer the possibilities to design solar cells with a large flexibility in shape, color, and transparency.

The components of liquid DSCs usually include four parts, which are introduced one by one as follows:

(1) Working electrode

As a backbone semiconductor material in DSCs, nanostructured metal oxides are typically used as working electrode, such as TiO_2 , ZnO , SnO , and Nb_2O_5 .^{79,80} Besides

these simple oxides, ternary oxides, such as SrTiO_3 ⁸¹ and Zn_2SnO_4 ,⁸² have also been investigated, as well as core-shell structures, such as ZnO coated with TiO_2 ,⁸³⁻⁸⁵ ZnO coated with SnO_2 .⁸⁶

(2) Dye

The dye is one of the crucial parts in DSCs, it should fulfill some essential characteristics:⁷⁸ (i) The absorption spectrum of the dye should cover the whole visible region; (ii) The dye should have anchoring groups to strongly bind it onto the semiconductor surface; (iii) The excited state level of the photosensitizer should be higher in energy than the conduction band edge of n-type semiconductor; (iv) The oxidized state level of the dye must be more positive than the redox potential of electrolyte for dye regeneration; (v) The photostable, electrochemical and thermal stability of the dye are also required.

(3) Electrolyte

The redox electrolyte is a unique feature and a main component in DSCs. The redox potential of the electrolyte determines, in conjunction with the conduction band position of the mesoporous metal oxide, the maximum achievable open circuit voltage (V_{oc}). The I^-/I_3^- couple is the most investigated redox system for DSCs.^{87,88} Some alternative redox couples have been studied recently, such as: $\text{Br}^-/\text{Br}_3^-$,⁸⁹ $\text{SCN}^-/(\text{SCN})_3^-$,⁹⁰ $\text{S}^{2-}/\text{S}_x^{2-}$,⁹¹ cobalt (III/II) redox complexes.⁹²⁻⁹⁷ Among them, cobalt (III/II) redox complexes have been demonstrated as excellent alternatives to the I^-/I_3^- redox couple in DSC because it offers various advantages over I^-/I_3^- .^{96,97}

(4) Counter electrode

The counter electrode is used to make a connection to the electrolyte so that a current can be applied to the working electrode. It is usually made of an inert material to keep it from dissolving. A thin catalytic layer of platinum onto a conducting glass substrate has

been generally used.⁹⁸ Alternatively, carbon materials are also suited as catalysts for the reduction of triiodide.^{99,100} Very recently, low-cost quaternary $\text{Cu}_2\text{ZnSnS}_4$ nanocrystals were used to fabricate a novel Pt-free counter electrode for DSCs.¹⁰¹

1.3.2 ZnO NWs-based DSCs

While the highest efficiency reported for ZnO-based DSC up to now is 7.5% far from the record efficiency of 12.3% for TiO_2 ,^{95,102} ZnO presents excellent bulk electron mobility (more than one order of magnitude larger than anatase TiO_2)¹⁰³ and various morphologies of nanostructures. Moreover, vertically aligned ZnO NWs can significantly increase the electron diffusion length and decrease the recombination.⁶ This unique combination of properties opens wide possibilities of the rational design and development of ZnO NWs-based DSCs. However, the conversion efficiency of the DSCs based on ZnO NWs with the length around 10 μm is less than 1.6 % from the past reports.^{104,105} Recently, the ultralong ZnO NWs with up to 33 μm was employed to fabricate DSCs, which results in greatly improved performance compared to previously reported ZnO nanowire-based DSCs ($\eta=2.1\%$).¹⁰⁶ Subsequently, a record energy conversion efficiency of 7% has been demonstrated with multilayer assembly of ZnO NW arrays.⁸³ Meanwhile, ZnO Nanotubes,¹⁰⁷ ZnO nanosheet,¹⁰⁸ ZnO nanoflower/nanoforest,¹⁰⁹ hierarchical structure ZnO NWs/nanoporous layer,¹¹⁰ ZnO NWs/ TiO_2 shell⁸³⁻⁸⁵ have also been studied for fabrication of efficient DSCs.

In the structure of ZnO NWs-based DSCs, electrolyte plays an important role. In the past 20 years, the I^-/I_3^- redox shuttle has survived as the best performing electrolyte because it combines very fast dye regeneration with a slow back reaction of photo-injected electrons with the oxidized redox species. However, I^-/I_3^- electrolyte also has

some disadvantages:¹¹¹ (i) Inferior long-term stability and incompatibility with some metallic component materials; (ii) The Γ/I_3^- based redox electrolytes absorb light in the blue part of the spectrum, lowering the short circuit photocurrent and hence the power conversion efficiency of the devices; (iii) The potential mismatch between the redox couple and a typical sensitizer causes a loss V_{oc} in the device. Comparably, cobalt (III/II) polypyridyl complexes as a promising alternative redox couples offer various advantages over Γ/I_3^- :⁹²⁻⁹⁷ (i) Reduced corrosiveness towards relevant metals; (ii) Lower absorption in the visible; (iii) Facile tuning of the redox potential, with the capability to minimize energy loss in the dye regeneration step.

1.3.3 Characterization techniques of DSCs

(1) J - V characterization

The current-voltage (J - V) characteristics of a solar cell under illumination are used to determine the power conversion efficiency. The power conversion efficiency is given by:⁷⁸

$$\eta = \frac{|JV|_{max}}{P_{in}} = \frac{J_{sc}V_{oc}FF}{P_{in}}$$

Where J_{sc} is the short-circuit current, is determined at the $V=0$ V intercept. V_{oc} is the open-circuit potential, is found at the $I=0$ intercept. P_{in} is the power density of the incident light and FF is the fill factor.

(2) Incident photon to current conversion efficiency (IPCE)

In DSCs, the spectral response is determined by measuring the IPCE. The IPCE can be expressed as follows:⁷⁸

$$IPCE(\lambda) = LHE(\lambda)\varphi_{inj}(\lambda)\varphi_{reg}\eta_{cc}(\lambda)$$

where LHE is the light-harvesting efficiency, $LHE=(1-10^{-A})$, with A being the absorbance of the film. φ_{inj} and φ_{reg} are the quantum yields for electron injection and dye regeneration, respectively, and η_{cc} is the charge collection efficiency.

A very useful test is to calculate J_{sc} in full sunlight from the obtained IPCE spectrum:⁷⁸

$$J_{sc} = \int IPCE(\lambda) e\phi_{ph,AM1.5G}(\lambda)d\lambda$$

where e is the elementary charge and $\phi_{ph,AM1.5G}$ is the photon flux in AM 1.5 G, 100 mW cm^{-2} .

(3) Electron Lifetime Measurements

The electron lifetime (τ_e) in DSCs is used to determine the recombination dynamics in the solar cell. Charge carrier lifetimes can be determined from voltage decay transient using the following equation:¹¹²

$$\tau_e = -\frac{k_B T}{e} \left(\frac{dV_{oc}}{dt} \right)^{-1}$$

where k_B stands for the Boltzmann constant, T for temperature and e represents the elementary electron charge.

(4) Charge extraction measurements

Charge extraction (Q) measurements are useful to study the relationship between the photovoltage decay and the charge stored in the cell. The exponential behaviour of the charge versus open circuit voltage is consistent with an exponential distribution of trap states below the conduction band edge, the density of trap states $g(E)$ is given by:¹¹³

$$g(E) = g_0 \exp \left[\frac{E - E_{F0}}{m_c} \right]$$

where g_0 is the trap density at the equilibrium-Fermi level of the ZnO electrode in darkness, and m_c is the slope of the exponential trap distribution.

1.4 References

1. Xu, S.; Wang, Z. L. *Nano Res.* **2011**, *4*, 1013–1098.
2. Li, L.; Zhai, T. Y.; Bando, Y.; Golberg, D. *Nano Energy*, **2012**, *1*, 91–106.
3. Wang, Z. L. *J. Phys.: Condens. Matter* **2004**, *16*, 829–858.
4. McCune, M.; Zhang, W.; Deng, Y. L. *Nano Lett.* **2012**, *12*, 3656–3662.
5. Xu, C. K.; Wu, J. M.; Desai, U. V.; Gao, D. *Nano Lett.*, **2012**, *12*, 2420–2424.
6. Martinson, A. B. F.; Goes, M. S.; Fabregat-Santiago, F.; Bisquert, J.; Pellin, M. J.; Hupp, J. T. *J. Phys. Chem. A* **2009**, *113*, 4015–4021.
7. Sun, Y.; Fuge, G. M.; Ashfold, M. N. R. *Chem Phys Lett.* **2004**, *396*, 21–6.
8. Park, W. I.; Kim, D. H.; Jung, S. W.; Yi, G. C. *Appl. Phys. Lett.* **2002**, *80*, 4232–4234.
9. Kong, Y. C.; Yu, D. P.; Zhang, B.; Fang, W.; Feng, S. Q. *Appl. Phys. Lett.*, **2001**, *78*, 407–409.
10. Wang, Z. L.; Kong, X. Y.; Zuo, J. M. *Phys. Rev. Lett.* **2003**, *91*, 185502.
11. Vayssieres, L. *Adv. Mater.* **2003**, *15*, 464–466.
12. Xu, C. K.; Shin, P.; Cao, L. L.; Gao, D. *J. Phys. Chem. C* **2010**, *114*, 125–129.
13. Fan, J. D.; Shavel, A.; Zamani, R.; Fábrega, C.; Rousset, J.; Haller, S.; Güell, F.; Carrete, A.; Andreu, T.; Arbiol, J.; Morante, J. R.; Cabot, A. *Acta Mater.* **2011**, *59*, 6790–6800.
14. Izaki, M.; Omi, T. *J. Electrochem. Soc.* **1996**, *143*, 53–55.
15. Peulon, S.; Lincot, D. *J. Electrochem. Soc.* **1998**, *145*, 864–784.
16. Peulon, S.; Lincot, D. *Adv. Mater.* **1996**, *8*, 166–170.
17. Thomas, M. A.; Cui, J. B. *J. Vac. Sci. Technol. B* **2009**, *27*, 1673–1677.
18. Elias, J.; Tena-Zaera, R.; Lévy-Clément, C. *J. Phys. Chem. C* **2008**, *112*, 5736–5741.
19. Cui, J. B.; Soo, Y. C.; Chen, T. P.; Gibson, U. J. *J. Phys. Chem. C* **2008**, *112*, 4475–4479.

20. Qiu, J.J.; Li, X. M.; Zhuge, F. W.; Gan, X. Y.; Gao, X. D.; He, W. Z.; Park, S.-J.; Kim, H.-K.; Hwang, Y.-H. *Nanotechnology*, **2010**, *21*, 195602.
21. Ristov, M.; Sinadinovski, G. J.; Grozdanov, I. *Thin Solid Films* **1985**, *123*, 63-67.
22. Nicolau, Y. F. *Appl. Surf. Sci.* **1985**, *22-23*, 1061-1074.
23. Nicolau, Y. F.; Minnard, J. C. *J. Cryst. Growth* **1988**, *92*, 128-142.
24. Pathan, H. M.; Lokhande, C. D. *Bull. Mater. Sci.* **2004**, *27*, 85-111.
25. Wang, B. Q.; Shan, X. D.; Fu, Q.; Javed, I.; Lv, Y.; Fu, H. G.; Yu, D. P. *Physica E* **2009**, *41*, 413-417.
26. Kataoka, T.; Yamazaki, Y.; Singh, V. R. *Physical Review B*, **2011**, *84*, 153203.
27. Kim, K. P.; Chang, D.; Lim, S. K.; Lee, S. K.; Lyu, H. K.; Hwang, D.K. *Curr. Appl. Phys.* **2011**, *11*, 1311-1314.
28. Wang, D.; Xing, G.; Gao, M.; Yang, L.; Yang, J.; Wu, T. *J. Phys. Chem. C* **2011**, *115*, 22729-22735.
29. Kedem, N.; Edri, E.; Kokotov, M.; Cohen, H.; Bendikov, T.; Popovitz-Biro, R.; Huth, P. Ginley, D.; Hodes, G. *Cryst. Growth Des.* **2010**, *10*, 4442-4448.
30. Xu, H. Y.; Liu, Y. C.; Mu, R.; Shao, C. L.; Lu, Y. M.; Shen, D. Z.; Fan, X. W. *Appl. Phys. Lett.* **2005**, *86*, 123107.
31. Rousset, J.; Saucedo, E.; Lincot, D. *Chem Mater*, **2009**, *21*, 534-540.
32. Shen, G. Z.; Cho, J. H.; Jung, S. I.; Lee, C. J. *Chem. Phys. Lett.* **2005**, *401*, 529-533.
33. Yang, X. Y.; Wolcott, A.; Wang, G. M.; Sobo, A.; Fitzmorris, R. C.; Qian, F.; Zhang, J. Z.; Li, Y. *Nano Lett.* **2009**, *9*, 2331-2336.
34. Yuan, G. D.; Zhang, W. J.; Jie, J. S.; Fan, X.; Zapien, J. A.; Leung, Y. H.; Luo, L. B.; Wang, P. F.; Lee, C. S.; Lee, S. T. *Nano Lett.* **2008**, *8*, 2591-2597.
35. Zou, C. W.; Shao, L. X.; Guo, L. P.; Fu, D. J.; Kang, T. W. *J. Cryst. Grow.* **2011**, *331*, 44-48.
36. Li, H.; Huang, Y.; Zhang, Q. *Nanoscale* **2011**, *3*, 654-660.
37. Mora-Sero, I.; Fabregat-Santiago, F.; Denier, B.; Bisquert, J. *Appl. Phys. Lett.* **2006**, *89*, 203117.
38. Wolcott, A.; Smith, W. A.; Kuykendall, T. R.; Zhao, Y. P.; Zhang, J. Z. *Adv. Funct. Mater.* **2009**, *19*, 1849-1856.
39. Mani, A.; Huisman, C.; Goossens, A.; Schoonman, J. *J. Phys. Chem. B* **2008**, *112*, 10086-10091.
40. Fabregat-Santiago, F.; Garcia-Belmonte, G.; Bisquert, J.; Bogdanoff, P.; Zaban, A. *J. Electrochem. Soc.* **2003**, *150*, E293-E298.

41. Djurišić, A. B.; Leung, Y. H. *Small* **2006**, *2*, 944-961.
42. Fan, J. D.; Güell, F.; Fábrega, C.; Fairbrother, A.; Andreu, T.; López, A. M.; Morante, J. R.; Cabot, A. *J. Phys. Chem. C* **2012**, *116*, 19496–19502.
43. Djurišić, A. B.; Ng, A. M. C.; Chen, X. Y. *Prog. Quant. Electron.* **2010**, *34* 191–259.
44. Vanheusden, K.; Seager, C. H.; Warren, W. L.; Tallant, D. R.; Voigt, J. A. *Appl. Phys. Lett.* **1996**, *68*, 403-405.
45. Ahn, M.-W.; Park, K.-S.; Heo, J.-H.; Park, J.-G.; Kim, D.-W.; Choi, K. J.; Lee, J. H.; Hong, S.-H. *Appl. Phys. Lett.* **2008**, *93*, 263103.
46. Van Dijken, A.; Meulenkamp, E. A.; Vanmaekelberg, D.; Meijerink, A. *J. Phys. Chem. B* **2000**, *104*, 4355-4360.
47. Fan, X. M.; Lian, J. S.; Jiang, Q.; Zhou, Z. W. *J. Mater. Sci.* **2007**, *42*, 2678-2683.
48. Chang, S.-S. *J. Korean Ceram. Soc.* **2011**, *48*, 251-256.
49. Janotti, A.; Van de Walle, C. G. *Phys. Rev. B* **2007**, *76*, 165202.
50. Manzano, C. V.; Alegre, D.; Caballero-Calero, O.; Alén, B.; Martín-González, M. *S. J. Appl. Phys.* **2011**, *110*, 043538.
51. Liua, Z. W.; Ong, C. K.; Yu, T.; Shen, Z. X. *Appl. Phys. Lett.* **2006**, *88*, 053110.
52. Zeng, H.; Duan, G.; Li, Y.; Yang, S.; Xu, X.; Cai, W. *Adv. Funct. Mater.* **2010**, *20*, 561-572.
53. Manzano, C. V.; Alegre, D.; Caballero-Calero, O.; Alén, B.; Martín-González, M. S. *J. Appl. Phys.* **2011**, *110*, 043538.
54. Shalish, I.; Temkin, H.; Narayanamurti, V. *Phys. Rev. B* **2004**, *69*, 245401.
55. Chang, P.-C.; Chien, C.-J.; Stichtenoth, D.; Ronning, C.; Lu, J. G. *Appl. Phys. Lett.* **2007**, *90*, 113101.
56. Ahn, C. H.; Kim, Y. Y.; Kim, D. C.; Mohanta, S. K.; Cho, H. K. *J. Appl. Phys.* **2009**, *105*, 013502.
57. Ross, M. J. *Ann. Biomed. Eng.* **1992**, *20*, 289-305.
58. Wang, Q.; Moser, J.-E.; Grätzel, M. *J. Phys. Chem. B* **2005**, *109*, 14945-14953.
59. Bisquert, J. *Phys. Chem. Chem. Phys.* **2000**, *2*, 4185-4192.
60. Bisquert, J.; Garcia-Belmonte, G.; Fabregat-Santiago, F.; Ferriols, N. S.; Bogdanoff, P.; Pereira, E. C. *J. Phys. Chem. B* **2000**, *104*, 2287-2298.
61. Schwarzburg, K.; Willig, F. *J. Phys. Chem. B* **2003**, *107*, 3552-3555.
62. Bisquert, J. *J. Phys. Chem. B* **2002**, *106*, 325-333.

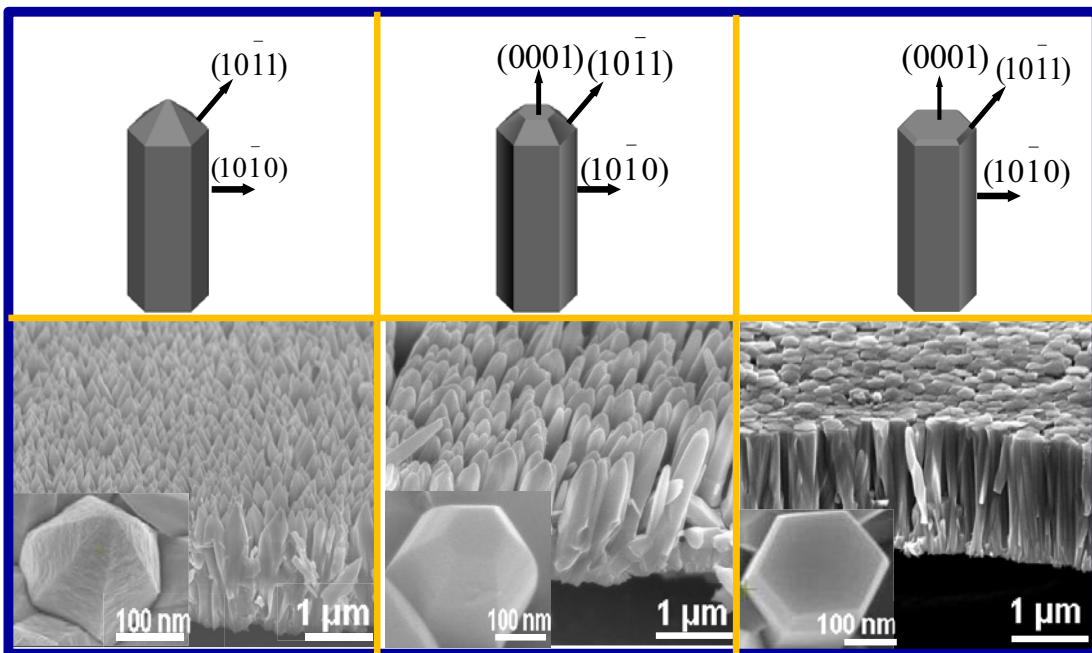
63. Ross, M. J.; William, K. R. *Impedance Spectroscopy: Emphasizing Solid Materials and Systems*; John Wiley & Sons: New York, 1987.
64. Kern, R.; Sastrawan, R.; Ferber, J.; Stangl, R.; Luther, J. *Electrochim. Acta* **2002**, *47*, 4213-4255.
65. Li, Y.; Zhang, J. Z. *Laser Photonics Rev.* **2010**, *4*, 517-528.
66. Bak, T.; Nowotny, J.; Rekas, M.; Sorrell, C. C. *Int. J. Hydrogen Energy* **2002**, *27*, 991-1022.
67. Fujishima, A.; Honda, K. *Nature* **1972**, *238*, 37-38.
68. Khaselev, O.; Turner, J. A. *Science* **1998**, *280*, 425-427.
69. Ahn, K.-S.; Shet, S.; Deutsch, T.; Jiang, C.-S.; Yan, Y. F.; Al-Jassim, M.; Turner, J. *J. Power Sources* **2008**, *176*, 387-392.
70. Fan, J. D.; Guell, F.; Fabrega, C.; Shavel, A.; Carrete, A.; Andreu, T.; Morante, J. R.; Cabot, A. *Appl. Phys. Lett.* **2011**, *99*, 262102.
71. Fan, J. D.; Fábrega, C.; Zamani, R.; Shavel, A.; Güell, F.; Carrete, A.; Andreu, T.; López, A. M.; Morante, J. R.; Arbiol, J.; Cabot, A. *J. Alloy. Compd.* **2013**, *555*, 213-218.
72. Tak, Y.; Hong, S. J.; Lee, J. S.; Yong, K. J. *J. Mater. Chem.* **2009**, *19*, 5945-5951.
73. Cho, S.; Jang, J.-W.; Lim, S.-H.; Kang, H. J.; Rhee, S.-W.; Lee, J. S.; Lee, K.-H. *J. Mater. Chem.* **2011**, *21*, 17816-17822.
74. Chen, H. M.; Chen, C. K.; Chang, Y. C.; Tsai, C. W.; Liu, R. S.; Hu, S. F.; Chang, W. S.; Chen, K. H. *Angew. Chem., Int. Ed.* **2010**, *49*, 5966-5969.
75. Wang, X.; Zhu, H.; Xu, Y.; Wang, H.; Tao, Y.; Hark, S.; Xiao, X.; Li, Q. *ACS Nano* **2010**, *4*, 3302-3308.
76. Li, H. X.; Cheng, C. W.; Li, X. L.; Liu, J. P.; Guan, C.; Tay, Y. Y.; Fan, H. J. *J. Phys. Chem. C*, **2012**, *116*, 3802-3807.
77. O'Regan, B.; Grätzel, M. *Nature* **1991**, *353*, 737-740.
78. Hagfeldt, A.; Boschloo, G.; Sun, L. C.; Kloo, L.; Pettersson, H. *Chem. Rev.* **2010**, *110*, 6595-6663.
79. Hamann, T. W.; Jensen, R. A.; Martinson, A. B. F.; Van Ryswyk, H.; Hupp, J. T. *Energy Environ. Sci.* **2008**, *1*, 66-78.
80. Pagliaro, M.; Palmisano, G.; Ciriminna, R.; Loddo, V. *Energy Environ. Sci.* **2009**, *2*, 838-844.
81. Yang, S. M.; Kou, H. Z.; Wang, J. C.; Xue, H. B.; Han, H. L.; *J. Phys. Chem. C* **2010**, *114*, 4245-4249.

82. Tan, B.; Toman, E.; Li, Y. G.; Wu, Y. Y. *J. Am. Chem. Soc.* **2007**, *129*, 4162-4163.
83. Xu, C. K.; Wu, J. M.; Desai, U. V.; Gao, D. *J. Am. Chem. Soc.* **2011**, *133*, 8122–8125.
84. Law, M.; Greene, L.E.; Radenovic, A.; Kuykendall, T.; Liphardt, J.; Yang, P. D. *J. Phys. Chem. B* **2006**, *110*, 22652–22663.
85. Fan, J. D.; Zamani, R.; Fábrega, C.; Shavel, A.; Flox, C.; Ibáñez, M.; Andreu, T.; López, A. M.; Arbiol, J.; Morante, J. R.; Cabot, A. *J. Phys. D: Appl. Phys.* **2012**, *45*, 415301.
86. Kay, A.; Grätzel, M. *Chem. Mater.* **2002**, *14*, 2930-2935.
87. Hagfeldt, A.; Grätzel, M. *Chem. Rev.* **1995**, *95*, 49-68.
88. Grätzel, M. *Inorg. Chem.* **2005**, *44*, 6841-6851.
89. Wang, Z. S.; Sayama, K.; Sugihara, H. *J. Phys. Chem. B* **2005**, *109*, 22449-22455.
90. Butler, M. A.; Ginley, D. S. *J. Electrochem. Soc.* **1978**, *125*, 228-232.
91. Liu, J.; Yang, X. C.; Cong, J. Y.; Kloo, L.; Sun, L. C. *Phys. Chem. Chem. Phys.* **2012**, *14*, 11592–11595.
92. Wang, M. K.; Grätzel, C.; Zakeeruddin, S. M.; Grätzel, M. *Energy Environ. Sci.* **2012**, *5*, 9394-9405.
93. Aribia, K. B.; Moehl, T.; Zakeeruddin, S. M.; Grätzel, M. *Chem. Sci.* **2013**, *4*, 454-459.
94. Mosconi, E.; Yum, J. H.; Kessler, F.; Gomez-Garcia, C. J.; Zuccaccia, C.; Cinti, A.; Nazeeruddin, M. K.; Grätzel, M.; De Angelis, F. *J. Am. Chem. Soc.* **2012**, *134*, 19438-19453.
95. Yella, A.; Lee, H. W.; Tsao, H. N.; Yi, C. Y.; Chandiran, A. K.; Nazeeruddin, Md. K.; Diau, E. W. G.; Yeh, C. Y.; Zakeeruddin, S. M.; Grätzel, M. *Science* **2011**, *334*, 629-634.
96. Feldt, S. M.; Gibson, E. A.; Gabrielsson, E.; Sun, L. C.; Boschloo, G.; Hagfeldt, A. *J. Am. Chem. Soc.* **2010**, *132*, 16714–16724.
97. Fan, J. D.; Hao, Y.; Cabot, A.; Johansson, E. M. J.; Boschloo, G.; Hagfeldt, A. *ACS Appl. Mater. Interfaces* **2013**, *5*, 1902–1906.
98. Papageorgiou, N.; Maier, W. F.; Grätzel, M. *J. Electrochem. Soc.* **1997**, *144*, 876-884.
99. Kay, A.; Grätzel, M. *Sol. Energy Mater. Sol. Cells* **1996**, *44*, 99-117.

100. Murakami, T. N.; Ito, S.; Wang, Q.; Nazeeruddin, M. K.; Bessho, T.; Cesar, I.; Liska, P.; Humphry-Baker, R.; Comte, P.; Pechy, P.; Grätzel, M. *J. Electrochem. Soc.* **2006**, *153*, A2255-A2261.
101. Xin, X. K.; He, M.; Han, W.; Jung, J.; Lin, Z. Q. *Angew. Chem. Int. Ed.* **2011**, *50*, 11739–11742.
102. Memarian, N.; Concina, I.; Braga, A.; Rozati, S. M.; Vomiero, A.; Sberveglieri, G. *Angew. Chem., Int. Ed.* **2011**, *50*, 12321–12325.
123. Wang, Z. L. *Mater. Today* **2004**, *7*, 26–33.
104. Lupan, O.; Guérin, V. M.; Tiginyanu, I. M.; Ursaki, V. V.; Chow, L.; Heinrich, H.; Pauporté, T. J. *Photoch. Photobio. A* **211** (2010) 65–73.
105. Law, M.; Greene, L.E.; Johnson, J.C.; Saykally, R.; Yang, P.D. *Nat. Mater.* **2005**, *4*, 455–459.
106. Xu, C. K.; Shin, P.; Cao, L. L.; Gao, D. *J. Phys. Chem. C* **2010**, *114*, 125–129.
107. Martinson, A. B. F.; Elam, J. W.; Hupp, J. T.; Pellin, M. J. *Nano Lett.* **2007**, *7*, 2183–2187.
108. Lin, C.-Y.; Lai, Y.-H.; Chen, H.-W.; Chen, J.-G.; Kung, C.-W.; Vittal, R.; Ho, K.-C. *Energy Environ. Sci.* **2011**, *4*, 3448–3455.
109. Ko, S. H.; Lee, D.; Kang, H. W.; Nam, K. H.; Yeo, J. Y.; Hong, S. J.; Grigoropoulos, C. P.; Sung, J. H. *Nano Lett.* **2011**, *11*, 666–671.
110. Guérin, V.-M.; Pauporté, T. *Energy Environ. Sci.* **2011**, *4*, 2971–2979.
111. Boschloo, G.; Hagfeldt, A. *Acc. Chem. Res.* **2009**, *42*, 1819-1826.
112. Zaban, A.; Greenshtein, M.; Bisquert, J. *ChemPhysChem* **2003**, *4*, 859–864.
113. Boschloo, G.; Halggman, L.; Hagfeldt, A. *J. Phys. Chem. B* **2006**, *110*, 13144-13150.

Chapter 2

Control of the Doping Concentration, Morphology and Optoelectronic Properties of Vertically Aligned Chlorine-Doped ZnO Nanowires



2.1 Abstract

Vertically-aligned single-crystal and chlorine-doped ZnO NWs were grown by a low-cost, high-yield and seed-free electrochemical route. The effects of the applied potential and the concentration of ammonium chloride (NH_4Cl) on the morphology, structural and optoelectronic properties of the ZnO:Cl NWs were comprehensively investigated. The amount of Cl ions introduced in the ZnO structure increased almost linearly with both the concentration of NH_4Cl in solution, and the electrodeposition

potential. As side effects, the presence of NH_4Cl in the growth solution slowed down the electrodeposition rate and resulted in closer packed and lower aspect ratio NWs, but having a higher degree of vertical alignment and less defective surfaces. The NWs tip morphology also changed with the NH_4Cl concentration, from pyramidal to flat tips. By changing the amount of NH_4Cl in the growth solution, the carrier concentration of such ZnO:Cl NWs could be tuned in the range between 5×10^{17} and $4 \times 10^{20} \text{ cm}^{-3}$. The optical gap of the heavily doped NWs increased due to the Moss-Burstein effect. At the same time, a band gap narrowing was detected from photoluminescence measurements.

2.2 Introduction

Zinc oxide is an important technological material with a broad range of applications which take advantage of its abundance, stability, biocompatibility and a unique combination of chemical and physical properties.¹ Among other fields, ZnO is used in the rubber industry, in paints and sunscreens, as a gas sensor and as a biosensor.²⁻⁴ Its piezoelectric properties make it a suitable material for mechanical actuators, piezoelectric sensors and for energy scavenging.⁵⁻⁷ ZnO wide direct band gap (3.37 eV) and large exciton binding energy (60 meV) make it an excellent candidate for particular optoelectronic applications, such as light-emitting diodes,⁸ laser diodes⁹ and solar cells.¹⁰

While ZnO is an intrinsic n-type semiconductor, an increase of its electrical conductivity is necessary in those applications where ZnO has an active electronic role, especially when used as a transparent conductive oxide^{11,12} and in transistors.¹³⁻¹⁶ Extrinsic doping is the main strategy to increase ZnO electrical conductivity and/or change it to p-type. In particular, cationic-doping obtained by the replacement of Zn by

Al,^{17,18} Co¹⁹ or Ag^{20,21} has been commonly targeted. While anionic-doping offers the potential advantage of a higher processing simplicity, the replacement of oxygen by fluorine, chlorine, iodide, bromide, nitrogen or phosphor ions in the ZnO structure has not been so widely studied.²²⁻²⁷

Driven by their promising technological potential, the synthesis and characterization of one-dimensional ZnO nanostructures have recently attracted much attention.²⁸⁻³⁰ ZnO NWs enable the use of ZnO in new technologies, e.g. field emitters,³¹⁻³³ while offering significant benefits to current applications, e.g. device miniaturization and increased interface/surface areas. ZnO NWs can be prepared by vapor-phase transport,³⁴ pulsed laser deposition³⁵ or chemical vapor deposition.³⁶ However, these technologies are neither particularly low-cost nor versatile for the production of large area devices, because of the relatively high energies and controlled atmospheres they require and the low growth rates and yields they provide. Alternative low cost methods, such as chemical bath deposition³⁷⁻³⁹ and electrochemical deposition,⁴⁰ allow the preparation of large areas of aligned NWs arrays at low temperatures and at high production rates and yields. Additional advantages of the electrochemical deposition over chemical bath deposition are that it does not require the use of seeds and provides faster growth rates and higher deposition yields.⁴¹

We report here on the preparation of vertically aligned ZnO:Cl NW arrays by a seed-free electrochemical deposition method. In the present work, the influence of the growth potential and the concentration of ammonium chloride on the doping concentration, morphology and optoelectronic properties of the obtained ZnO:Cl NWs is detailed.

2.3 Experimental section

2.3.1 NWs growth

ZnO NWs were electrochemically grown in an aqueous solution inside a three-electrode cell. The growth solution was prepared by incorporating 10 mL of a 0.1 M aqueous solution (MilliQ+, 18.2 M Ω ·cm) of zinc nitrate ($\text{Zn}(\text{NO}_3)_2 \cdot 4\text{H}_2\text{O}$) and 10 mL of a 0.1 M aqueous solution of methenamine ($\text{C}_6\text{H}_{12}\text{N}_4$) in 80 mL of deionized water and quickly heating up the solution to 90 °C on a hot plate. A platinum wire immersed in the solution was used as a counter electrode. An Ag/AgCl electrode in saturated KCl (3 M) was used as the reference electrode. A negative DC potential in the range between -0.4 and -1.4 V relative to the reference electrode was applied to a soda lime glass coated with fluorine doped tin oxide (FTO) or a copper foil, which were used as substrates. After a 1 hour growth time, the samples were immediately rinsed with deionized water. Chlorine ions were introduced in a controlled way by replacing between 0.5 and 10 mL of deionized water with a 1 M aqueous solution of ammonium chloride (NH_4Cl).

2.3.2 Characterization

X-ray diffraction (XRD) was used to characterize the crystallographic phase of as-grown ZnO NWs. For XRD characterization, a PANalytical X'Pert PRO MPD Alpha1 powder diffractometer with Focalizing Ge (111) primary monochromator and Cu $\text{K}\alpha_1$ radiation ($\lambda = 1.5406 \text{ \AA}$) was used.

Field emission scanning electron microscopy (SEM) was used to characterize the morphology of the obtained materials and measure the density of NWs and their length

and width distributions. Both cross-sectional and top-down views were obtained using a FEI Nova NanoSEM 230.

X-ray photoelectron spectroscopy (XPS) spectra were obtained using a *SPECS SAGE ESCA* System employing Mg K α ($E = 1253.6$ eV) with a supplied power of 203 W as the X-ray source. The general spectra were scanned to confirm the presence of Zn, O and Cl with 30 eV pass energy and 0.5 eV steps. High-resolution scans were obtained to provide information regarding the bonding environment and oxidation state of Zn, O and Cl. These scans were performed with 15 eV pass energy and 0.10 eV steps. All spectra were shifted to account for sample charging using inorganic carbon at 284.80 eV as a reference.

The morphology and crystallographic structure of the nanowires were further characterized with atomic resolution by means of HRTEM in a Jeol 2010F field emission gun microscope with a 0.19 nm point to point resolution. For TEM and HRTEM characterization, samples were prepared by scraping the ZnO:Cl NWs off of the substrate over carbon-coated copper grids.⁴²

A double beam spectrophotometer (Perkin Elmer Lambda 950) equipped with an integrated sphere was used for the UV-vis transmission measurements in the range from 250 to 800 nm.

Raman measurements were made using a micro-Raman spectrometer Labram HR 800. Excitation was provided by a diode laser at 532 nm or a He-Cd laser at 325 nm. Measurements were performed in backscattering configuration. The focused spot size on the measured surface was about 100 μm . The excitation power was 4 mW at 532 nm and 20 mW at 325 nm.

Room-temperature photoluminescence (PL) measurements were obtained using a Kimmon IK Series HeCd CW laser (325 nm and 40 mW). Fluorescence was dispersed through an Oriel Corner Stone 1/8 74000 monochromator, detected with a Hamamatsu R928 photomultiplier, and amplified through a Stanford Research Systems SR830 DSP Lock-in amplifier.

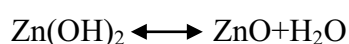
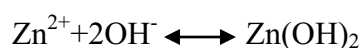
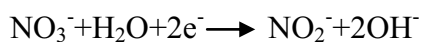
I-V characteristics of ZnO NWs were obtained using a Park XE-100 Advanced Scanning Probe Microscope (SPM). For SPM characterization, Cu was used as a substrate to grow the ZnO NW. A platinum-coated tip was used to apply a voltage in the range between -10 and 10 V.

Mott-Schottky measurements were performed in a three-electrode cell using ZnO:Cl films (area: 0.07 cm²) as the working electrodes. A Pt wire and a mercury sulfate electrode (MSE) were used as counter and reference electrodes, respectively. The electrolyte used in the electrochemical impedance spectroscopy measurements was a phosphate buffer solution (pH = 7) where a 0.1 M concentration of KCl was added. The potential scan was carried out from -1 to 0 V/MSE. The weak current densities measured during the Mott-Schottky measurements (< 50 μAcm^{-2}) allowed us to assume that the samples were not altered by this experiment.

2.4 Results and Discussion

Arrays of vertically aligned and single crystal ZnO:Cl NWs were obtained by electrodeposition from a solution containing Zn(NO₃)₂·4H₂O. The electrochemical growth of ZnO from a single source of Zn and oxygen, such as Zn(NO₃)₂·4H₂O, is based on the generation of OH⁻ ions by the electroreduction of nitrate to nitrite and their posterior combination with Zn²⁺ to form Zn(OH)₂. ZnO NWs grow at the cathode from

the preferential Zn(OH)_2 decomposition at the polar $\{0001\}$ surfaces of the ZnO structure. The primary deposition reactions of the ZnO NWs on the cathode can be described by the following scheme:⁴³



In this scenario, the ratio between the OH^- generation rate and the Zn^{2+} diffusion from solution to the cathode are the main parameters controlling the growth rate of the ZnO NWs.^{24, 44}

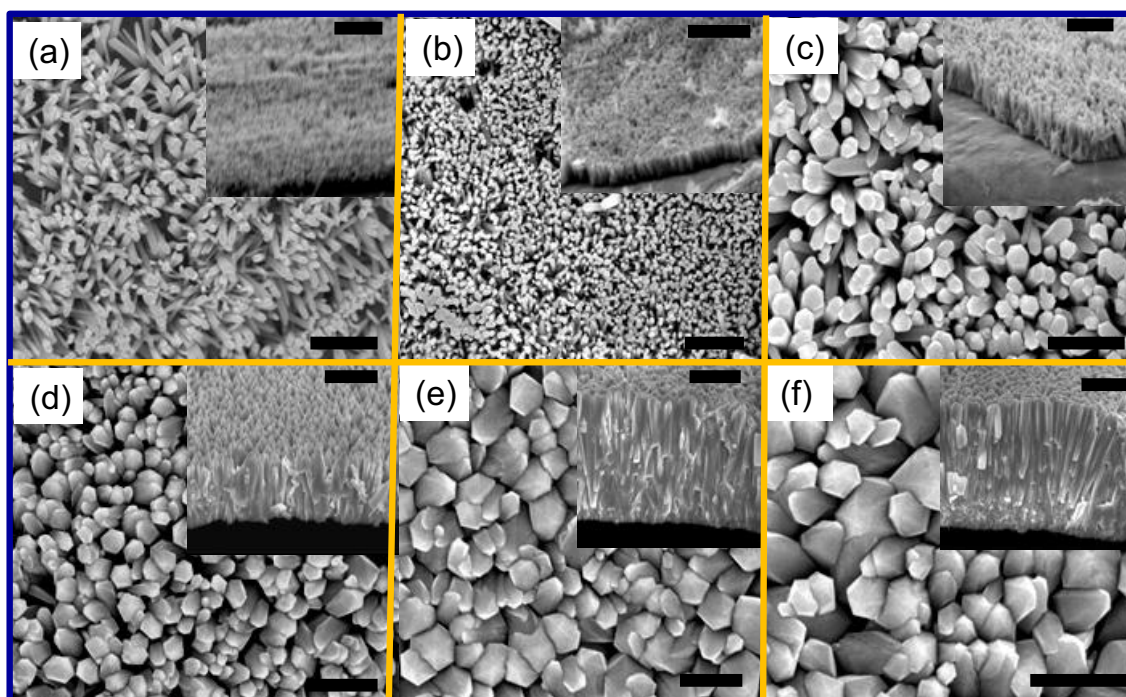


Figure. 1 Top-down and cross-section (inset) SEM images of ZnO:Cl NWs grown using different electrodeposition potentials: (a) -0.4 V; (b) -0.6 V; (c) -0.8 V; (d) -1 V; (e) -1.2 V; (f) -1.4 V. The scale bar of the top-down images corresponds to 1 μm , while the insets one corresponds to 3 μm . Reaction time was set to 1 hour.

Figure 1 shows the top-down and cross-section (insets) SEM images of the ZnO:Cl NWs obtained at different applied potentials, in the range from -0.4 to -1.4 V. For this set of samples, the NH_4Cl concentration was fixed to 0.02 M. Figure 2a shows the diameter and length of the ZnO:Cl NWs obtained after 1 hour of reaction time as a function of the applied potential. Notice how there is a ten-fold increase in the growth rate when raising the applied voltage from -0.4 to -1.4 V. The increase of the growth rate is associated to the higher rate of hydroxide generation at the substrate with the applied negative potential.⁴¹ It should be pointed out that the growth rate at the lowest potentials used is still a factor 2 higher than that obtained hydrothermally. The electrodeposition method has also the additional advantage of not requiring seeds to produce vertically aligned ZnO NWs.

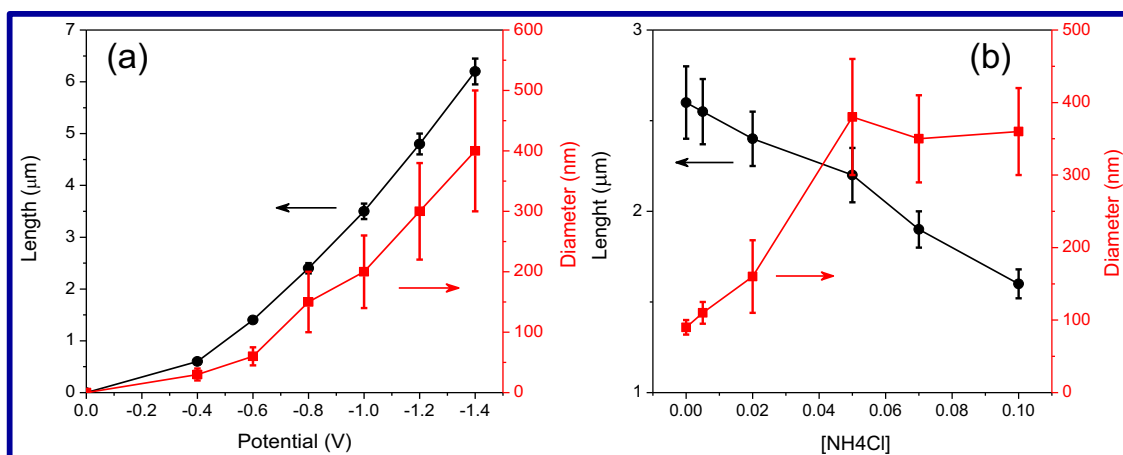


Figure. 2 Diameter and length of the ZnO:Cl NWs as a function of (a) electrodeposition potential ($[\text{NH}_4\text{Cl}] = 0.02 \text{ M}$) and (b) concentration of NH_4Cl in the precursor solution (electrodeposition potential = -0.8 V).

The concentration and chemical state of chlorine ions were analyzed by XPS (Figure 3a). At a set NH_4Cl concentration in solution (0.02 M), the amount of chloride introduced in the ZnO NWs increased almost linearly with the applied potential (Figure

4). We believe this increase of the Cl concentration introduced in the ZnO crystal structure to be kinetically driven. The applied potential drives the deposition process away from equilibrium to a mass-transport-limited regime.⁴¹ In this scenario, the faster the growth rate, the higher the concentration of defects/impurities that incorporates into the growing crystal structure. In contrast, slow growth rates allow a higher thermodynamically-driven self-purification of the obtained nanostructures, resulting in lower defect densities, including ion substitution.

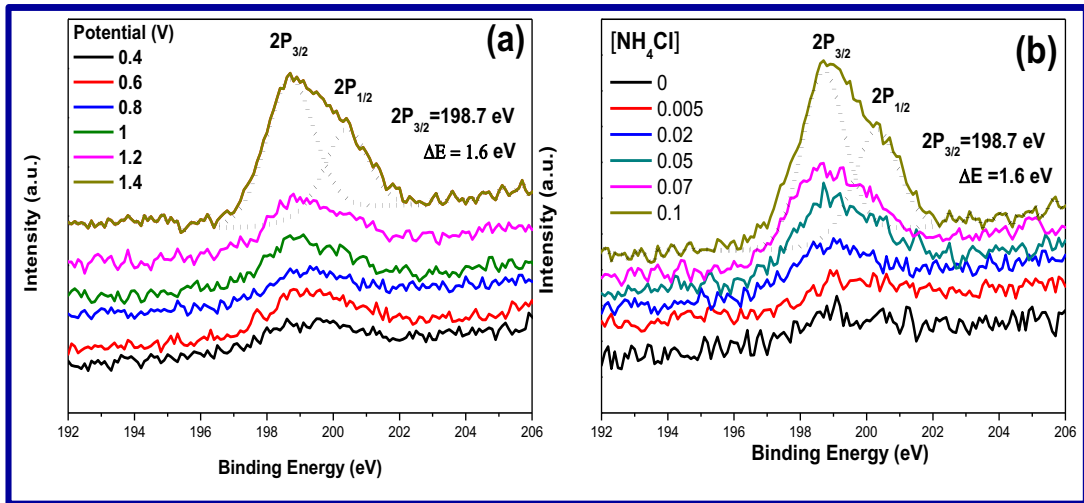


Figure. 3 XPS spectra of the chlorine region in ZnO:Cl NWs grown at: (a) different applied potential and (b) different concentration of NH_4Cl . The fitting of the chlorine 2P band with two peaks, corresponding to $2\text{P}_{3/2}$ and $2\text{P}_{1/2}$ is also shown.

The XPS spectra of the chlorine region were fitted with two bands at 198.7 eV and 197.1 eV. The energy of these bands matched the $2\text{P}_{3/2}$ and $2\text{P}_{1/2}$ electron transitions in ZnCl_2 ,⁴⁵ what pointed towards the incorporation of Cl^- in substitution of O^{2-} ions.

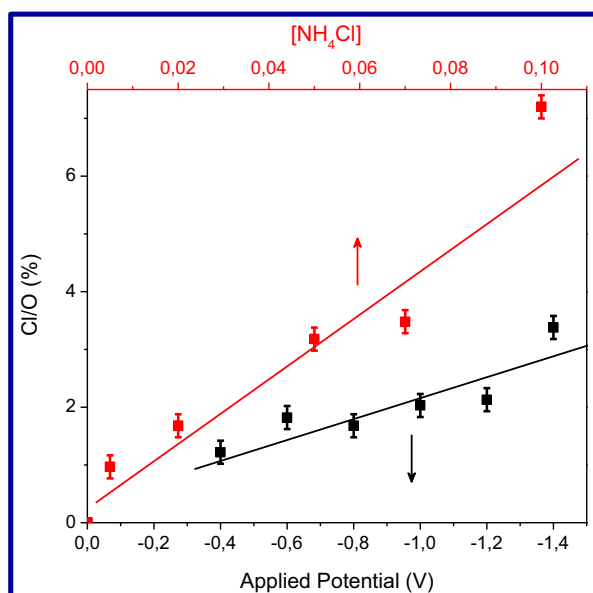


Figure. 4 Chlorine concentration calculated from the XPS spectra as a function of the electrodeposition potential ($[\text{NH}_4\text{Cl}] = 0.02 \text{ M}$) and NH_4Cl concentration (applied potential = -0.8 V).

In figure 3b, the XPS spectra of the ZnO:Cl NWs prepared using different concentration of NH_4Cl is shown. As expected, the Cl concentration increased almost linearly with the concentration of NH_4Cl in solution (Figure 4). No saturation of the incorporated Cl was obtained in the NH_4Cl concentration range tested and no shift of the XPS spectra was detected when increasing the Cl amount. However, at NH_4Cl concentrations higher than 0.1 M , non-homogeneous layers were systematically obtained, and at NH_4Cl concentrations above 0.3 M , almost no ZnO NWs were grown on the substrate.

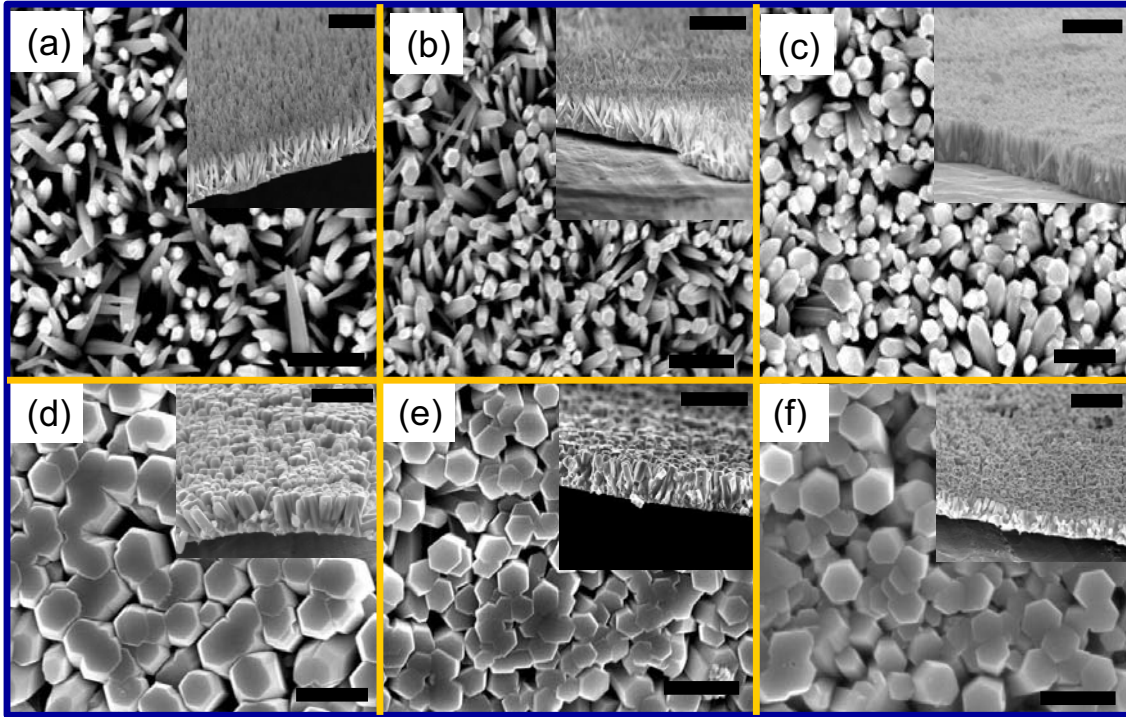
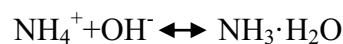


Figure. 5 Top-down and cross section (inset) SEM images of ZnO:Cl NWs grown using different concentration of NH_4Cl : (a) 0; (b) 0.005 M; (c) 0.02 M; (d) 0.05 M; (e) 0.07 M; (f) 0.1 M. The scale bar of the top-down images corresponds to 1 μm , while the insets one corresponds to 3 μm . The electrodeposition potential was set at -0.8 V.

Figure 5 shows the top-down and cross-section (insets) images of the ZnO:Cl NWs grown in solutions containing a concentration of NH_4Cl in the range between 0.001 M and 0.1 M. Notice how the length of the ZnO:Cl NWs decreased when increasing the NH_4Cl concentration in solution. At the same time, the NWs thickness increased with the presence of NH_4Cl up to a 0.05 M concentration and it remained constant for higher concentrations (Figure 2b).

We believe that the presence of NH_4^+ and Cl^- ions both influenced the lateral and longitudinal growth rates. On the one hand, the introduction of NH_4^+ ions depleted the solution from OH^- groups through the production of $\text{NH}_3 \cdot \text{H}_2\text{O}$:



Thus, the introduction of NH_4^+ diminished the ZnO growth rate in all crystallographic directions, and an excess of NH_4^+ did not allow the growth of ZnO NWs.

On the other hand, the Cl^- presence partially inhibited the NW growth by adsorbing/incorporating to the ZnO crystal structure. The decrease of the NWs aspect ratio with the Cl^- presence points towards its preferential adsorption at the $\{0001\}$ surface, possibly due to its polarity.^{46,47}

Not only the aspect ratio changed with the presence of Cl^- ions, also the tip morphology was modified (Figure 6). In spite of the importance of the tip morphology in applications such as field emission, scanning probing microscopy and high sensitive sensing, little research has been focused on this area.^{33,48,49} Laudise and Ballman were the first to describe the growth habit of a ZnO crystal.⁵⁰ They measured the growth rate in the $\langle 0001 \rangle$ direction to be about twice higher than that in the $\langle 10\bar{1}0 \rangle$ direction. Since then, it has been experimentally and theoretically confirmed that the relationship between the ZnO crystal growth rates in different directions is:

$$V_{\langle 0001 \rangle} > V_{\langle 10\bar{1}1 \rangle} > V_{\langle 10\bar{1}0 \rangle}.^{51}$$

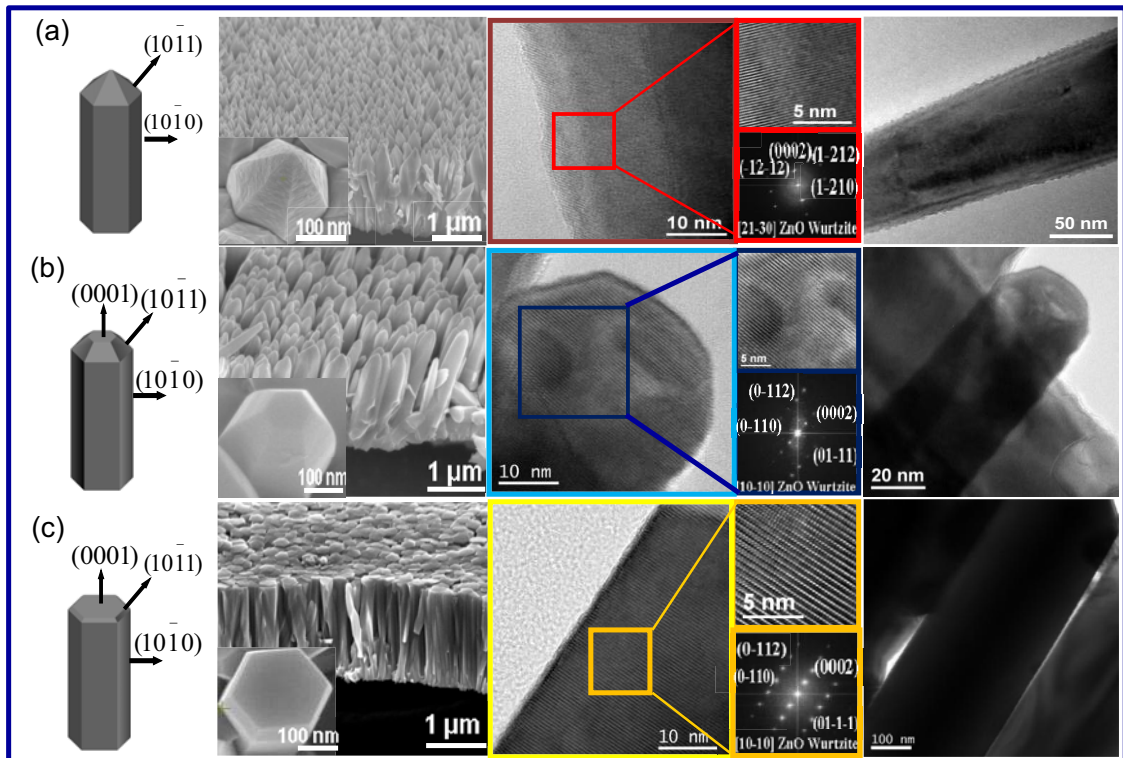


Figure. 6 Cartoon, SEM, TEM and HRTEM images of the ZnO:Cl NWs morphology obtained at different NH_4Cl concentrations: (a) 0.02 M; (b) 0.04 M; (c) 0.05 M.

For the electrodeposited ZnO:Cl NWs, the ratio of the different facets was experimentally observed to depend on the NH_4Cl concentration. In particular, the $\{0001\}$ facet systematically increased with the concentration of NH_4Cl in solution (Figure 5 and 6). This result is consistent with a preferential adsorption of chlorine at the polar $\{0001\}$ facet and an associated decrease of the growth rate in the $\langle 0001 \rangle$ direction. Such preferential adsorption is at the origin of the NW aspect ratio decrease.

TEM and HRTEM characterization of the ZnO:Cl NWs confirmed them to be single crystalline and to grow in the $\langle 0001 \rangle$ direction of the ZnO hexagonal wurtzite structure (Figure 6). It was also observed how the roughness of the lateral NWs surfaces decreased with the NH_4Cl concentration in the growth solution. The higher the NH_4Cl

concentration, the slower the growth rate in the $\langle 0001 \rangle$ direction and thus the smoother the lateral surfaces obtained (Figure 6).

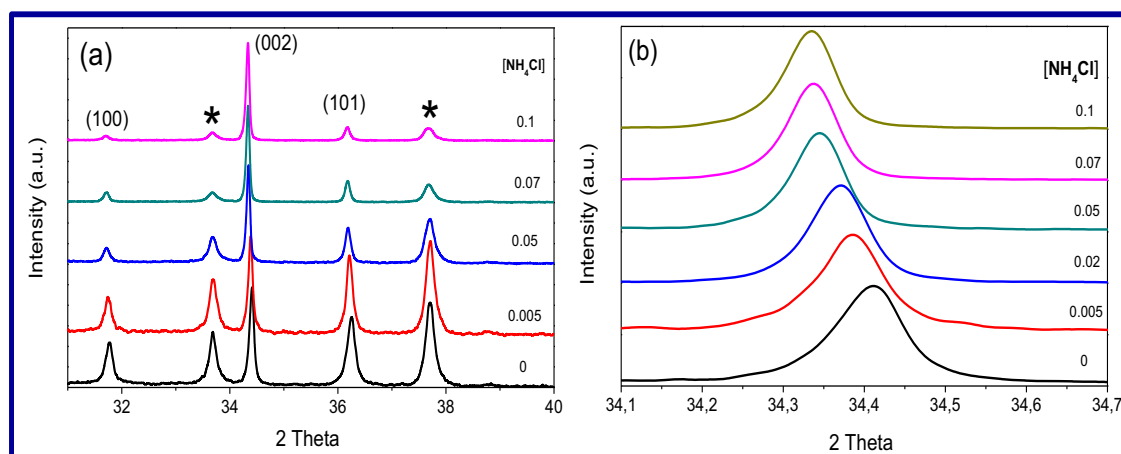


Figure 7 (a) XRD spectra of the ZnO:Cl NWs grown using different concentrations of NH_4Cl . The peaks marked with “*” correspond to the FTO substrate. (b) Detail of the XRD spectra around the ZnO (002).

Figure 7 shows the XRD patterns of the ZnO and ZnO:Cl NWs obtained at different NH_4Cl concentrations in solution. The XRD patterns were identified with those of a ZnO hexagonal wurtzite structure (JCPDS card 01-1136) oriented along the $\langle 0001 \rangle$ direction, in good agreement with HRTEM analyses. The degree of alignment of the ZnO:Cl NWs, estimated from the area ratio between the XRD peak corresponding to the $\langle 0001 \rangle$ crystallographic direction and the peaks corresponding to other crystal directions, increased with the NH_4Cl concentration. At the same time, the ZnO XRD pattern shifted to lower angles with the incorporation of Cl, which is consistent with an expansion of the ZnO lattice due to the replacement of O^{2-} ions with the larger Cl^- ones (Figure 7b).

Figure 8a shows the room temperature Raman scattering spectra of pure and Cl-doped ZnO NWs obtained using 532 nm excitation. The main feature observed is the

$E_2(2)$ Raman mode of the wurtzite phase at 438 cm^{-1} . The A_{1T} Raman mode is also appreciated at 380 cm^{-1} . These modes widened and their intensity slightly decreased when increasing the NH_4Cl concentration. However, their position did not noticeably shift with the NH_4Cl concentration, denoting a minor stressing of the ZnO lattice by the Cl incorporation.

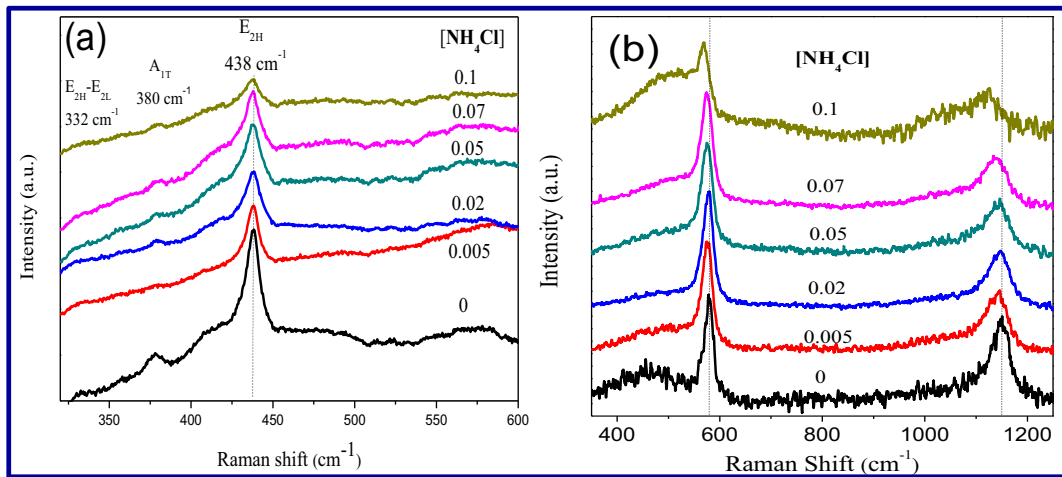


Figure. 8 Room temperature Raman spectra of pure and Cl-doped ZnO NWs obtained using (a) 532 nm excitation and (b) 325 nm excitation.

Figure 8b shows the room temperature resonant Raman scattering spectra of the pure and Cl-doped ZnO NWs obtained using 325 nm excitation. The broad background associated with the excitonic luminescence emission was subtracted. Only the Raman mode at around 580 cm^{-1} and its overtones were observed. The mode intensity increased with the doping concentration up to a NH_4Cl concentration of 0.05 M. However, the intensity of this mode and overtones strongly decreased for the highest NH_4Cl concentrations analyzed. Notice how this Raman mode shifted to lower energies with the NH_4Cl concentration, from 580 to 569 cm^{-1} . This mode is a combination of the two LO Raman modes $A_1(\text{LO})$ and $E_1(\text{LO})$, which have been previously identified close to

568 and 586 cm^{-1} , respectively.⁵²⁻⁵⁴ The A1 (LO) and E1(LO) modes are polar; their vibrations polarize the unit cell, which results in the creation of a long-range electrostatic field. At resonance conditions, the intensity of the two LO modes is strongly enhanced via the Frohlich interaction, as previously described.^{52, 55-58} While the A1(LO) mode is allowed from the c face in backscattering geometry, the E1(LO) mode is a forbidden mode in a backscattering geometry from this face. Thus from a layer completely texturized in the c direction, only the A1(LO) mode should be observed in backscattering geometry. We believe the observed red-shift of the LO Raman mode with the increase of the NH_4Cl concentration to be related to the increase of the NWs alignment degree also observed from the XRD spectra and SEM images. The pure ZnO NWs, having a higher degree of misalignment, had a higher E1(LO) contribution than those highly aligned ZnO:Cl NWs obtained at the highest NH_4Cl concentrations. These last highly vertically aligned NWs showed an almost pure A1(LO) mode. These results demonstrate that Raman spectroscopy could be an efficient quality control technique able to monitor in a continuous production line not only the NWs composition, crystallinity and stress, but also their degree of alignment.⁵⁹

The ZnO:Cl NWs carrier concentration was estimated from Mott-Schottky (MS) measurements. This method is based on the Schottky barrier formation between the semiconductor material and an electrolyte.^{23, 60-62} The depletion zone created in the semiconductor material was characterized by a capacitance measurement. The variation of the differential capacitance of the space charge layer, C_{sc} , was measured as a function of the applied potential. The theory predicts a linear dependence of C_{sc}^{-2} with the applied potential, as described by the following equation for an n-type semiconductor:

$$\frac{1}{C_{sc}^2} = \frac{2}{\epsilon \epsilon_0 e_0 N_d A^2} \left(E - E_{FB} - \frac{kT}{e_0} \right)$$

Where ϵ_0 is the permittivity of the free space, ϵ is the relative dielectric constant of ZnO (8.5), e_0 is the electron charge, N_d is the free carrier concentration of the semiconductor, A is the area in contact with the electrolyte, E is the applied potential, E_{FB} is the flatband potential, k is the Boltzmann constant and T is the absolute temperature.

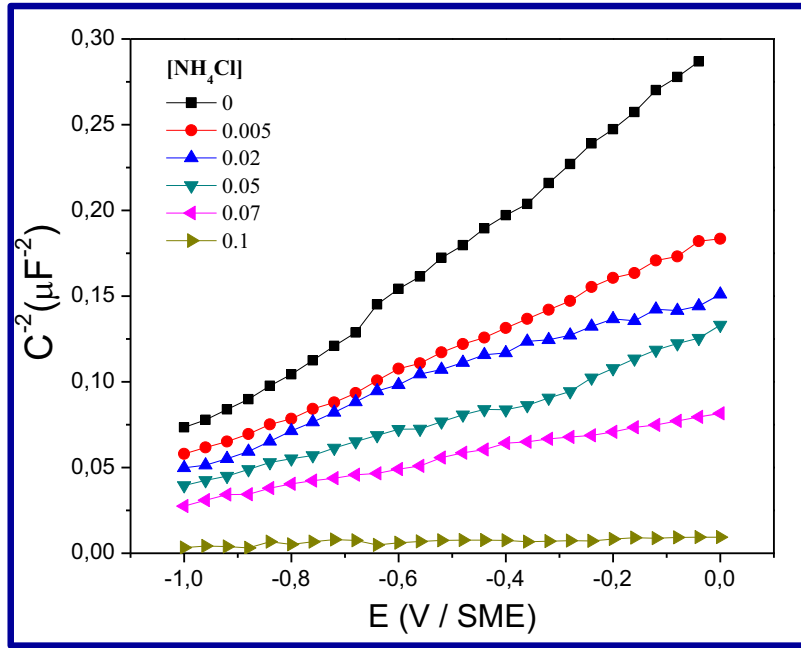


Figure. 9 Mott-Schottky plots of the pure and Cl-doped ZnO NWs.

Figure 9 displays the Mott-Schottky curves obtained for the pure and Cl-doped ZnO NWs. Table 1 displays the carrier concentration obtained from the linear fitting of the curves. For this calculation, the total ZnO NWs surface area was estimated from the density, average length and thickness of the ZnO:Cl NWs obtained at different NH_4Cl concentrations. An increase of three orders of magnitude in the carrier concentration was obtained between the pure ZnO NWs and the ZnO:Cl NWs grown with a 0.1 M concentration of NH_4Cl in solution, proving the doping effect of Cl ions inside the ZnO crystal structure. However, the obtained carrier concentrations accounted for a small fraction of the Cl concentrations estimated from XPS measurements. This result

indicates that a significant part of the chlorine ions may be found interstitially or in the ZnCl_2 form, as previously proposed for $\text{ZnO}:\text{Cl}$ films.²³ Nevertheless, the existence of a non-homogeneous distribution of Cl inside the ZnO NWs cannot be ruled out.⁶³ Notice in this regard that the XPS is a surface characterization technique proving the composition of the material in the first few nanometers from the NWs surface.

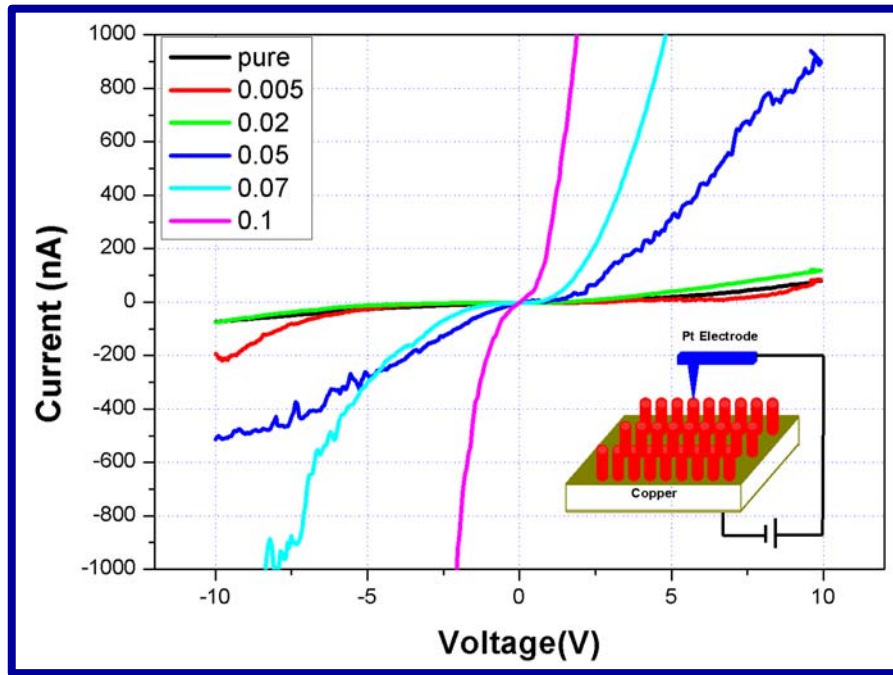


Figure. 10 I - V characteristics the $\text{ZnO}:\text{Cl}$ NWs deposited on Cu substrates and measured by conducting SPM using a Pt tip. The inset shows a cartoon of the experimental set-up.

The I - V characteristics of single $\text{ZnO}:\text{Cl}$ NWs were measured with a conductive SPM using a Pt-coated tip (Figure 10). All $\text{ZnO}:\text{Cl}$ NWs exhibited a quasi-symmetric I - V response at forward and reverse bias, which is a common observation in SPM measurements of semiconductor NWs using a metal-semiconductor-metal geometry.⁶⁴

When a positive voltage was applied to the Pt-coated tip, the total applied voltage (V) across the M-S-M structure was equal to the sum of voltage drops at Pt-ZnO(V_1),

ZnO(V_2) and ZnO-Cu(V_3): $V=V_1+V_2+V_3$. At very low applied voltages, the voltage drop occurred mainly at the Schottky barriers (Pt-ZnO and ZnO-Cu). At relatively high applied voltages, the $I-V$ curve of the Pt-ZnO-Cu structure approached a straight line having a slope equal to the resistance of the Cl-doped ZnO NWs. From these measurements, and taking into account the NW geometrical parameters, the ZnO:Cl NWs resistivity was estimated. The resistivity values obtained are listed in Table 1. As expected, the NW resistivity decreased when increasing NH_4Cl concentration. A decrease of two orders of magnitude in the resistivity was obtained for NWs grown in a 0.1 M NH_4Cl solution, respect to the non-doped ones. These values are comparable to those previously reported for Cl-doped ZnO thin films grown by MOCVD.^{65, 66} The mobility values estimated from the obtained resistivities and carrier concentrations are also shown in Table 1. As expected, a decrease of the charge carrier mobility with the Cl introduction was obtained.

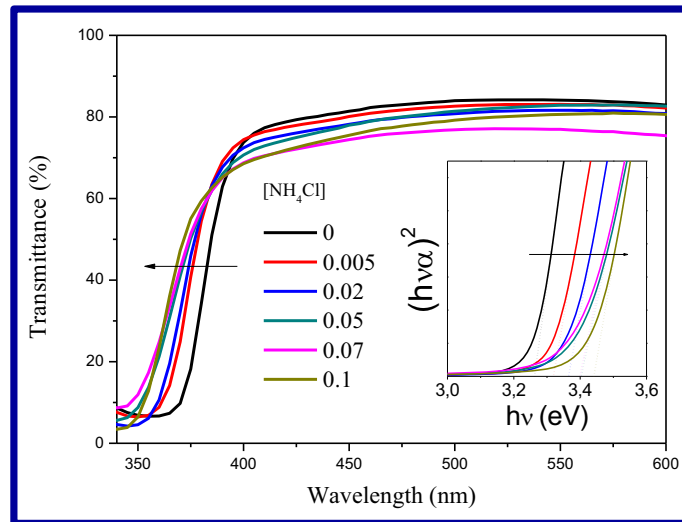


Figure. 11 Transmittance spectra of the ZnO:Cl NWs obtained at different NH_4Cl concentrations. The inset shows the dependence of $(ah\nu)^2$ vs. $h\nu$ and the lineal fit used to determine the optical band gap.

Table 1. Structural, optical and electronic parameters of the electrodeposited ZnO:Cl NWs

[NH ₄ Cl] (M)	0	0.005	0.02	0.05	0.07	0.1
[Cl]/[O] % (XPS)	0	0.97	1.68	3.18	3.48	7.2
NWs Density (μm^{-2})	15 \pm 2	15 \pm 2	13 \pm 2	6 \pm 1	6 \pm 1	6 \pm 1
NWs Length (μm)	2.6 \pm 0.2	2.55 \pm 0.2	2.4 \pm 0.15	2.2 \pm 0.15	1.9 \pm 0.1	1.6 \pm 0.08
NWs Diameter (μm)	0.09 \pm 0.01	0.11 \pm 0.015	0.16 \pm 0.05	0.38 \pm 0.08	0.35 \pm 0.06	0.36 \pm 0.06
Geometric area factor	11.1	12.0	12.8	5.4	3.1	2.8
Optical gap (eV)	3.26	3.32	3.365	3.40	3.40	3.44
PL Maximum (eV)	3.205	3.190	3.167	3.161	3.158	3.157
PL FWHM (nm)	23.6	28.6	30.0	30.4	29.8	30.3
Carrier concentration (cm^{-3})	5.7 \times 10 ¹⁷	8.8 \times 10 ¹⁷	9.7 \times 10 ¹⁷	6.5 \times 10 ¹⁸	3.3 \times 10 ¹⁹	4.2 \times 10 ²⁰
NW resistance at high forward bias ($10^6 \Omega$)	70	67	61	7.7	1.4	0.43
Resistivity ($\Omega \text{ cm}$)	1.90	1.81	1.79	0.25	0.051	0.019
Mobility ($\text{cm}^2 \text{ V}^{-1} \text{ s}^{-1}$)	5.8	3.9	3.6	3.9	3.7	0.8

Figure 11 displays the UV-vis transmittance spectra of the ZnO NWs deposited on FTO-covered glass substrates. The optical gap of the ZnO:Cl NWs was estimated by a linear fit of $(\alpha \cdot h\nu)^2$ vs. the photon energy ($h\nu$) (Figure 11 inset). The optical gap of ZnO:Cl NWs blue-shifted with the increase of the NH₄Cl concentration as shown in Table 1. This shift is mainly attributed to the so-called Moss-Burstein effect.⁶⁷⁻⁶⁹ The high density of electrons introduced by the large Cl concentration filled the bottom of the conduction band. As a result, optical absorption in the degenerated ZnO took place from the top of the valence band to the Fermi level inside the conduction band, thus overestimating the semiconductor band gap. Similar observations were found for chlorine,²² aluminum⁷⁰ and yttrium-doped ZnO films.⁷¹ At the same time, the structural modifications and defects introduced by the high concentration of Cl inside the ZnO

structure may have a contribution on the optical-absorption blue-shift by slightly modifying the energy band structure of ZnO.

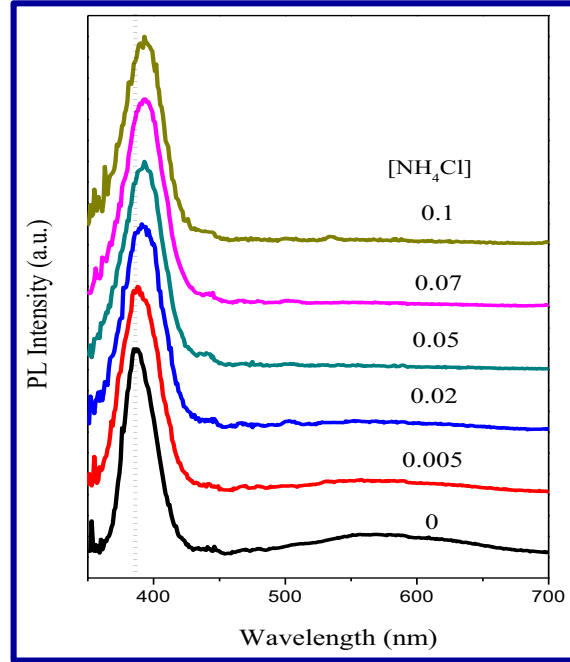


Figure. 12 Photoluminescence spectra of pure and Cl-doped ZnO NWs obtained using 325 nm excitation wavelength.

The room temperature photoluminescence spectra of the ZnO:Cl NWs are shown in Figure 12. The PL peak corresponding to the band-to-band transition becomes wider and its maximum shifts to lower energies when increasing the concentration of NH₄Cl in the growth solution. Both observations are related to the high density of charge carriers introduced by the presence of Cl in the ZnO crystal structure. In heavily doped semiconductors, the electron-electron interactions shift the conduction and valence bands towards each other and cause band-gap narrowing. This phenomenon has been extensively investigated in a large number of semiconductors.^{70,72-75} The high density of free charge carriers introduced with the Cl doping shrinks the ZnO band gap as noted by the shift of the PL maximum to lower energies. At the same time, the semiconductor

becomes degenerated, as evidenced by the blue-shift of the UV-vis absorption edge. This degeneration significantly widens the emission band. The band-to-band emission extends from the reduced band-gap energy, which is the difference between the top of the valence band and the bottom of the conduction band, to the energy of the optical gap, which blue-shifts with the NH_4Cl concentration due to the band filling.

Besides, a broad band at around 600 nm was also observed. The relative intensity of this band decreased with the NH_4Cl concentration. This band was previously assigned to the emission from surface defects in ZnO.⁷⁶⁻⁷⁸ In particular, I. Shalish et al. already observed that the relative intensity of this PL band was reduced with the increase of the NW diameter.⁷⁷ Thus, we believe the NH_4Cl concentration to have an indirect effect in the reduction of such band intensity. The increase of the NH_4Cl concentration had associated an increase of the ZnO:Cl NWs thickness, which reduced the surface-to-bulk ratio and thus decreased the relative intensity of the surface related PL bands. The smoother surfaces obtained when increasing the NH_4Cl concentration may also contribute to the reduction of the defects originating this PL band.

2.5 Conclusions

The influence of the electrodeposition potential and the concentration of NH_4Cl in the growth solution on the morphological, structural and optoelectronic properties of ZnO:Cl NWs was investigated. It was observed that an increase of the electrodeposition potential had associated higher ZnO growth rates. This higher growth rates kinetically promoted the incorporation of Cl inside the ZnO structure. The presence of NH_4Cl in the growth solution decreased the overall growth rate due to the reaction of NH_4^+ with OH^- groups. At the same time, Cl^- ions preferentially adsorbed on the $\{0001\}$ surface,

influencing both the NWs aspect ratio and the tip morphology. Furthermore, increasingly higher NH_4Cl concentrations had associated higher degrees of NW vertically alignment, as observed both by XRD and resonant Raman scattering spectroscopy. The carrier concentration increased with the Cl introduction inside the ZnO crystal structure, probing its doping role. However, a significant part of the Cl introduced was found interstitially or forming ZnCl_2 , thus not contributing to an increase of the ZnO NW conductivity. In any case, the carrier concentration could be tuned in the range between 5×10^{17} and $4 \times 10^{20} \text{ cm}^{-3}$. Such high carrier concentration resulted in a degeneration of the semiconductor, which lead to a blue-shift of its optical gap due to the Moss-Burstein effect. At the same time, a band-gap narrowing was observed from band-to-band photoluminescence measurements at high doping concentrations.

2.6 References

1. Özgür, Ü.; Alivov, Y. I.; Liu, C.; Teke, A.; Reshchikov, M. A.; Doğan, S. *J. Appl. Phys.* **2005**, *98*, 041301.
2. Liao, L.; Lu, H. B.; Shuai, M.; Li, J. C.; Liu, Y. L.; Liu, C.; et al. *Nanotechnology* **2008**, *19*, 175501.
3. Wang, J. X.; Sun, X. W.; Wei, A.; Lei, Y.; Cai, X. P.; Li, C. M.; et al. *Appl. Phys. Lett.* **2006**, *88*, 233106.
4. Wei, A.; Sun, X. W.; Wang, J. X.; Lei, Y.; Cai, X. P.; Li, C. M.; et al. *Appl Phys Lett.* **2006**, *89*, 123902.
5. Wang, Z. L. *J. Phys: Condens Matter* **2004**, *16*, 829-858.
6. Qin, Y.; Wang, X.; Wang, Z. L. *Nature* **2008**, *451*, 809-814.
7. Wang, Z. L.; Song, J. *Science* **2006**, *312*, 242-246.
8. Könenkamp, R.; Word, R. C.; Godinez, M. *Nano Lett.* **2005**, *5*, 2005-2008.
9. Pauproté, T.; Lincot, D.; Viana, B.; Pellé, F. *Appl. Phys. Lett.* **2006**, *89*, 233112.
10. Claude, L. C.; Ramon, T. Z.; Ryan, M. A. *Adv. Mater.* **2005**, *17*, 1512-1515.

11. Ginley, D. S.; Bright, C. *MRS Bull.* **2000**, *25*, 15-18.
12. Kim, H.; Gilmore, C. M.; Horwitz, J. S.; Piqué, A.; Murata, H.; Kushto, G. P.; et al. *Appl. Phys. Lett.* **2000**, *76*, 259-261.
13. Hoffman, R. L.; Norris, B. J.; Wager, J. F. *Appl. Phys. Lett.* **2003**, *82*, 733-735.
14. Nishii, J.; Hossain, F. M.; Takagi, S.; Aita, T.; Saikusa, K.; Ohmaki, Y.; et al. *Jpn. J. Appl. Phys.* **2003**, *42*, 347-349.
15. Fortunato, E. M. C.; Barquinha, P. M. C.; Pimentel, A. C. M. B. G.; Gonçalves, A. M. F.; Marques, A. J. S.; Pereira, L. M. N.; et al. *Adv. Mater.* **2005**, *17*, 590-594.
16. Fortunato, E. M. C.; Barquinha, P. M. C.; Pimentel, A. C. M. B. G.; Gonçalves, A. M. F.; Marques, A. J. S.; Martins, R. F. P.; et al. *Appl. Phys. Lett.* **2004**, *85*, 2541-2543.
17. Zimmermann, G.; Lange, M.; Cao, B.; Lorenz, M.; Grundmann, M. *Phys. Stat. Sol. (RRL)* **2010**, *4*, 82-84.
18. Banerjee, P.; Lee, W. J.; Bae, G. Y.; Lee, S. B.; Rubloff, G. W. *J. Appl. Phys.* **2010**, *108*, 043504.
19. Yuhas, B. D.; Zitoun, D. O.; Pauzauskie, P. J.; He, R. R.; Yang, P. D. *Angew. Chem. Int. Ed.* **2006**, *45*, 420-423.
20. Thomas, M. A.; Cui, J. B. *J. Vac. Sci. Technol. B* **2009**, *27*, 1673-1677.
21. Thomas, M. A.; Cui, J. B. *J. Phys. Chem. Lett.* **2010**, *1*, 1090-1094.
22. Cui, J. B.; Soo, Y. C.; Chen, T. P.; Gibson, U. J. *J. Phys. Chem. C* **2008**, *112*, 4475-4479.
23. Rousset, J.; Saucedo, E.; Lincot, D. *Chem. Mater.* **2009**, *21*, 534-540.
24. Elias, J.; Tena-Zaera, R.; Lévy-Clément, C. *J. Phys. Chem. C* **2008**, *112*, 5736-5741.
25. Tchelidze, T.; Chikoidze, E.; Gorochoy, O.; Galtier, P. *Thin Solid Films* **2007**, *515*, 8744-8747.
26. Yang, X.; Wolcott, A.; Wang, G.; Sobo, A.; Fitzmorris, R. C.; Qian, F.; et al. *Nano Lett.* **2009**, *9*, 2331-2336.
27. Xu, H. Y.; Liu, Y. C.; Mu, R.; Shao, C. L.; Lu, Y. M.; Shen, D. Z.; et al. *Appl. Phys. Lett.* **2005**, *86*, 123107.
28. Wang, Z. L. *J. Phys.: Condens Matter.* **2004**, *16*, 829-858.
29. Djurišić, A. B.; Leung, Y. H. *Small* **2006**, *2*, 944-961.
30. Chu, D.; Masuda, Y.; Ohji, T.; Kato, K. *J. Am. Ceram. Soc.* **2010**, *93*, 887-893.
31. Lee, C. J.; Lee, T. J.; Lyu, S. C.; Zhang, Y.; Ruh, H.; Lee, H. J. *Appl. Phys. Lett.* **2002**, *81*, 3648-3650.

32. Zhu, Y. W.; Zhang, H. Z.; Sun, X. C.; Feng, S. Q.; Xu, J.; Zhao, Q.; et al. *Appl. Phys. Lett.* **2003**, *83*, 144-146.
33. Wang, R. C.; Liu, C. P.; Huang, J. L.; Chen, S. J.; Tseng, Y. K.; Kung, S. C. *Appl. Phys. Lett.* **2005**, *87*, 013110.
34. Huang, M. H.; Wu, Y.; Feick, H.; Tran, N.; Weber, E.; Yang, P. *Adv. Mater.* **2001**, *13*, 113-116.
35. Sun, Y.; Fuge, G. M.; Ashfold, M. N. R. *Chem. Phys. Lett.* **2004**, *396*, 21-26.
36. Park, W. I.; Kim, D. H.; Jung, S. W.; Yi, G. C. *Appl. Phys. Lett.* **2002**, *80*, 4232-4234.
37. Greene, L. E.; Law, M.; Tan, D. H.; Montano, M.; Goldberger, J.; Somorjai, G.; et al. *Nano Lett.* **2005**, *5*, 1231-1236.
38. Grene, L. E.; Yuhas, B. D.; Law, M.; Zitoun, D.; Yang, P. *Inorg. Chem.* **2006**, *45*, 7535-7543.
39. Govender, K.; Boyle, D. S.; Kenway, P. B.; Brien, P. O. *J. Mater. Chem.* **2004**, *14*, 2575-2591.
40. Peulon, S.; Lincot, D. *Adv. Mater.* **1996**, *8*, 166-170.
41. Cui, J. B.; Gibson, U. J. *J. Phys. Chem. B* **2005**, *109*, 22074-22077.
42. Morral, A. F. I.; Arbiol, J.; Prades, J. D.; Cirera, A.; Morante, J. R. *Adv. Mater.* **2007**, *19*, 1347-1351.
43. Izaki, M.; Omi, T. *J. Electrochem. Soc.* **1996**, *143*, 53-55.
44. Peulon, S.; Lincot, D. *J. Electrochem. Soc.* **1998**, *145*, 864-784.
45. Moulder, J. F.; Stickle, W. F.; Sobol, P. E.; Bomben, K. D. X-ray photoelectron spectroscopy, Perkin-Elmer corporation physical electronics division. United State of America: Minnesota; 1992.
46. Xu, L.; Guo, Y.; Liao, Q.; Zhang, J.; Xu, D. *J. Phys. Chem. B* **2005**, *109*, 13519-13522.
47. Wang, Z. L.; Kong, X. Y.; Ding, Y.; Gao, P.; Hughes, W. L.; Yang, R.; et al. *Adv. Funct. Mater.* **2004**, *14*, 943-956.
48. Ye, Z. Z.; Huang, J. Y.; Xu, W. Z.; Zhou, J.; Wang, Z. L. *Solid State Comm.* **2007**, *141*, 464-466.
49. Wang, J.; Luo, H. F.; Chen, T.; Yuan, Z. H. *Nanotechnology* **2010**, *21*, 505603.
50. Laudise, R. A.; Ballman, A. A. *J. Phys. Chem.* **1960**, *64*, 688-691.
51. Li, W. J.; Shi, E. W.; Zhong, W. Z.; Yin, Z. W. *J. Cryst. Growth* **1999**, *203*, 186-196.

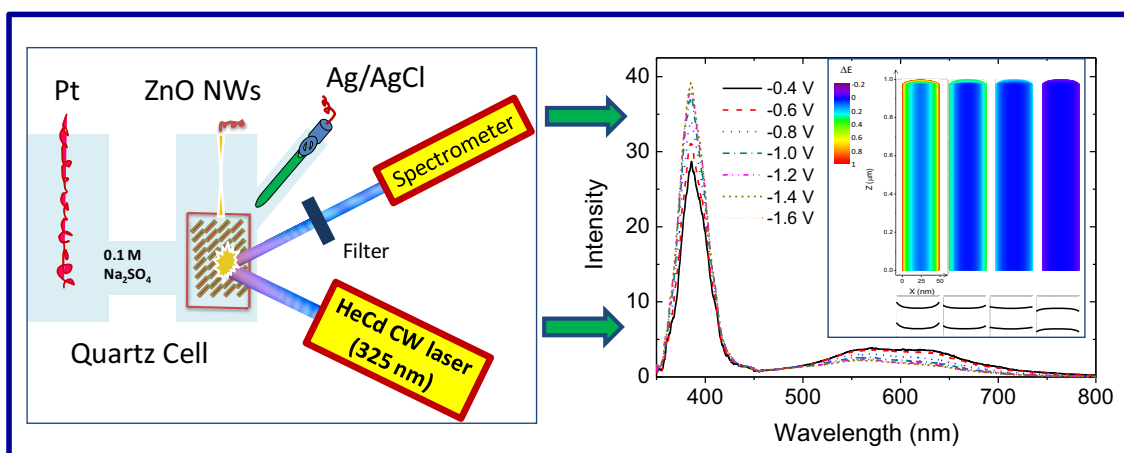
52. Bergman, L.; Chen, X. B.; Huso, J.; Morrison, J. L.; Hoeck, H. *J. Appl. Phys.* **2005**, *98*, 093507.
53. Zhu, X.; Wu, H. Z.; Qiu, D. J.; Yuan, Z.; Jin, G.; Kong, J.; Shen, W. *Opt. Comm.* **2010**, *283*, 2695-2699.
54. Damen, T. C.; Porto, S. P. S.; Tell, B. *Phys. Rev.* **1966**, *142*, 570-574.
55. Oka, Y.; Kushida, T. *J. Phys. Soc. Jpn.* **1972**, *33*, 1372-1380.
56. Calleja, J. M.; Cardona, M. *Phys. Rev. B* **1977**, *16*, 3753-3761.
57. Scott, J. F. *Phys. Rev. B* **1970**, *2*, 1209-1211.
58. Wagner, M. R.; Zimmer, P.; Hoffmann, A.; Thomsen, C. *Phys. Stat. Sol. (RRL)* **2007**, *1*, 169-171.
59. Izquierdo-Roca, V.; Shavel, A.; Saucedo, E.; Jaime-Ferrer, S.; Álvarez-García, J.; Cabot, A.; et al. *Sol. Energ. Mat. Sol. Cells* **2011**, *95*, 83-88.
60. Cardon, F.; Gomes, W. P. *J. Phys. D: Appl. Phys.* **1978**, *11*, 63-67.
61. Windisch, C. F.; Exarhos, G. J. *J. Vac. Scien. Technol.* **2000**, *18*, 1677-1680.
62. Mora-Seró, I.; Fabregat-Santiago, F.; Denier, B.; Bisquert, J.; Tena-Zaera, R.; Elias, J.; et al. *Appl. Phys. Lett.* **2006**, *89*, 203117.
63. Lupan, O.; Pauporté, T.; Chow, L.; Viana, B.; Pellé, F.; Ono, L. K.; et al. *Appl. Surf. Sci.* **2010**, *256*, 1895-1907.
64. Zhang, Z.; Yao, K.; Liu, Y.; Jin, C.; Liang, X.; Chen, Q.; et al. *Adv. Funct. Mater.* **2007**, *17*, 2478-2489.
65. Chikoidze, E.; Nolan, M.; Modreanu, M.; Sallet, V.; Galtier, P. *Thin Solid Films* **2008**, *516*, 8146-8149.
66. Chikoidze, E.; Modreanu, M.; Sallet, V.; Gorochoy, O.; Galtier, P. *Phys. Stat. Sol. (a)* **2008**, *205*, 1575-579.
67. Burstein, E. *Phys. Rev.* **1954**, *93*, 632-633.
68. Moss, T. S. *Proc. Phys. Soc. London, Sect. B* **1954**, *67*, 775-782.
69. Lu, J. G.; Fujita, S.; Kawaharamura, T.; Nishinaka, H.; Kamada, Y.; Ohshima, T.; et al. *J. Appl. Phys.* **2007**, *101*, 083705.
70. Sernelius, B. E.; Berggren, K.-F.; Jin, Z.-C.; Hamberg, I.; Granqvist, C. G. *Phys. Rev. B* **1988**, *37*, 10244.
71. Jain, A.; Sagar, P.; Mehra, R. M. *Solid State Electron.* **2006**, *50*, 1420-1424.
72. Ghosh, S. *Phys. Rev. B* **2000**, *62*, 8053-8057.
73. Borghs, G.; Bhattacharyya, K.; Deneffé, K.; Mieghem, P. V.; Mertens, R. *J. Appl. Phys.* **1989**, *66*, 4381-4386.

74. Wagner, J. *Phys. Rev. B* **1985**, *32*, 1323-1325.
75. Roth, A. P.; Webb, J. B.; Williams, D. F. *Phys. Rev. B* **1982**, *25*, 7836-7839.
76. Andelman, T.; Gong, Y.; Polking, M.; Yin, M.; Kuskovsky, I.; Neumark, G.; et al. *J. Phys. Chem. B* **2005**, *109*, 14314-14318.
77. Shalish, I.; Temkin, H.; Narayanamurti, V. *Phys. Rev. B* **2004**, *69*, 245401.
78. Gu, Y.; Kuskovsky, I. L.; Yin, M.; Brien, S. O.; Neumark, G. F. *Appl. Phys. Lett.* **2004**, *85*, 3833-3835.

Chapter 3

Visible Photoluminescence Components of Solution-Grown ZnO

Nanowires: Influence of the Surface Depletion Layer



3.1 Abstract

Arrays of electrodeposited ZnO NWs were used to illustrate the dependence of the ZnO visible PL emission on the extension of the surface depletion layer and obtain further insight on the localization of the related states. With this goal in mind, three sets of measurements were carried out: (i) Analysis of the PL spectra of ZnO:Cl NWs as a function of their carrier concentration; (ii) Analysis of the PL spectra of ZnO:Cl/ZnO core-shell NWs as a function of the thickness of their intrinsic ZnO shell; (iii) In situ analysis of the PL dependence on the polarization of ZnO:Cl photoelectrodes. The obtained experimental results evidenced that the yellow and orange emissions from electrodeposited ZnO NWs are correlated with the extension of the NWs surface

depletion region. This result points out the surface localization of the states at the origin of these transitions. On the other hand, the green emission that dominates the visible part of the PL spectra in annealed ZnO NWs, showed no dependence on the surface band bending, thus pointing toward its bulk origin.

3.2 Introduction

Zinc oxide, having a wide direct band gap (3.37 eV) and large exciton binding energy (60 meV), is an excellent candidate for optoelectronic applications, such as light-emitting diodes,¹ laser diodes² and solar cells.³ Its wide range of applications has motivated a comprehensive characterization of its properties and an intensive investigation of its potential applications. Nevertheless, a lack of consensus on important optical properties, such as the origin of its visible PL emission still exists.⁴⁻⁶ The various contributions to the visible emission has been associated with oxygen vacancies,⁷⁻¹⁴ oxygen antisites, oxygen interstitial,^{15,16} zinc vacancy,¹⁷⁻²⁰ zinc interstitials,^{21,22} trapped OH⁻ groups¹⁸ and even Cu impurities.²³ On the other hand, evidences exist that the intensity of some contributions to the visible emission band depends on the material surface-to-bulk ratio.²⁴⁻²⁹ Such experimental evidences has been rationalized by considering the surface localization of the related states, their surface activation by the hole accumulation at the surface depletion region, or the promotion of slower recombination processes by charge separation in the built-in electric field surface layer.^{9-12,30-36} The surface band bending has also been reported to activate indirect band-to-band transitions.³⁷

The controversy about the association of the transitions behind the visible PL emission is in part originated from the strong dependence of the PL emission on the

ZnO preparation techniques, the specific growth parameters used and the applied post-growth treatments.³⁸ The large variety of methods available for the synthesis of ZnO crystals with different geometries and sizes does not help to solve this puzzle. In this scenario, a particularly interesting geometry at the nanometer scale is that of NWs.^{4,39,40} Its interest originates from the potential concurrence of a high electrical conductivity and a high surface area in the same structure. ZnO NWs can be prepared by vapor-phase transport,⁴¹ pulsed laser deposition⁴² or chemical vapor deposition.⁴³ However, alternative solution-growth methods, such as chemical bath deposition^{44,45} and electrochemical deposition,^{46,47} are more suitable for the preparation of large areas of aligned NWs arrays with controlled doping concentrations, at low temperatures and at high production rates and yields.

In this chapter, the PL properties of solution-grown ZnO NWs are characterized. In particular, the dependence of the UV and visible PL band intensities on the surface band bending is analyzed and detailed. Evidences of a strong dependence of the yellow and orange emission on the extension of the surface depletion layer are revealed and discussed.

3.3 Experimental section

3.3.1 NWs growth.

ZnO NWs were electrochemically grown in an aqueous solution inside a three-electrode cell. The growth solution was prepared by incorporating 10 mL of a 0.1 M aqueous solution (MilliQ+, 18.2 M Ω ·cm) of zinc nitrate ($\text{Zn}(\text{NO}_3)_2 \cdot 4\text{H}_2\text{O}$) and 10 mL of a 0.1 M aqueous solution of methenamine ($\text{C}_6\text{H}_{12}\text{N}_4$) in 80 mL of deionized water and quickly heating up the solution to 90 °C on a hot plate. A platinum wire immersed

in the solution was used as a counter electrode. An Ag/AgCl electrode in saturated KCl (3 M) was used as the reference electrode. A negative DC potential in the range between -0.4 and -1.4 V relative to the reference electrode was applied to a soda lime glass coated with FTO, indium doped tin oxide (ITO) or Pt, which was used as substrate for the ZnO NWs growth. After a 1 hour growth time, the samples were immediately rinsed with deionized water. Chlorine ions were introduced in a controlled manner by replacing part of the deionized water with a 1 M aqueous solution of ammonium chloride (NH_4Cl). To obtain the coaxial ZnO:Cl/ZnO homojunction NWs, the initial ZnO:Cl NWs were thoroughly washed and subsequently subjected to additional electrodeposition growth steps in the absence of NH_4Cl . The applied potential was fixed at -0.4 V vs Ag/AgCl, The thickness of the ZnO shell could be controlled by the electrodeposition time (300 s) and/or the number (1-5) of additional electrodeposition growth steps.

3.3.2 Characterization

Field emission SEM was used to characterize the morphology of the obtained materials and measure the density of NWs and their length and width distributions. Both cross-sectional and top-down views were obtained using a FEI Nova Nanosem 230. XPS spectra were obtained using a *SPECS SAGE ESCA* system employing Mg K α ($E = 1253.6$ eV) with a supplied power of 203 W as the X-ray source. The general spectra were scanned to confirm the presence of Zn, O and Cl with 30 eV pass energy and 0.5 eV steps. High-resolution scans were obtained to provide information regarding the bonding environment and oxidation states of Zn, O and Cl. These scans were performed with 15 eV pass energy and 0.10 eV steps. All spectra were shifted to account for sample charging using inorganic carbon at 284.80 eV as a reference. Room-temperature

PL measurements were obtained using a Kimmon IK Series HeCd CW laser (325 nm and 40 mW). Light was dispersed through an Oriel Corner Stone 1/8 74000 monochromator, detected with a Hamamatsu R928 photomultiplier, and amplified through a Stanford Research Systems SR830 DSP lock-in amplifier. The dependence of the PL intensity on an external applied field was measured by introducing the NWs inside a quartz electrochemical cell. Potential was applied using a three-electrode potentiostat system with an Ag/AgCl electrode in saturated KCl (3 M) as the reference electrode and a Pt wire as counter electrode. A 0.1 M Na₂SO₄ aqueous solution was used as electrolyte.

3.4 Results and Discussion

Figures 1a and 1b show representative top-down and cross-sectional SEM images of an array of vertically aligned and single crystal ZnO:Cl NWs grown by electrodeposition along the <0001> direction. ZnO:Cl NWs had an average thickness of 170 nm and an average length of 2.3 μm. A controlled concentration of chlorine ions was introduced by dissolving the required amount of ammonium chloride inside the electrodeposition solution. The concentration and chemical state of chlorine ions within the ZnO structure were analyzed by XPS (Figure 1c-e). Chlorine ions are well known to act as n-type impurities within the ZnO structure. Thus controlling the amount of chlorine, the ZnO:Cl charge carrier concentration could be adjusted in the range from 10^{17} to 10^{20} cm⁻³.⁴⁷

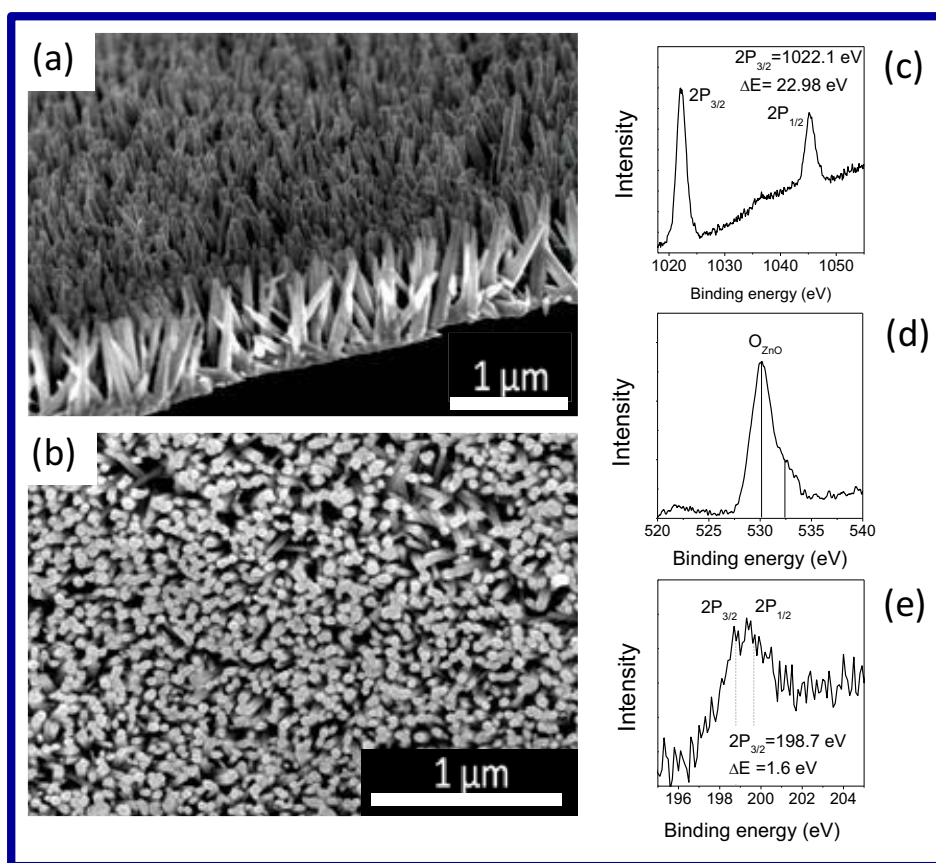


Figure 1. (a) Cross-sectional and (b) top-down SEM images of ZnO:Cl NWs. (c) Zinc region, (d) Oxygen region, (e) Chlorine region of the XPS spectra of ZnO:Cl NWs.

The room temperature PL spectra of ZnO:Cl NWs having different doping concentration are shown in figure 2a. A strong UV peak, associated to the band-to-band recombination is clearly seen at 390 nm. The slight red shift of the UV emission peak with the Cl doping concentration may be related to a small band gap narrowing associated with the high density of charge carriers introduced in the ZnO crystal structure or to the preponderance in the PL emission spectra of ZnO:Cl NWs of an exciton slightly below the conduction band edge.^{47,48} A broad emission band in the visible part of the spectra is also observed. The visible band has at least two contributions centered at approximately 570 nm (yellow) and 620 nm (orange). A third band, centered at 510 nm (green) could be also fitted (Figure 2a). Similar bands are

commonly observed in solution-processed ZnO nanoparticles and nanowires.^{18,33} Our experimental results evidenced that when increasing the doping concentration, the relative intensity of the broad visible band decreases respect to the UV emission band (figure 2a and 2c). The doping concentration affected the two main visible contributions, yellow and orange, in a similar way. However, the intensity of the potential green band was not influenced by the doping concentration.

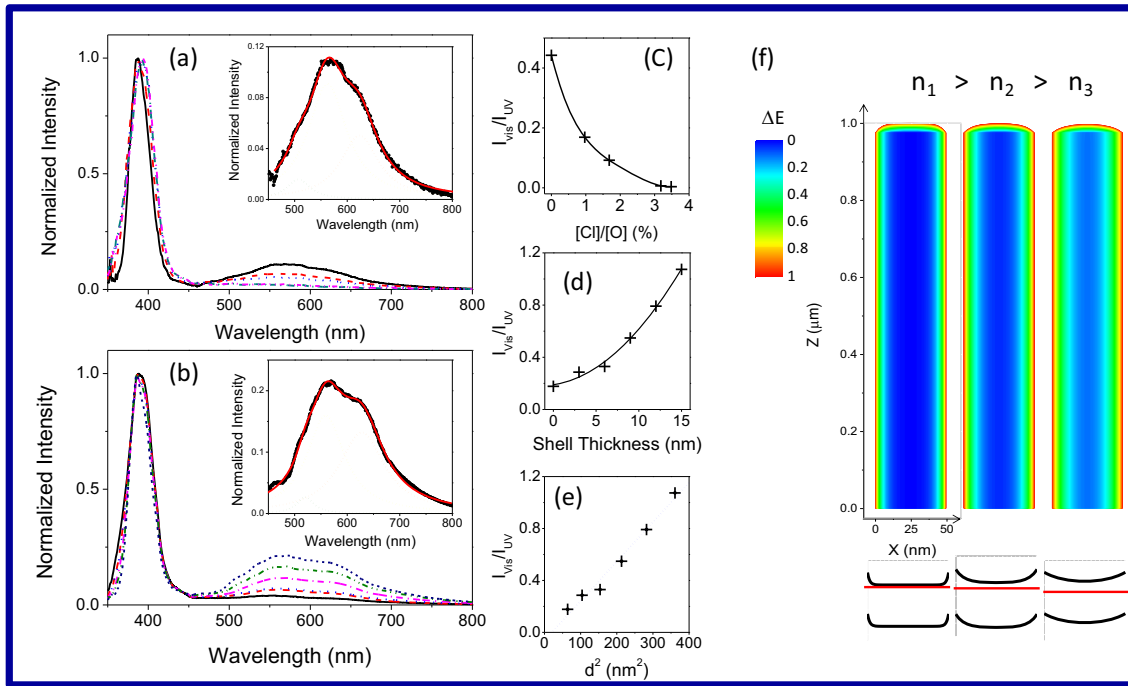


Figure 2. (a) Room temperature PL spectra of ZnO:Cl NWs with different Cl concentrations. The ratios [Cl]/[O], as measured by XPS were 0, 1.0, 1.7, 3.2 and 3.5 %. Inset shows the visible emission in more detail and the fitting of the different emission bands; (b) Room temperature PL spectra of ZnO:Cl NWs and ZnO:Cl/ZnO homojunction NWs with increasingly thicker shells: 0 nm, 3 nm, 6 nm, 9 nm and 15 nm; (c) Chlorine dependence of the PL intensity ratio between the UV and visible bands; (d) Shell-thickness dependence of the PL intensity ratio between the UV and visible bands; (e) Dependence of the UV-Vis emission intensity ratio on the square of the depletion layer thickness; (f) Schematic view of the energy levels variation across nanowires with different carrier concentrations.

In figure 2b, the room temperature PL spectra of ZnO:Cl/ZnO core-shell NWs having different shell thicknesses are plotted. These homojunction ZnO:Cl/ZnO NWs were produced by a two-step electrodeposition process. The [Cl]/[O] ratio of the ZnO:Cl core measured by XPS was 3.2 %. The PL spectra obtained from these NW arrays was very similar to those measured from ZnO:Cl NWs. However, in this case, the relative intensity of the visible band increased with the thickness of the intrinsic ZnO shell (figure 2b and 2d). This increase was correlated with the thickness of the calculated surface depletion layer (Figure 2e). Again, the shell thickness seems to affect the two main visible contributions, yellow and orange, in the same direction.

Both experimental observations can be explained using the same model. It is well known that the electrical and optical properties of wide band gap oxide semiconductors are highly susceptible to the surrounding gas atmosphere. In ambient conditions, the surface of ZnO NWs is covered by ionized oxygen species and hydroxyl groups that trap conduction band electrons. This negative surface charge distribution causes an upward bending of the ZnO energy bands at the surface. The surface barrier height depends on the relative position of the chemisorbed species energy levels with respect to the ZnO Fermi level. On the other hand, the width of the depletion layer is strongly dependent on the doping concentration and can be estimated by solving the Poisson equation:

$$d = \left[\frac{2\epsilon\epsilon_0\Phi_s}{e^2N_D} \right]^{1/2}$$

Where ϵ is the ZnO relative dielectric constant (8.7), ϵ_0 is the vacuum permittivity, Φ_s is the height of potential barrier, e is the electron charge, and N_D is the donor concentration. For ZnO in ambient atmosphere, the barrier height is typically close to

0.55 eV.¹⁷ While highly conducting ZnO:Cl NWs are able to screen the surface charge within a very thin surface depletion layer, undoped ZnO NWs are characterized by much thicker depletion regions. In this regard, the width of the depletion layer is calculated to be 70 nm for ZnO with a donor concentration of 10^{17} cm^{-3} and less than 2 nm for a carrier concentration of 10^{20} cm^{-3} .^{10, 49-52}

As illustrated in Figure 2c, the variation of the relative visible PL band intensity with the doping concentration correlates well with the reduction of the thickness of the surface depletion layer required to screen the surface charge. At the same time, in core-shell nanowires, the presence of an undoped ZnO shell on the surface of highly doped ZnO:Cl NWs allowed increasing the thickness of the depletion layer while conserving a highly conductive core. The visible PL band increased with the thickness of the surface depletion layer (Figures 2d and 2e). These two evidences were indirect probes that the yellow and orange PL bands obtained from solution-grown ZnO NWs had their origin at the NW surface.

To obtain direct evidences of the influence of the surface depletion layer on the relative intensity of the visible band and discard the influence of other chemical, structural or geometrical parameters, the PL properties of ZnO:Cl NWs were characterized while adjusting their surface band bending by means of an applied potential.⁵³⁻⁵⁵ For this purpose, the ZnO:Cl NWs were immersed inside a quartz electrochemical cell filled with a 0.1 M Na_2SO_4 aqueous solution as electrolyte. A potential was applied using a three-electrode potentiostat system with an Ag/AgCl electrode in saturated KCl (3 M) as the reference electrode and a Pt wire as counter electrode (Figure 3). When immersing a semiconductor electrode in a redox electrolyte, a gradient of electrochemical potential across the interface exists. The polarization of the ZnO:Cl NWs immersed in the electrolyte shifts the energy bands

upwards/downwards in the NW core, altering in this way the surface band bending, as illustrated in figure 4b and c. In these conditions, a controllable gradient of electrochemical potential across the interface can be created.

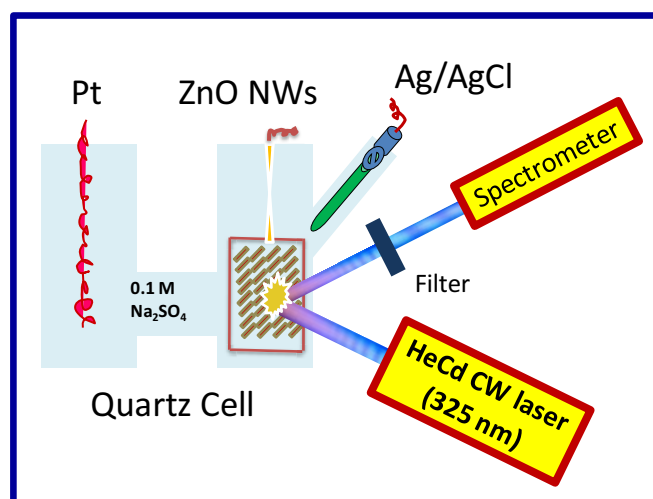


Figure 3. Schematic illustration of the setup used to measure the PL spectra of ZnO:Cl NWs under polarization. ZnO:Cl NWs were immersed in a 0.1 M Na_2SO_4 aqueous solution inside a quartz electrochemical cell. A potential was applied to the ZnO:Cl NWs-based photoelectrodes using a three-electrode potentiostat system with an Ag/AgCl electrode in saturated KCl (3 M) as the reference electrode and a Pt wire as counter electrode.

Positive potentials shift the energy levels of the NW core downward, thus increasing the potential barrier between the core and the pinned surface states. In these conditions, the anodic current associated with the injection of photogenerated holes from the semiconducting electrode to the electrolyte is extremely small in the dark (Figure 4a). This is because of the lack of holes in the n-type ZnO:Cl electrode. If holes are photogenerated within the ZnO:Cl electrode, an anodic photocurrent is measured at all anodic potentials. As illustrated in Figure 4(b), positive potentials facilitate the separation of electron-hole pairs by extending the charge depletion layer where a built-in electric field drives holes toward the electrolyte and electrons toward the substrate

through the ZnO:Cl NW core. Thus the measured photocurrent increases with the positive applied potential, until reaching a saturation photocurrent that depends on the illumination intensity.⁵⁶

Negative applied voltages shift up the energy bands at the NW core, reducing in this way the surface band bending. Such a decrease of the surface depletion layer results in a reduction of the measured photocurrents. At high enough negative polarizations, negative currents are measured, corresponding to the injection of electrons from the semiconductor to the electrolyte (Figure 4c).

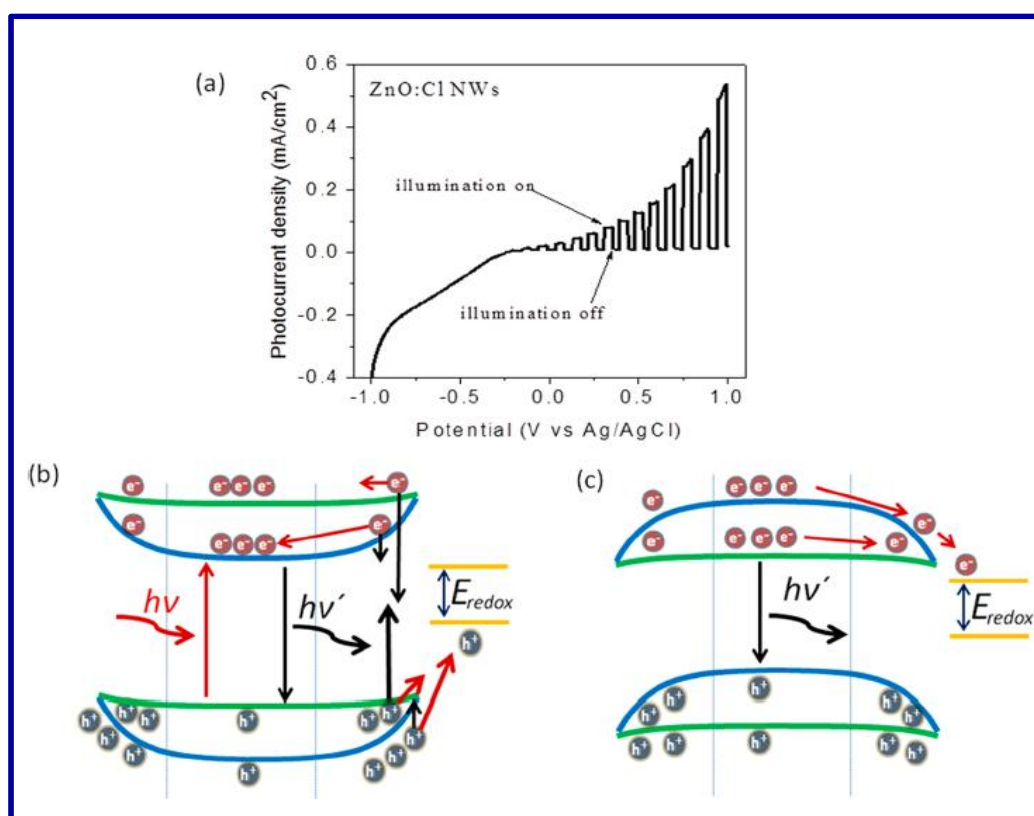


Figure 4. (a) Photocurrent density vs. applied potential (V vs. Ag/AgCl) for ZnO:Cl NWs measured under chopped UV illumination in a 0.1 M Na₂SO₄ aqueous solution. (b) Representation of the effects of band bending on the competing evolution of electron-hole separation (red arrow) and recombination (black arrow) process at positive applied potential. (c) Representation of the effects of band bending on the electrochemical-photoluminescence induced by electron-hole recombination at negative applied potential. Intraband gap states were omitted for simplicity.

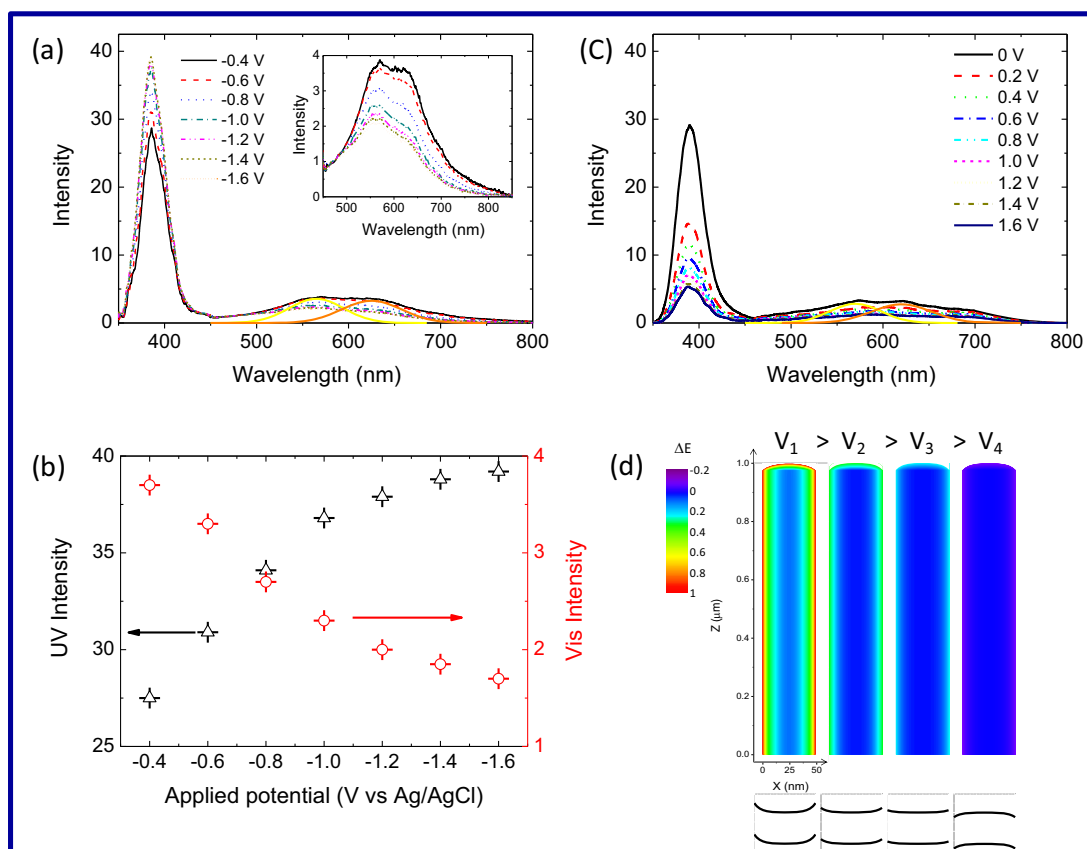


Figure 5. (a) Room temperature PL spectra of ZnO:Cl NWs at different negative potential. Inset shows the visible emission in more detail. (b) Evolution of UV and visible emission intensities with the applied potential. (c) Room temperature PL spectra of ZnO:Cl NWs at positive potentials. (d) Schematic view of the energy level variation across NWs polarized at different potentials.

Figure 5 shows the room-temperature PL spectra at different applied potentials of a ZnO:Cl NW array immersed inside the electrochemical cell. At positive applied potential, the intensity of both UV and visible bands significantly decreased (Figure 5c). There is an obvious competition between the radiative recombination of electron-hole pairs photogenerated upon UV illumination and the extraction of minority carriers (Figure 4b). This competition could explain a reversible quenching of PL when increasing the positive applied voltage. However, the PL quenching with the positive potential was not reversible. An ocular examination of the layer after PL

characterization at positive applied voltages revealed the decomposition of the ZnO NWs. A detailed SEM exploration of the area exposed to the UV light revealed that ZnO NWs had been mostly dissolved with the relatively high photocurrents generated by the combination of the strong UV laser radiation and the positive applied potential (Figure 6).⁵⁷ At the edge of the UV-exposed area ZnO nanotubes were observed. The conservation of the ZnO NWs in the nonexposed area demonstrated that the UV exposure was necessary to dissolve the ZnO NWs. The ZnO spectro-electrochemical dissolution could result from a reverse electrosynthesis reaction at positive potentials under UV illumination. Similar photo-electrochemical dissolution reactions have been previously reported.⁵⁵

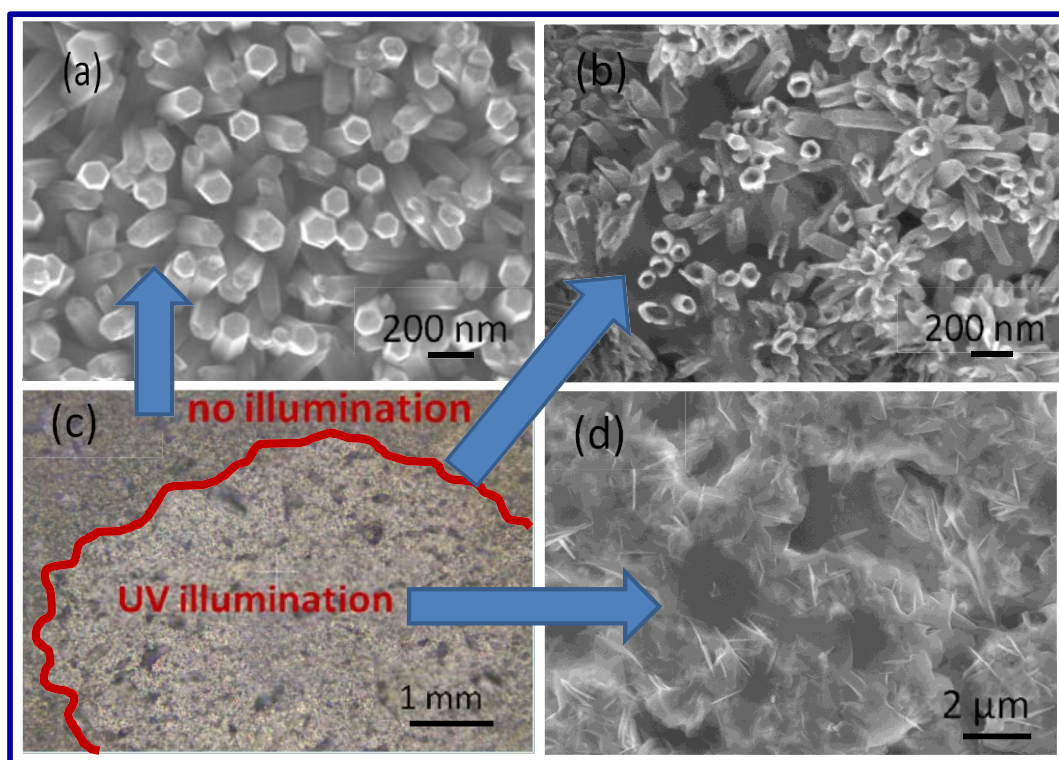


Figure 6. SEM images of ZnO:Cl NWs without UV illumination(a), junction area(b), whole region(c), upon UV illumination(d).

On the other hand, when changing the applied potential toward negative values, the intensity of the visible band clearly decreased. At the same time, the UV emission peak intensity evidently increased (Figure 5a, b). The variation of the visible band intensity affected both yellow and orange contributions in a similar way. It is worth noting that the PL spectra evolution with the applied voltage was reversible, allowing the recovery of the initial spectra when reducing the applied negative voltage.

These results evidence that orange and yellow PL bands obtained from solution-grown ZnO NWs were strongly dependent on the surface band bending. Yellow and orange emissions were previously associated with transitions from the conduction band, donor OH⁻ states or Zinc interstitials to oxygen interstitials or zinc vacancies.^{18,33,58} The results reported here do not allow determining the specific chemical identity of the trap state, but evidence their surface localization. The electric field inside the depletion layer helps to separate photogenerated electron-hole pairs, driving electrons to the bulk and holes to the surface. The contribution from states localized directly at the ZnO surface would increase with the extension of the surface depletion layer because of the higher amount of holes harvested. On the other hand, hole accumulation at the depletion layer, localized either in the valence band or in defect states, such as ionized oxide vacancies, could also activate radiative states not active within the nanocrystal bulk. A third possibility is the slowdown of band-to-band transitions at the depletion region due to the existence of a driving force for exciton separation. In this scenario, slower radiative recombination processes with much lower efficiencies in the ZnO bulk, would be promoted at the ZnO surface (Figure 7a).

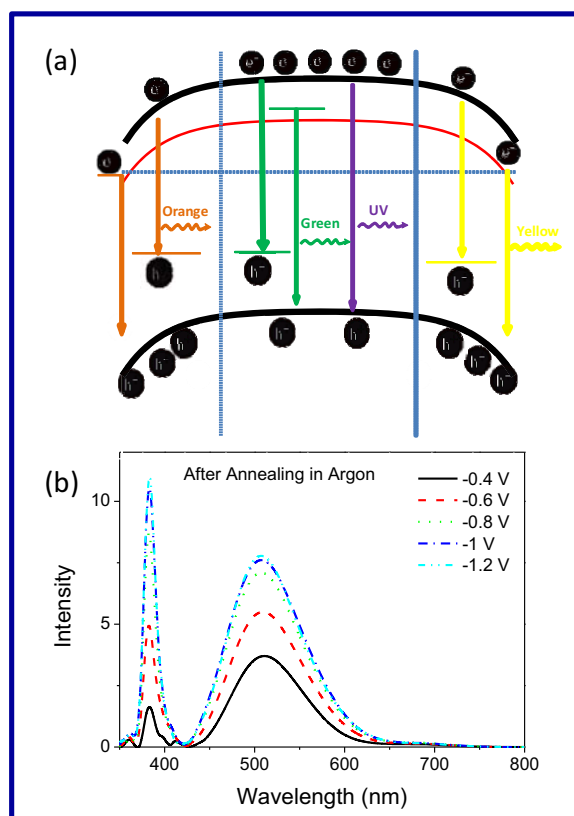


Figure 7. (a) Scheme of the possible localization of the states contributing to the visible emission within ZnO NWs. (b) Room-temperature photoluminescence spectra of annealed ZnO:Cl NWs at increasingly higher negative potentials.

Finally, the ZnO NW arrays obtained by electrodeposition were annealed in argon at 450 °C during 1 h. The morphology and composition of ZnO:Cl NWs before and after annealing were analyzed using the exact same sample. The O/Zn atomic ratio was 1.76 before annealing and 1.62 after annealing, as measured by EDX. It should be pointed out that the measured O/Zn atomic ratios were influenced by the ITO-covered glass substrate. However, results obtained from the exact same sample before and after annealing clearly pointed out toward a decrease of the oxygen concentration with the annealing treatment in argon. This decrease could be attributed to the decomposition of $\text{Zn}(\text{OH})_2$ to ZnO and/or the desorption of chemisorbed oxygen or hydroxyl groups from the ZnO NWs surface with the annealing process.

The annealing treatment substantially modified the PL spectra. Figure 7b shows the room temperature PL spectra obtained from the annealed NWs. The UV peak corresponding to band-to-band recombination and a relatively broad visible band could be easily identified. The intensity of both bands clearly increased with the annealing process mainly due to the improvement of the crystalline structure and the removal of non-radiative defects. At the same time, the relative intensity of the visible band increased considerably. However, in this case, the visible band showed only one contribution, centered at around 510 nm (green). Such emission, at 510 nm was previously associated with transitions involving oxygen vacancies and zinc interstitials.⁵⁹

It is generally accepted that annealing in argon facilitates the removal of chemisorbed oxygen or other oxygen-containing species (e.g. OH⁻) from the ZnO surface, reducing the defect concentration and the charge depletion region and thus enhancing the UV emission.⁶⁰ The decrease of the yellow and orange emission intensities with the annealing process is also consistent with the reduction of the defect concentration. In particular, the defects at the origin of these emissions are clearly eliminated with the annealing treatment. On the other hand, the relatively strong green emission obtained after the annealing process can be associated with the decrease of the oxygen concentration and the consequent increase of the concentration of oxygen vacancies and zinc interstitial defects with the annealing process in an inert atmosphere.

The PL spectra measured under electrical polarization showed that both the UV and green bands increased with the negative potential (Figure 7). This general feature is in good agreement with an earlier report on electroluminescence spectroscopy of polycrystalline ZnO electrode and can be explained by the injection of minority carriers from the electrolyte to the semiconductor.⁶¹ These results point toward the bulk

localization of the states at the origin of the green PL emission in annealed ZnO NWs obtained by solution-processing methods. Like in the case of as-grown ZnO NWs, the annealed arrays were not stable at positive potential when exposed to UV light.

3.5 Conclusions

Three sets of measurements were performed to demonstrate the strong dependence of the visible PL emission in solution-grown ZnO NWs on the thickness of the surface depletion region. The obtained results evidenced that the orange and yellow emission bands are originated from transitions taking place between states localized at or near the NW surface. On the other hand, the green emission measured from annealed ZnO NWs showed no dependence on the extension of the surface depletion layer and followed the same trend as the UV emission, which points toward its bulk origin.

3.6 References

1. Tsukazaki, A.; Ohtomo, A.; Onuma, T. et al. *Nat. Mater.* **2005**, *4*, 42-46.
2. Pauproté, T.; Lincot, D.; Viana, B.; Pellé, F. *Appl. Phys. Lett.* **2006**, *89*, 233112.
3. Claude, L. C.; Ramon, T. Z.; Ryan, M. A. *Adv. Mater.* **2005**, *17*, 1512-1515.
4. Djurišić, A. B.; Leung, Y. H. *Small* **2006**, *2*, 944-961.
5. Güell, F.; Ossó, J. O.; Goñi, A. R.; Cornet, A.; Morante, J. R. *Superlattice Microst.* **2009**, *45*, 271-276.
6. Güell, F.; Ossó, J. O.; Goñi, A. R.; Cornet, A.; Morante, J. R. *Nanotechnology* **2009**, *20*, 315701.
7. Zheng, M. J.; Zhang, L.D.; Li, G. H.; Shen, W. Z. *Chem. Phys. Lett.* **2002**, *363*, 123-128.
8. Vanheusden, K.; Seagera, C. H.; Warren, W. L.; Tallant, D. R.; Caruso, J.; Hampden-Smith, M. J.; Kodas, T. T. *J. Luminescence* **1997**, *75*, 11-16.

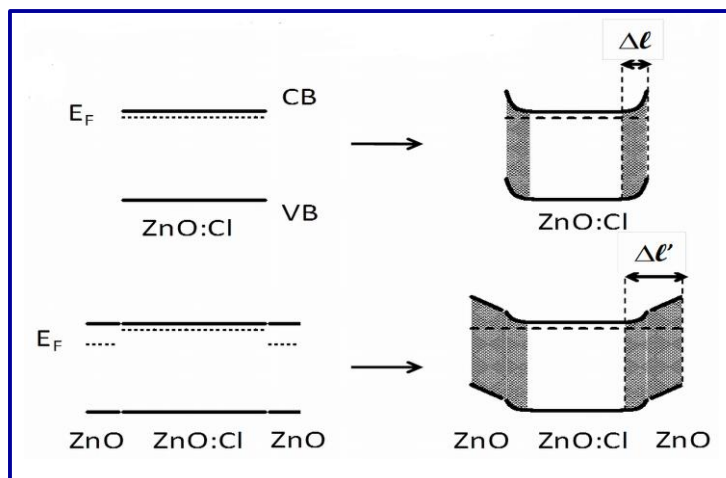
9. Vanheusden, K.; Warren, W. L.; Seager, C. H.; Tallant, D. R.; Voigt, J. A.; Gnade, B. E. *J. Appl. Phys.* **1996**, *79*, 7983-7990.
10. Liao, Z. -M.; Zhang, H.-Z.; Zhou, Y.-B.; Xu, J.; Zhang, J.-M.; Yu, D. -P. *Phys. Lett. A* **2008**, *372*, 4505-4509.
11. Bouzid, K.; Djelloul, A.; Bouzid, N.; Bougdira, J. *Phys. Status Solidi A* **2009**, *206*, 106-115.
12. Vanheusden, K.; Seager, C. H.; Warren, W. L.; Tallant, D. R.; voigt, J. A. *Appl. Phys. Lett.* **1996**, *68*, 403-405.
13. Ahn, M.-W.; Park, K.-S.; Heo, J.-H.; Park, J.-G.; Kim, D.-W.; Choi, K. J.; Lee, J.-H.; Hong, S.-H. *Appl. Phys. Lett.* **2008**, *93*, 263103.
14. Van Dijken, A.; Meulenkamp, E. A.; Vanmaekelberg, D.; Meijerink, A. *J. Phys. Chem. B* **2000**, *104*, 4355-4360.
15. Fan, X. M.; Lian, J. S.; Jiang, Q.; Zhou, Z. W. *J. Mater. Sci.* **2007**, *42*, 2678-2683.
16. Chang, S.-S. *J. Korean Ceram. Soc.* **2011**, *48*, 251-256.
17. Lin, B.; Fu, Z.; Jia, Y. *Appl. Phys. Lett.* **2001**, *79*, 943-945.
18. Manzano, C. V.; Alegre, D.; Caballero-Calero, O.; Alén, B.; Martín-González, M. S. *J. Appl. Phys.* **2011**, *110*, 043538.
19. Janotti, A.; Van de Walle, C. G. *Phys. Rev. B* **2007**, *76*, 165202.
20. Roro, K. T.; Dangbegnon, J. K.; Sivaraya, S.; Leitch A. W. R.; Botha, J. R. *J. Appl. Phys.* **2008**, *103*, 053516.
21. Liua, Z. W.; Ong, C. K.; Yu, T.; Shen, Z. X. *Appl. Phys. Lett.* **2006**, *88*, 053110.
22. Zeng, H.; Duan, G.; Li, Y.; Yang, S.; Xu, X.; Cai, W. *Adv. Funct. Mater.* **2010**, *20*, 561-572.
23. Garces, N. Y.; Wang, L.; Bai, L.; Giles, N. C.; Halliburton, L. E.; Cantwell, G. *Appl. Phys. Lett.*, **2002**, *81*, 622-624.
24. Gu, X.; Huo, K.; Qian, G.; Fu, J.; Chu, P. K. *Appl. Phys. Lett.* **2008**, *93*, 203117.
25. Andelman, T.; Gong, Y.; Polking, M.; Yin, M.; Kuskovsky, I.; Neumark, G.; O'Brien, S. *J. Phys. Chem. B* **2005**, *109*, 41314-14318.
26. Shalish, I.; Temkin, H.; Narayanamurti, V. *Phys. Rev. B* **2004**, *69*, 245401.
27. Chang, P.-C.; Chien, C.-J.; Stichtenoth, D.; Ronning, C.; Lu, J. G. *Appl. Phys. Lett.* **2007**, *90*, 113101.
28. Van Dijken, A.; Meulenkamp, E. A.; Vanmaekelbergh, D.; Meijerink, A. *J. Phys. Chem. B* **2000**, *104*, 1715-1723.
29. Yousefi, R.; Kamaluddin, B. *J. Alloys and Compounds* **2009**, *479*, 11-14.

30. Wu, X. L.; Siu, G. G.; Fu, C. L.; Ong, H. C. *Appl. Phys. Lett.* **2001**, *78*, 2285-2287.
31. Djurišić, A. B.; Leung, Y. H.; Choy, W. C. H.; Cheah, K. W.; Chan, W. K. *Appl. Phys. Lett.* **2004**, *84*, 2635-2637.
32. Richters, J.-P.; Voss, T.; Kim, D. S.; Scholz, R.; Zacharias, M. *Nanotechnology* **2008**, *19*, 305202.
33. Shi, S.; Xu, J.; Zhang, X.; Li, L. *J. Appl. Phys.* **2011**, *109*, 103508.
34. Ye, J. D.; Gu, S. L.; Qin, F. et al. *Appl. Phys. A* **2005**, *81*, 759-762.
35. Fan, J.; Guell, F.; Fabrega, C.; Shavel, A.; Carrete, A.; Andreu, T.; Morante, J. R.; Cabot, A. *Appl. Phys. Lett.* **2011**, *99*, 262102.
36. House, R. L.; Mehl, B. P.; Kirschbrown, J. R.; Barnes, S. C.; Papanikolas, J. M. *J. Phys. Chem. C* **2011**, *115*, 10806-10816.
37. Yang, L. L.; Zhao, Q. X.; Israr, M. Q.; Sadaf, J. R.; Willander, M.; Pozina, G.; Yang, J. H. *J. Appl. Phys.* **2010**, *108*, 103513.
38. Ahn, C. H.; Kim, Y. Y.; Kim, D. C.; Mohanta, S. K.; Cho, H. K. *J. Appl. Phys.* **2009**, *105*, 013502.
39. Wang, Z. L. *J. Phys.: Condens. Matter.* **2004**, *16*, 829-858.
40. Chu, D.; Masuda, Y.; Ohji, T. Kato, K. *J. Am. Ceram. Soc.* **2010**, *93*, 887-893.
41. Huang, M. H.; Wu, Y.; Feick, H.; Tran, N.; Weber, E. Yang, P. *Adv. Mater.* **2001**, *13*, 113-116.
42. Sun, Y.; Fuge, G. M.; Ashfold, M. N. R. *Chem. Phys. Lett.* **2004**, *396*, 21-26.
43. Park, W. I.; Kim, D. H.; Jung S. W.; Yi, G. C. *Appl. Phys. Lett.* **2002**, *80*, 4232-4234.
44. Grene, L. E.; Yuhas, B. D.; Law, M.; Zitoun, D.; Yang, P. *Inorg. Chem.* **2006**, *45*, 7535-7543.
45. Govender, K.; Boyle, D. S.; Kenway, P. B.; O'Brien, P. *J. Mater. Chem.* **2004**, *14*, 2575-2591.
46. Peulon, S.; Lincot, D. *Adv. Mater.* **1996**, *8*, 166-170.
47. Fan, J.; Shavel, A.; Zamani, R.; Fábrega, C. et al. *Acta Mater.* **2011**, *59*, 6790-6800.
48. Egelhaaf, H.-J.; Oelkrug, D. *J. Crystal Growth* **1996**, *161*, 190-194.
49. Liao, Z.-M.; Liu, K.-J.; Zhang, J.-M.; Xu, J. Yu, D.-P. *Phys. Lett. A* **2007**, *367*, 207-210.
50. Liao, Z.-M.; Hou, C.; Zhou, Y.-B.; Xu, J.; Zhang, J.-M.; Yu, D.-P.; *J. Chem. Phys.* **2009**, *130*, 084708.

51. Prades, J. D.; Hernandez-Ramirez, F.; Jimenez-Diaz, R.; Manzanares, M.; Andreu, T.; Cirera, A.; Romano-Rodriguez A.; Morante, J. R. *Nanotechnology* **2008**, *19*, 465501.
52. Mora-Seró, I.; Fabregat-Santiago, F.; Denier, B.; Bisquert, J.; Tena-Zaera, R.; Elias J.; Lévy-Clément, C. *Appl. Phys. Lett.* **2006**, *89*, 203117.
53. Bradley, R. K.; Arthur, B. E. *J. Am. Chem. Soc.* **1980**, *30*, 968-980.
54. Petermann, G.; Tributsch, H.; Bogomolni, R. *J. Chem. Phys.* **1972**, *57*, 1026-1032.
55. Noguchi, H.; Kondo, T.; Uosaki, K. *J. Phys. Chem. B* **1997**, *101*, 4978-4981.
56. Williams, R. *J. Chem. Phys.* **1960**, *32*, 1505-1514.
57. Gerischer, H. *J. Electrochem. Soc.* **1966**, *113*, 1174-1182.
58. Djurišić, A. B.; Ng, A. M. C.; Chen, X. Y. *Prog. Quant. Electron.* **2010**, *34*, 191-259.
59. Liu, X.; Wu, X. H.; Cao, H.; Chang, R. P. H. *J. Appl. Phys.* **2004**, *95*, 3141-3147.
60. Sun, Y.; George Ndifor-Angwafor, N.; Jason Riley, D.; Ashfold Michael, N. R. *Chem. Phys. Lett.* **2006**, *431*, 352-357.
61. Fichou, D.; Kossanyi, J. *J. Electrochem. Soc.* **1986**, *133*, 1607-1617.

Chapter 4

Enhancement of the Photoelectrochemical Properties of Cl-Doped ZnO Nanowires by Tuning Their Coaxial Doping Profile



4.1 Abstract

Arrays of vertically aligned ZnO:Cl@ZnO core-shell NWs were used to demonstrate that the control of the coaxial doping profile in homojunction nanostructures can improve their surface charge carrier transfer while conserving potentially excellent transport properties. It is experimentally shown that the presence of a ZnO shell enhances the photoelectrochemical properties of ZnO:Cl NWs up to a factor 5. Likewise, the ZnO shell promotes the visible photoluminescence band in highly conducting ZnO:Cl NWs. These lines of evidence are associated with the increase of the nanowires' surface depletion layer.

4.2 Introduction

The potential for combined high efficiency charge carrier transport and surface charge carrier transfer/separation has stimulated interest in semiconductor NWs and nanotubes for an ample range of applications. In particular, ZnO NWs find multiple technological uses where the optimization of the charge carrier transport and transfer is fundamental: e.g. gas sensing, photovoltaics, photodetectors, photocatalysis and photoelectrocatalysis. In all these applications, ZnO plays multiple roles: (i) It supports the photo- or catalytically-active species; (ii) It plays a catalytic/photocatalytic role itself; (iii) It collects/separates charge carriers from photo-active or catalytically-active sites and species; (iv) It provides the avenues for charge carrier transportation between reaction sites or between the reaction/photogeneration/recombination site and the electrodes. This multiplicity of roles makes very strong demands on material qualities. Independent optimization of the various material qualities required for each role is frequently incompatible with the limited degrees of freedom available in a single material. A particularly important case is the simultaneous maximization of charge carrier transfer and transport. While NWs already provide favorable geometry, a promotion of the ZnO electrical conductivity, usually accomplished by extrinsic doping, is still required in those applications where ZnO has an active electronic role. However, high carrier concentrations reduce the extent of the surface space charge region. The narrowing of the surface depletion layer decreases the volume within the nanowires where the presence of an electric field drives charge separation, thus reducing the efficiency of charge carrier transfer/collection/separation.¹⁻⁴

Compositional graded and core-shell nanostructures are interesting architectures that provide higher levels of control over the material's functional properties.⁵ In this direction, ZnO/TiO₂ nanostructures have been shown to enhance photovoltaics

efficiency.^{6,7} ZnO/Al₂O₃ nanostructures provide excellent surface passivation, promoting radiative recombination.⁸ Shells of lower band gap materials can extend the NW's core optical absorption to the visible part of the spectrum, thus promoting charge carrier photogeneration.⁹ Nevertheless, the use of coaxial heterojunctions has the challenge of the lattice mismatch, which generally introduces a significant density of interface defects that can decrease the optoelectronic properties of the formed heterostructure.

In this chapter, we show that adjusting the surface doping level in ZnO:Cl NWs promotes their surface charge transfer and photoelectrochemical properties without influencing their core's charge carrier concentration. Our goal is to show that it is feasible to produce coaxial homojunction nanowires with controlled surface depletion layers but conserving their optical properties and their high bulk electrical conductivity. Such control of the surface depletion regions in coaxial homojunction nanowires opens new perspective for the production of more efficient photoelectrochemical, photovoltaic or photocatalytic devices.

4.3 Experimental section

4.3.1 NWs growth

ZnO NWs were electrochemically grown in an aqueous solution inside a three-electrode cell. The growth solution was prepared by incorporating 10 mL of a 0.1 M aqueous solution (MilliQ+, 18.2 M Ω ·cm) of zinc nitrate (Zn(NO₃)₂·4H₂O) and 10 mL of a 0.1 M aqueous solution of methenamine (C₆H₁₂N₄) in 80 mL of deionized water and quickly heating up the solution to 90 °C on a hot plate. A platinum wire immersed in the solution was used as a counter electrode. An Ag/AgCl electrode in saturated KCl

(3 M) was used as the reference electrode. A negative DC potential in the range between -0.4 and -1.4 V relative to the reference electrode was applied to a soda lime glass coated with FTO, ITO or Pt, which was used as substrate for the ZnO NWs growth. After a 1 hour growth time, the samples were immediately rinsed with deionized water. Chlorine ions were introduced in a controlled way by replacing between 0.5 and 10 ml of deionized water with 1 M aqueous solution of ammonium chloride (NH_4Cl). To obtain the coaxial ZnO:Cl@ZnO homojunction NWs, the initial ZnO:Cl NWs were thoroughly washed and subsequently subjected to additional electrodeposition growth steps in the absence of NH_4Cl . The applied potential was fixed at -0.4 V vs Ag/AgCl. The thickness of the ZnO shell could be controlled by the electrodeposition time (300 s) and/or the number (1-5) of additional electrodeposition growth steps.

4.3.2 Characterization

A double beam spectrophotometer (Perkin Elmer Lambda 950) equipped with an integrated sphere was used for the UV-vis transmission measurements in the range from 250 to 800 nm.

Room-temperature PL measurements were obtained using a Kimmon IK Series HeCd CW laser (325 nm and 40 mW). Light was dispersed through an Oriel Corner Stone 1/8 74000 monochromator, detected with a Hamamatsu R928 photomultiplier, and amplified through a Stanford Research Systems SR830 DSP Lock-in amplifier.

PEC properties of core-shell NW arrays were examined using a three-electrode potentiostat system with an Ag/AgCl electrode in saturated KCl (3 M) as the reference electrode and a Pt wire as counter electrode. 0.1 M Na_2SO_4 aqueous solutions were used as electrolytes to study the PEC properties of ZnO:Cl@ZnO homojunction photo-

electrodes. The photocurrent and voltage of the cell were measured for a specific area (1 cm^2) of the obtained core/shell NW arrays working electrode under UV illumination (HgXe lamp with 365 nm filter) .

4.4 Results and discussion

Coaxial ZnO:Cl@ZnO NWs were grown by a simple electrodeposition two-step process. First, arrays of vertically aligned and single crystal ZnO:Cl NWs were produced by electrodeposition from a solution containing $\text{Zn}(\text{NO}_3)_2 \cdot 4\text{H}_2\text{O}$ and NH_4Cl , as previously reported.¹⁰ The carrier density of these NWs was previously estimated to be close to 10^{19} cm^{-3} .¹⁰ To obtain coaxial ZnO:Cl@ZnO homojunction, the initial ZnO:Cl NWs were thoroughly washed in water and subsequently subjected to one or more additional electrodeposition growth steps in the absence of NH_4Cl . The thickness of the ZnO shell was controlled by the electrodeposition time and/or the number of additional electrodeposition growth steps.

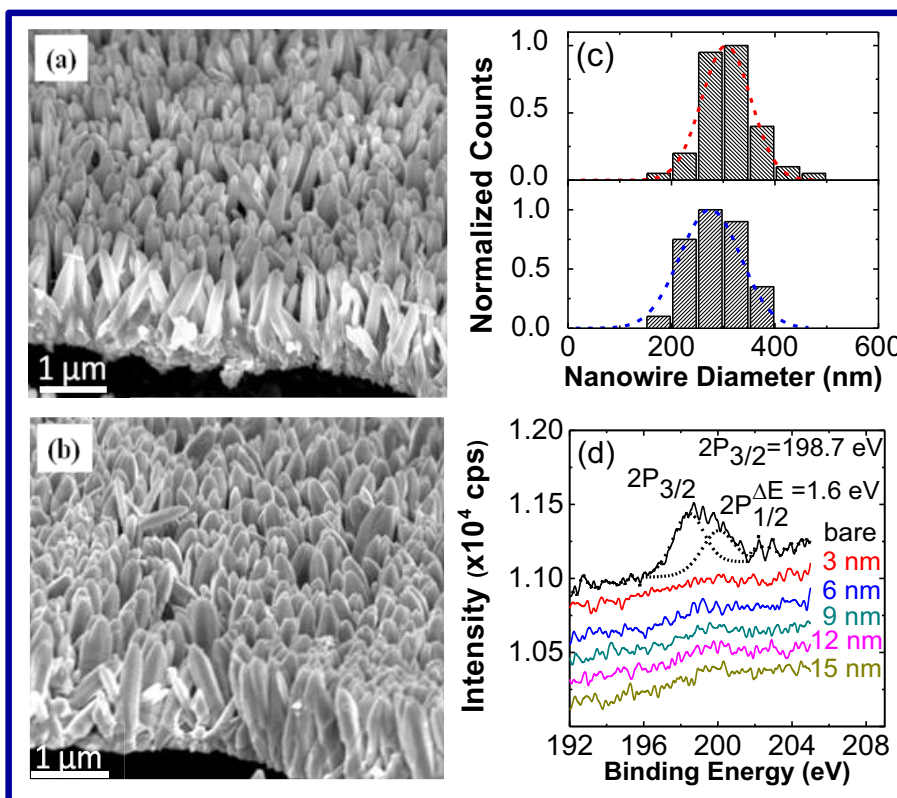


Figure 1. Cross-section SEM images of bare ZnO:Cl NWs (a) and ZnO:Cl@ZnO homojunction NWs with a 15 nm shell thickness (b). (c) Histograms of the thickness distribution of the ZnO:Cl@ZnO (up) and the bare ZnO:Cl (down) NWs. (d) Chlorine region of the XPS spectra of ZnO:Cl and ZnO:Cl@ZnO NWs with increasingly thicker shell thicknesses as noted in the graph. The fitting of the chlorine 2P band with two peaks, corresponding to 2P_{3/2} and 2P_{1/2} is also shown.

Figure 1 shows SEM images of the ZnO:Cl before and after growing a 15 nm ZnO shell. As expected from the epitaxial growth of the ZnO shell, at first view, no clear differences between the ZnO:Cl and the ZnO:Cl@ZnO NWs were observed in the SEM images. Importantly, neither branching nor nucleation of additional NWs or nanoparticles was observed. Statistical measurements of the NWs dimensions allowed us to determine their ZnO shell thickness (~ 15 nm) and the shell growth rate in the used electrodeposition conditions (~ 36 nm/h) (Figure 1c). This value was consistent with XPS characterization of the evolution of the Cl composition with the shell thickness

(Figure 1d). For these measurements, the same sample was subjected to successive ZnO growth steps while an XPS spectrum was obtained in between each step. The Cl concentration was already below the XPS detection limit in ZnO:Cl@ZnO NWs with a shell grown for 5 minutes, which roughly corresponded to a 3 nm width. The lack of Cl signal from the ZnO:Cl@ZnO samples also pointed towards a highly homogeneous ZnO deposition on the surface of the ZnO:Cl NWs.

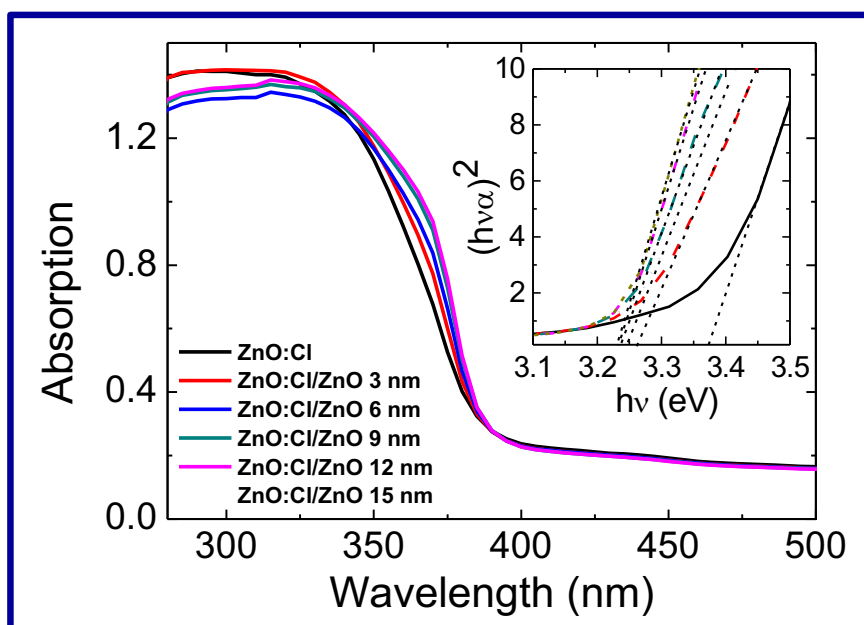


Figure 2. Absorbance spectra of ZnO:Cl NWs and ZnO:Cl@ZnO homojunction NWs with increasingly thicker shell thicknesses. The inset shows the dependence of $(\alpha h\nu)^2$ vs. $h\nu$ and the lineal fit used to point the shift of the optical band gap.

Figure 2 shows the UV-vis spectra of ZnO:Cl@ZnO NWs obtained from the exact same initial ZnO:Cl NWs, which underwent 5 successive ZnO growth steps. UV-vis spectra of the ZnO:Cl@ZnO NWs were obtained in between each electrodeposition step. The optical band gap showed a slight red shift with the successive ZnO growth steps. The origin of such a red shift was found on the optical band gap of the original ZnO:Cl

NWs, which was slightly blue-shifted respect to pure ZnO NWs due to the Moss-Burstein effect.¹⁰⁻¹³ The growth of a pure ZnO shell on the surface of the ZnO:Cl NWs introduced empty states in the conduction band which allowed the recovery of the electron transitions between the valence band maximum and the conduction band minimum, thus recovering the pure-ZnO optical band gap. The absolute absorbance above the semiconductor band gap did not significantly change with the increase of the ZnO shell thickness. This is consistent with the small increase of the total ZnO volume associated with the growth of the thin ZnO shell.

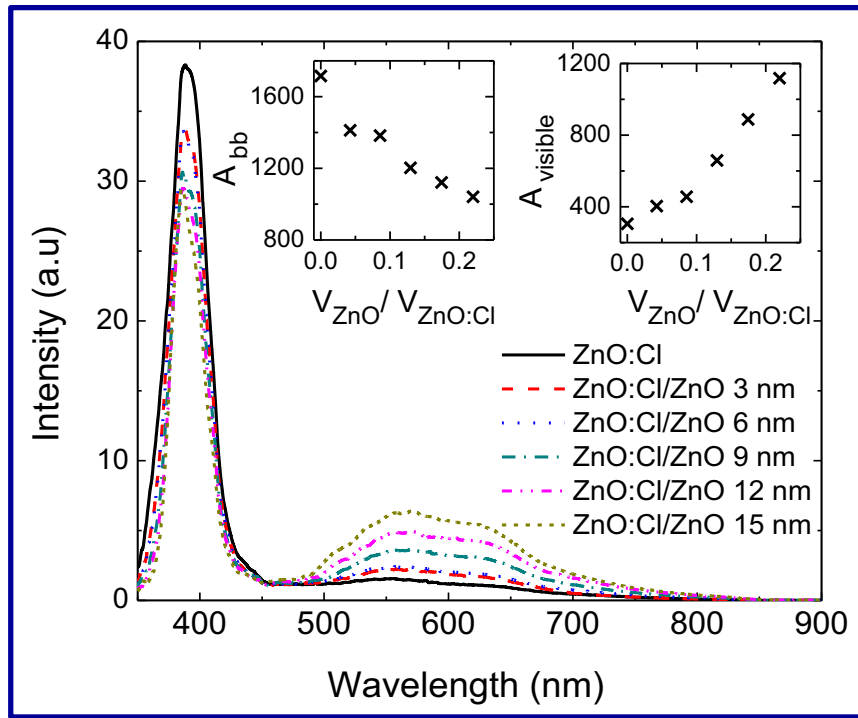


Figure 3. Room temperature PL spectra of ZnO:Cl NWs and ZnO:Cl@ZnO homojunction NWs with increasingly thicker shell thicknesses obtained using 325 nm excitation wavelength. Insets show the evolution of the PL peak area corresponding to the band-to-band transition and to the visible emission, as noted.

Figure 3 shows the results from the room-temperature PL measurements of ZnO:Cl@ZnO NWs obtained using a HeCd CW laser (325 nm). PL spectra were

measured using the exact same ZnO:Cl NWs which were subjected to 5 successive electrodeposition steps to grow an increasingly thicker ZnO shell. Quite unexpectedly, the intensity of the PL peak corresponding to the band-to-band transition decreased slightly with the growth of the pure ZnO shell. At the same time, an enhancement of the PL broad band in the visible part of the spectrum was observed. While the area of the band-to-band PL peak was reduced by a factor 1.7, the visible emission increased almost a factor 4 from the bare ZnO:Cl NWs to the ZnO:Cl@ZnO NWs, which has the thickest ZnO shell tested here (Figure 3, inset). The enhancement of the visible band with the ZnO shell could be originated by a higher density of impurities introduced by a more-defective ZnO shell when compared with the ZnO:Cl core. However, no evidence was found to support this hypothesis.

The visible band emission in ZnO is associated with impurity levels within the ZnO structure.^{14,15} The variety of possible transition and the diversity of ZnO preparation and sintering procedures employed did not allow a consensus on the exact origin of the energy levels contributing to these transitions. In ZnO NWs, the intensity of the visible band has been previously correlated with the materials surface-to-bulk ratio.¹⁶ Such correlation pointed towards an important role of the surface in the associated radiative recombination processes.^{14,16-19} Again, there is no agreement on the origin of such a surface enhancement of the visible band in NWs. It could be related with a higher surface density of the contributing states, their surface activation by the hole accumulation at the surface depletion, or the promotion of slower recombination processes related with the charge separation occurring in the built-in electric field layer.^{8,14,20-26}

In ambient conditions, the ZnO NWs surface is covered by ionized oxygen species and hydroxyl groups that trap conduction electrons, causing an upward bending of the

ZnO energy bands at the surface. While highly doped ZnO screens the surface charge within a very thin surface layer, much thicker depletion regions characterize undoped semiconductors. Considering a typical barrier height of 0.55 eV,²⁷ the width of the calculated depletion layer increases from 7 nm to 230 nm when reducing the carrier concentration from 10^{19} cm^{-3} to 10^{16} cm^{-3} .²⁷⁻²⁹ In this scenario, the growth of an undoped ZnO shell on the surface of ZnO:Cl NWs offers an effective way to adjust the depletion region without modifying the NW's bulk conductivity (Figure 4b).

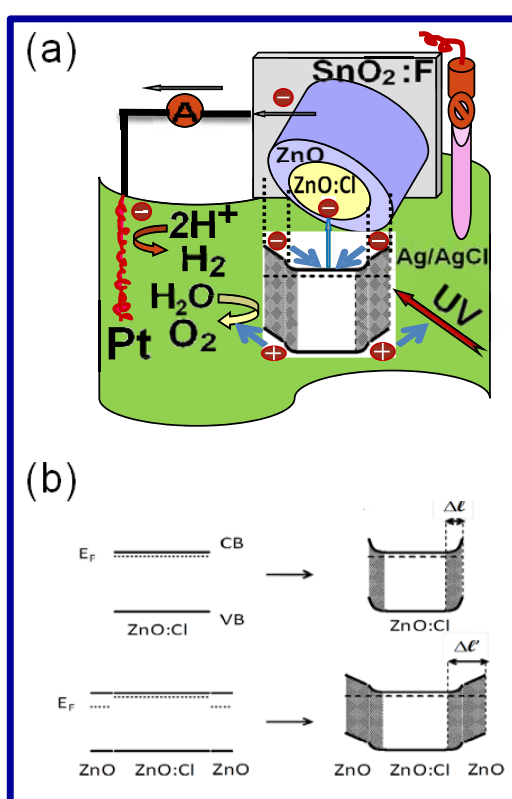


Figure 4. (a) Schematic illustration of the PEC reaction taking place at the ZnO:Cl@ZnO NWs surface. Photogenerated carriers are separated at the depletion region. Holes are driven to the surface where the water oxidation reaction takes place. Electrons are swept to the NW core and funnelled inside there towards the platinum electrode where the reduction reaction takes place. (b) Band diagrams of the ZnO:Cl and ZnO:Cl@ZnO NWs illustrating the increase of the surface depletion region with the growth of the ZnO shell.

The excellent correlation existing between the increase of the visible PL band intensity and the growth of the surface depletion layer when increasing the ZnO shell thickness points towards a direct role of the surface band bending in the promotion of the visible PL. This is consistent with previous studies.^{16,20} The parallel reduction of the interband PL intensity may be associated with a shell screening of both the incident UV photons and of those emitted by the NWs core.

The increase of the depletion layer by the presence of the ZnO shell also augments the volume for charge photogeneration within the nanowires where the presence of an electric field drives charge separation.³⁰ Charge carriers photogenerated in the bulk ZnO need to diffuse to reach the depletion layer where an electric field can drive holes to the surface. However, in bulk ZnO, the holes, the minority carriers, have short diffusion length as they rapidly recombine with electrons, the majority carriers, inside the bulk. In contrast, when photogeneration takes place in the depletion layer, carriers are rapidly separated and swept in opposite directions by the built-in electric field.

The promotion of the charge carrier separation and transfer by the presence of a ZnO shell was verified by the characterization of the NWs PEC properties in a standard three-electrode cell using UV excitation from an HgXe lamp (Figure 4a). In Figure 4a, the photocurrent generated by the ZnO:Cl@ZnO NWs is shown. Again, the same NWs were measured in between successive ZnO electrodeposition steps to avoid any effect of the NWs geometry, density or compositional differences from batch to batch. The photocurrent measured from the ZnO:Cl@ZnO NWs was clearly promoted by the presence of the ZnO shell. Up to a 5-fold increase of the photocurrent was obtained with a 12 nm thick ZnO shell, from 0.6 mA/cm² to 3.1 mA/cm². Both, the correlation of the PEC enhancement with the ZnO shell thickness and the apparent photocurrent saturation for shells thicker than 12 nm were systematically obtained (Figure 5a and b).

The relatively low photocurrent saturation thickness is most probably related to the non-intrinsic character of the ZnO shell. While no extrinsic doping was intentionally introduced, it is well known that electrodeposited ZnO contain significant densities of n-type impurities, which translate into carrier concentrations in the range of 10^{17} .¹⁰ At the same time, a considerable number of charge carriers are transferred from the ZnO:Cl core to the ZnO shell when forming the homojunction. Both effects may explain the relatively low saturation thicknesses obtained. The plot of photoconversion efficiency versus applied potential (Figure 5c) shows the maximum value of efficiency is 0.62%, which is obtained at an applied potential of +0.6 V with a 12 nm thick ZnO shell. This efficiency is almost one order of magnitude higher with respect to the ZnO:Cl NWs.

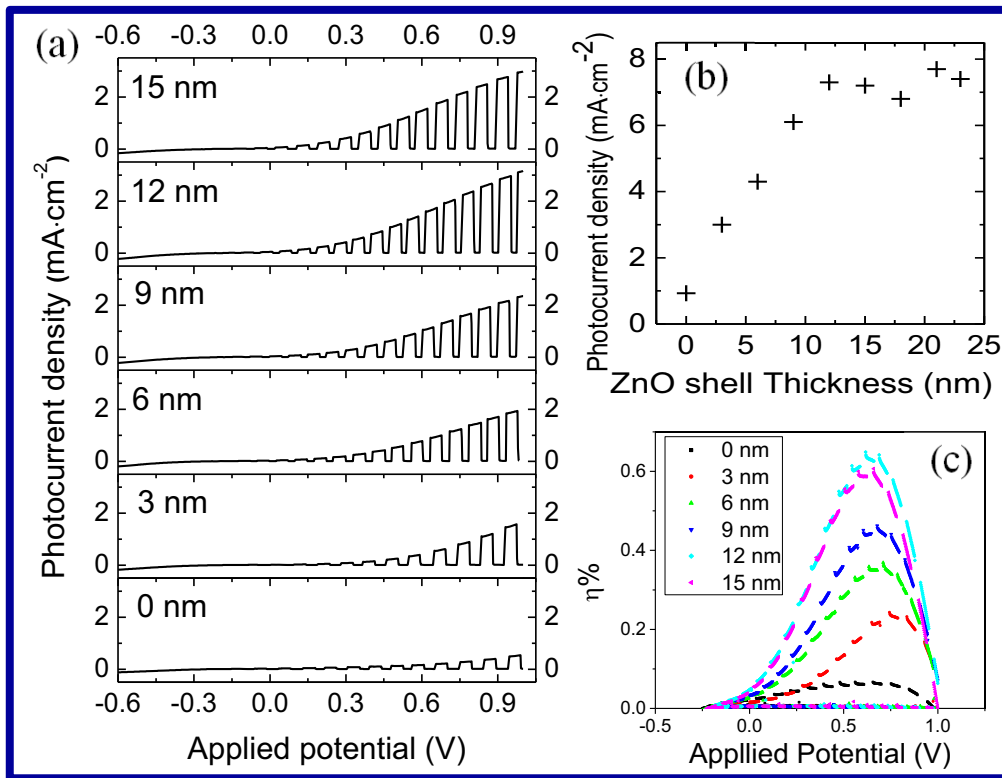


Figure 5. (a) Photocurrent density vs. applied potential (V vs. Ag/AgCl) for ZnO:Cl NWs and ZnO:Cl@ZnO homojunction NWs with increasingly thicker shell, measured under chopped UV illumination (100 mW/cm^2) in $0.1 \text{ M Na}_2\text{SO}_4$ aqueous solution. (b) Photocurrent as a function of the shell thickness for a second set of ZnO:Cl and ZnO:Cl@ZnO NWs. (c) Photoconversion

efficiency of the PEC cell with ZnO:Cl nanowires and ZnO:Cl@ZnO homojunction NWs electrode as a function of applied potential.

4.5 Conclusions

In summary, the control of the doping profile in ZnO:Cl@ZnO NWs allowed adjustment of the thickness of the depletion layer and the volume within the NWs with a built-in electric field. Such homojunction NWs promote charge separation and transfer to the surface as evidenced by an enhancement of the surface-related PL band and the improvement of the PEC properties of the material. We believe such core-shell homojunction nanowires are good candidates to improve the efficiency of photoelectrochemical, photocatalytic and photovoltaic devices.

4.6 References

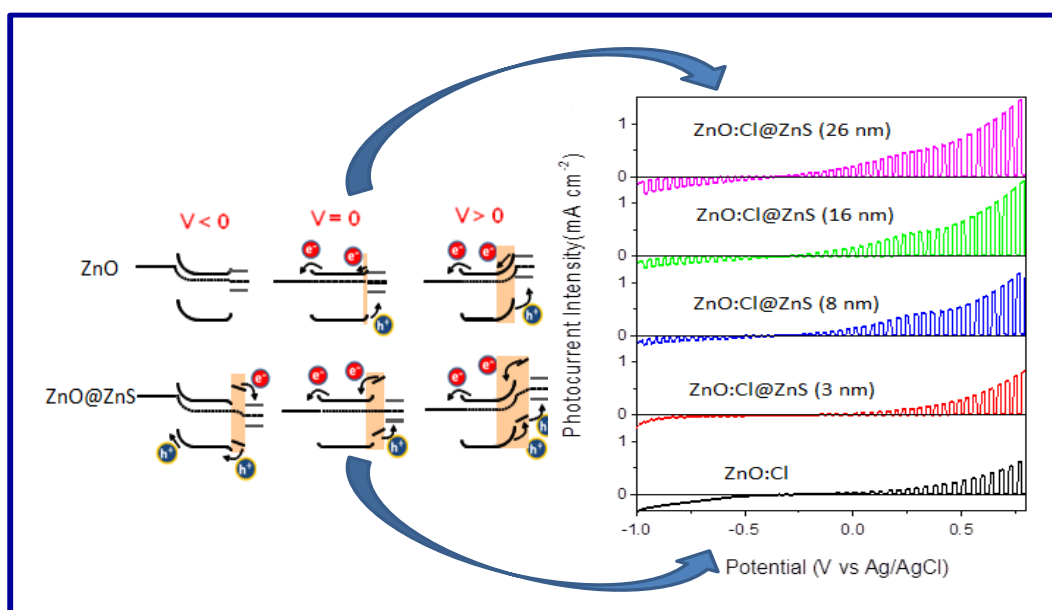
1. Ono, M.; Fujii, K.; Ito, T.; Iwaki, Y.; Hirako, A.; Yao, T.; Ohkawa, K. *J. Chem. Phys.* **2007**, *126*, 054708.
2. Reichman, J. *Appl. Phys. Lett.* **1980**, *36*, 574-577.
3. Gartner, W. W. *Phys. Rev.* **1959**, *116*, 84-87.
4. Sah, C.-T.; Noyce, R. N.; Shockley, W. *Proc. IRE* **1957**, *45*, 1228-1243.
5. Hall, C. R.; Dao, L. V.; Koike, K.; Sasa, S.; Tan, H. H.; Inoue, M.; Yano, M.; Jagadish C.; Davis, J. A. *Appl. Phys. Lett.* **2010**, *96*, 193117.
6. Greene, L. E.; Law, M.; Yuhas B. D.; Yang, P. *J. Phys. Chem. C* **2007**, *111*, 18451-18456.
7. Law, M.; Greene, L. E.; Radenovic, A.; Kuykendall, T.; Liphardt, J.; Yang, P. *J. Phys. Chem. B* **2006**, *110*, 22652-22663.
8. Richters, J.-P.; Voss, T.; Kim, D. S.; Sholz, R.; Zacharias, M. *Nanotechnology* **2008**, *19*, 305202.
9. Wang, X.; Zhu, H.; Xu, Y.; Wang, H.; Tao, Y.; Hark, S.; Xiao, X.; Li, Q. *ACS Nano* **2010**, *4*, 3302-3308.

10. Fan, J.; Shavel, A.; Zamani, R.; Fábrega, C.; et al. *Acta Mater.* **2011**, *59*, 6790-6800.
11. Burstein, E. *Phys. Rev.* **1954**, *93*, 632-633.
12. Moss, T. S. *Proc. Phys. Soc. London, Sect. B* **1954**, *67*, 775-782.
13. Lu, J. G.; Fujita, S.; Kawaharamura, T.; Nishinaka, H.; Kamada, Y.; Ohshima, T.; Ye, Z. Z.; Zeng, Y. J.; Zhang, Y. Z.; Zhu, L. P.; He, H. P.; Zhao, H. *J. Appl. Phys.* **2007**, *101*, 083705.
14. Djurišić, A. B.; Ng A. M. C.; Chen, X. Y. *Prog. Quant. Electron.* **2010**, *34*, 191-259.
15. Manzano, C. V.; Alegre, D.; Caballero-Calero, O.; Alén, B.; Martín-González, M. *S. J. Appl. Phys.* **2011**, *110*, 043538.
16. Shalish, I.; Temkin, H.; Narayanamurti, V. *Phys. Rev. B* **2004**, *69*, 245401.
17. Prades, J. D.; Cirera, A.; Morante, J. R.; Cornet, A. *Thin Solid Films* **2007**, *515*, 8670-8673.
18. Gu, X.; Huo, K.; Qian, G.; Fu, J.; Chu, P. K. *Appl. Phys. Lett.* **2008**, *93*, 203117.
19. Chang, P.-C.; Chien, C.-J.; Stichtenoth, D.; Ronning, C.; Lu, J. G. *Appl. Phys. Lett.* **2007**, *90*, 113101.
20. Shi, S.; Xu, J.; Zhang, X.; Li, L. *J. Appl. Phys.* **2011**, *109*, 103508.
21. Van Dijken, A.; Meulenkaamp, E. A.; Vanmaekelbergh, D.; Meijerink, A. *J. Phys. Chem. B* **2000**, *104*, 1715-1723.
22. Van Dijken, A.; Meulenkaamp, E. A.; Vanmaekelbergh, D.; Meijerink, A. *J. Phys. Chem. B* **2000**, *104*, 4355-4360.
23. Vanheusden, K.; Warren, W. L.; Seager, C. H.; Tallant, D. R.; Voigt, J. A.; Gnade, B. E. *J. Appl. Phys.* **1996**, *79*, 7983-7990.
24. Ye, J. D.; Gu, S. L.; Qin, F.; Zhu, S. M.; Liu, S. M.; Zhou, X.; Liu, W.; Hu, L. Q.; Zhang, R.; Shi, Y.; Zheng, Y. D. *Appl. Phys. A* **2005**, *81*, 759-762.
25. House, R. L.; Mehl, B. P.; Kirschbrown, J. R.; Barnes, S. C.; Papanikolas, J. M. *J. Phys. Chem. C* **2011**, *115*, 10806-10816.
26. Liao, Z.-M.; Zhang, H.-Z.; Zhou, Y.-B.; Xu, J.; Zhang, J.-M.; Yu, D.-P. *Phys. Lett. A* **2008**, *372*, 4505-4509.
27. Liao, Z.-M.; Liu, K.-J.; Zhang, J.-M.; Xu, J.; Yu, D.-P. *Phys. Lett. A* **2007**, *367*, 207-210.

28. Prades, J. D.; Hernandez-Ramirez, F.; Jimenez-Diaz, R.; Manzanares, M.; Andreu, T.; Cirera, A.; Romano-Rodriguez, A.; Morante, J. R. *Nanotechnology* **2008**, *19*, 465501.
29. Mora-Seró, I.; Fabregat-Santiago, F.; Denier, B.; Bisquert, J.; Tena-Zaera, R.; Elias, J.; Lévy-Clément, C.; *Appl. Phys. Lett.* **2006**, *89*, 203117.
30. Yang, L. L.; Zhang, Q. X.; Israr, M. Q.; Sadaf, J. R.; Willander, M.; Pozina, G.; Yang, J. H. *J. Appl. Phys.* **2010**, *108*, 103513.

Chapter 5

Solution-Growth and Optoelectronic Properties of ZnO:Cl@ZnS Core-Shell Nanowires with Tunable Shell Thickness



5.1 Abstract

Arrays of vertically aligned ZnO:Cl@ZnS core-shell NWs were grown by a facile low-cost, high-yield and seed-free two-step process. These NWs were used to demonstrate the potential of 3D electrodes based on core-shell heterostructures to enhance charge carrier separation and transfer. With this goal in mind, the photocurrent density of ZnO:Cl@ZnS NWs was characterized as a function of the shell thickness. Although no significant variations in the absorption and PL spectra were found with the presence of the shell, the photocurrent measured from the core-shell NWs was highly enhanced with respect to bare ZnO:Cl NWs. These photocurrent variations are

associated with the control of the band bending in the core-shell NW surface, which modifies the efficiency of charge carrier transfer between the NW and the electrolyte.

5.2 Introduction

Aligned NW arrays allow the concurrence of high efficiencies of charge carrier transport with large interface areas for charge separation and/or transfer with the surrounding species/material/electrolyte. Therefore, NW- and nanotube-based electrodes are widely used to improve the efficiency of a plethora of applications where both charge carrier transport and separation/transfer are fundamental. In this scenario, core-shell NWs are ideal candidates to independently optimize both properties.

In particular, ZnO and ZnS are well studied II-VI semiconductors with direct band gaps of 3.37 and 3.73 eV, respectively.^{1,2} They find multiple applications in the fields of photonics, optoelectronics, photocatalysts and also piezoelectrics.³⁻⁶ At the same time, ZnO-ZnS heterostructures are used as photocatalysts,⁷ efficient UV emitters and photodetectors,^{8,9} chemical sensors,¹⁰ n-type support/transparent-electrode/buffer layer in dye-sensitized¹¹ and CIGS solar cells,^{12,13} and they have been also proposed as absorber material in a new class of stable and low-cost photovoltaic solar cells^{14,15}

Recently, the production of ZnO@ZnS heterostructured NWs has been attempted by various techniques including chemical vapor deposition,^{15,16} thermal evaporation,⁶ and ion exchange.¹¹ Nevertheless, an especially convenient and efficient approach for the synthesis of arrays of vertically aligned ZnO@ZnS heterostructured NWs, owing to its simplicity and potential for large scale and low cost production, is the SILAR. SILAR deposition routes have been rarely reported for the synthesis of ZnO@ZnS

heterostructured NWs.¹⁷ At the same time, to the best of our knowledge, a study on the PEC properties of ZnO@ZnS core-shell NWs is not yet available in the literature.

In the present chapter, we present a novel approach to produce ZnO:Cl@ZnS core-shell NWs prepared by a facile two step process at low temperature and ambient pressure. The proposed approach allows adjusting the core conductivity of the NWs by means of controlling the chlorine concentration. The ZnO:Cl electrodeposition parameters allow also tuning the NW density, thickness and length. Likewise, the SILAR procedure offers a precise control of the thickness and characteristics of the shell. These ZnO:Cl@ZnS NWs were used to demonstrate the potential of core-shell heterostructures to enhance the photoelectrochemical properties of ZnO NWs. The obtained experimental results are discussed here in view of the energy band alignment and the depletion regions created in the formed heteronanostructures. We believe such core-shell NWs are excellent 3D photoelectrodes to improve the efficiency of photoelectrochemical, photocatalytic and optoelectronic devices.

5.3 Experimental section

5.3.1 ZnO:Cl NWs growth

ZnO:Cl NWs were electrochemically grown in an aqueous solution inside a three-electrode cell, as previously reported.¹⁸ The growth solution was prepared by incorporating 10 mL of 0.1 M aqueous solution (MilliQ+, 18.2 M Ω ·cm) of zinc nitrate ($\text{Zn}(\text{NO}_3)_2 \cdot 6\text{H}_2\text{O}$), 5 mL of 1 M NH_4Cl and 10 mL of 0.1 M aqueous solution of methenamine ($\text{C}_6\text{H}_{12}\text{N}_4$) in 77 mL of deionized water and quickly heating up the solution to 90 °C on a hot plate. A platinum wire immersed in the solution was used as a counter electrode. An Ag/AgCl electrode in saturated KCl (3 M) was used as the

reference electrode. A negative DC potential of -1.0 V relative to the reference electrode was applied to a soda lime glass coated with FTO, which were used as substrates. After a 1 hour growth time, the samples were immediately rinsed with deionized water.

5.3.2 ZnS shell growth

The ZnS shell was prepared by SILAR method. In particular, the obtained ZnO NW arrays were successively immersed in two different aqueous solutions for 30 s, one containing Zn^{2+} cations (25 mM $\text{Zn}(\text{NO}_3)_2$) and the other containing S^{2-} anions (25 mM Na_2S). Between each immersion step, the samples were rinsed with de-ionized water for 30 s to remove excess ions that were weakly bound to the NW surfaces. This two-step procedure was repeated 100 cycles. After cycles 10, 30, 60 and 100 the obtained samples were dried by means of a N_2 flow. These intermediate samples were used to characterize the influence of the ZnS thickness on the optoelectronic and photoelectrochemical properties of ZnO@ZnS NWs. Thus, it should be kept in mind that the results reported here were obtained from the exact same ZnO NWs, which were coated with increasingly thicker ZnS shells.

5.3.3 Characterization techniques

The morphology of the obtained sample was observed using field emission SEM (FEI Nova Nanosem 230). The detailed morphology and chemical composition of the ZnO@ZnS core-shell NWs were further confirmed by high-resolution scanning transmission electron microscopes (STEM, Jeol J2100 (LaB₆)).

XPS spectra were obtained using a *SPECS SAGE ESCA* System employing Mg K α ($E = 1253.6$ eV) with a supplied power of 203 W as the X-ray source. High-resolution

scans were obtained to provide information regarding the bonding environment and oxidation state of Zn, O and S. Scans including the valence band spectrum were performed with 15 eV pass energy and 0.10 eV steps. All spectra were shifted to account for sample charging using inorganic carbon at 284.80 eV as a reference.

XRD was used to characterize the crystallographic phase the materials produced. For XRD characterization, a Bruker D8 Advance diffractometer with Cu $K\alpha_1$ radiation ($\lambda = 1.5406 \text{ \AA}$) was used.

A double beam spectrophotometer (Perkin Elmer Lambda 950) equipped with an integrated sphere was used for the UV-vis transmission measurements in the range from 250 to 800 nm.

PL measurements were obtained using a Kimmon IK Series HeCd CW laser (325 nm). Fluorescence was dispersed through an Oriel Corner Stone 1/8 74000 monochromator, detected with a Hamamatsu R928 photomultiplier, and amplified through a Stanford Research Systems SR830 DSP lock-in amplifier.

PEC properties of core-shell NW arrays were examined using a typical three-electrode potentiostat system with an Ag/AgCl electrode in saturated KCl (3 M) as the reference electrode and a Pt wire as counter electrode. 0.1 M Na_2SO_4 or 0.5 M Na_2S aqueous solutions were used as electrolytes to study the PEC properties of ZnO:Cl@ZnS core-shell photo-electrodes. The photocurrent and voltage of the cell were measured for a specific area (1 cm^2) of the obtained core-shell NW arrays working electrode under UV excitation from an HgXe lamp.

5.4 Results and Discussion

Vertically aligned and single-crystal ZnO:Cl NWs were electrochemically grown in FTO-coated soda lime glass. A controlled concentration of chlorine ions was introduced by dissolving the required amount of ammonium chloride inside the electrodeposition solution. In this way, the ZnO:Cl charge carrier concentration could be selected in the range from 10^{17} to 10^{20} cm^{-3} . In the present study, the Cl concentration was adjusted to produce ZnO:Cl NWs with an electrical conductivity of approximately $4 \text{ S}\cdot\text{cm}^{-1}$ and a carrier concentrations in the order of 7×10^{18} cm^{-3} , as previously characterized.¹⁸

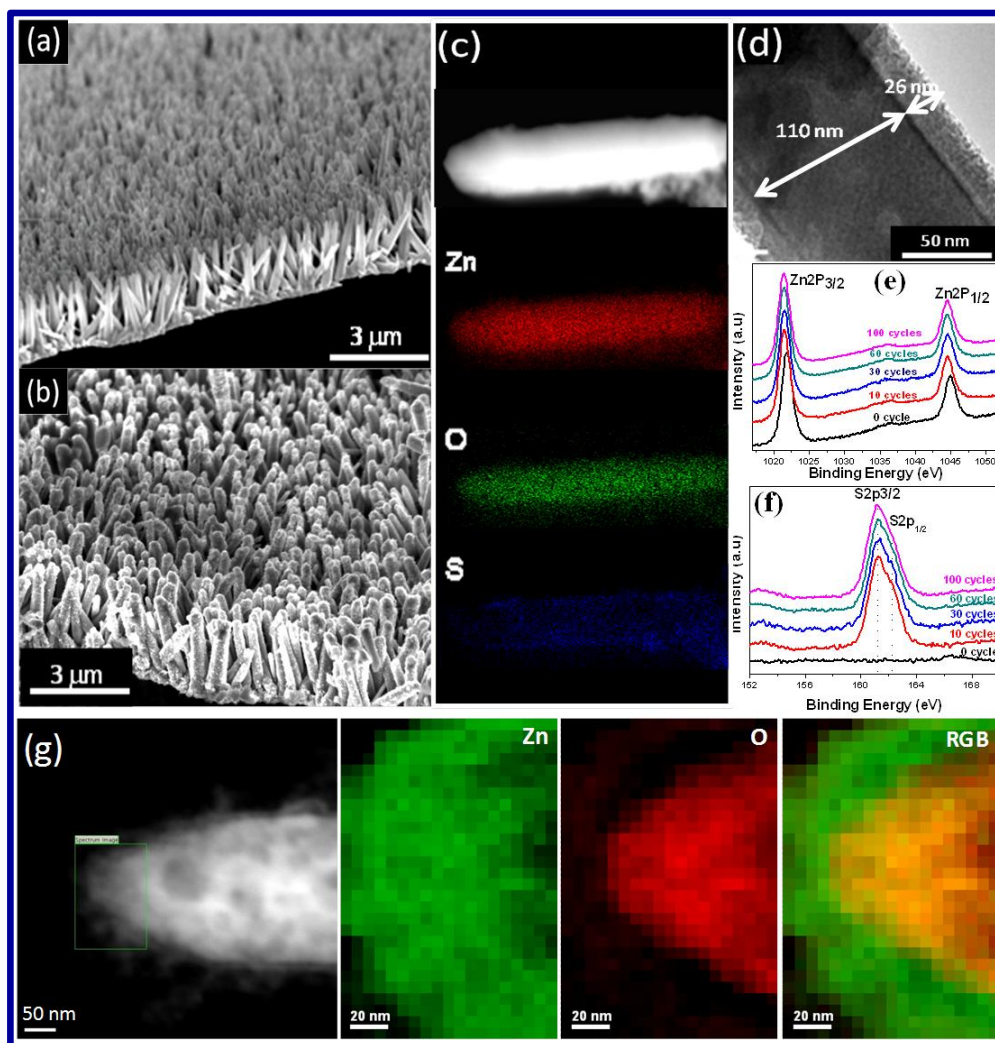


Figure 1. Cross-section SEM images of bare ZnO:Cl NWs (a) and ZnO:Cl@ZnS core-shell NWs (b). (c) EDX mapping of the different elements within a single ZnO:Cl@ZnS core-shell NW. (d) TEM image of single ZnO:Cl@ZnS core-shell NW. (e) Zinc region and (f) Sulfur region of the XPS spectra of ZnO:Cl NWs and ZnO:Cl@ZnS NWs with increasingly thicker shell thicknesses as noted in the figure. (g) EELS mapping of the different elements within a single ZnO:Cl@ZnS core-shell NW.

Figure 1 shows SEM images of an array of electrodeposited ZnO:Cl NWs before (Figure 1a) and after (Figure 1b) growing a ZnS shell using 100 SILAR cycles. The core-shell NWs showed noticeable surface roughness due to the nanoscale inhomogeneities of the grown ZnS shells. Such inhomogeneities should be associated with the lattice mismatch between ZnO and ZnS and with a multiplicity of ZnS

nucleation centres at the ZnO surface. Figure 1c and 1g show the elemental maps within a single core-shell NW obtained with EDX and EELS, respectively. As expected, a homogeneous distribution of Zn is observed across the whole ZnO:Cl@ZnS NW, while oxygen concentrates in the NW core and S in the surface. TEM analysis of single NWs allowed us to determine the ZnS shell growth rate. This was approximately 0.26 nm/cycle (Figure 1d). The growth rate was found to be directly proportional to the concentration of Zn²⁺ cations and S²⁻ anions in the precursor solution. Herein, it should be noted that uniform core-shell NWs were not grown if the concentration of Zn²⁺ and S²⁻ were increased above 0.5 M. Instead, a ZnS layer was found to cover all ZnO NW tips.

The results obtained from the XPS characterization of the NW arrays are shown in figure 1e. The Zn binding energy was slightly shifted to lower energies for the ZnS shell when compared with the ZnO core. This shift is attributed to the different binding energy of the Zn-O and the Zn-S bond due to the dissimilar anion electronegativity.¹⁹

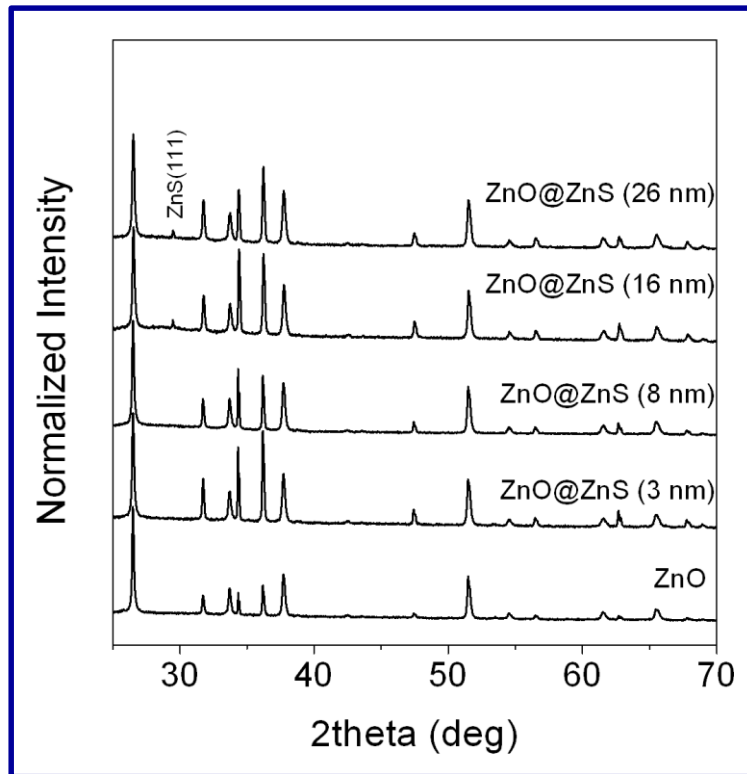


Figure 2. XRD patterns of the ZnO:Cl NWs and ZnO:Cl@ZnS core-shell NWs with increasingly thicker shell thicknesses; Approximated shell thicknesses (from bottom to top): 0 nm, 3 nm, 8 nm, 16 nm and 26 nm.

The XRD patterns of the ZnO:Cl and ZnO:Cl@ZnS NWs is shown in figure 2. The peak corresponding to the ZnS (111) diffraction was observed for samples with ZnS shell thicknesses higher than 10 nm.

Figure 3(a) shows the UV-vis spectra of ZnO:Cl@ZnS NWs with different shell thicknesses. Notice that results correspond to the exact same sample, which was submitted to consecutive shell growth cycles. UV-vis spectra were taken in between each set of cycles. While the presence of a ZnS shell, having a larger band-gap, would not be expected to improve the optical absorption of ZnO NWs, a few works have reported that the combination of two wide band gap semiconductors can yield a material with a lower photoexcitation threshold than the individual components.^{20,21}

Nevertheless, from our experimental results, no differences were observed when comparing the absorption spectra of the ZnO:Cl NWs with those of the ZnO:Cl@ZnS heterostructures.

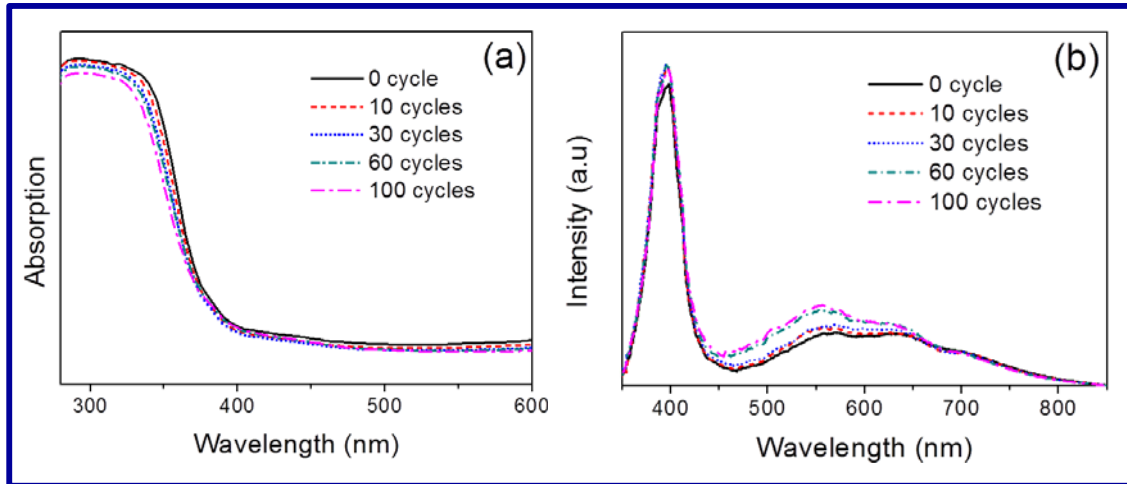


Figure 3. (a) Absorbance spectra of ZnO:Cl NWs and ZnO:Cl@ZnS core-shell NWs with increasingly thicker shell thicknesses. (b) Room temperature PL spectra of ZnO:Cl NWs and ZnO:Cl@ZnS core-shell NWs with increasingly thicker shells obtained using 325 nm excitation wavelength.

In figure 3(b), the room temperature PL spectra of the ZnO:Cl NWs is shown. In the same graph, the room temperature PL spectra of ZnO:Cl@ZnS NW heterostructures obtained by subsequent SILAR cycles is also shown. Note that the same sample was used to obtain all the PL spectra, which were measured in between every set of SILAR cycles. While a slight increase of the band-to-band PL peak was noticed with the presence of the ZnS shell, not a significant variation of the UV emission efficiency of the core-shell NWs was observed. In the same way, no large variations of the visible band emission associated to ZnO were obtained with the ZnS shell growth. In this regard, contradictory results have been reported in the literature. Some authors noticed large increases of PL with the introduction of the ZnS shell and explained them by the larger ZnS band gap, which promoted charge carrier recombination within the ZnO

structure.^{22,23} Other authors claimed no variation or even a reduction of the PL intensity with the ZnS shell growth. This was associated with the type II semiconductor heterostructure formed.^{15,24} From our results, we concluded that the presence of a ZnS shell did not significantly modify the optical properties of the ZnO NWs. Only a green PL band appeared with the ZnS shell growth. The intensity of this band was clearly correlated with the ZnS shell thickness. A similar band was observed in ZnS-coated ZnO NWs.⁸ This band has been previously associated with self-activated centres, vacancy states or interstitial states within the ZnS structure.²⁵⁻²⁸

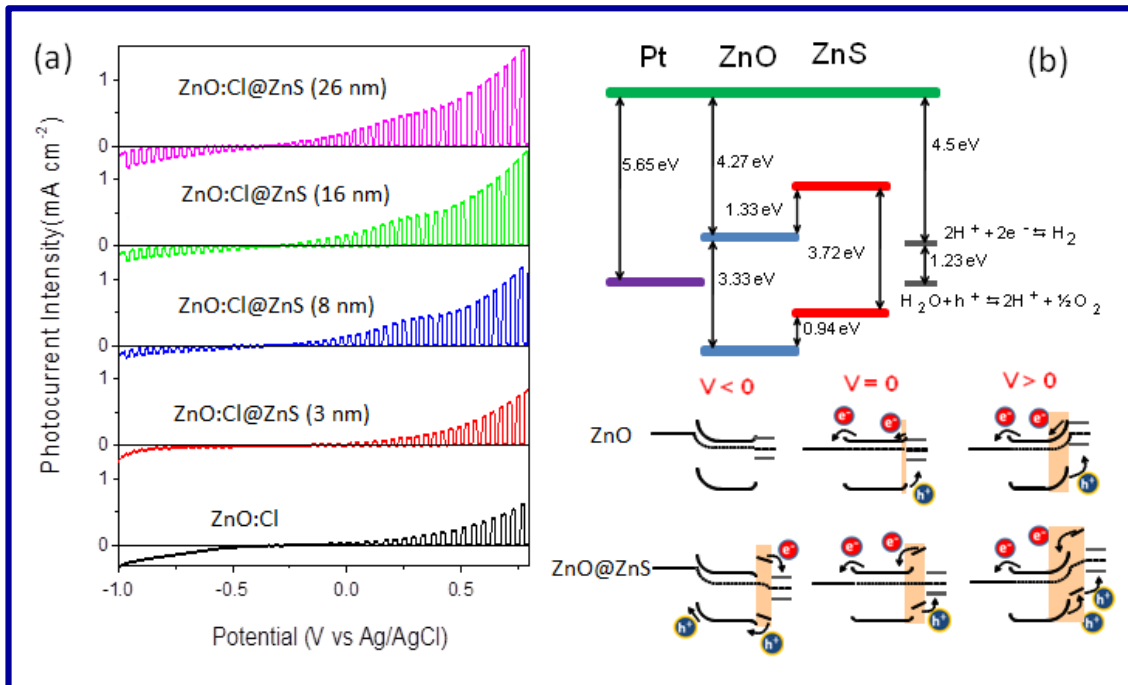


Figure 4. (a) Photocurrent density vs. applied potential (V vs. Ag/AgCl) from ZnO:Cl NWs and ZnO:Cl@ZnS core-shell NWs with increasingly thicker shells. Measurements were performed under chopped ($T_{\text{period}}=2$ s) UV illumination ($100 \text{ mW}/\text{cm}^2$) from a HgXe lamp in $0.1 \text{ M Na}_2\text{SO}_4$ aqueous solution. (b) Schematic representation of the energy band alignment, the depletion regions created in the formed heteronanostructures and the charge transfer for bare ZnO:Cl NWs and ZnO:Cl@ZnS core-shell NWs at different applied potential ($V < 0$, $V = 0$ and $V > 0$).

The photoelectrolysis of water to generate H_2 on a semiconductor/electrolyte interfaces has the attractive advantages of being a clean and energy-efficient process. The optimization of semiconductor PEC properties requires very large surface areas to maximize the semiconductor/electrolyte interface, and very high electrical conductivities to facilitate charge carrier transport between oxidation and reduction sites. In this scenario, NW arrays are very interesting candidates for PEC reactions. The results of the characterization of the PEC properties of the core-shell ZnO@ZnS NWs in a Na_2SO_4 aqueous solution are shown in figure 4(a). Once again, for these measurements of the evolution of photocurrent density with the thickness of ZnS shell, the exact same NW array was measured before the ZnS growth and after each successive set of SILAR cycles. Remarkably, while the ZnS growth did not noticeably modify the NWs' UV-vis absorption spectra or PL emission, the ZnS shells presence clearly promoted the collected photocurrent. The increase of the PEC photocurrent reached up to a factor 2.5 for the thickest shell tested here (26 nm). In particular, ZnS shells promoted photocurrent at lower voltages than bare ZnO:Cl. Meanwhile, the effective photoconversion efficiency of ZnO:Cl NWs with a ZnO shell of 26 nm is then calculated to be 0.22%, which is higher than the values for bare ZnO:Cl NWs. We believe this enhancement of the PEC properties to be related with the extension of the depletion layer region with the ZnS shell growth. The highly doped ZnO:Cl NWs are able to screen the charge accumulated at the surface by means of thin depletion layers. Therefore, surface depletion regions extend just a few nanometers from the surface. On the other hand, the depletion layer expands over the whole intrinsic ZnS shell in ZnO:Cl@ZnS core-shell NWs (figure 4b). Thus, the region within the core-shell NWs with a built in electric field able to split the photogenerated electron-hole pairs significantly increases with the presence of the ZnS shell. This increase of the volume

of materials with a built in electric field promotes the separation of photogenerated charge carriers, as represented in the cartoon of figure 4b. Thus, higher PEC currents are obtained in the presence of the ZnS shell. An alternative explanation for such a PEC increase is the enhancement of the absorption of photons with energy below the ZnO and ZnS band gap by a electron transition from the ZnS valence band to the ZnO conduction band. However, this mechanism must have a very small influence as no signal of such low probability transition was obtained from the UV-vis and PL characterization of the materials.

While no cathodic photocurrent was obtained with the bare ZnO:Cl NWs in a Na₂SO₄ electrolyte, a small photocurrent was also measured at cathodic scan in ZnO:Cl@ZnS core-shell heterostructures. Furthermore, it is worth to remark that the cathodic current density gradually increased with the thickness of the ZnS shell (figure 4a). Such photocurrent may be originated in a reversed shell depletion region where the built-in electric field drives photogenerated holes towards the ZnO:Cl core and photogenerated electrons towards the electrolyte solution (Figure 4b). The efficiency of this process is low, most probably due to the low hole mean free path inside the highly n-doped ZnO:Cl core.

A critical parameter to develop PEC cells is the electrode stability. Electrolytes play a crucial role in the degradation of the electrodes. The amperometric I-t curves collected at a constant potential and UV light illumination showed that the photocurrent generated by the ZnO:Cl@ZnS NWs in the presence of Na₂SO₄ decreased around a 10 % before stabilizing (Figure 5a). To determine any possible degradation of the layer, XPS measurements before and after 5000 s illumination were carried out. In figures 5c and 5d, the XPS spectra on the Cl and O regions are plotted. No appreciable change was detected. To further discard a major influence of a potential ZnS deterioration in the

ZnO:Cl@ZnS photocurrent enhancement, the photocurrent generated using a 0.5 M Na₂S aqueous solution as electrolyte was also measured (figure 5e). In this case, because of the low standard potential of S²⁻/S_n²⁻ (+ 0.77 V), S²⁻ plays an electron donor role and undergoes successive oxidation to form polysulfides S_n²⁻.^{29,30} Therefore, in the presence of S²⁻ as sacrificial reagent for photocatalytic hydrogen generation, the measured photocurrent densities were much higher and *V*_{oc} shifted to lower voltages. Nevertheless, still a large enhancement of the photocurrent was also obtained with the ZnS shell. During long time illumination, the photocurrent values remained almost constant (figure 5b). These results further confirm the actual charge carrier transfer enhancement accomplished with the presence of the ZnS layer.

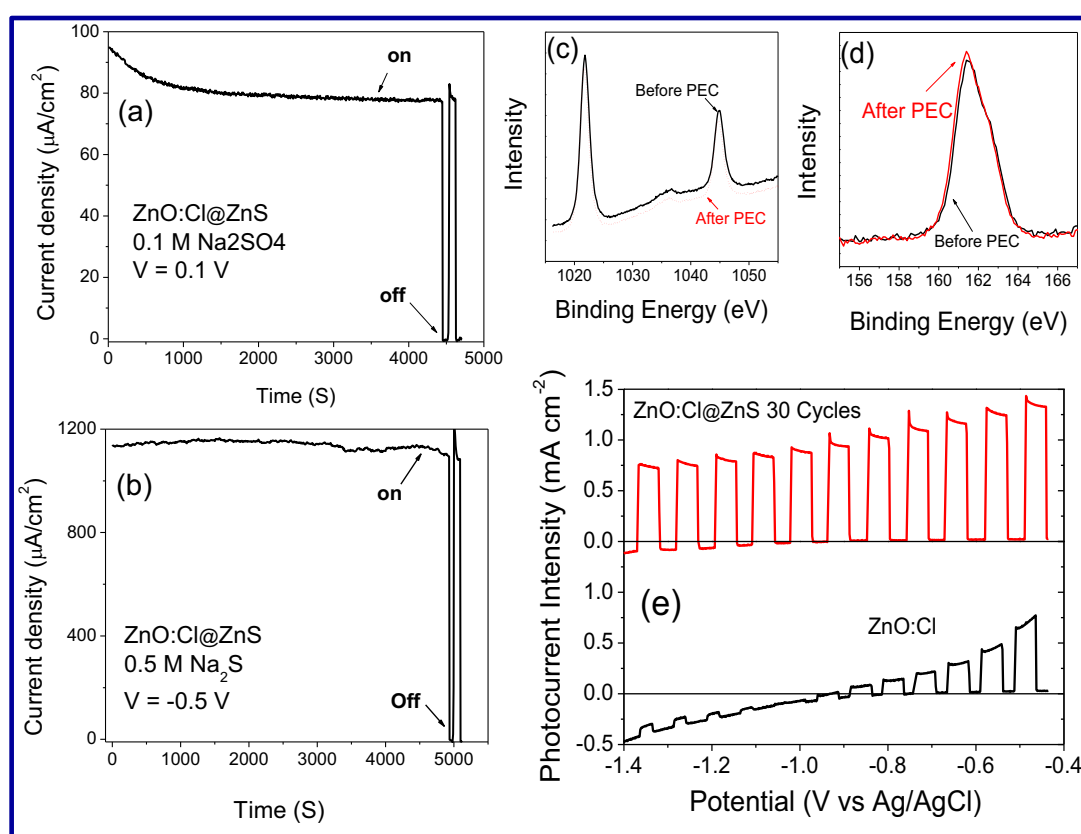


Figure 5. Degradation and stability test for ZnO:Cl@ZnS core-shell NWs under UV illumination (100 mW/cm²) (a) in 0.1 M Na₂SO₄ aqueous solution at 0.1 V vs. Ag/AgCl and (b) in 0.5 M Na₂S aqueous solution at -0.5 V vs. Ag/AgCl. (c) Zinc region and (d) sulfur region of the XPS spectra of ZnO:Cl@ZnS NWs before and after photoelectrochemical measurement. (e)

Photocurrent density vs. applied potential (V vs. Ag/AgCl) response to on/off cycles of ZnO:Cl@ZnS core-shell NWs measured under chopped UV illumination (100 mW/cm^2) in $0.5 \text{ M Na}_2\text{S}$ aqueous solution. Shell thickness was set to 8 nm for these analyses.

Finally, figure 6 shows the PEC current obtained from an array of ZnO:Cl NWs, the same array after growing a 100 cycle shell and again the same ZnO:Cl@ZnS array after annealing at $450 \text{ }^\circ\text{C}$ for 1 h in Ar atmosphere. The annealing of the NWs significantly promoted PEC currents. Such enhancement must be associated to the improved crystallinity of the ZnO:Cl core, the ZnS shell and their interface, which reduced the density of trapping states and increased charge carrier mobilities, thus increasing charge carrier transport and collection efficiencies.

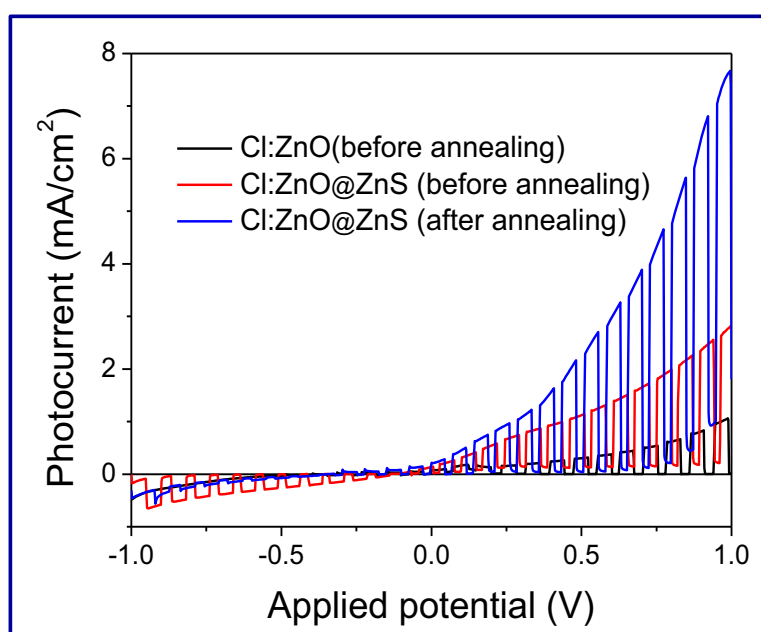


Figure 6. Photocurrent density vs. applied potential (V vs. Ag/AgCl) for ZnO:Cl NWs (before annealing) and ZnO:Cl@ZnS core-shell NWs (before and after annealing), measured under chopped UV illumination (100 mW/cm^2) in $0.1 \text{ M Na}_2\text{SO}_4$ aqueous solution.

5.5 Conclusions

Arrays of vertically obtained ZnO:Cl@ZnS NWs prepared by a facile route were used to probe the enhancement of the photoelectrochemical properties obtained with the ZnS shell. While the ZnS shell growth did not significantly modify the absorption or the PL spectra of ZnO:Cl NWs, a clear promotion of the photocurrent was obtained. This photocurrent enhancement was associated with an increase of the surface depletion layer. The presence of the ZnS shell expands the region where a build in electric field is able to separate the photogenerated charge carriers and drive them towards the core ZnO:Cl material (electrons) and towards the NW/electrolyte interface (holes) where the photooxidation of water takes place.

5.6 References

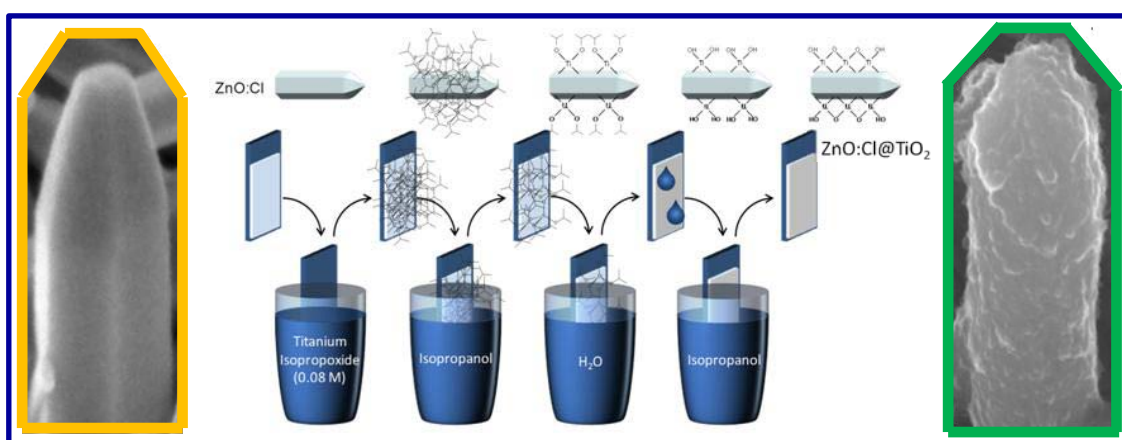
1. Özgür, Ü.; Alivov, Ya. I.; Liu, C.; Teke, A.; Reshchikov, M. A.; Doğan, S.; Avrutin, V.; Cho, S.-J.; Morkoç, H. *J. Appl. Phys.* **2005**, *98*, 041301.
2. Fang, X.S.; Bando, Y.S.; Gautam, U. K.; Zhai, T. Y.; Zeng, H. B.; Xu, X. J.; Liao, M. Y.; Golberg, D. *Crit. Rev. Solid State* **2009**, *34*, 190–223.
3. Kind, H.; Yan, H. Q.; Messer, B.; Law, M.; Yang, P. D. *Adv. Mater.* **2002**, *14*, 158–160.
4. Fang, X. S.; Bando, Y.; Liao, M. Y.; Gautam, U. K.; Zhi, C.Y.; Dierre, B.; Liu, B. D.; Zhai, T. Y.; Sekiguchi, T.; Koide, Y.; Golberg, D. *Adv. Mater.* **2009**, *21*, 2034–2039.
5. Fang, X. S.; Bando, Y.; Gautam, U. K.; Zhai, T. Y.; Gradecak, S.; Golberg, D. *J. Mater. Chem.* **2009**, *19*, 5683–5689.
6. Lu, M. Y.; Song, J. H.; Lu, M. -P.; Lee, C.-Y.; Chen, L.-J.; Wang, Z. L. *ACS nano* **2009**, *3*, 357–362.
7. Lahiri, J.; Batzill, M. *J. Phys. Chem. C* **2008**, *112*, 4304–4307.
8. Bera, A.; Basak, D. *ACS Appl. Mater. Inter.* **2010**, *2*, 408–412.
9. Yan, J.; Fang, X.; Zhang, L.; Bando, Y.; Gautam, U. K.; Dierre, B.; Sekiguchi T.; Goldberg, D. *Nano Lett.* **2008**, *8*, 2794–2799.

10. Shuai, X. M.; Shen, W. Z. *J. Phys. Chem. C* **2011**, *115*, 6415-6422.
11. Yu, X.-L.; Song, J.-G.; Fu, Y.-S.; Xie, Y.; Song, X.; Sun J.; Du, X.-W. *J. Phys. Chem. C* **2010**, *114*, 2380-2384.
12. Nakada, T.; Mizutani, M.; Hagiwara, Y.; Kunioka, A. *Sol. Energ. Mat. Sol. C* **2001**, *67*, 255-260.
13. Nakada, T.; Hongo, M.; Hayashi, E. *Thin solid Films* **2003**, *431-432*, 242-248.
14. Schrier, J.; Demchenko, D. O.; Wang, L. -W. *Nano Lett.* **2007**, *7*, 2377-2382.
15. Wang, K.; Chen, J. J.; Zeng, Z. M.; Tarr, J.; Zhou, W. L.; Zhang, Y.; Yan, Y. F.; Jiang, C. S.; Pern, J.; Mascarenhas, A. *Appl. Phys. Lett.* **2010**, *96*, 123105.
16. Wang, Z.; Liu, X.; Gong, J.; Huang, H.; Gu, S.; Yang, S. *Cryst. Growth Des.* **2008**, *8*, 3911-3913.
17. Chung, J. Y.; Myoung, J. Y.; Oh, J. S.; Lim, S. W. *J. Phys. Chem. C* **2010**, *114*, 21360-21365.
18. Fan, J. D.; Shavel, A.; Zamani, R.; Fábrega, C.; Rousset, J.; Haller, S.; Güell, F.; Carrete, A.; Andreu, T.; Arbiol, J.; Morante, J. R.; Cabot, A. *Acta Mater.* **2011**, *59*, 6790-6800.
19. Liao, H. -C.; Kuo, P. -C.; Lin, C. -C.; Chen, S. -Y. *J. Vac. Sci. Technol. B* **2006**, *24*, 2198-2201.
20. Lahiri, J.; Batzill, M. *J. Phys. Chem. C* **2008**, *112*, 4304-4307.
21. Schrier, J.; Demchenko, D. O.; Wang, L. -W.; Alivisatos, A. P. *Nano Lett.* **2007**, *7*, 2377-2382.
22. Li, J. H.; Zhao, D. X.; Meng, X. Q.; Zhang, Z. Z.; Zhang, J. Y.; Shen, D. Z.; Lu, Y. M.; Fan, X. W. *J. Phys. Chem. B* **2006**, *110*, 14685-14687.
23. Panda, S. K.; Dev, A.; Chaudhuri, S. *J. Phys. Chem. C* **2007**, *111*, 5039-5043.
24. Liu, Z. Q.; Lu, X. H.; Xie, S. L.; Zhang, J. H.; Liu, Z. L.; Tong, Y. X. *J. Electrochem.Soc.* **2011**, *158*, 84-87.
25. Ye, C.; Fang, X.; Li G.; Zhang, L. *Appl. Phys. Lett.* **2004**, *85*, 3035-3037.
26. Hu, J.; Bando, Y.; Zhan, J.; Golberg, D. *Adv. Funct. Mater.* **2005**, *15*, 757-762.
27. Gong, J.; Yang, S.; Duan, J.; Zhang, R.; Du, Y. *Chem. Comm.* **2005**, *3*, 351-353.
28. Yin, L.-W.; Bando, Y.; Zhan, J. -H.; Li, M. -S.; Golberg, D. *Adv. Mater.* **2005**, *17*, 1972-1977.
29. Bouroushian, M.; Scholz, F. *Electrochemistry of Metal Chalcogenides*. Springer **2010**, Berlin.
30. Nozik, Y.; Memming, R. *J. Phys. Chem.* **1996**, *100*, 13061-13078.

Chapter 6

Solution-Growth and Optoelectronic Performance of ZnO:Cl@TiO₂ and ZnO:Cl@Zn_xTiO_y@TiO₂ Core-Shell Nanowires with Tunable Shell Thickness

Thickness



6.1 Abstract

Arrays of vertically-aligned ZnO:Cl@TiO₂ and ZnO:Cl@Zn_xTiO_y@TiO₂ core-shell NWs were prepared by means of the combination of two solution-growth processes. First, single-crystal ZnO NWs with controlled n-type doping were grown on conducting substrates by a low-cost, high-yield and seed-free electrochemical route. These nanowires were covered by a titanium oxide shell of tunable thickness mediating successive adsorption-hydrolysis-condensation steps. Using this atomic-layer growth procedure, titania shells with controlled thickness and the anatase TiO₂ phase were obtained after sintering at 450 °C. Higher sintering temperatures resulted in the formation of ZnO:Cl@Zn_xTiO_y@TiO₂ core-shell NWs by the interdiffusion of Zn and

Ti ions at the ZnO-TiO₂ interface. The performance of ZnO:Cl@TiO₂ and ZnO:Cl@Zn_xTiO_y@TiO₂ core-shell NWs towards PEC water splitting was investigated as a function of the titania shell thickness. Furthermore the performance of such core-shell NWs as photoelectrodes in DSCs was also characterized. The TiO₂ presence at the ZnO:Cl surface promoted a two fold increase on the produced photocurrent densities, probing their potential for PEC and optoelectronic applications. EIS was used to corroborate the lower resistance for charge transfer between the NWs and the electrolyte in the presence of the TiO₂ shell.

6.2 Introduction

NWs find multiple applications in the fields of optoelectronics and photoelectrocatalysis. The NW geometry habitates the combined optimization of both, charge carrier injection/separation and charge transport. On the other hand, the NW composition needs to satisfy the strong demands on the materials qualities usually required, especially in terms of surface chemistry and electrical conductivities. In this scenario, core-shell nanostructures allow the synergic combination of two different materials to take full advantage of the NW geometry.

A particularly interesting example is the use of ZnO@TiO₂ core-shell NWs in photovoltaic or photoelectrocatalytic applications. ZnO and TiO₂ are both important technological material with a broad range of applications which take advantage of their abundance, stability, biocompatibility and a unique combination of chemical and physical properties. Both oxide semiconductors have similar wide band gaps (3.2-3.4 eV) and band edge energies. In particular, ZnO large exciton binding energy (60 meV) makes it an excellent candidate for particular optoelectronic applications, such as light-emitting diodes,¹ laser diodes² and solar cells.³ ZnO exhibits higher electron mobility

and longer lifetime of carrier than TiO_2 .⁴⁻⁶ At the same time, ZnO NWs can be grown over a large variety of substrates with controlled doping by multiple techniques. These include vapor-phase transport,⁷ pulsed laser deposition,⁸ chemical vapor deposition⁹ and more interestingly, owing to their simplicity, low-cost and high area potential, chemical bath deposition^{10,11} and electrochemical deposition.¹²⁻¹⁴ On the other hand, ZnO surfaces contain multiple charge trapping states, are less chemically stable than that of TiO_2 and may not present suitable interfaces with dyes, electrolytes and organic polymers for charge separation.^{4,15-17} Thus, the combination of a ZnO core with controlled electrical conductivity and a TiO_2 shell with optimized surface chemistry can potentially result in superior photoelectrodes for high efficiency DSCs and photoelectrocatalysis. This synergic effect has been already demonstrated in ZnO-based DSCs using TiO_2 shells prepared by chemical vapor deposition,^{18,19} atomic layer deposition^{15,17,20,21} and sputtering.^{5,22,23} While these techniques allow a large degree of control over the shell thickness, they are neither particularly low-cost nor versatile for the production of large area devices, because of the high energies and controlled atmospheres required and their associated low growth rates and material yields. Recently, alternative solution-processing methods for the production of ZnO@ TiO_2 NWs were demonstrated.²⁴⁻²⁷ However, a precise control of the shell thickness is still lacking in these procedures. At the same time, the production of such core shell NWs with a controlled core electrical conductivity is mandatory to optimize their performance. This implies the extrinsic doping of the core ZnO NWs. In a previous study, we detailed the successful introduction of chlorine ions within the ZnO NW structure, significantly increasing in this way their electrical conductivity.¹³

In the present work, a room-temperature liquid-phase layer deposition procedure²⁴⁻²⁸ is used to grow TiO_2 shells with tunable thickness on ZnO:Cl NWs having controlled

doping concentrations. The presented growth method allows the production ZnO:Cl@TiO₂ core-shell NWs at room temperature and ambient conditions and the formation of ZnO:Cl@Zn_xTiO_y@TiO₂ NWs after sintering at temperatures above 500 °C. The improved performance of ZnO:Cl@TiO₂ core-shell nanostructures towards photoelectrochemical water splitting and in DSCs is experimentally demonstrated here. Furthermore, EIS measurements are used to discuss the performance enhancement in the presence of the TiO₂ shell.

6.3 Experimental details

6.3.1 ZnO NWs growth

Arrays of vertically aligned and single crystal ZnO:Cl NWs were electrochemically grown in an aqueous solution inside a three-electrode cell.¹³ The growth solution was prepared by incorporating 10 mL of 0.1 M aqueous solution (MilliQ+, 18.2 MΩ·cm) of zinc nitrate (Zn(NO₃)₂·4H₂O) and 10 mL of 0.1 M aqueous solution of methenamine (C₆H₁₂N₄) in 80 mL of deionized water and quickly heating up the solution to 90 °C on a hot plate. A platinum wire immersed in the solution was used as a counter electrode. An Ag/AgCl electrode in saturated KCl (3 M) was used as the reference electrode. A negative DC potential in the range between -0.4 and -1.4 V relative to the reference electrode was applied to a soda lime glass coated with FTO, which were used as substrates. After a 1 hour growth time, the samples were immediately rinsed with deionized water. Chlorine ions were introduced in a controlled way by replacing between 0.5 and 10 ml of deionized water with 1 M aqueous solution of ammonium chloride (NH₄Cl). The NWs thickness, length, doping concentration and tip morphology could be controlled by adjusting the growth potential and the concentration of the

growth solution.¹³ Moreover, ZnO:Cl NWs could be grown in a large variety of conducting substrates, from glass covered with a transparent conducting oxide to metal foils.

6.3.2 TiO₂ shell growth

Electrodeposited ZnO:Cl NWs grown on ITO-covered glass substrates were used to obtain ZnO:Cl@TiO₂ core-shell NWs. TiO₂ shells with controlled thickness were grown by multiple successive adsorption-activation-decomposition steps as schematized in figure 1. In a first step, titanium isopropoxide [Ti(OC₃H₇)₄] was adsorbed on the ZnO:Cl surface by immersing the NW array on an anhydrous isopropanol solution of titanium isopropoxide (0.08 M) for 30 s. In the second successive step, excess titanium isopropoxide was removed by immersing the layer in anhydrous isopropanol. In a third step, titanium isopropoxide was hydrolyzed by introducing the NW array in water.³³ In one last step excess of water was removed with anhydrous isopropanol. This 4-step cycle was repeated up to 100 times. The final samples were dried by means of a N₂ flow and annealed at 450 °C for 30 minutes to improve crystallinity.

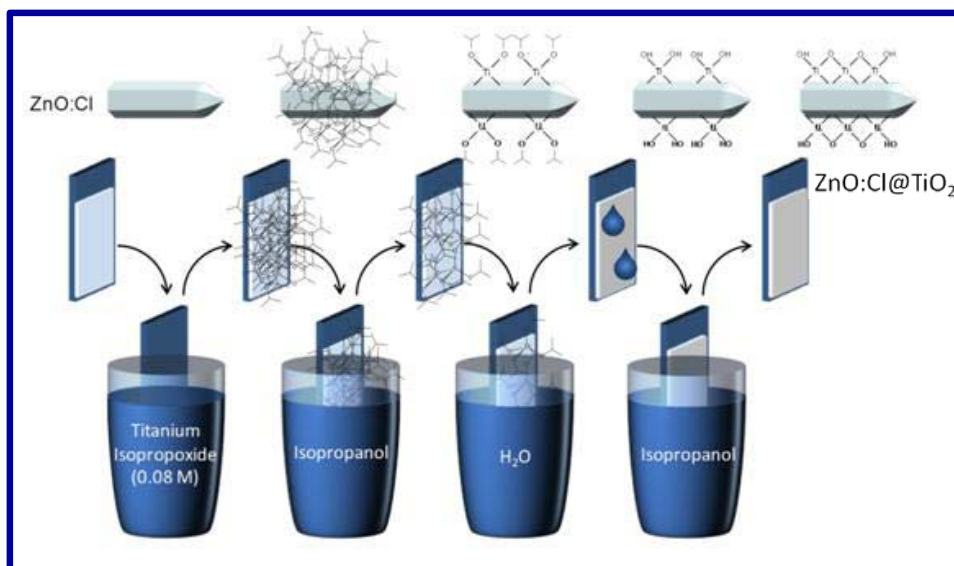


Figure 1. Scheme of the successive coating and reaction steps used to produce ZnO:Cl@TiO₂ core-shell NWs with controlled thickness. The process involves the adsorption of titanium isopropoxide molecules at the ZnO:Cl surface, its hydrogenation and its posterior polymerization to TiO₂.

6.3.3 Materials characterization

XRD was used to characterize the crystallographic phase the materials produced. For XRD characterization, a Bruker D8 Advance diffractometer with Cu K α_1 radiation ($\lambda = 1.5406 \text{ \AA}$) was used. Field emission SEM was used to characterize the morphology of the obtained materials and measure the NWs density, length and width distributions. Both cross-sectional and top-down views were obtained using a FEI Nova Nanosem 230. The detailed morphology of the ZnO:Cl@TiO₂ core-shell NWs were further confirmed by TEM using a Jeol J2100 microscope. The crystallographic structure of the NWs was further characterized with atomic resolution by means of high-resolution TEM in a Jeol 2010F field emission gun microscope with a 0.19 nm point to point resolution.

6.3.4 Photoelectrochemical characterization

PEC properties of core-shell NW arrays were examined using a three-electrode potentiostat system with an Ag/AgCl electrode in saturated KCl (3 M) as the reference electrode and a Pt wire as counter electrode. 0.1 M Na₂SO₄ aqueous solutions were used as electrolytes to study the PEC properties of ZnO/TiO₂ core-shell photo-electrodes. The photocurrent and voltage of the cell were measured for a specific area (1 cm²) of the obtained core/shell NW arrays working electrode under UV illumination (HgXe lamp with 365 nm filter) and under simulated solar irradiation (ABET Technology Xe lamp 150 W with AM.0 and AM1.5 solar filters).

6.3.5 DSCs fabrication and characterization

For the fabrication of DSCs, the ZnO:Cl and ZnO:Cl@TiO₂ NW-based photoanodes (0.05 cm²) were immersed into an ethanol solution (0.5 mM) of N719 (Solaronix SA) at room temperature. To maximize dye adsorption, the NWs were soaked for 48 h in the dye solution. A Pt-coated counter electrode was prepared by drop casting a 5 mM H₂PtCl₆ ethanol solution onto an FTO-coated glass, followed by sintering at 450 °C in air for 30 min. A 25 μm thick hot-melt film (Solaronix) was sandwiched between the ZnO:Cl or ZnO:Cl@TiO₂ NW-based photoanodes and the Pt counter electrode. The iodide-based low viscosity electrolyte with 50 mM of tri-iodide in acetonitrile (Iodolyte AN-50, Solaronix) was injected into the space between the cell's anode and cathode to complete the device. Current–voltage (I–V) characteristics of the solar cells were measured with a Keithley 2420 source meter under AM1.5G simulated solar irradiation (100 mW/cm²) supplied by a Sun 3000 solar simulator (ABET Technology).

6.3.6 Electrochemical impedance spectroscopy

EIS measurements were carried out on ZnO:Cl and ZnO:Cl@TiO₂ NWs both in dark and under AM 1.5 simulated solar radiation at different applied potentials (0 V, 0.2 V, 0.4 V, 0.6 V and 0.8 V vs Ag/AgCl). For these measurements, an electrochemical system (PARSTAT 2273) and a typical three-electrode set-up with an Ag/AgCl electrode in saturated KCl (3 M) as the reference electrode, a Pt wire as counter electrode and 0.1 M Na₂SO₄ aqueous solutions as electrolytes were employed. The frequency range tested was 0.1 Hz –1 MHz and the amplitude of the alternating signal was 1 mV.

6.4 Results and Discussion

Vertically aligned and single-crystal ZnO:Cl NWs were electrochemically grown in FTO-coated soda lime glass. A controlled concentration of chlorine ions was introduced by dissolving the required amount of ammonium chloride inside the electrodeposition solution. Thus controlling the amount of chlorine, the ZnO:Cl charge carrier concentration could be adjusted in the range from 10¹⁷ to 10²⁰ cm⁻³. In the present study, the Cl concentration was adjusted to produce ZnO:Cl NWs with an electrical conductivity of approximately 4 S·cm⁻¹ and a carrier concentrations in the order of 7 x 10¹⁸ cm⁻³, as previously characterized.¹³ Figure 2a shows a representative SEM micrograph of the ZnO:Cl NWs grown in a 0.05 M aqueous solution of ammonium chloride. ZnO:Cl NWs were 2.5 μm long and had an average thickness of 320 nm. This ZnO:Cl NWs were afterwards coated with a TiO₂ layer of tunable thickness mediating successive adsorption-hydrolysis-condensation steps. Figure 2b displays a representative SEM image of the ZnO:Cl@TiO₂ core-shell NWs obtained using 30 deposition cycles and annealed at 450 °C for 30 min. While the growth of the titanium

oxide layer was highly homogeneous at the macroscopic scale, core-shell NWs showed noticeable surface roughness (Figures 2c and 2d). The nanoscale thickness inhomogeneities of the grown titania shells were associated to the multiplicity of titania nucleation centres at the ZnO surface and the lattice mismatch between ZnO and TiO₂ phases, which prevents epitaxial growth. From the measurement of the average NW thickness variation between the ZnO:Cl and the ZnO:Cl@TiO₂ core-shell NWs, the growth rate was estimated to be 0.75 nm per cycle. The composition of the obtained core-shell NWs was further confirmed by EDX analysis (figure 2f). From this analysis, no impurity was detected at significantly high concentration. Figure 2g and 2h show a HRTEM micrograph of the polycrystalline TiO₂ shell and its corresponding fast Fourier transformed image. The two rings observed from the power spectrum analysis were associated to the (103) and (113) plane families of anatase, with 0.243 and 0.204 nm distances, respectively. These analyses evidenced that the TiO₂ shell had an anatase structure with tetragonal symmetry in I4₁/amd space group. This conclusion is further supported by the XRD patterns obtained from the characterization of the ZnO:Cl@TiO₂ core-shell NWs sintered at 450 °C (Figure 3a).

An extensive bibliography exists on the formation of titanium oxide from titanium (IV) alkoxide precursors.³⁴⁻⁵⁰ The process involves the hydrolyzation of the titanium alkoxide and the subsequent polymerization to form an inorganic network. It is generally accepted that the exact complex scheme of formation of Ti-O-Ti chains is strongly dependent on the relative water concentration.⁵¹ In the same way, the composition of the hydrous oxide network obtained and the size of the final particles or crystallographic domains obtained also depend on the growth conditions. In the particular case reported here, the high relative water concentration during the hydrolysis

step may favor oxolation over alcoxolation and thus the formation of Ti-O-Ti chains from the hydroxide species through water elimination.^{52,53}

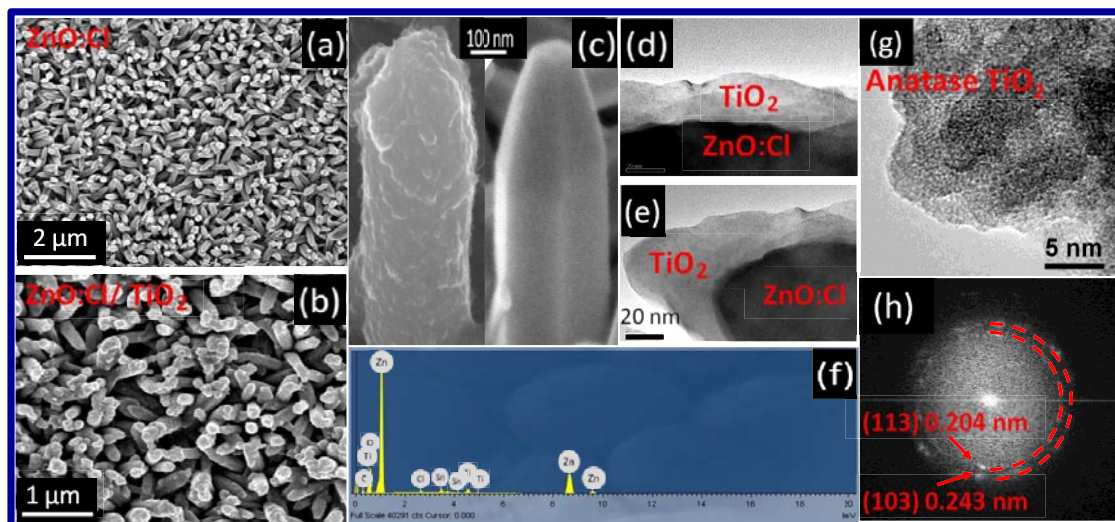


Figure 2. (a) Top-down view of bare ZnO:Cl NWs; (b) Top-down view of ZnO:Cl@TiO₂ core-shell NWs grown for 30 cycles; (c) SEM images of single ZnO:Cl (left) and ZnO:Cl@TiO₂ (right) NWs; (d) (e) TEM images of a single ZnO:Cl@TiO₂ NW; (f) EDX spectrum of ZnO:Cl@TiO₂ core-shell NWs; (g) HRTEM micrograph of anatase TiO₂ shell; (h) Fast Fourier transformed image of the anatase TiO₂ shell.

Figure 3a shows the XRD patterns of the core-shell NWs obtained after 100 cycles and sintered at 450 °C, 600 °C and 700 °C. As detailed above, in the experimental conditions here detailed, by means of successive layer deposition-hydrolysis-drying steps and after a thermal treatment at 450 °C in an air atmosphere, the resultant titania shell displayed the anatase TiO₂ phase. It is well known that anatase TiO₂ transforms to rutile above ~550 °C.⁵⁴ However, in the present study, no rutile TiO₂ was obtained even after annealing the ZnO:Cl@TiO₂ NWs at 700°C. Instead, the hexagonal ZnTiO₃ phase was obtained along the interface between the wurtzite ZnO core and thick anatase TiO₂ shells at 600 °C and above. The thermal annealing of the NWs at 700 °C clearly promoted the crystallinity of both the anatase TiO₂ and ZnTiO₃ phases as observed from

the XRD patterns (Figure 3a). The ZnTiO_3 interface layer resulted from the solid state reaction between the interdiffusing ZnO core and the TiO_2 shell.^{55,56} This is the same mechanism previously reported for the formation of spinel oxides such as ZnFe_2O_4 , ZnAl_2O_4 or Zn_2TiO_4 from solid state reactions at the core-shell interface of NWs.⁵⁷

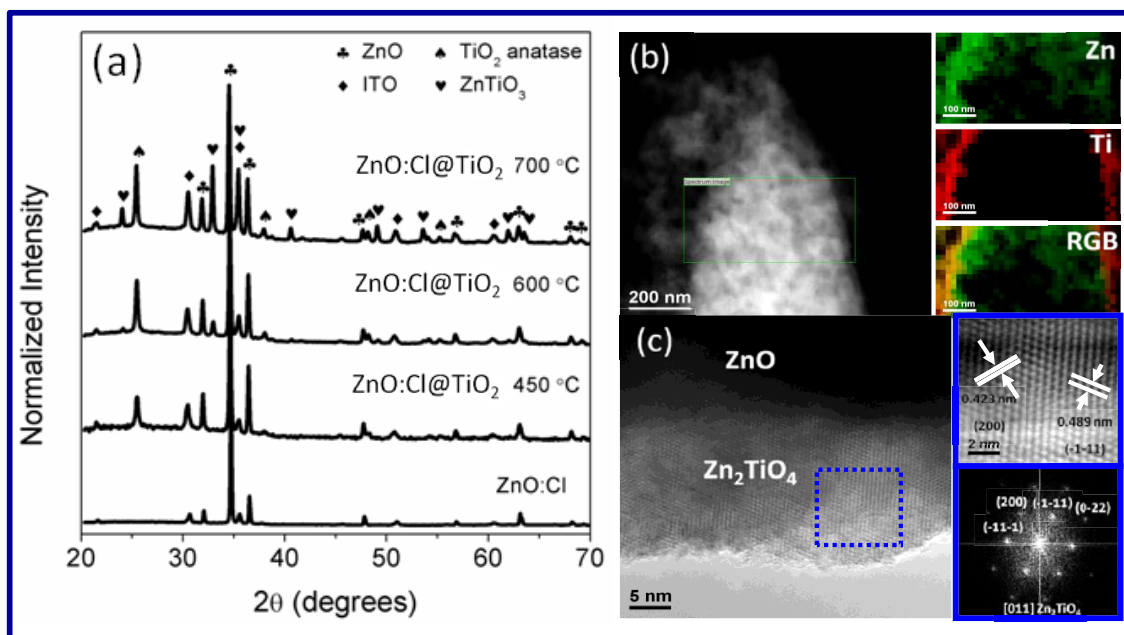


Figure 3. (a) XRD patterns of the bare ZnO:Cl NW arrays and of the ZnO:Cl@ TiO_2 core-shell NWs grown for 100 cycles after annealing at 450 °C, 600 °C and 700 °C in an air atmosphere. As a reference, the peak positions of ITO (♦, JCPDS 01-089-4598), ZnO (♣, JCPDS 01-075-0576) anatase TiO_2 (♠, JCPDS 03-065-5741) and ZnTiO_3 (♥, JCPDS 01-085-0547) are marked; (b) Z-contrast scanning TEM images and Zn and Ti elemental mappings obtained from electron energy loss spectroscopy of ZnO:Cl/ Zn_2TiO_4 NWs grown for 20 cycles and annealed at 700 °C; (c) HRTEM micrograph and fast Fourier transformed image of the same ZnO:Cl@ Zn_2TiO_4 NWs grown for 20 cycles and annealed at 700 °C.

In order to further investigate the crystal structure at the interface between the ZnO:Cl core and the TiO_2 shell, the core-shell NWs were characterized by means of EELS and HRTEM. Due to the thickness limitations of the TEM characterization technique, NWs with thinner shells, obtained after just 20 TiO_2 growth cycles were used for this investigation. Figure 3b shows the Zn and Ti elemental maps and the HRTEM

micrograph of ZnO:Cl@TiO₂ NWs with approximately 15 nm shells and sintered at 700 °C. EELS analysis clearly demonstrate the presence of both Ti and Zn ions in the shell. Meanwhile, HRTEM analysis evidenced that the shell crystallographic structure is that of cubic Zn₂TiO₄. The different crystallographic structures obtained at the ZnO-TiO₂ interface in core-shell NWs with different shell thicknesses can be explained by the variety of phases in the Zn-Ti-O system. The hexagonal ZnTiO₃, the cubic Zn₂TiO₄ or a coexistence of both phases are commonly found in the ternary Zn-Ti-O system depending on the stoichiometric ratios of the precursor materials and the annealing temperature.⁵⁷⁻⁶⁰ In the present study, the ZnTiO₃ phase was found at the ZnO-TiO₂ interface of NWs having shells with thicknesses above 20 nm, while the Zn₂TiO₄ phase was observed all across the shell in NWs initially coated with thinner TiO₂ shells. Differences may be due to variations in the ratio of interdiffused Zn and Ti ions at the ZnO-TiO₂ interface. Within thin shells, the relative high mobility of Zn allows an excess of this element all across the shell and the formation of the Zn₂TiO₄ phase. On the other hand, in thicker shells equivalent ratios of Zn and Ti ions result in the formation of ZnTiO₃ just at the interface of the wurtzite ZnO and anatase TiO₂.

The photocatalytic hydrogen generation has the attractive advantages of being a clean process of conversion of solar energy into storable chemical energy.⁶¹ Efficient photoanodes require very large electrode/electrolyte interfaces, excellent chemical stability and very high electrical conductivities to facilitate charge carrier transport between oxidation and reduction sites. In this scenario, arrays of titania NWs are very attractive candidates for PEC reactions. Figure 4 displays the results of the characterization of the PEC properties of ZnO:Cl and ZnO:Cl@TiO₂ NWs with different shell thicknesses. For these measurements of the evolution of photocurrent density with the TiO₂ shell thickness, large arrays of ZnO:Cl NWs were

electrodeposited on ITO-covered glass substrates. Each array was divided into four pieces, which were individually analyzed. Afterwards, in each of the arrays a different TiO₂ shell thickness was deposited, from 10 nm to 45 nm. The presence of the TiO₂ shell clearly promoted the photocatalytic activity both under UV and under AM1.5 simulated solar irradiation. Upon UV illumination, the increase of the photocurrent densities measured reached up to a 2-fold increase for the ZnO:Cl@TiO₂ NWs with a 23 nm TiO₂ shell (Figure 4a). Meanwhile, the photoconversion efficiency in this case has increased up to a value of 0.53% at +0.4V. However, while a progressive increase of the photocurrent density with the shell thickness was obtained for the thinnest shells, the thickest shell tested here (~45 nm) resulted in lower photocurrents. This decrease of the collected photocurrent was associated to a decrease of the electrode surface area available for electrode/electrolyte interaction. This surface area decrease is associated with the partial coalescence of the NWs obtained for too thick TiO₂ shells (Figure 4b).

The photocurrent density generated from solution-grown ZnO-based photoelectrodes strongly increased with the annealing treatment.¹⁴ However, the photocurrent enhancement obtained with the TiO₂ shell was lost after thermal treatments at temperatures above 500 °C. In figure 5 the photocurrent density of the ZnO:Cl@Zn_xTiO_y@TiO₂ core-shell NWs with 20 nm shells and obtained after a thermal treatment at 700 °C is compared with the photocurrent density obtained from the same ZnO:Cl NW arrays also annealed at 700 °C. A decrease of the photocurrent density of the core-shell NWs compared with that of ZnO:Cl NWs was consistently obtained when a zinc titanate layer was formed. Therefore, we associated this experimental observation to an increase of the resistance for charge transfer between the electrolyte and the highly conducting ZnO:Cl core in the presence of the zinc titanate dielectric layer between the ZnO:Cl core and the TiO₂ shell.

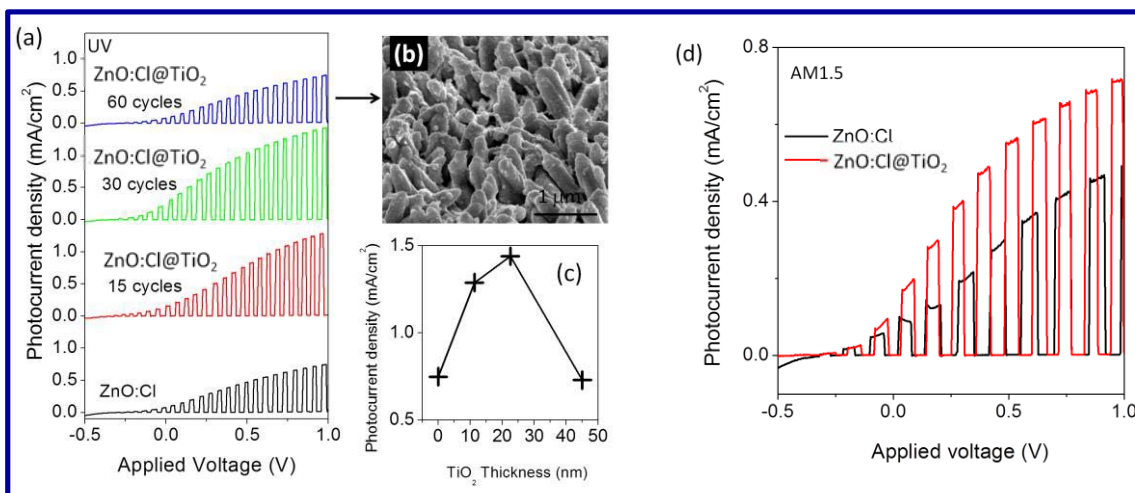


Figure 4. (a) Photocurrent density vs. applied potential (V vs. Ag/AgCl) for ZnO:Cl NWs and ZnO:Cl@TiO₂ core-shell NWs with increasingly thicker shell thicknesses, measured under chopped UV illumination in 0.1 M Na₂SO₄ aqueous solution. (b) SEM image of the ZnO:Cl@TiO₂ NWs with the thickest TiO₂ shell measured. (c) Photocurrent density as a function of the shell thickness. (d) Photocurrent density vs. applied potential (V vs. Ag/AgCl) for ZnO:Cl NWs and ZnO:Cl@TiO₂ core-shell NWs with 23 nm-thicker TiO₂ shell, measured under chopped AM1.5 simulated solar irradiation in 0.1 M Na₂SO₄ aqueous solution.

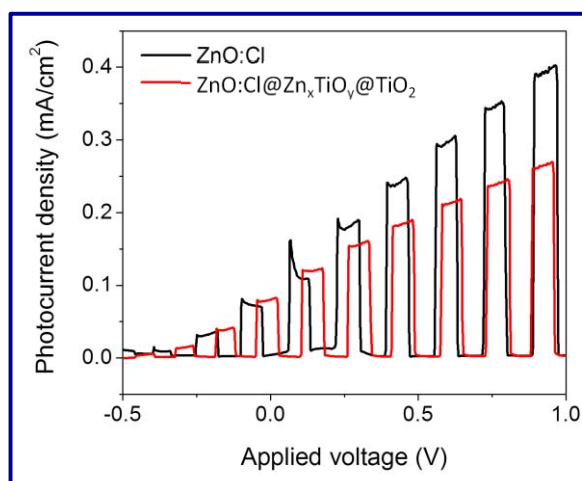


Figure 5. Photocurrent density vs. applied potential (V vs. Ag/AgCl) for ZnO:Cl and ZnO:Cl@Zn_xTiO_y@TiO₂ NWs measured under chopped AM1.5 simulated solar irradiation in 0.1 M Na₂SO₄ aqueous solution.

To further assess the potential of the ZnO:Cl@TiO₂ NW arrays produced here, DSCs were fabricated. For this purpose, a ZnO:Cl NW arrays was divided in two identical pieces. In one of them ~ 20 nm thick TiO₂ shells were grown. Both arrays were thermally annealed at 450 °C under air for 1 h to improve crystallinity. Afterwards, ZnO:Cl and ZnO:Cl@TiO₂ NW-based photoanodes were impregnated at room temperature for 48 h with N719 as the standard dye for DSCs purposes. Pt coated FTO glass was used as a counter electrode and a 50 mM solution of iodide/tri-iodide in acetonitrile as the electrolyte. Figure 6 displays the current–voltage characteristics of the ZnO:Cl and ZnO:Cl@TiO₂ NW-based solar cells measured under 100 mW/cm² of simulated AM1.5G solar irradiation. The relatively low efficiencies obtained were in part associated to the low dye loading due to the reduced surface areas available. An increase of the NW length and the introduction of branches or nanoparticles hierarchically assembled to the NWs will certainly enhance the device efficiency.⁶² Regardless, a two-fold increase of efficiency was consistently obtained with the presence of the TiO₂ shell. The efficiency increase was associated with higher photocurrent densities. This photocurrent enhancement could be in part associated to a slightly higher dye loading at the TiO₂ surface due to the increased roughness. However, we believe the TiO₂ shell to play an important active electronic role by allowing a faster charge carrier transfer between the dye and the conductive ZnO:Cl core and thus reducing the charge carrier recombination.^{4,63}

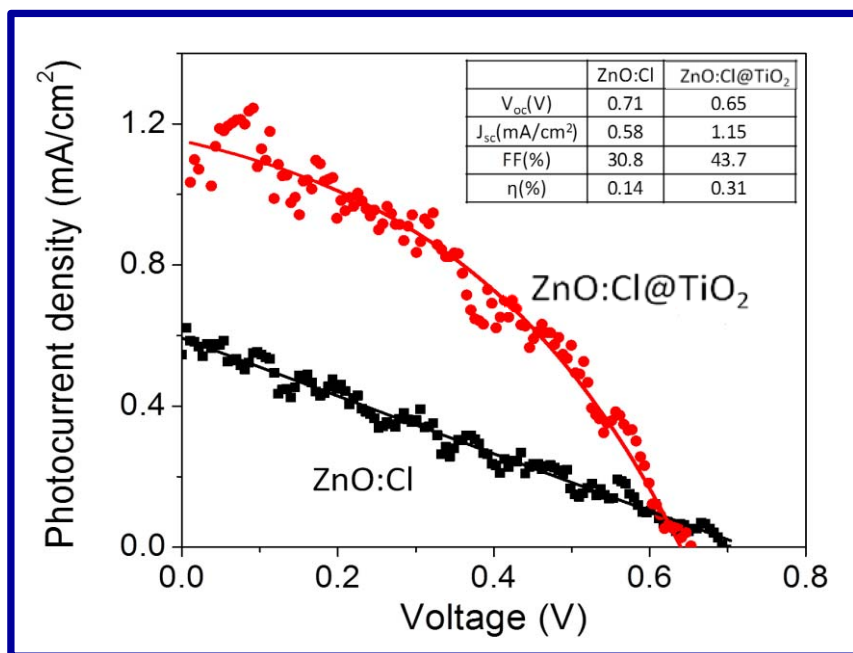


Figure 6. Current-voltage curves for ZnO:Cl and ZnO:Cl@TiO₂ NW-based DSCs measured under simulated AM1.5G illumination of 100 mW/cm².

EIS was used to analyze the resistance for charge carrier transfer between the ZnO:Cl, ZnO:Cl@TiO₂ and ZnO:Cl@Zn_xTiO_y@TiO₂ NWs and the electrolyte.⁶⁴⁻⁶⁷ Figures 7a and 7b shows the Nyquist plots of the impedance data obtained for the ZnO:Cl NWs, ZnO:Cl@TiO₂ NWs and ZnO:Cl@Zn_xTiO_y@TiO₂ NWs in dark and at 1.8 V vs Ag/AgCl. Figures 7c and 7d display the Nyquist plots obtained with the ZnO:Cl and ZnO:Cl@TiO₂ under simulated AM1.5 solar irradiation at voltages in the range from 0 to 0.8 V vs Ag/AgCl. For these measurements, the ZnO:Cl@TiO₂ NWs were obtained by growing the TiO₂ shell over the same ZnO:Cl NWs used as a reference in figure 7a and annealing both arrays at 450 °C in air for 1h. In the same way, the ZnO:Cl@Zn_xTiO_y@TiO₂ NWs were obtained by growing the TiO₂ shell over the same ZnO:Cl NWs used as a reference in figure 7b and thermally annealing both arrays at 700°C in air for 1h. Herein, the impedance spectra were analyzed by Z-view software using the equivalent circuit model shown in the inset of figure 7a.⁶¹⁻⁶⁴

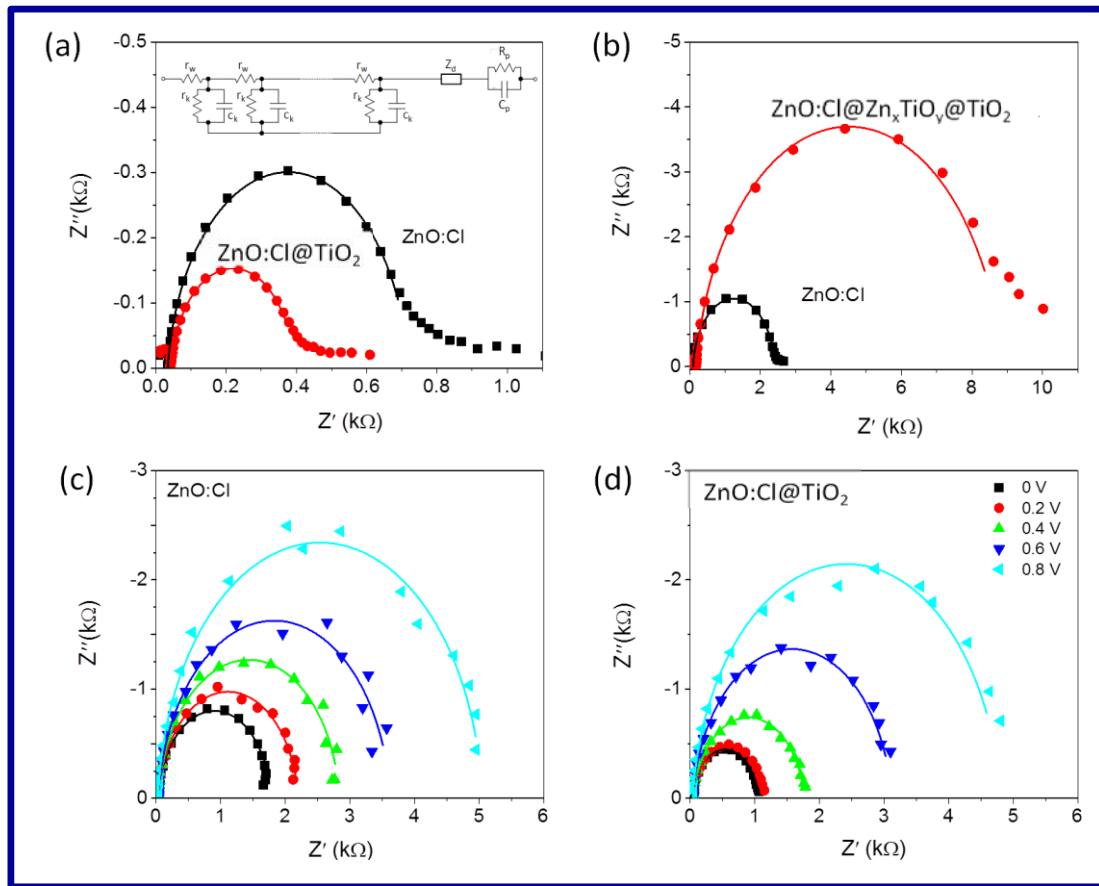


Figure 7. Nyquist plots of the impedance data of (a) ZnO:Cl NWs and ZnO:Cl@TiO₂ NWs in dark at open-circuit voltage of 1.8 V vs Ag/AgCl; (b) ZnO:Cl NWs and ZnO:Cl@Zn_xTiO_y@TiO₂ NWs in dark at open-circuit voltage of 1.8 V vs Ag/AgCl; (c) ZnO:Cl NWs and (d) ZnO:Cl@TiO₂ NWs under AM1.5 simulated solar irradiation at open-circuit voltage in the range of 0-0.8 V vs Ag/AgCl. The solid lines are the fitting results based on the equivalent circuit model shown in the inset.

The high frequency semicircle was ascribed to the charge transfer process at the interfaces between the electrolyte and the platinised counter electrode. The large semicircle at the lower frequency (in the 10–100 Hz range) is related to the transport process of the injected electrons within NWs and the charge transfer process of the injected electrons at the interfaces between NWs and the electrolyte. Following previous works on the determination of parameters of electron transport in DSCs using EIS,⁶¹ the effective recombination rate K_{eff} , the NW-electrolyte charge-transfer resistance R_k , the

electron diffusion coefficient D_{eff} and the resistance associated to the Pt-electrolyte interface R_p were calculated and displayed in table 1. Notice how in dark, the presence of the TiO_2 shell reduced the effective recombination rate and the electrolyte charge-transfer resistance. Under illumination, $ZnO:Cl@TiO_2$ NWs were characterized by a faster charge carrier transfer as denoted by the lower NW-electrolyte charge-transfer resistance and the higher electron diffusion coefficients at each applied potential. The improved fill factors obtained for the $ZnO:Cl@TiO_2$ NW-based DSCs (44 %) as compared with the $ZnO:Cl$ NW-based DSCs (31 %) may be also explained by the decreased rate of electron-hole recombination across the oxide-electrolyte interface with the presence of the TiO_2 shell. However, with the solid state reaction of ZnO and TiO_2 during the annealing treatment at temperatures above 600 °C and the consequent formation of the zinc titanate layer, an increase of the charge transfer resistance was obtained. EIS results correlated well with the improved PEC and DSCs performance obtained for $ZnO:Cl@TiO_2$ NW electrodes when compared with $ZnO:Cl$ arrays. EIS results also reflected the limitation in terms of sintering temperature that the formation of the Zinc titanate dielectric layer at the core-shell interface represents

Table 1. Properties determined by electrochemical impedance spectroscopy measurements.

Dark; V=1.8 V		K_{eff}	R_k	R_p	ω_{max}	D_{eff}
		(s^{-1})	(Ω)	(Ω)	(kHz)	($10^{-5}\text{cm}^2\text{s}^{-1}$)
ZnO:Cl NWs (450 °C)		30	680	34	540	1.9
ZnO:Cl@TiO₂ NWs (450 °C)		17	350	42	150	1.1
ZnO:Cl NWs (700 °C)		30	2400	100	440	1.9
ZnO:Cl@Zn_xTiO_y@TiO₂ NWs (700 °C)		6	8800	190	380	0.4
AM1.5	Potential	k_{eff}	R_k	r_p	ω_{max}	D_{eff}
	(V)	(s^{-1})	($\text{k}\Omega$)	(Ω)	(kHz)	($10^{-6}\text{cm}^2\text{s}^{-1}$)
ZnO:Cl NWs	0	1.7	1.7	35	200	1.1
	0.2	5.2	2.1	34	600	3.3
	0.4	3.8	2.8	33	600	2.4
	0.6	2.7	3.6	33	600	1.7
	0.8	2.7	4.9	34	600	1.7
ZnO:Cl@TiO₂ NWs	0	2.4	1.0	40	210	1.5
	0.2	7.4	1.1	40	570	4.6
	0.4	4.5	1.7	39	570	2.8
	0.6	3.1	3.0	40	570	1.9
	0.8	1.9	4.8	40	570	1.2

6.5 Conclusions

A facile procedure for the production of ZnO:Cl@TiO₂ NWs with controlled shell thickness was detailed. The procedure involved the adsorption of titanium isopropoxide, its hydrolyzation, the posterior polymerization and the final thermal crystallization to anatase TiO₂. ZnO:Cl@TiO₂ core-shell NWs showed improved photocatalytic performances towards water splitting. In the presence of the TiO₂ shell, an enhancement

of the photocurrent densities up to a two-fold increase respect with bare ZnO:Cl NWs was obtained for TiO₂ shell thicknesses of around 20 nm. Thicker TiO₂ shells resulted in a decrease of the total surface area due to the NWs coalesce. DSCs devices based on ZnO:Cl@TiO₂ NWs had also associated improved efficiencies when compared with those obtained from bare ZnO:Cl NWs. However, the sintering of the ZnO:Cl@TiO₂ NWs at 600 °C and above promoted the solid state reaction between the ZnO and TiO₂ and the formation of a zinc titanate layer at the core-shell interface. This zinc titanate layer was probed to decrease the optoelectronic performance of the NW arrays. EIS measurements demonstrated the ZnO:Cl@TiO₂ core-shell NWs to be characterized by a faster charge carrier transfer and a lower interface resistance than ZnO:Cl NWs. The rapid, low-cost, large-area, facile and controllable deposition method to produce ZnO:Cl@TiO₂ NWs detailed here represents an advantageous approach to improve the efficiency of photoelectrochemical and photovoltaic devices.

6.6 References

1. Könenkamp, R.; Word, R. C.; Godinez, M. *Nano Lett.* **2005**, *5*, 2005-2008.
2. Pauproté, T.; Lincot, D.; Viana, B.; Pellé, F. *Appl. Phys. Lett.* **2006**, *89*, 233112.
3. Claude, L. C.; Ramon, T. Z.; Ryan, M. A. *Adv. Mater.* **2005**, *17*, 1512-1515.
4. Quintana, M.; Edvinsson, T.; Hagfeldt, A.; Boschloo, G. *J. Phys. Chem. C.* **2007**, *111*, 1035-1041.
5. Wang, M. L.; Huang, C. G.; Cao, Y. G.; Yu, Q. J.; Guo, W.; Liu, Q. L.; Liang, J. K.; Hong, M. C. *Nanotechnology* **2009**, *20*, 285311.
6. Özgür, Ü.; Alivov, Ya. I.; Liu, C.; Teke, A.; Reshchikov, M. A.; Doğan. S.; Avrutin, V.; Cho, S.-J.; Morkoç, H. *J. Appl. Phys.* **2005**, *98*, 041301
7. Huang, M. H.; Wu, Y.; Feick, H.; Tran, N.; Weber, E.; Yang, P. D. *Adv. Mater.* **2001**, *13*, 113-116.
8. Sun, Y.; Fuge, G. M.; Ashfold, M. N. R. *Chem. Phys. Lett.* **2004**, *396*, 21-26.

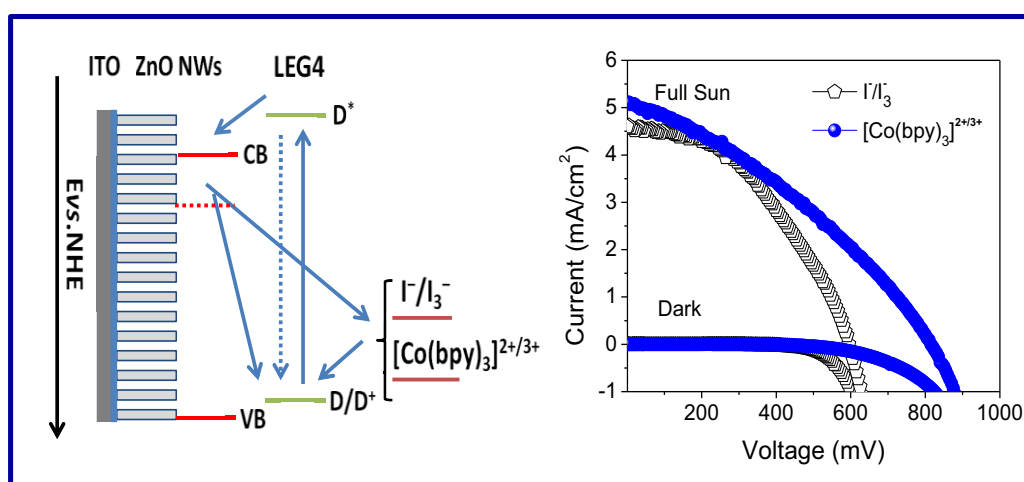
9. Park, W. I.; Kim, D. H.; Jung, S. W.; Yi, G. C. *Appl. Phys. Lett.* **2002**, *80*, 4232-4234.
10. Govender, K.; Boyle, D. S.; Kenway, P. B.; O'Brien, P. *J. Mater. Chem.* **2004**, *14*, 2575-2591.
11. Greene, L. E.; Yuhas, B. D.; Law, M.; Zitoun, D.; Yang, P. D. *Inorg. Chem.* **2006**, *45*, 7535-7543.
12. Peulon, S.; Lincot, D. *Adv. Mater.* **1996**, *8*, 166-170.
13. Fan, J. D.; Shavel, A.; Zamani, R.; Fábrega, C.; Rousset, J.; Haller, S.; Güell, F.; Carrete, A.; Andreu, T.; Arbiol, J.; Morante, J. R.; Cabot, A. *Acta Mater.* **2011**, *59*, 6790-6800.
14. Fan, J. D.; Güell, F.; Fábrega, C.; Shavel, A.; Carrete, A.; Andreu, T.; Morante, J. R.; Cabot, A. *Appl. Phys. Lett.* **2011**, *99*, 262102.
15. Greene, L. E.; Law, M.; Yuhas, B. D.; Yang, P. D. *J. Phys. Chem. C* **2007**, *111*, 18451-18456.
16. Anderson, N. A.; Ai, X.; Lian, T. Q. *J. Phys. Chem. B* **2003**, *107*, 14414-14421.
17. Bendall, J. S.; Etgar, L.; Tan, S. C.; Cai, N.; Wang, P.; Zakeeruddin, S. M.; Grätzel, M.; Welland, M. E. *Energy Environ. Sci.* **2011**, *4*, 2903-2908.
18. Irannejad, A.; Janghorban, K.; Tan, O. K.; Huang, H.; Lim, C. K.; Tan, P. Y.; Fang, X.; Chua, C. S.; Maleksaeedi, S.; Hejazi, S.; M, H.; Shahjamali, M. M.; Ghaffari, M. *Electrochimica Acta* **2011**, *58*, 19-24.
19. Sartori, A.; Visentin, F.; Habra, N.; Zorzi, C.; Natali, M.; Garoli, D.; Gerbasi, R.; Casarin, M.; Rossetto, G. *Cryst. Res. Technol.* **2011**, *46*, 885-890.
20. Thomas, M. A.; Cui, J. B. *J. Vac. Sci. Technol.* **2012**, *30*, 01A116.
21. Law, M.; Greene, L. E.; Radenovic, A.; Kuykendall, T.; Liphardt, J.; Yang, P. D. *J. Phys. Chem. B* **2006**, *110*, 22652-22663.
22. Wang, M. L.; Huang, C. G.; Cao, Y. G.; Yu, Q. J.; Deng, Z. H.; Liu, Y.; Huang, Z.; Huang, J. Q.; Huang, Q. F.; Wang, G.; Liang, J. K. *J. Phys. D: Appl. Phys.* **2009**, *42*, 155104.
23. Wang, M. L.; Huang, C. G.; Cao, Y. G.; Yu, Q. J.; Wang, G.; Huang, Q. F.; Liu, Y.; Huang, Z.; Huang, J. Q.; Wang, H.; Deng, Z. H. *Appl. Phys. Lett.* **2009**, *94*, 263506.
24. Gan, X.; Li, X.; Gao, X.; Zhuge, F.; Yu, W. *Thin Solid Films* **2010**, *518*, 4809-4812.

25. Liao, Z. M.; Zhang, H. Z.; Zhou, Y. B.; Xu, J.; Zhang, J. M.; Yu, D. P. *Phys. Lett. A* **2008**, *372*, 4505-4509.
26. Atienzar, P.; Ishwara, T.; Illy, B. N.; Ryan, M. P.; O'Regan, B. C.; Durrant, J. R.; Nelson, J. *J. Phys. Chem. Lett.* **2010**, *1*, 708-713.
27. Panigrahi, S.; Basak, D. *Nanoscale*. **2011**, *3*, 2336-2341.
28. Ichione, I.; Senzu, H.; Kunitake, T. *Chem. Lett.* **1996**, *25*, 831-832.
29. Ichione, I.; Senzu, H.; Kunitake, T. *Chem. Mater.* **1997**, *9*, 1296-1298.
30. Foong, T. R. N.; Shen, Y.; Hu, X.; Sellinger, A. *Adv. Funct. Mater.* **2010**, *20*, 1390-1396.
31. Bao, L. L.; Mahurin, S. M.; Dai, S. *Anal. Chem.* **2004**, *76*, 4531-4536.
32. Yan, W. F.; Chen, B.; Mahurin, S. M.; Hagaman, E. W.; Dai, S.; Overbury, S. H. *Chem. Mater.* **2005**, *17*, 1923-1925.
33. Pinna, N.; Niederberger, M. 2009 Metal oxide nanoparticles in organic solvents synthesis, formation, assembly and application. *Springer* ISBN: 978-1-84882-670-0.
34. Fabrega, C.; Andreu, T.; Cabot, A.; Morante, J. R. *J. Photochem. Photobiol. A: Chem.* **2010**, *211*, 170-175.
35. Kominami, H.; Takada, Y.; Yamagiwa, H.; Kera, Y.; Inoue, M.; Inui, T. *Ind. Eng. Chem. Res.* **1999**, *38*, 3925-3931.
36. Barlier, V.; Bounor-Legaré, V.; Boiteux, G.; Davenas, J.; Léonard, D. *Appl. Surf. Sci.* **2008**, *254*, 5408-5412.
37. Léaustic, A.; Babonneau, F.; Livage, J. *Chem. Mater.* **1989**, *1*, 240-247.
38. Ahonen, P. P.; Tapper, U.; Kauppinen, E. I.; Joubert, J.-C.; Deschanvres, J.-L. *Mater. Sci. Eng. A* **2001**, *315*, 113-121.
39. Chen, J. Y.; Gao, L.; Huang, J. H.; Yan, D. S. *J. Mater. Sci.* **1996**, *31*, 3497-3500.
40. Barbé, C. J.; Arendse, F.; Comte, P.; Jirousek, M.; Lenzmann, F.; Shklover, V.; Gratzel, M. *J. Am. Ceram. Soc.* **1997**, *80*, 3157-3171.
41. Vorkapic, D.; Matsoukas, T. *J. Colloid Interf. Sci.* **1999**, *214*, 283-291.
42. Vorkapic, D.; Matsoukas, T. *J. Am. Ceram. Soc.* **1998**, *81*, 2815-2820.
43. Jean, J. H.; Ring, T. A. *Langmuir* **1986**, *2*, 251-255.
44. Barringer, E. A.; Bowen, H. K. *Langmuir* **1985**, *1*, 414-420.
45. Barringer, E. A.; Bowen, H. K. *Langmuir* **1985**, *1*, 420-428.
46. Mahshid, S.; Askari, M.; Ghamsari, M. S. *J. Mater. Process. Tech.* **2007**, *189*, 296-300.

47. Lee, S.; Jeon, C.; Park, Y. C. *Chem. Mater.* **2004**, *16*, 4292-4295.
48. Yoldas, B. E. *J. Mater.Sci.* **1986**, *21*, 1087-1902.
49. Yang, S. G.; Quan, X.; Li, X. Y.; Liu, Y. Z.; Chen, S.; Chen, G. H. *Phys. Chem. Chem. Phys.* **2004**, *6*, 659-664.
50. Chen, X.; Mao, S. S. *Chem. Rev.* **2007**, *107*, 2891-2959.
51. Oskam, G.; Nellore, A.; Penn, R. L.; Searson, P. C. *J. Phys. Chem. B* **2003**, *107*, 1734-1738.
52. Bessekhoud, Y.; Robert, D.; weber, J. V. *J. Photochem. Photobio A: Chem.* **2003**, *157*, 47-53.
53. Livage, J.; Henry, M.; Sanchez, C. *Prog. Solid State Chem.* **1988**, *18*, 259-341.
54. Yoshida, R.; Suzuki, Y.; Yoshikawa, S. *J. Solid State Chem.* **2005**, *178*, 2179-2185.
55. Qian, D.; Gerward, L.; Jiang, J. Z. *J. Mater. Sci.* **2004**, *39*, 5589-5392.
56. Liu, R.; Ye, H.; Xiong, X.; Liu, H. *Mater. Chem. Phys.* **2010**, *121*, 432-439.
57. Fan, H. J.; Yang, Y.; Zacharias, M. *J. Mater. Chem.* **2009**, *19*, 885-900.
58. Liang, Y. C.; Hu, C. Y.; Liang, Y. C. *CrystEngComm* **2012**, *14*, 5579-5584.
59. Manika, S. K.; Pradhan, S. K. *Physica E* **2006**, *33*, 69-76.
60. Chai, Y. L.; Chang, Y. S.; Hsiao, Y. J.; Lian, Y. C. *Mater. Res. Bull.* **2008**, *43*, 257-263.
61. Chen, X.; Shen, S.; Guo, L.; Mao, S. S. *Chem. Rev.* **2010**, *110*, 6503-6570.
62. Cheng, H.-M.; Chiu, W.-H.; Lee, C.-H.; Tsai, S.-Y.; Hsieh, W.-F. *J. Phys. Chem. C* **2008**, *112*, 16359-16364.
63. Wang, M.; Huang, C.; Cao, Y.; Yu, Q.; Guo, W.; Liu, Q.; Liang, J.; Hong, M. *Nanotechnology* **2009**, *20*, 285311
64. Wang, Q.; Moser, J.-E.; Graetzel, M. *J. Phys. Chem. B* **2005**, *109*, 14945-14953.
65. Fabregat-Santiago, F.; Barea, E. M.; Bisquert, J.; Mor, G. K.; Shankar, K.; Grimes, A. *J. Am. Chem. Soc.* **2008**, *130*, 11312-11316.
66. Wang, Q.; Ito, S.; Gratzel, M.; Fabregat-Santiago, F.; Mora-Seró, I.; Bisquert, J.; Bessho, T.; Imai, H. *J. Phys. Chem. B* **2006**, *110*, 25210-25221.
67. Adachi, M.; Sakamoto, M.; Jiu, J.; Ogata, Y.; Isoda, S. *J. Phys. Chem. B* **2006**, *110*, 13872-13880.

Chapter 7

Cobalt (II/III) Redox Electrolyte in ZnO Nanowire-Based Dye-Sensitized Solar Cells



7.1 Abstract

In this chapter, we explore the use of cobalt complex redox shuttles in DSCs based on ZnO NWs. Arrays of vertically aligned ZnO NWs produced by a low-cost hydrothermal method are used to fabricate DSCs with $[\text{Co}(\text{bpy})_3]^{2+/3+}$ as electrolyte. A direct comparison of the performance of $[\text{Co}(\text{bpy})_3]^{2+/3+}$ -based ZnO DSCs with I^-/I_3^- -based ones demonstrates the higher suitability of the cobalt complex, both in terms of a larger open circuit voltage (V_{OC}) and a higher photocurrent. The $[\text{Co}(\text{bpy})_3]^{2+/3+}$ electrolyte results in V_{OC} enhancements above 200 mV. This V_{OC} increase is associated with the better match between the cobalt complex redox potential and the oxidation potential of the dye. The IPCE enhancement is attributed to a less competitive visible light

absorption of the cobalt redox couple. Thus the present study opens new opportunities to improve energy conversion efficiency in ZnO-based DSCs.

7.2 Introduction

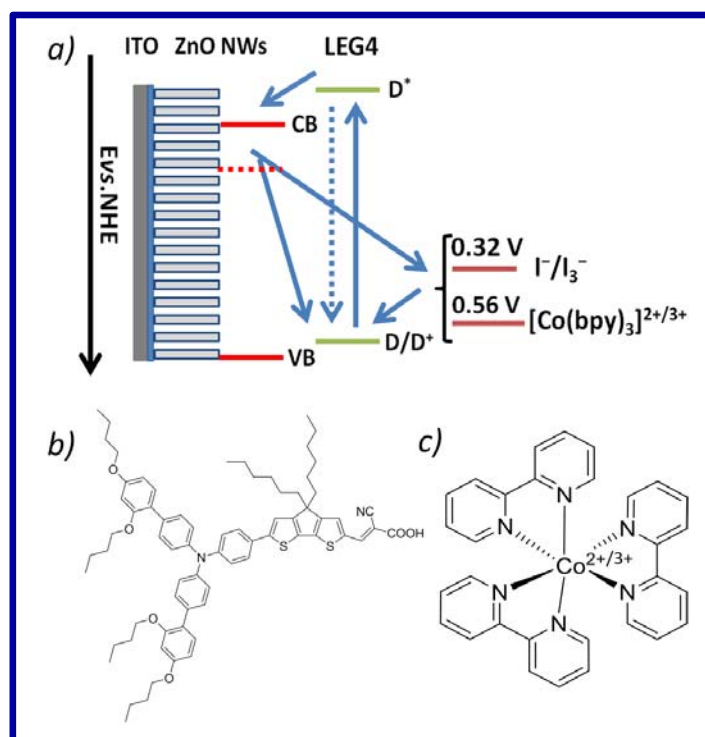
Since the first efficient DSC was demonstrated by O'Regan and Grätzel in 1991,¹ each of its components have been thoroughly analyzed and optimized with the aim to maximize DSCs power conversion efficiency.²⁻⁴ During all this time, the Γ/I_3^- redox shuttle has survived as the best performing electrolyte because it combines a very fast dye regeneration with a slow back reaction of photoinjected electrons with the oxidized redox species. However, the Γ/I_3^- electrolyte has some disadvantages and leaves some room for improvement:^{5,6} (i) It is corrosive toward metals such as Ag, Au and Cu, which limits the use of these elements in modules; (ii) It absorbs light in the blue part of the spectrum, lowering the DSC photocurrent and hence the power conversion efficiency; (iii) Its redox potential is not well adjusted to typical sensitizers, which limits V_{OC} in TiO₂-based solar cells to 0.7-0.8 V.^{5,7}

Very recently, cobalt (III/II) redox complexes have been demonstrated as excellent alternatives to the Γ/I_3^- redox couple in TiO₂-based DSCs.⁸⁻¹² Cobalt (III/II)-based electrolytes offer various advantages over Γ/I_3^- : (i) Reduced corrosiveness toward relevant metals; (ii) Lower absorption in the visible; and (iii) Facile tuning of the redox potential, with the capability to minimize energy loss in the dye regeneration step. In a previous study, we demonstrated that V_{OC} above 900 mV and efficiencies up to 6.7% can be obtained using $[Co(bpy)_3]^{2+/3+}$ in TiO₂-based DSCs.¹² Subsequently, TiO₂-based DSCs employing the $[Co(bpy)_3]^{2+/3+}$ redox couple were reported to reach power conversion efficiency exceeding 12%.¹¹

ZnO is the main alternative wide band gap semiconductor to replace TiO₂ as an electron conductor.¹³⁻¹⁷ Although a dye optimized to sensitize ZnO-based DSCs remains to be found, ZnO is considered as an excellent backbone to produce high-efficiency DSCs. ZnO has higher bulk electron mobilities than TiO₂. Furthermore, its morphology is easily tunable. This allows the rational design and development of hierarchical ZnO nanostructures able to simultaneously optimize charge carrier path and dye loading.

A particularly advantageous geometry in terms of improving electron transport properties and minimizing recombination during charge carrier transport to the external circuit is that of NWs.¹⁸⁻²² Vertically aligned ZnO NWs can significantly increase the electron diffusion length up to the order of 100 μm.^{23,24} Although charge collection efficiencies are already close to 100% in randomly oriented TiO₂ nanoparticles using I⁻/I₃⁻, NWs may be an advantageous framework structure for DSCs with hole conductors presenting faster recombination, such as Co-based redox couples or solid hole collectors.^{11,13,25,26} NWs may also allow getting around one of the drawbacks of bulky cobalt-based redox couples and solid electrolytes: their limited mass transport through structures with narrow pores.^{27,28} However, no study has yet reported the use of cobalt-based redox couples on ZnO-based DSCs or NW-based DSCs.

In this chapter, we explore the performance of the [Co(bpy)₃]^{2+/3+} redox couple on ZnO NWs-based DSCs. We first test the new redox electrolyte using ZnO NW arrays with different lengths. Then, using the exact same NW array and LEG4 dye as sensitizer, we perform a direct comparison of the performance of [Co(bpy)₃]^{2+/3+} and I⁻/I₃⁻ redox couples as electrolytes in ZnO NW DSCs (Scheme 1).



Scheme 1. a) Schematic energy diagram of the ZnO NWs solar cell sensitized with LEG4 and using I^-/I_3^- or $[\text{Co}(\text{bpy})_3]^{2+/3+}$ as electrolyte. b) Molecular structure of the LEG4 dye. c) Molecular structure of $[\text{Co}(\text{bpy})_3]^{2+/3+}$.

7.3 Experimental section

7.3.1 Synthesis of ZnO NWs

ZnO NWs were obtained by a low-cost, high-throughput, high-yield and large-area hydrothermal process. First, we sputtered an 80 nm layer of intrinsic ZnO nanoparticle on a glass substrate coated with ITO (Figure 1). The intrinsic ZnO layer has a double role: (i) It seeds the ZnO NWs growth and (ii) It blocks the direct contact between the electrolyte and ITO. The ZnO NWs growth solution consisted of 0.02 M zinc nitrate, 0.015 M hexamethylenetetramine (HMTA), 0.004 M polyethyleneimine (PEI) (end-capped, molecular weight 800 g/mol LS, Aldrich), and 0.024 M ammonium hydroxide. The seeded substrate was then placed inside 100 mL of the aqueous growth solution. The container was covered and then placed inside a water bath preheated at 88 °C

during 3 h. By this procedure, 6 μm long ZnO NWs were obtained. Longer NWs were produced by multiple growth steps, placing the substrate in a fresh zinc nitrate solution every 3 h. The resulting ZnO arrays were rinsed with M.Q water and annealed in Air at 350 $^{\circ}\text{C}$ for 60 min. Surface organic ligands were burned out during this annealing treatment.

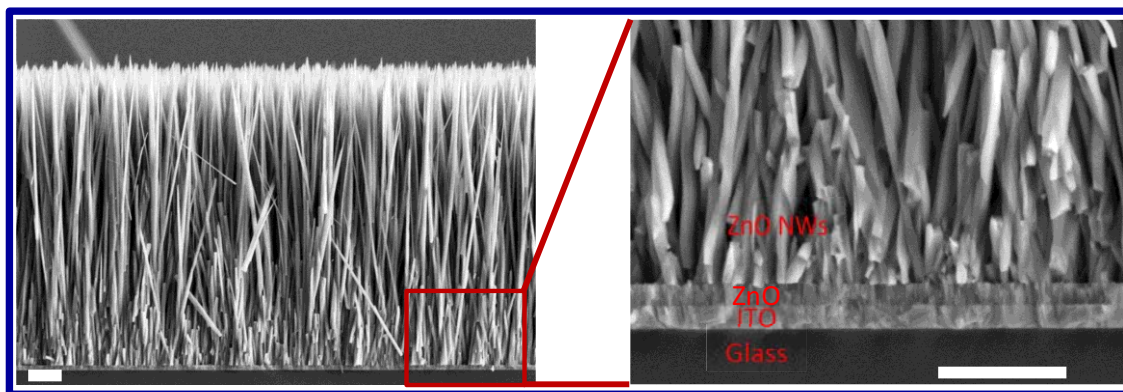


Figure 1. SEM image of the interface between the ZnO NWs and the ITO substrate. The intrinsic ZnO blocking/seed layer is clearly observed. All scale bars correspond to 1 μm .

7.3.2 DSCs fabrication

Dye uptake was carried out by immersing the ZnO NWs photoanodes (0.25 cm^2) into an ethanol solution (0.2 mM) of LEG4 (Scheme 1) at room temperature for 20 h. A Pt-coated counter electrode was prepared by drop casting a 5 mM H_2PtCl_6 ethanol solution onto an FTO-coated glass, followed by sintering at 450 $^{\circ}\text{C}$ in air for 30 min. A 25 μm thick hot-melt film (Solaronix) was sandwiched between the ZnO NW-based photoanodes and the Pt counter electrode. To complete the device, the electrolyte was injected into the space between the cell's anode and cathode through a hole drilled on the counter electrode. The $[\text{Co}(\text{bpy})_3]^{2+/3+}$ electrolyte was obtained by mixing 0.22 M $\text{Co}(\text{bpy})_3(\text{PF}_6)_2$, 0.05 M $\text{Co}(\text{bpy})_3(\text{PF}_6)_3$, 0.1 M LiClO_4 , and 0.2 M 4-tert-butylpyridine

(TBP) in acetonitrile. Reference Γ/I_3^- DSCs were prepared using 0.1 M LiI, 0.1 M I_2 , 0.2 M TBP, and 0.6 M tetrabutylammonium iodide in acetonitrile.

7.3.3 Characterization

XRD patterns were obtained with Cu $K\alpha$ ($\lambda = 1.5406 \text{ \AA}$) radiation in a reflection geometry on a Bruker D8 operating at 40 kV and 40 mA. Field emission SEM was used to characterize the morphology of the obtained ZnO NWs. Both cross-section and top-down views were obtained using a FEI Nova NANOSEM 230.

Current-voltage ($J-V$) characteristics were measured using a Keithley 2400 source/meter and a Newport solar simulator (model 91160) with AM 1.5 G spectral distribution. The intensity power was adjusted to 1000 W m^{-2} using a certified reference solar cell (Fraunhofer ISE). Two neutral density filters were used to reduce intensity to 500 and 100 W m^{-2} . A black mask with an aperture ($0.5 \times 0.5 \text{ cm}^2$) was placed on top of the cell to avoid any significant contribution from outside of the active area.

IPCE spectra were recorded using a computer-controlled setup consisting of a xenon light source (Spectral Products ASBXE-175), a monochromator (Spectral Products CM110), and a potentiostat (EG&G PAR 273), calibrated using a certified reference solar cell (Fraunhofer ISE).

Electron lifetime and extracted charge measurements were performed using a white LED (Luxeon Star 1W) as the light source. Voltage and current traces were recorded with a 16-bit resolution digital acquisition board (National Instruments) in combination with a current amplifier (Stanford Research Systems SR570) and a custom-made system using electromagnetic switches. Lifetimes were determined by monitoring photocurrent and photovoltage transients at different light intensities upon applying a small square wave modulation to the base light intensity. Extracted charge measurements were

performed by illuminating the cell for 5 s under open-circuit conditions and then turning the lamp off to let the voltage to decay to a voltage V . The cell was then short circuited, and the current was measured under 5 s and integrated to obtain Q (V).

7.4 Results and discussion

Vertically aligned ZnO NWs were prepared by a low-cost, high-throughput, high-yield and potentially large-area hydrothermal process. Figure 2 display top-down and cross-section SEM micrographs of ZnO NWs with average lengths of 6 μm , 9 and 12 μm obtained by this procedure. The diameter of the ZnO NWs increased with the NW length, from 40 to 120 nm. XRD analysis confirmed the obtained ZnO NWs to grow in the (100) direction and to have the wurtzite crystal structure (Figure 1 and Figure 2).

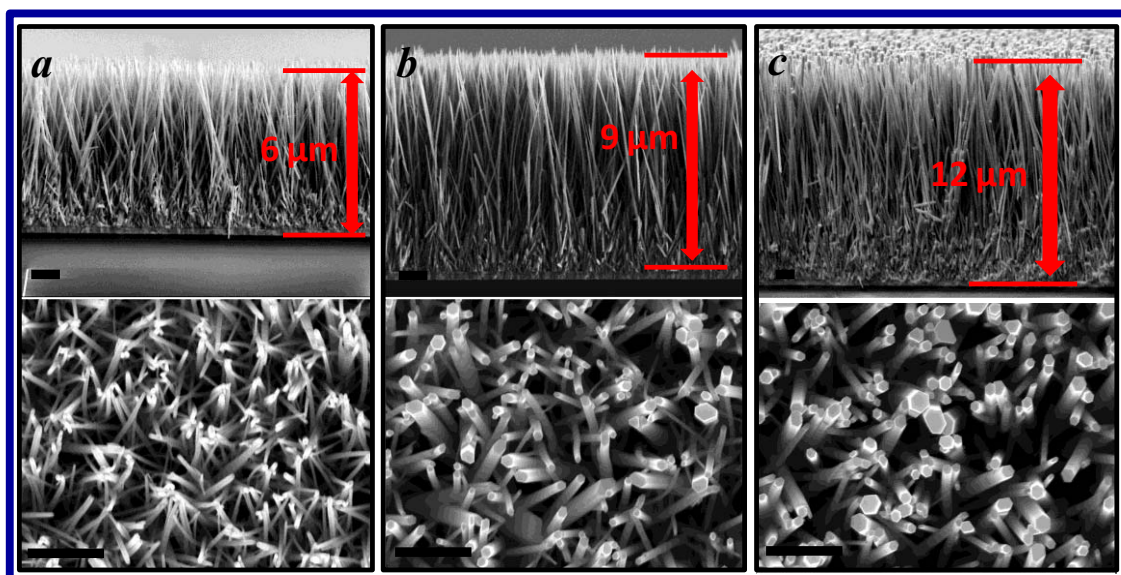


Figure 2. Cross-section and top-down SEM images of ZnO NWs with average length of 6 μm (a), 9 μm (b) and 12 μm (c). All scale bars correspond to 1 μm .

For DSCs fabrication, ZnO NWs were sensitized with LEG4 dyes by immersing the ZnO NW arrays (0.25 cm^2) into an ethanol solution (0.2 mM) of LEG4 during 20 h. An FTO-covered glass coated with Pt was used as the counter electrode. Figure 3 displays the J - V characteristic and IPCE of DSCs fabricated using $[\text{Co}(\text{bpy})_3]^{2+/3+}$ as electrolyte

and ZnO NWs with different lengths (6 μm -12 μm) as the photoanode. The measured photovoltaic parameters are summarized in Table 1. DSC performance and particularly the collected photocurrent were clearly enhanced when increasing the NW length. This enhancement is explained by the increase in the total surface area and thus of the dye loading in longer NW.^{14,15} The maximum power conversion efficiency was obtained for 12 μm ZnO NWs at 1.5%. Notice that when decreasing illumination intensity, higher efficiencies were obtained, up to 2.3% at 100 W/m^2 AM1.5G illumination (Table 1 and Figure 4). The same behavior was observed in previous reports using the cobalt redox couple in DSCs.^{11,12}

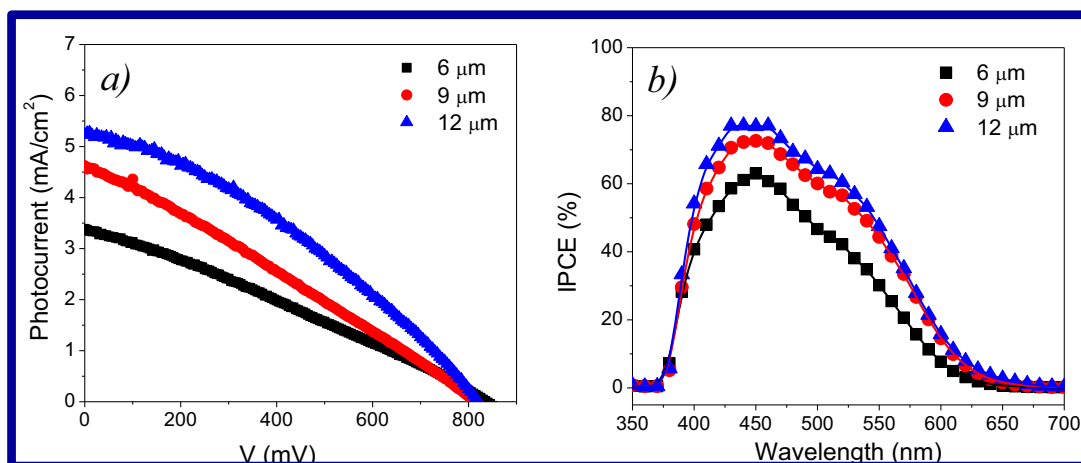


Figure 3. $J-V$ characteristic (a) and spectra of incident photon to current efficiency (b) under AM1.5G illumination of $[\text{Co}(\text{bpy})_3]^{2+/3+}$ DSCs using ZnO NWs with different lengths.

The efficiencies obtained here are higher than values previously reported for equivalent ZnO NWs-based DSCs using Γ^-/I_3^- as electrolyte.^{14,15} However, the FF for all ZnO NWs-based DSCs fabricated in the present study were relatively low. The low FFs always obtained in ZnO-based DSCs are generally attributed to a rapid charge carrier recombination at the ZnO-electrolyte interface.^{29,30} To solve this problem, it is experimentally proved that the addition of TiO_2 shells to ZnO wire cells results in a considerable improvement in FF.^{16,29}

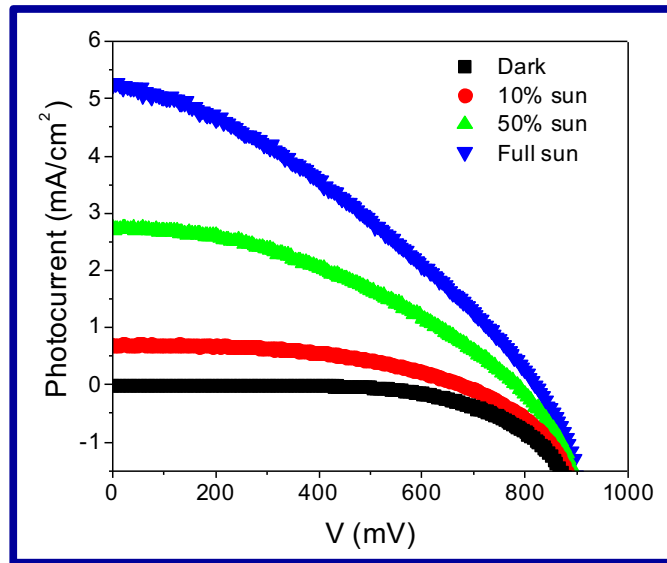


Figure 4. J - V characteristics of ZnO NWs-based DSCs under various light intensities

Table 1 Photovoltaic parameters of the DSCs based on ZnO NWs with different length using $[\text{Co}(\text{bpy})_3]^{2+/3+}$ as electrolyte.

Length (μm)	Light intensity (W/m^2)	V_{oc} (mV)	J_{sc} (mA/cm^2)	FF (%)	PCE (%)
6	1000	835	3.39	28.4	0.80
9	1000	815	4.63	27.2	1.03
12	1000	820	5.23	34.2	1.47
12	500	785	2.75	39.2	1.69
12	100	680	0.70	47.9	2.27

For a direct comparison of the $[\text{Co}(\text{bpy})_3]^{2+/3+}$ and Γ/I_3^- electrolyte performances, we fabricated iodine- and cobalt-based DSCs using two pieces of the exact same $10 \mu\text{m}$ ZnO NW arrays. Figure 5a displays representative J - V characteristics of Γ/I_3^- and $[\text{Co}(\text{bpy})_3]^{2+/3+}$ DSCs. Table 2 summaries the performance parameters of two DSCs obtained from splitting a ZnO NW arrays. Although FF require further improvement, $[\text{Co}(\text{bpy})_3]^{2+/3+}$ -based DSCs systematically displayed slightly higher photocurrents and much higher V_{OC} than Γ/I_3^- -based DSCs. In particular, V_{OC} was significantly improved with the use of $[\text{Co}(\text{bpy})_3]^{2+/3+}$, from values around 600 mV obtained with Γ/I_3^- to V_{OC}

above 800 mV with $[\text{Co}(\text{bpy})_3]^{2+/3+}$. The V_{OC} obtained using $[\text{Co}(\text{bpy})_3]^{2+/3+}$ were even higher than those previously measured from ZnO@TiO₂ core-shell NWs.^{16,17} The outstanding V_{OC} improvement obtained when using the cobalt-based electrolyte was attributed to the lower potential of the $[\text{Co}(\text{bpy})_3]^{2+/3+}$ redox couple when compared with Γ/I_3^- (Scheme 1). The better potential match with the dye ground state allows minimizing the energy loss in the dye regeneration step.

Table 2 Photovoltaic parameters of the DSCs based on ZnO NWs using Γ/I_3^- and $[\text{Co}(\text{bpy})_3]^{2+/3+}$ as electrolyte

Electrolyte	Light intensity (W/m ²)	V_{OC} (mV)	J_{SC} (mA/cm ²)	FF (%)	PCE (%)
Γ/I_3^-	1000	595	4.6	43.5	1.19
$[\text{Co}(\text{bpy})_3]^{2+/3+}$	1000	810	5.1	31.1	1.28

Figure 5b displays the IPCE of ZnO NW-based DSCs with $[\text{Co}(\text{bpy})_3]^{2+/3+}$ and Γ/I_3^- redox couples. IPCEs were systematically enhanced with the use of the $[\text{Co}(\text{bpy})_3]^{2+/3+}$ instead of Γ/I_3^- electrolyte, especially in the blue region of the visible spectrum (Figure 5b). The enhancement in the wavelength range from 350 nm - 450 nm was mainly associated to the reduced light absorption of $[\text{Co}(\text{bpy})_3]^{2+/3+}$ in this range.³¹

We further compared the charge extraction efficiency and charge carrier lifetime in ZnO NW DSCs fabricated using Γ/I_3^- and $[\text{Co}(\text{bpy})_3]^{2+/3+}$ electrolytes (Figure 5c and 5d). Measurements of the extracted charge (Q) were performed by illuminating the cell for 5 s under open-circuit conditions and then turning off the lamp to let the voltage decay to a voltage V. The cell was then short circuited, and the current was integrated during 5 s to obtain Q (V). A significant shift of the charge collected from ZnO NW-based DSCs was observed between the Γ/I_3^- and the $[\text{Co}(\text{bpy})_3]^{2+/3+}$ electrolyte. The amount of extracted charge at a given voltage was a factor 1.6 higher when using the

$[\text{Co}(\text{bpy})_3]^{2+/3+}$ electrolyte. This indicated a shift of the electronic states in ZnO toward lower energies with the $[\text{Co}(\text{bpy})_3]^{2+/3+}$ electrolyte.

Charge carrier lifetimes were determined by monitoring photovoltage transients at different light intensities upon applying a small square wave modulation to the base light intensity. The measured electron lifetime is plotted as function of the quasi-Fermi level of the ZnO NW under open circuit conditions in Figure 5d. Slightly faster decays were obtained with the use of the $[\text{Co}(\text{bpy})_3]^{2+/3+}$ electrolyte. The same behavior was previously observed when the comparison was performed between the Γ/I_3^- and $[\text{Co}(\text{bpy-pz})_2]^{2+/3+}$ electrolytes in TiO_2 -based DSCs.⁷ In our study, it is clear that the electron recombination lifetime is not responsible for the change in voltage. The higher V_{oc} is dominated by the position shift in the redox potential value of the $[\text{Co}(\text{bpy})_3]^{2+/3+}$ with respect to the one of the Γ/I_3^- electrolyte.

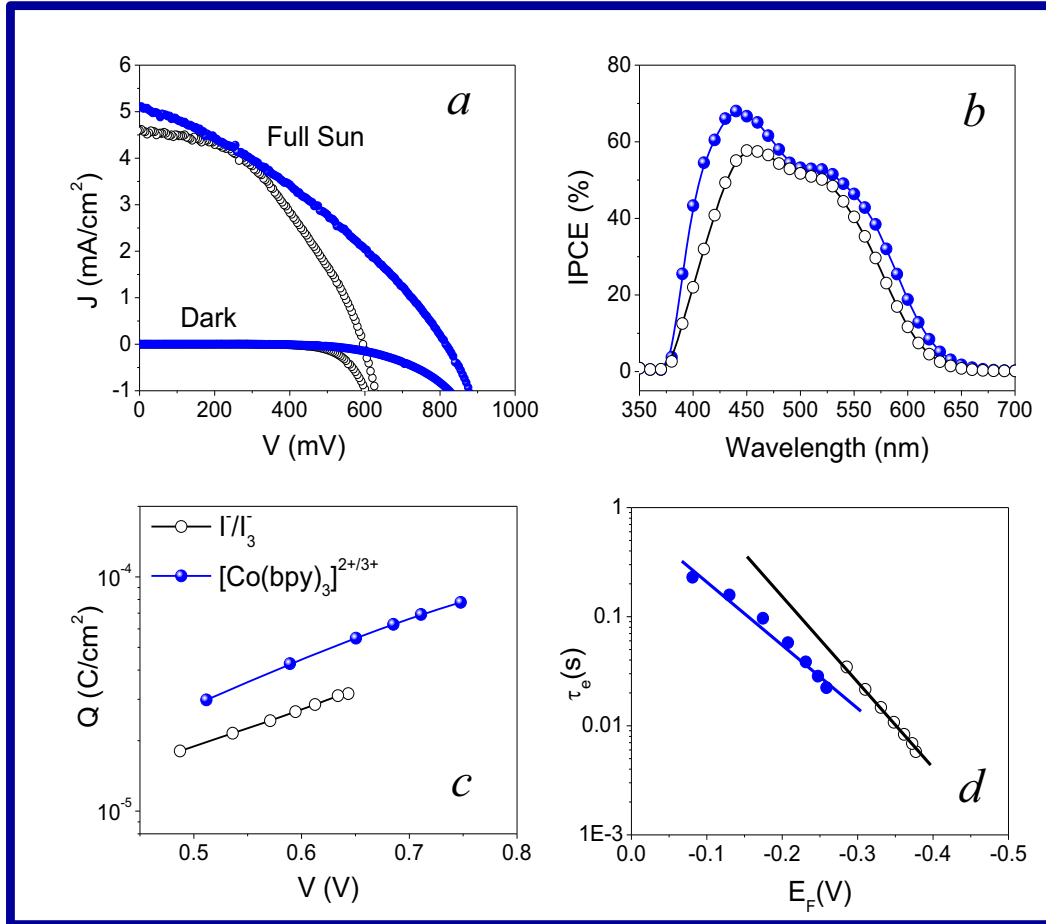


Figure 5. Comparison of ZnO NW DSCs fabricated using Γ/I_3^- (O) or $[Co(bpy)_3]^{2+/3+}$ (●) as electrolyte: (a) J - V characteristic under AM1.5G illumination; (b) Spectra of incident photon to current efficiency; (c) charge extraction as a function of voltage under open circuit conditions; (d) electron lifetime as a function of the quasi-Fermi level of the ZnO NW under open circuit conditions for DSCs employing Γ/I_3^- and $[Co(bpy)_3]^{2+/3+}$ based electrolytes, respectively.

There is plenty of room for improvement in ZnO NW-based DSCs. We believe the use of $[Co(bpy)_3]^{2+/3+}$ redox electrolyte represents one step in the correct direction, but we speculate that much higher efficiencies can be obtained in $[Co(bpy)_3]^{2+/3+}$ -based ZnO NW DSCs by the following modifications: (i) Use longer ZnO NWs and high surface area hierarchical nanostructures to increase dye uptake and enhance photocurrent;^{14,16} (ii) Coat a TiO_2 shell to improve V_{OC} and fill factor by lowering the rate of electron-hole recombination across the oxide-electrolyte interface;^{29,32} (iii) Reduce recombination at ZnO surface defects and facilitate dye charge transfer by

means of a more severe annealing process and the use of ZnO-based core-shell NW structures;^{33,34} (iv) Develop dyes better suited to ZnO surface chemistry;¹³ (v) Use high surface area-cathode material to reduce charge transfer resistance at the Pt counter electrode and improve fill factor.^{7, 35-37}

7.5 Conclusions

We demonstrated that $[\text{Co}(\text{bpy})_3]^{2+/3+}$ offers multiples advantages over Γ/I_3^- to produce efficient ZnO NW-based DSCs. The use of $[\text{Co}(\text{bpy})_3]^{2+/3+}$ instead of the conventional Γ/I_3^- electrolyte in ZnO NW-based DSCs resulted in a V_{OC} enhancement of above 200 mV. This was associated to the better match between the $[\text{Co}(\text{bpy})_3]^{2+/3+}$ redox potential and the oxidation potential of the dye. ZnO NW-based DSCs obtained with $[\text{Co}(\text{bpy})_3]^{2+/3+}$ were also characterized by slightly higher photocurrents. These were associated to a lower light absorption of the $[\text{Co}(\text{bpy})_3]^{2+/3+}$ electrolyte in the blue region of visible spectrum. These promising results confirm that cobalt complex redox shuttles are a serious alternative to the conventional Γ/I_3^- redox couple also in ZnO DSCs and represent an important step towards improving energy conversion efficiency in these devices.

7.6 References

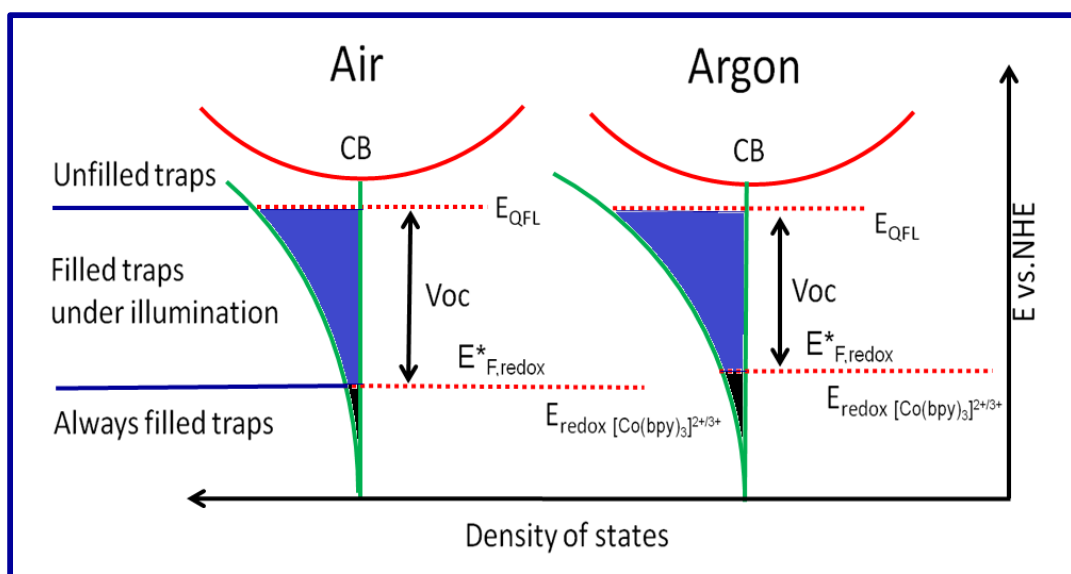
1. O'Regan, B.; Grätzel, M. *Nature* **1991**, *353*, 737-740.
2. Hagfeldt, A.; Boschloo, G.; Sun, L. C.; Kloo, L.; Pettersson, H. *Chem. Rev.* **2010**, *110*, 6595–6663.
3. Cong, J. Y.; Yang, X. C.; Kloo, L.; Sun, L. C. *Energy Environ. Sci.* **2012**, *5*, 9180-9194.
4. Tetreault, N.; Grätzel, M. *Energy Environ. Sci.* **2012**, *5*, 8506-8516.
5. Boschloo, G.; Hagfeldt, A. *Accounts Chem. Res.* **2009**, *42*, 1819–1826.

6. Gregg, B. A.; Pichot, F.; Ferrere, S.; Fields, C. L. *J. Phys. Chem. B* **2001**, *105*, 1422–1429.
7. Yum, J.-H.; Baranoff, E.; Kessler, F.; Moehl, T.; Ahmad, S.; Bessho, T.; Marchioro, A.; Ghadiri, E.; Moser, J.-E.; Yi, C.; Nazeeruddin, M. K.; Grätzel, M. *Nat. Commun.* **2012**, *3*, 631.
8. Wang, M. K.; Grätzel, C.; Zakeeruddin, S. M.; Grätzel, M. *Energy Environ. Sci.* **2012**, *5*, 9394-9405.
9. Aribia, K. B.; Moehl, T.; Zakeeruddin, S. M.; Grätzel, M. *Chem. Sci.* **2013**, *4*, 454-459.
10. Mosconi, E.; Yum, J. H.; Kessler, F.; Gomez-Garcia, C. J.; Zuccaccia, C.; Cinti, A.; Nazeeruddin, M. K.; Grätzel, M.; De Angelis, F. *J. Am. Chem. Soc.* **2012**, *134*, 19438-19453.
11. Yella, A.; Lee, H. W.; Tsao, H. N.; Yi, C. Y.; Chandiran, A. K.; Nazeeruddin, Md. K.; Diau, E. W. G.; Yeh, C. Y.; Zakeeruddin, S. M.; Grätzel, M. *Science* **2011**, *334*, 629-634.
12. Feldt, S. M.; Gibson, E. A.; Gabrielsson, E.; Sun, L. C.; Boschloo, G.; Hagfeldt, A. *J. Am. Chem. Soc.* **2010**, *132*, 16714–16724.
13. Anta, J. A.; Guillén, E.; Tena-Zaera, R. *J. Phys. Chem. C* **2012**, *116*, 11413–11425.
14. Xu, C. K.; Shin, P.; Cao, L. L.; Gao, D. *J. Phys. Chem. C* **2010**, *114*, 125–129.
15. Qiu, J. J.; Li, X. M.; Zhuge, F. W.; Gan, X. Y.; Gao, X. D.; He, W. Z.; Park, S.-J.; Kim, H.-K.; Hwang, Y.-H. *Nanotechnology* **2010**, *21*, 195602.
16. Xu, C. K.; Wu, J. M.; Desai, U. V.; Gao, D. *J. Am. Chem. Soc.* **2011**, *133*, 8122–8125,
17. Wang, M. L.; Wang, Y.; Li, J. B. *Chem. Commun.* **2011**, *47*, 11246–11248.
18. Law, M.; Greene, L. E.; Johnson, J. C.; Saykally, R.; Yang, P. Law, M.; Greene, L. E.; Johnson, J. C.; Saykally, R.; Yang, P. *Nat. Mater.* **2005**, *4*, 455–459.
19. Galoppini, E.; Rochford, J.; Chen, H. H.; Saraf, G.; Lu, Y. C.; Hagfeldt, A.; Boschloo, G. *J. Phys. Chem. B* **2006**, *110*, 16159–16161.
20. Baxter, J. B.; Aydil, E. S. *Appl. Phys. Lett.* **2005**, *86*, 053114.
21. Gonzalez-Valls, I.; Lira-Cantu, M. *Energy Environ. Sci.* **2009**, *2*, 19–34.
22. Baxter, J. B.; Aydil, E. S. *Sol. Energ. Mat. Sol. C.* **2006**, *90*, 607–622.
23. Martinson, A. B. F.; Goes, M. S.; Fabregat-Santiago, F.; Bisquert, J.; Pellin, M. J.; Hupp, J. T. *J. Phys. Chem. A* **2009**, *113*, 4015-4021.

24. Martinson, A. B. F.; McGarrah, J. E.; Parpia, M. O. K.; Hupp, J. T. *Phys. Chem. Chem. Phys.* **2006**, *8*, 4655-4659.
25. Bach, U.; Lupo, D.; Comte, P.; Moser, J. E.; Weissortel, F.; Salbeck, J.; Spreitzer, H.; Grätzel, M. *Nature* **1998**, *395*, 583-585.
26. González-Vázquez, J. P.; Morales-Florez, V.; Anta, J. A. *J. Phys. Chem. Lett.* **2012**, *3*, 386– 393.
27. Nelson, J. J.; Amick, T. J.; Elliott, C. M. *J. Phys. Chem. C* **2008**, *112*, 18255–18263.
28. Liberatore, M.; Petrocco, A.; Caprioli, F.; Mesa, C. L.; Decker, F.; Bignozzi, C. A. *Electrochim. Acta* **2010**, *55*, 4025–4029.
29. Law, M.; Greene, L.E.; Radenovic, A.; Kuykendall, T.; Liphardt, J.; Yang, P. D. *J. Phys. Chem. B* **2006**, *110*, 22652–22663.
30. Zhang, Q. F.; Chou, T. P.; Russo, B.; Jenekhe, S. A.; Cao, G. Z. *Adv. Funct. Mater.* **2008**, *18*, 1654–1660.
31. Thomas, W. H. *Dalton T.* **2012**, *41*, 3111-3115.
32. Fan, J. D.; Zamani, R.; Fábrega, C.; Shavel, A.; Flox, C.; Ibáñez, M.; Andreu, T.; López, A. M.; Arbiol, J.; Morante, J. R.; Cabot, A. *J. Phys. D: Appl. Phys.* **2012**, *45*, 415301.
33. Fan, J. D.; Guell, F.; Fábrega, C.; Shavel, A.; Carrete, A.; Andreu, T.; Morante, J. R.; Cabot, A. *Appl. Phys. Lett.* **2011**, *99*, 262102.
34. Fan, J. D.; Shavel, A.; Zamani, R.; Fábrega, C.; Rousset, J.; Haller, S.; Güell, F.; Carrete, A.; Andreu, T.; Arbiol, J.; Morante, J. R.; Cabot, A. *Acta Mater.* **2011**, *59*, 6790–6800.
35. Kavan, L.; Yum, J.-H.; Nazeeruddin, M. K.; Grätzel, M. *ACS nano* **2011**, *5*, 9171-9178.
36. Kavan, L.; Yum, J.-H.; Grätzel, M. *Nano lett.* **2011**, *11*, 5501–5506.
37. Kavan, L.; Yum, J.-H.; Grätzel, M. *ACS Appl. Mater. Inter.* **2012**, *4*, 6999–7006.

Chapter 8

Influence of the Annealing Atmosphere on the Performance of ZnO Nanowires-Based Dye-Sensitized Solar Cells



8.1 Abstract

Annealing treatments are key to promote crystallinity and reduce the defect density in solution-processed nanomaterials. In particular, the annealing atmosphere strongly influences the functional properties of ZnO NWs and specifically their performance as electrodes in DSCs. We prepared vertically aligned ZnO NWs by a low-cost, high-yield and up-scalable hydrothermal method and studied the effect of the post-annealing atmosphere on their optoelectronic properties and their performance in DSCs. When annealing ZnO NWs under argon instead of air, significantly higher photoluminescence (PL) UV emission and relatively lower defects-related visible PL emission were obtained. At the same time, Ar-annealing rendered ZnO NWs with higher electrical

conductivities, as observed from their scanning probe microscopy characterization. These functional properties variations pointed towards a strong influence of the annealing atmosphere on the performance of ZnO NW-based DSC. Indeed, DSCs based on ZnO NWs annealed in argon were characterized by 50 % higher photocurrents than those fabricated from air-annealed ZnO. As a result 30 % efficiency increases were systematically obtained when using argon as the annealing atmosphere. These results are discussed within the framework of a multiple trapping model for transport and charge transfer, taking into account differences in the defect concentration introduced during the annealing.

8.2 Introduction

Vertically aligned ZnO NW arrays are fundamentally and technologically important materials with a large variety of applications, e.g. water splitting,¹⁻³ dye-sensitized solar cells,^{4,5} light-emitting diodes,^{6,7} piezoelectric energy harvesting.^{8,9} Driven by their high technological potential, numerous growth methods have been used for their production.¹⁰⁻¹³ Among them, solution-based processes such as electrodeposition and hydrothermal growth have the technological advantages of low-cost, high-yield and ease of up-scaling.^{14,15} However, solution-grown ZnO NWs are usually characterized by relatively poor crystallinities and high defect concentrations. Therefore, post-synthesis annealing treatments are generally required to optimize the NW performance in electronic, photonic or optoelectronic applications. The annealing treatment promotes the NW crystallization and removes the organic ligands used during the NW growth in solution. Furthermore, annealing treatments determine the final density of intrinsic point defects such as zinc vacancy (V_{Zn}), Zn interstitials (Zn_i), oxygen vacancies (V_O) and

oxygen interstitials (O_i), which play an important electronic role in the performance of the final device.^{16,17}

The atmosphere composition is a critical parameter of the annealing process.¹⁸⁻²¹ Solution-grown ZnO NWs used for optoelectronic applications are usually annealed in air.²²⁻²⁵ However, an argon atmosphere may allow improving the performance of ZnO NWs-based devices. Indeed, W. Mtangi et al. proved that annealing ZnO films in argon instead of oxygen more efficiently reduced the concentration of intrinsic defects.²⁰ Wu et al. experimentally demonstrated that argon annealing effectively removed the structural defects in Co-implanted ZnO NWs rendering them with ferromagnetic order.²¹ In spite of these and other promising results, the effect of the annealing atmosphere on the optoelectronic and photovoltaic performance of ZnO NWs has not been systematically studied yet.

In the present study, vertically aligned ZnO NWs prepared by a low-cost, high-yield and high-throughput hydrothermal process were used to determine the effect of post-annealing atmosphere on the performance of ZnO NWs-based devices. We characterized the PL spectra, the chemical composition and the electrical properties of the ZnO NWs annealed in different atmospheres and tested their performance as electrodes for DSCs. Results are discussed taking into account the potential defects introduced or removed during the annealing treatment within the context of a multiple trapping model.

8.3 Experimental section

8.3.1 Synthesis of ZnO NWs

ZnO NWs were produced by a low-cost, high-yield and high-throughput hydrothermal process as previously reported.¹⁵ First, we sputtered an 80 nm layer of intrinsic ZnO on a glass substrate coated with ITO. The seeded substrate was then placed inside a 100 ml glass flask containing an aqueous solution with 0.02 M $\text{Zn}(\text{NO}_3)_2$, 0.015 M hexamethylenetetramine (HMTA), 0.004 M polyethyleneimine (PEI) (end-capped, molecular weight 800 g/mol LS, Aldrich), and 0.024 M ammonium hydroxide. The covered glass container was kept during 3 hours inside a water bath at 88 °C. By this procedure, 6 μm long ZnO NWs were grown. Longer NWs can be produced by multiple growth steps, placing the substrate in a fresh $\text{Zn}(\text{NO}_3)_2$ solution every 3 h. ZnO NW arrays were afterwards rinsed with Milli-Q water and finally annealed in air or argon flow at 350 °C for 60 min.

8.3.2 DSCs fabrication

Dyes were loaded to the ZnO NWs surface by immersing the ZnO photoanodes (0.25 cm^2) into a room-temperature ethanol solution (0.2 mM) of LEG4 for 20 h. The Pt-coated counter electrode was prepared by drop casting a 5 mM H_2PtCl_6 ethanol solution onto an FTO-coated glass, and sintering it at 450 °C in air for 30 min. To complete the device, a 25 μm thick hot-melt film (Solaronix) was sandwiched between the ZnO NW-based photoanodes and the Pt counter electrode and a $[\text{Co}(\text{bpy})_3]^{2+/3+}$ redox couple electrolyte was injected between the two glass pieces through a hole drilled on the counter electrode. The $[\text{Co}(\text{bpy})_3]^{2+/3+}$ electrolyte was prepared by mixing 0.22 M

Co(bpy)₃(PF₆)₂, 0.05 M Co(bpy)₃(PF₆)₃, 0.1 M LiClO₄, and 0.2 M 4-tert-butylpyridine (TBP) in acetonitrile.

8.3.3 Characterization

Field emission SEM was used to characterize the morphology of the obtained materials and measure the density, length and width distributions of the ZnO NWs. Both cross-section and top-down micrographs were obtained using a FEI Nova Nanosem 230. XPS spectra were obtained using a SPECS SAGE ESCA system employing Mg K α (E = 1253.6 eV) with a supplied power of 203 W as the X-ray source. All spectra were shifted to account for sample charging using inorganic carbon at 284.80 eV as a reference. Room-temperature PL measurements were obtained using a Kimmon IK Series HeCd CW laser (325 nm and 40 mW). Light was dispersed through an Oriel Corner Stone 1/8 74000 monochromator, detected with a Hamamatsu R928 photomultiplier, and amplified through a Stanford Research Systems SR830 DSP Lock-in amplifier.

I-V characteristics of single ZnO NWs were measured by scanning probe microscopy (SPM) using a Park XE-100 Advanced Scanning Probe Microscope.

Current-voltage (*J-V*) characteristics of ZnO NW-based DSCs were measured using a Keithley 2400 source/meter and a Newport solar simulator (model 91160) with AM 1.5 G spectral distribution. The illumination power at the sample was adjusted to 1000 W m⁻² using a certified reference solar cell (Fraunhofer ISE). Two neutral density filters were used to reduce intensity to 500 and 100 W m⁻². A black mask with an aperture (0.5 × 0.5 cm²) was placed on top of the cell to avoid any significant contribution from outside of the active area.

IPCE spectra were recorded using a computer-controlled setup consisting of a xenon light source (Spectral Products ASBXE-175), a monochromator (Spectral Products CM110), and a potentiostat (EG&G PAR 273), calibrated using a certified reference solar cell (Fraunhofer ISE).

Electron lifetime and extracted charge measurements were performed using a white LED (Luxeon Star 1W) as the light source. Voltage and current traces were recorded with a 16-bit resolution digital acquisition board (National Instruments) in combination with a current amplifier (Stanford Research Systems SR570) and a custom-made system using electromagnetic switches. Lifetimes were determined by monitoring photocurrent and photovoltage transients at different light intensities upon applying a small square wave modulation to the base light intensity. Extracted charge measurements were performed by illuminating the cell for 5 s under open-circuit conditions and then turning the lamp off to let the voltage decay to a voltage V . The cell was then short circuited, and the current was measured under 5 s and integrated to obtain Q (V).

8.4 Results and Discussion

Figure 1 displays top-down and cross-sectional SEM micrographs of the ZnO NWs produced by hydrothermal growth. The ZnO NWs characterized in the present work were 6 μm long and 100 nm thick and NW arrays typically contained between 10 and 20 $\text{NW}/\mu\text{m}^2$. The NW length and diameter could be controlled by the synthesis time and the precursor concentration as we reported previously.¹⁵ ZnO NWs were subsequently annealed in a tubular furnace under air or argon flow at 350 °C for 60 min.

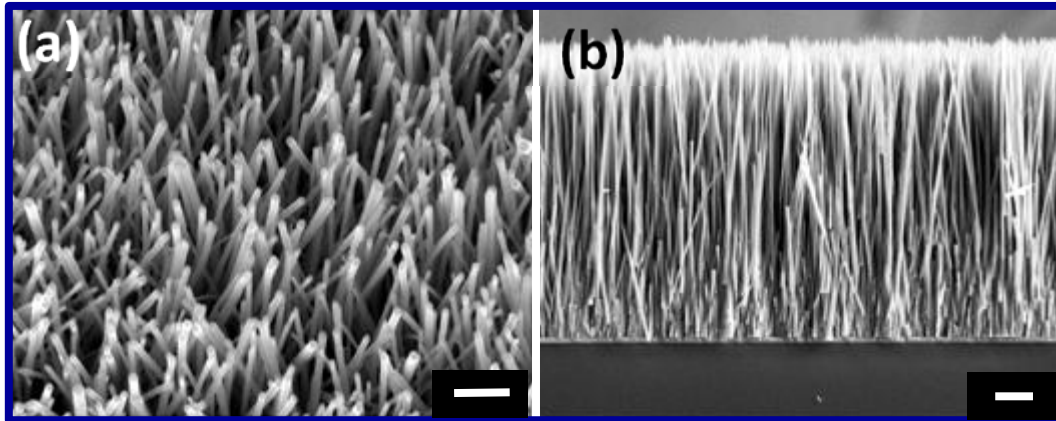


Figure 1. Top-down and cross-sectional SEM images of ZnO NWs with average length of 6 μm . Scale bars correspond to 1 μm .

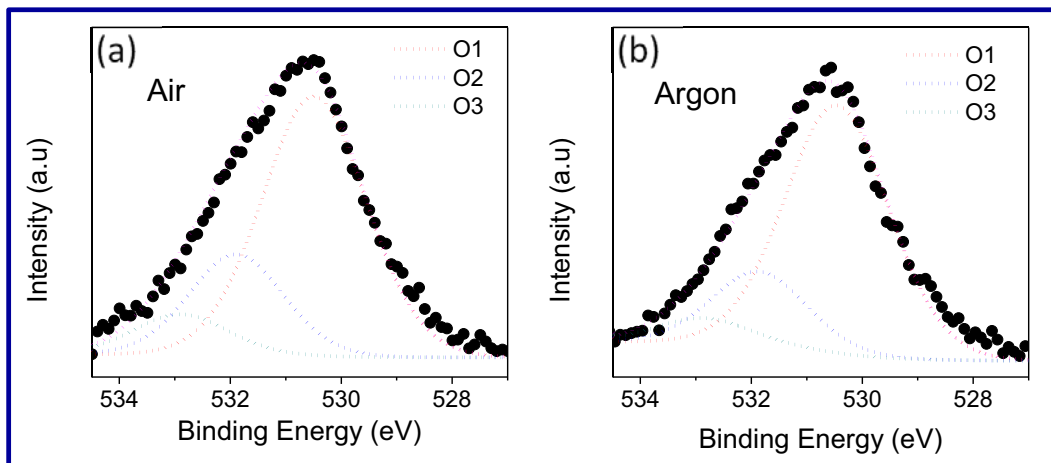


Figure 2. O1s region of the XPS spectra of the ZnO NWs annealed in (a) air and (b) argon.

Figure 2 shows the oxygen O1s region of the XPS spectra from the argon- or air-annealed ZnO NWs. The O1s band showed at least three contributions. The dominant one was located at 530.5 eV (O1) and was associated to O^{2-} ions within the ZnO wurtzite lattice.^{26,27} The band at 531.90 eV (O2) was associated to lattice O^{2-} ions located in a more electronegative chemical environments such as zinc oxyhydroxide,

ZnO(OH), zinc hydroxide, Zn(OH)₂, or in local chemical environments influenced by the proximity of oxygen vacancies.^{27,28} Finally, the band at 532.9 eV (O3) was associated with surface-adsorbed oxygen-containing species, e.g. CO₂, O₂⁻, O²⁻, O⁻, OH⁻ or H₂O.²⁷⁻²⁹ From the fitting of the O1s band, the relative atomic concentration of each oxygen species was calculated (Table 1). The ratio of lattice oxygen to zinc, (O1+O2)/Zn, was 0.95 for the sample annealed in argon and 1.03 for the one annealed in air. As expected, the Ar-annealed sample was slightly oxygen-deficient, while the ZnO NWs annealed in air were slightly oxygen rich. On the other hand, the concentration of adsorbed oxygen-containing species was slightly larger for the air-annealed sample than for the NWs annealed in argon: 5.4% and 3.6%, respectively.

Oxygen vacancies act as electron donors in ZnO, increasing its charge carrier concentration. On the other hand, adsorbed oxygen species act as electron acceptors, trapping free carriers and thus lowering the ZnO electrical conductivity.³⁰ Therefore, both the relatively higher concentration of oxygen vacancies and the lower concentration of adsorbed oxygen groups in argon-annealed ZnO NWs pointed towards a boost of their electrical conductivity.

Table 1. XPS binding energies (BE) and chemical composition of ZnO NWs annealed in air or argon.

Annealing Atmosphere		O1	O2	O3	Zn2p3/2	O1/Zn	O2/Zn
Air	BE (eV)	530.5	531.9	532.9	1022.0	0.88	0.15
	Percentage (%)	37.93	13.40	5.37	43.30		
Argon	BE (eV)	530.5	531.9	532.9	1022.0	0.84	0.11
	Percentage (%)	39.23	10.69	3.57	46.50		

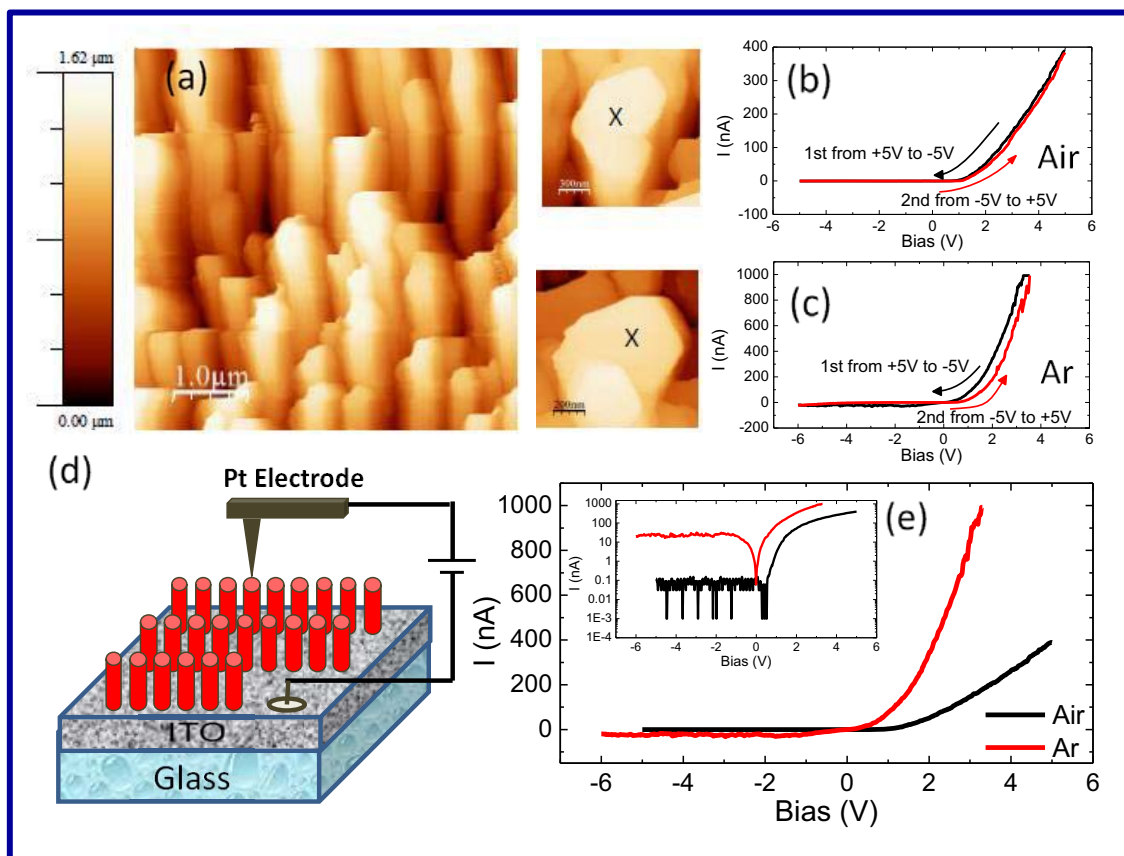


Figure 3. (a) SPM topographic image of ZnO NWs; (b)-(c) I - V characteristics the ZnO NWs annealed in air (b) and argon (c); (d) Cartoon of the experimental set-up showing the ZnO NWs deposited on ITO substrate and measured by conducting SPM using a Pt tip; (e) Direct comparison of the I - V curves taken on the samples annealed in air and in argon atmosphere.

The electrical transport properties of individual ZnO NWs annealed in different atmospheres were studied by means of conducting SPM using a Pt tip (Figure 3). Measurements were performed sweeping the potential from positive to negative values and then reversing the potential (Figure 3b, 3c). All I - V curves showed a clear asymmetric and rectifying behavior attributed to the Schottky contact between the Pt-coated tip and the ZnO NW. For both, ZnO NWs annealed in air or argon, the voltage at which current started to flow was in the range ~ 1 - 1.5 V. At negative tip voltages, very low currents were measured, especially from the NWs annealed in air. At positive tip

voltages, almost one order of magnitude higher currents were obtained for argon-annealed ZnO NWs. From the fitting of single NW I-V curves, over 4-fold lower electrical resistivities were calculated for argon-annealed ZnO NWs when compared to air-annealed samples: 3.6 Ωcm and 15.6 Ωcm , respectively (Table 2). This 4-fold increase of the electrical conductivity is attributed to the higher charge carrier concentrations associated to the larger oxygen vacancy density and lower concentration of surface charge trapping species in argon-annealed ZnO NWs.

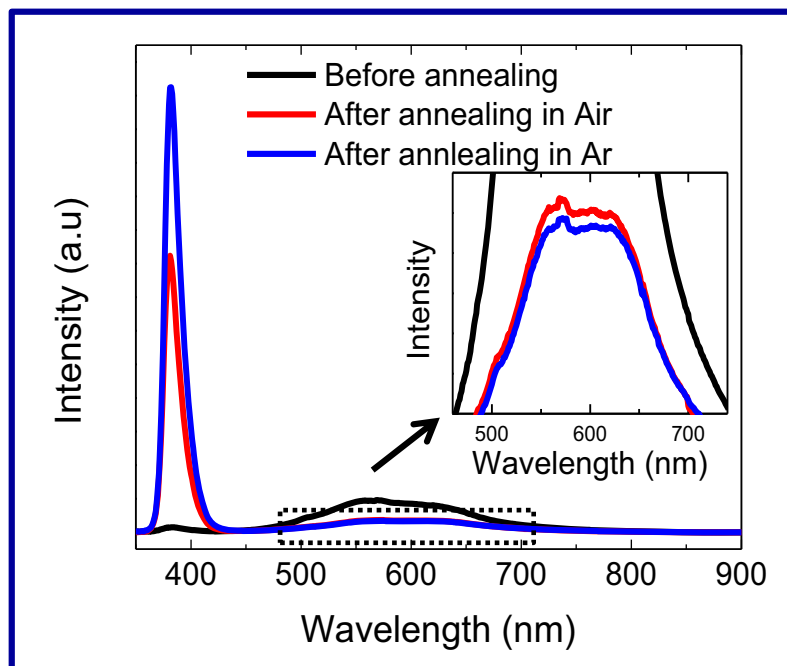


Figure 4. PL spectra of ZnO NWs before and after annealing in argon or air atmosphere as noted. Inset shows an enlargement of the visible region.

Figure 4 shows the PL spectra of ZnO NWs before and after annealing in air or argon. A significant increase of the band-to-band UV emission was observed after the annealing process. This is associated with a crystallinity enhancement and the related reduction of the density of defects involved in non-radiative recombinations. On the other hand, the annealing process resulted in a decrease of the visible PL emission intensity, which is related to the presence of defect-states within the ZnO bandgap. The

UV emission and the ratio of UV-to-visible emission of the annealed materials were larger for the argon-annealed NWs than for those annealed in air. A slight reduction of the visible emission was also observed when comparing the NWs annealed in argon with those annealed in air (Figure 4 inset), which is consistent with our previous report.³¹ Differences could be explained by the more efficient removal of oxygen-based non-radiative recombination centers at the ZnO NW surface, such as chemisorbed oxygen and other oxygen-containing species (e.g., OH⁻) during argon-annealing.^{32,33} Annealing in argon may also facilitate the removal of interstitial oxygen defects and surface species at the origin of the interband radiative recombinations resulting in the visible PL bands.^{34,35}

To study the effect of the annealing atmosphere on the performance of ZnO NWs-based DSCs, photovoltaic devices were fabricated using [Co(bpy)₃]^{2+/3+} as electrolyte, ZnO NWs annealed in air or argon as photocathodes and LEG4 as the dye. The exact details on the device fabrication can be found in our previous report.¹⁵ To rule out indirect effects related to differences in NW density, length or diameter, DSCs were fabricated in pairs from the exact same ZnO NW arrays. ZnO NWs were grown in 2x3 cm² ITO substrates. Each substrate was cut into two 2x1.5 cm² pieces and each piece was annealed in a different atmosphere: argon or air. These paired ZnO NW arrays, having the same density of identical NWs, were used for the fabrication of paired DSCs, one based on argon-annealed ZnO NWs (Ar-DSCs) and one based on air-annealed NWs (Air-DSCs). Figure 5a and 5b show the *J-V* characteristics and IPCE of the Ar-DSCs and Air-DSCs. Much higher, up to a 50 %, photocurrents were systematically measured from Ar-DSCs when compared with Air-DSCs. Slightly lower (2%) *V*_{ocs} and FF (12 %) were also obtained for Ar-DSCs. Still, an overall 30 % increase of conversion efficiency,

up to 1.62%, was finally calculated from Ar-DSCs when compared to Air-DSCs (Table 2).

Note that the relative porosity of the 6 μm -long and 100 nm-thick ZnO NW arrays used in the present study for the fabrication of DSCs was in between a 0.1 and a 0.01 %, which contrasts with values close to 50% in nanoparticle films. ZnO NW arrays had surface areas a 40-fold larger than the cross section area. This value is more than one order of magnitude lower than typical surface areas of nanoparticle-based films commonly used for DSCs. Such highly reduced surface areas translate into much lower dye concentrations, and therefore much lower photocurrents. This is the main parameter behind the relatively low overall efficiencies measured here from ZnO NW-based DSCs when compared with nanoparticle-based DSCs. Higher efficiencies require the use of longer NWs or hierarchical nanostructures. Still, notice that while keeping the structure as simple as possible, very large performances were obtained, since a 1.6 % energy conversion efficiency is a very high value for 6 μm -long ZnO NW-based DSCs. These very high performances are in part explained by the very large open circuit voltage values, above 900 mV, systematically obtained when using the $[\text{Co}(\text{bpy})_3]^{2+/3+}$ electrolyte. The 200 mV larger V_{oc} s compared with conventional Γ^-/I_3^- electrolytes are attributed to the better match of the $[\text{Co}(\text{bpy})_3]^{2+/3+}$ redox couple potential with the ZnO photoanode and the dye levels. The optimization of the energy level positions allowed minimizing energy losses in the dye regeneration step, as we previously discussed.¹⁵

The slight V_{oc} decrease between Ar-DSCs and Air-DSCs could be related to a slightly higher Fermi level in dark of the former (Figure 6). This Fermi level shift of the argon-annealed ZnO electrode is associated with the larger concentration of charge carriers introduced by oxygen vacancies and is consistent with the higher electrical conductivities in dark obtained from single NW in SPM measurements.

Table 2. Electronic and photovoltaic parameters of the DSCs based on ZnO NWs annealed in air or argon.

Atmosphere	Light intensity (W/m ²)	V_{oc} (mV)	J_{sc} (mA/cm ²)	FF (%)	Eff (%)	R (Ω cm)	g_o (C/cm ²)	m_c (meV)
Argon	1000	910	4.1	44.1	1.62	3.6	5.3×10^{-6}	410
Air	1000	930	2.7	49.8	1.26	15.6	3.4×10^{-6}	401

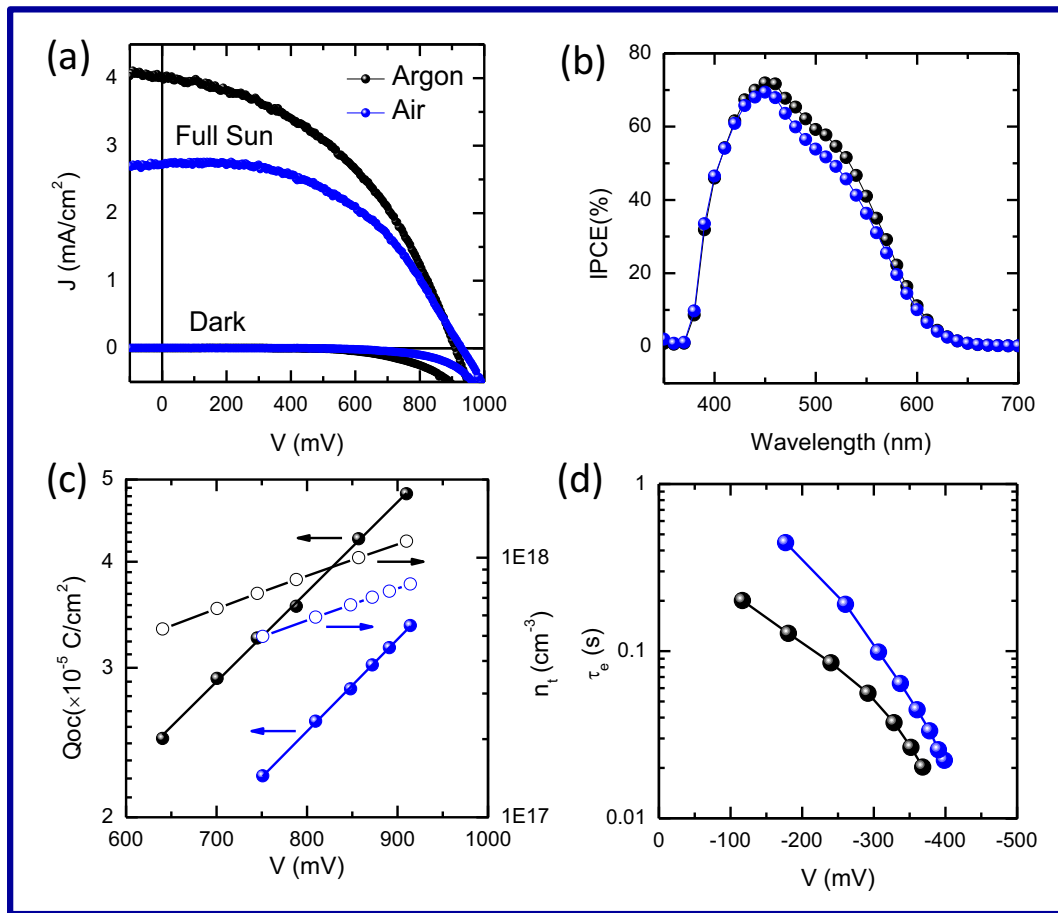


Figure 5. Comparison of DSCs based on ZnO NW annealed in air or argon: (a) J - V characteristic under AM1.5G illumination; (b) Spectra of incident photon to current efficiency (IPCE); (c) charge extraction and trapped electron density as a function of voltage under open circuit conditions; (d) electron lifetime as a function of the quasi-Fermi level of the ZnO NW under open circuit conditions.

It is widely accepted that electron transport in nanostructured materials is in large part controlled by trapping and detrapping of electrons in inter-bandgap states.³⁶ Furthermore it is generally considered that this distribution of bandgap states exponentially decays within the band-gap.³⁷⁻⁴¹ While more controversy exists on the origin of this exponential conduction band tail, it is normally considered that transport limiting traps in oxide materials are located predominately at the particle surface^{41,42} To determine the trap distribution in ZnO NWs annealed in air or argon, charge extraction experiments were performed in Ar- and Air-DSCs (Figure 5c). This measurement relates V_{oc} and the charge accumulated in the nanostructure under open-circuit conditions, Q_{oc} . Charge extraction measurements were carried out by illuminating the cell for 5 s under open-circuit conditions and then turning off the lamp to let the voltage decay to a voltage V . The cell was then short circuited, and the current was integrated during 5 s to obtain $Q_{oc}(V)$. Figure 5c shows the charge extraction as a function of V for both argon and air-annealed ZnO NWs. The amount of extracted charge at a given voltage was between a 1.1- and a 1.4-fold larger for Ar-DSCs than for Air-DSCs. This result points towards a higher density of shallow traps in the Ar-annealed ZnO NWs, which may be in part associated to oxygen vacancies.

Figure 6 shows a schematic representation of the trap distribution inside ZnO NWs annealed in argon and air, respectively. Traps below the redox potential are always filled. Under illumination, charge carriers are photogenerated and the quasi-Fermi level is shifted to higher energies, filling traps below it.

The exponential dependence of the charge versus open circuit voltage measured from ZnO NW-based DSCs (Figure 5c) is consistent with a multiple trapping model for transport and charge transfer including an exponential distribution of trap states $g(E)$ below the conduction band edge.^{36,38-40,43-49}

$$g(E) = g_0 \exp \left[\frac{E - E_{F0}}{m_c} \right] \quad (1)$$

where g_0 is the trap density at the equilibrium-Fermi level of the ZnO electrode in darkness, and m_c is the slope of the exponential trap distribution. The values of g_0 and m_c obtained at each voltage by fitting the data in Figure 5c with equation 1 are shown in Table 2.

We further considered that the extracted charge is proportional to the density of trapped electrons, n_t , given by:⁴⁶

$$n_t = \int_{E_{F0}}^{E_{Fn}} g(E) dE = m_c g_0 \left[\exp \left[\frac{E_{Fn} - E_{F0}}{m_c} \right] - 1 \right] \quad (2)$$

where E_{Fn} is the quasi-Fermi level (QFL) under illumination. From the geometrical parameters of the ZnO NW array, trapped electron densities of 10^{17} to 10^{18} cm^{-3} were calculated for both Ar-DSCs and Air-DSCs. Notice that the geometrical parameters for both Ar- and Air-DSCs are exactly the same as both argon-annealed and air-annealed ZnO NWs were cut from the same NW array (Figure 5c). Thus the higher charge measured in Ar-DSCs directly translates into a higher concentration of charge carriers trapped at each voltage for the argon-annealed material. From another point of view, at the same total electron concentration, the QFL created under illumination in Ar-DSCs was at a lower energy valued than in Air-DSCs. At the same charge value, the voltage of Ar-DSCs was about 130 mV lower than Air-DSCs. Nevertheless, the V_{ocs} measured in Ar-DSCs were just 20 mV lower than those obtained in Air-DSCs. The larger charge carrier concentration in Ar-DSCs seems at first view inconsistent with the very similar V_{oc} values obtained for both Ar- and Air-DSCs. One would expect a 110-130 mV decrease of the V_{oc} in Ar-DSCs due to the larger density of shallow traps, as this larger density would prevent the QFL from reaching as high energies as in Air-DSCs.

However, it should be taken into account that in open circuit conditions, the charge density and the QFL strongly depend on the recombination kinetics.

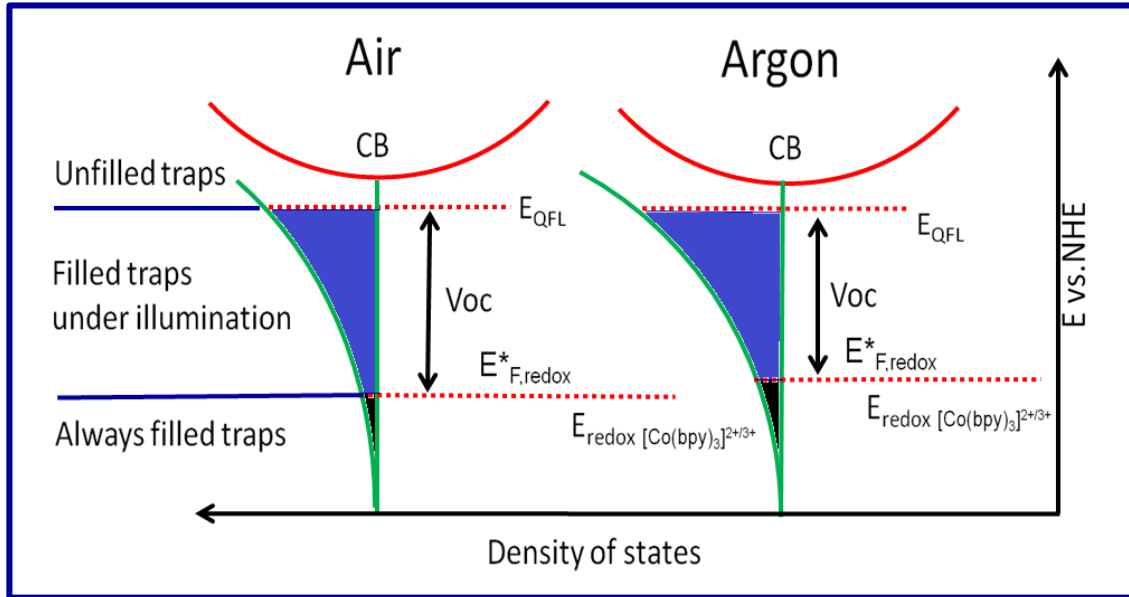


Figure 6. Schematic representation of the multi trapping mechanism with an exponential trap distribution inside ZnO NWs annealed in argon and air.

Electron lifetimes (τ_e) were calculated from voltage decay transients using the following equation:⁵⁰

$$\tau_e = -\frac{k_B T}{e} \left(\frac{dV_{oc}}{dt} \right)^{-1} \quad (3)$$

where k_B stands for the Boltzmann constant, T for temperature and e is the electron charge. The measured electron lifetime is plotted as a function of the ZnO QFL under open circuit conditions in Figure 5d. Decay times are controlled by the electrons trapped in inter-bandgap states, which contribute to maintain a photovoltage by releasing electrons into the conduction band. Thus decay time not only depends on the recombination rate of conduction electrons but also on the density of trapped electrons that buffer the voltage decay.

In spite of the larger density of trapped charge in Ar-DSCs, slightly longer recombination times were obtained from Air-DSCs (Figure 5d). These longer electron lifetimes obtained for the air-annealed ZnO NWs clearly points towards a decrease of the recombination rate constant for the reaction of electrons with the $[\text{Co}(\text{bpy})_3]^{3+}$ in this material. These longer recombination rate constants may be originated by the negatively charge surface of the air-annealed ZnO NWs. The air-annealed ZnO NWs conserve a higher density of chemically absorbed species, which are negatively-charged. These negatively-charged surface species may influence recombination by different means. Negatively charged species introduce a higher surface band bending which could slow down the recombination of electrons from the conduction band to the electrolyte. Notice that unlike nanoparticles, 100 nm ZnO NWs are capable of standing a surface band bending without being totally depleted of charge. The higher surface band bending in air-annealed materials could also slow down the injection of charge from the dye to the ZnO conduction band, which could explain part of the lower photocurrent intensities obtained in Air-DSCs.

Another explanation to the slower recombination in Air-DSCs compared to Ar-DSCs could be a physical blocking of the surface or specific recombination sites on the surface due to the presence of chemically absorbed molecules. This physical blocking by chemisorbed molecules could also reduce the dye loading. However, such decrease of the dye loading was not observed when comparing UV-vis measurements from air-annealed and argon-annealed ZnO NWs loaded with dye.

8.5 Conclusions

In conclusion, the effect of the annealing atmosphere on the performance of solution-grown ZnO NWs-based DSCs was studied. *I-V* characteristics of single NW demonstrated argon-annealed ZnO NWs to have higher electrical conductivities than air-annealed NWs. The enhanced conductivity was associated with the lower concentration of negatively-charged surface species and with the higher concentration of oxygen vacancies acting as electron donors formed during argon-annealing. This was supported by XPS and PL measurements. DSCs based on argon-annealed ZnO NWs were characterized by larger trap densities but lower recombination times than air-DSCs, which allowed them to show up to 50% higher short circuit intensities while keeping similarly high Voc's. An overall 30 % increase of conversion efficiency, up to 1.63%, was obtained when annealing the ZnO NWs in argon instead of air.

8.6 References

1. Li, Y.; Zhang, J. Z. *Laser Photonics Rev.* **2010**, *4*, 517-528.
2. Fan, J. D.; Guell, F.; Fabrega, C.; Shavel, A.; Carrete, A.; Andreu, T.; Morante, J. R.; Cabot, A. *Appl. Phys. Lett.* **2011**, *99*, 262102.
3. Fan, J. D.; Fábrega, C.; Zamani, R.; Shavel, A.; Güell, F.; Carrete, A.; Andreu, T.; López, A. M.; Morante, J. R.; Arbiol, J.; Cabot, A. *J. Alloy. Compd.* **2013**, *555*, 213–218.
4. Xu, C. K.; Wu, J. M.; Desai, U. V.; Gao, D. *J. Am. Chem. Soc.* **2011**, *133*, 8122–8125.
5. Law, M.; Greene, L.E.; Radenovic, A.; Kuykendall, T.; Liphardt, J.; Yang, P. D. *J. Phys. Chem. B* **2006**, *110*, 22652–22663.
6. Könenkamp, R.; Word, R. C.; Godinez, M. *Nano Lett.* **2005**, *5*, 2005-2008.
7. Yang, Q.; Liu, Y.; Pan, C. F.; Chen, J.; Wen, X. N.; Wang, Z. L. *Nano Lett.* **2013**, *13*, 607–613.

8. Qin, Y.; Wang, X.; Wang, Z. L. *Nature* **2008**, *451*, 809-813.
9. Wang, Z. L.; Song, J. H. *Science* **2005**, *312*, 242-246.
10. Park, W. I.; Yi, G.-C.; Kim, M.; Pennycook, S. J. *Adv. Mater.* **2002**, *14*, 1841-1843.
11. Djurišić, A. B.; Chen, X. Y.; Leung, Y. H.; Ng, A. M. C. *J. Mater. Chem.* **2012**, *22*, 6526-6535.
12. Wang, Z. L.; Kong, X. Y.; Zuo, J. M. *Phys. Rev. Lett.* **2003**, *91*, 185502.
13. Vayssieres, L. *Adv. Mater.* **2003**, *15*, 464-466.
14. Fan, J. D.; Shavel, A.; Zamani, R.; Fábrega, C.; Rousset, J.; Haller, S.; Güell, F.; Carrete, A.; Andreu, T.; Arbiol, J.; Morante, J. R.; Cabot, A. *Acta Mater.* **2011**, *59*, 6790-6800.
15. Fan, J. D.; Hao, Y.; Cabot, A.; Johansson, E. M. J.; Boschloo, G.; Hagfeldt, A. *ACS Appl. Mater. Interfaces* **2013**, *5*, 1902-1906.
16. Djurišić, A. B.; Leung, Y. H. *small* **2006**, *2*, 944 - 961.
17. Djurišić, A. B.; Ng, A. M. C.; Chen, X. Y. *Prog. Quantum Electron.* **2010**, *34*, 191-259.
18. Lin, B. X.; Fu, Z. X.; Jia, Y. B. *Appl. Phys. Lett.* **2001**, *79*, 943-945.
19. Shinobu, F.; Yusuke, O.; Asayo, K. *Chem. Mater.* **2004**, *16*, 2965-2968.
20. Mtangi, W.; Auret, F. D.; Meyer, W. E.; Legodi, M. J.; Janse van Rensburg, P. J.; Coelho, S. M. M.; Diale, M.; Nel, J. M. *J. Appl. Phys.* **2012**, *111*, 094504.
21. Wu, Z. Y.; Chen, F. R.; Kai, J. J.; Jian, W. B.; Lin, J. J. *Nanotechnology* **2006**, *17*, 5511-5518.
22. Xu, C. K.; Wu, J. M.; Desai, U. V.; Gao, D. *J. Am. Chem. Soc.* **2011**, *133*, 8122-8125,
23. Law, M.; Greene, L. E.; Johnson, J. C.; Saykally, R.; Yang, P. Law, M.; Greene, L. E.; Johnson, J. C.; Saykally, R.; Yang, P. *Nat. Mater.* **2005**, *4*, 455- 459.
24. Xu, C. K.; Wu, J. M.; Desai, U. V.; Gao, D. *Nano Lett.* **2012**, *12*, 2420-2424.
25. Fan, J. D.; Zamani, R.; Fábrega, C.; Shavel, A.; Flox, C.; Ibáñez, M.; Andreu, T.; López, A. M.; Arbiol, J.; Morante, J. R.; Cabot, A. *J. Phys. D: Appl. Phys.* **2012**, *45*, 415301.
26. Ramgir, N. S.; Late, D. J.; Bhise, A. B.; More, M. A.; Mulla, I. S.; Joag, D. S.; Vijayamohan, K. *J. Phys. Chem. B* **2006**, *110*, 18236-18242.
27. Coppa, B. J.; Davis, R. F.; Nemanich, R. J. *Appl. Phys. Lett.* **2003**, *82*, 400.

28. Rosa, E. D. L.; Sepúlveda-Guzman, S.; Reeja-Jayan, B.; Torres, A.; Salas, P.; Elizondo, N.; Yacaman, M. J. *J. Phys. Chem. C* **2007**, *111*, 8489-8495.
29. Cabot, A.; Arbiol, J.; Rossinyol, E.; Morante, J. R.; Chen, F.; Liu, M. *Electrochem. Solid ST.* **2004**, *7*, 93-97.
30. Lagowski, L.; Sproles, E. S.; Gatos, H. C. *J. Appl. Phys.* **1977**, *48*, 3566.
31. Fan, J. D.; Güell, F.; Fábrega, C.; Fairbrother, A.; Andreu, T.; López, A. M.; Morante, J. R.; Cabot, A. *J. Phys. Chem. C* **2012**, *116*, 19496–19502.
32. Kang, H. S.; Kang, J. S.; Kim, J. W.; Lee, S. Y. *J. Appl. Phys.* **2004**, *95*, 1246-1250.
33. Sun, Y.; George Ndifor-Angwafor, N.; Jason Riley, D.; Ashfold Michael, N. R. *Chem. Phys. Lett.* **2006**, *431*, 352–357.
34. Kwok, W. M.; Djurišić, A. B.; Leung, Y. H.; Li, D.; Tam, K. H.; Phillips, D. L.; Chan, W. K. *Appl. Phys. Lett.* **2006**, *89*, 183112.
35. Studenikin, S. A.; Golego, N.; Cocivera, M. *J. Appl. Phys.* **1998**, *84*, 2287-2294.
36. de Jongh, P. E.; Vanmaekelbergh, D. *Phys. Rev. Lett.* **1996**, *77*, 3427-3430.
37. Nelson, J. *Phys. Rev. B* **1999**, *59*, 15374-15380.
38. Schlichthörl, G.; Huang, S. Y.; Sprague, J.; Frank, A. J. *J. Phys. Chem. B* **1997**, *101*, 8141-8155.
39. Fisher, A. C.; Peter, L. M.; Ponomarev, E. A.; Walker, A. B.; Wijayantha, K. G. U. *J. Phys. Chem. B* **2000**, *104*, 949-958.
40. Kambili, A.; Walker, A. B.; Qiu, F. L.; Fisher, A. C.; Savin, A. D.; Peter, L. M. *Physica E* **2002**, *14*, 203-209.
41. Cabot, A.; Arbiol, J.; Ferré, R.; Morante J. R.; Chen, F.; Liu, M. *J. Appl. Phys.* **2004**, *95*, 2178-2180.
42. Kopidakis, N.; Neale, N. R.; Zhu, K.; van de Lagemaat, J.; Frank, A. J. *Appl. Phys. Lett.* **2005**, *87*, 202106.
43. Bisquert, J.; Vikhrenko, V. S. *J. Phys. Chem. B* **2004**, *108*, 2313-2322.
44. Van de Lagemaat, J.; Frank, A. J. *J. Phys. Chem. B* **2000**, *104*, 4292-4294.
45. Bisquert, J.; Zaban, A. *Appl. Phys. A* **2003**, *77*, 507-514.
46. Mohammadpour, R.; Iraj Zad, A.; Hagfeldt, A.; Boschloo, G. *ChemPhysChem* **2010**, *11*, 2140– 2145.
47. Boschloo, G.; Halggman, L.; Hagfeldt, A. *J. Phys. Chem. B* **2006**, *110*, 13144-13150.

48. Peter, L.; Duffy, N.; Wang, R.; Wijayantha, K. *J. Electroanal. Chem.* **2002**, *524*, 127-136.
49. Fabregat-Santiago, F.; Mora-Sero, I.; Garcia-Belmonte, G.; Bisquert, J. *J. Phys. Chem. B* **2003**, *107*, 758-768.
50. Zaban, A.; Greenshtein, M.; Bisquert, J. *ChemPhysChem* **2003**, *4*, 859–864.

Conclusions

This dissertation has focused on three main topics: (i) Synthesis and characterization of ZnO:Cl NWs; (ii) Hetero and homo nanostructures based on ZnO:Cl NWs for efficient PEC cells; (iii) Photovoltaic performance of DSCs based on ZnO NWs.

The work developed has allowed reaching the following conclusions:

- (1) Vertically aligned single-crystal and chlorine-doped ZnO NWs can be grown by a low-cost, high-yield and seed-free electrochemical route with controlled morphology, structural and optoelectronic properties. The carrier concentration of such ZnO:Cl NWs could be tuned in the range between 5×10^{17} and $4 \times 10^{20} \text{ cm}^{-3}$ by varying the Cl doping concentration. Besides, intrinsic ZnO NWs with various lengths of 6-12 μm and diameters of 40-120 nm can also be obtained by hydrothermal deposition for the application in DSCs.
- (2) Vertically aligned core@shell ZnO:Cl@ZnO homostructures and ZnO:Cl@ZnS and ZnO:Cl@TiO₂ heterostructures NWs can be obtained by electrodeposition and/or SILAR two-step process. The PEC properties of these NWs can be highly enhanced up to a factor 5 with the presence of these shell layers. The enhancement factor depends on the shell thickness. These performances are associated with the improvement of the photogenerated charge carrier separation and surface to neutral inner part transfer capability achieved when increasing the space charge area within the NWs with a built-in electric field introduced by the doping profile.
- (3) We have employed $[\text{Co}(\text{bpy})_3]^{2+/3+}$ redox couple as electrolyte in ZnO NWs-based DSCs. A direct comparison of the performance of $[\text{Co}(\text{bpy})_3]^{2+/3+}$ and Γ^-/I_3^- redox couples demonstrated the higher suitability of the cobalt complex, both in terms of

a significantly improved V_{oc} (~200 mV) and a increased photocurrent (~10%). The post-annealing of the NWs in argon allowed further improving the power conversion efficiency with a value of 30% compared to air. The improved efficiency was dominated by significantly higher photocurrents (~50%) measured from Ar-DSCs when compared with Air-DSCs.

Future work

I have studied the synthesis and properties of ZnO NWs as well as the applications in PEC cells and DSCs. The design and fabrication of novel device based on vertically aligned ZnO NWs just started, it still requires a lot of work in future study.

- (1) While hydrothermal deposition is an effective way to grow ultra-long ZnO NWs, the quantified results demonstrated that there is almost no chlorine doping when we tried to introduce chlorine inside ZnO nanostructures with an aim to improve the charge carrier concentration. It would effectively boost the efficiency of ZnO-NWs based device if the anion and/or cation can be really introduced into ZnO crystal structure.
- (2) It should be noted that PEC performance depends strongly on the band gap and band edge positions of the photoanodes, and the large band gap of metal oxides significantly limits the light harvesting in the visible region of the solar spectrum. More sophisticated nanostructures need to be developed including heterogeneous nanostructures and quantum-dots sensitized nanostructures, which offer the possibility to manipulate the band structure and thereby to enhance visible-light absorption and PEC performance.
- (3) It is experimentally proved that the cobalt complex is an alternative and efficient electrolyte in ZnO NWs-based DSCs. However, the efficiency is still quite low. A lot of effort is still needed to further improve the fill factor and photocurrent density: (i) Use longer ZnO NWs and high surface area hierarchical nanostructures to increase dye uptake and enhance photocurrent; (ii) Coat a TiO₂ shell to improve V_{OC} and fill factor by lowering the rate of electron-hole recombination across the oxide-electrolyte interface; (iii) Reduce recombination at

ZnO surface defects and facilitate dye charge transfer by means of a more severe annealing process and the use of ZnO-based core-shell NW structures; (iv) Use high surface area-cathode material to reduce charge transfer resistance at the Pt counter electrode and improve fill factor.

- (4) One dimensional ZnO NWs-based all-solid-state solar cell is a promising construction since the possibility of being fabricated by low-cost and easy-scalable solution processing techniques. We are now trying to fabricate the vertically aligned ZnO NWs-based inorganic/hybrid all-solid-state solar cell.

Abbreviations

DSCs	Dye-sensitized solar cells
e	Electron charge
E_{cb}	Conduction band potential
E_{fb}	Flat band potential
$E_{F,n}$	Electron Fermi energy
$E_{F,redox}$	Reduction-oxidation energy
EIS	Electrochemical impedance spectroscopy
FF	Fill factor
FTO	Fluorine doped tin dioxide
HRTEM	High-resolution transmission electron microscopy
IPCE	Incident photon to current conversion efficiency
ITO	Indium doped tin oxide
I^-/I_3^-	Iodide/tri-iodide
J_{sc}	Short circuit current density
n	Electron concentration
NWs	Nanowires
PEC	Photoelectrochemical
PL	Photoluminescence
QFL	Quasi-Fermi level
R_s	Serial resistance
SEM	Scanning electron microscopy
SILAR	successive ionic layer adsorption and reaction

SPM	Scanning Probe Microscope
TEM	Transmission Electron Microscopy
UV-vis	Ultra violet-visible light
V_{oc}	Open circuit voltaje
XPS	X-ray photoelectron spectroscopy
XRD	X-ray diffraction
η	Energy conversion efficiency
λ	Wavelength
τ_n	Electron lifetime

Curriculum Vitae

Personal Data

Name: Jiandong Fan
Birthday: 4th August, 1979
Nationality: Chinese
Address: Catalonia Institute for Energy Research(IREC), Jardí de les Dones de Negre 1, 08930, Sant Adrià del Besós, Barcelona, Spain.
Mobile phone: +34 698 441 980
Email: jdfanya@gmail.com

Education

Ph.D. 12/2009-07/2013	Physics	University of Barcelona	Spain
M. S. 09/2003-07/2006	Material Science	Shandong University	China
B. S. 09/1999-07/2003	Material Science	Jinan University	China

Fellowships/Grants/Awards

05/2013	Chinese Government Award for Outstanding Self-financed Students Abroad	6000 \$	Chinese Government
05/2011	Best Graduate Student Award	450 €	European Material Research Society
02/2010-02/2013	Pre-doctorate scholarships (FI-DGR)	64800€	Catalan Government
06/2012-12/2012	Fellowship for study aboard (BE-DGR)	6657 €	Catalan Government

Academic Research Experience

06/2012- 12/2012	Fabrication and Characterization of Liquid and Solid-state Dye-Sensitized Solar Cells	Visiting PhD student	Uppsala University Sweden Prof. Anders Hagfeldt
01/2011- 01/2011	Mott-Schottky measurements	Visiting PhD student	Institute for Research and Development of Photovoltaic Energy Paris, France
03/2010- 03/2010	Characterization of X-ray Photoelectron Spectroscopy(XPS)	Training	University of Barcelona Spain
11/2007- 12/2007	Characterization of X-ray Photoelectron Spectroscopy(XPS)	Training	ThermoFisher SCIENTIFIC Company London, U.K
09/2006- 12/2009	Crystallography	Researcher	Shandong University China

Research Interest

- Synthesis and characterization of metal oxide NWs (ZnO NWs, TiO₂ NWs, SnO₂ NWs etc) by various techniques.
- Photoelectrochemical cell for water splitting based on 3D metal oxide NWs.
- Synthesis inorganic nanostructures and application of nanostructures in organic-inorganic hybrid solar cells, e.g. Perovskite and ternary/quaternary nanomaterials-based solar cell.
- Liquid- and Solid-state Dye-Sensitized Solar Cells based on 3D metal oxide NWs;
- Characterication and physical mechanism of solar cell.

Publications

1. Maria Ibáñez, Reza Zamani, Stephane Gorsse, **Jiandong Fan**, Silvia Ortega, Doris Cadavid, Joan Ramon Morante, Jordi Arbiol, and Andreu Cabot. “Core-shell Nanoparticles as Building Blocks for the Bottom-Up Production of Functional Nanocomposites: PbTe-PbS Thermoelectric Properties.” *ACS Nano*. 2013, 7, 2573-2586.
2. **Jiandong Fan**, Yan Hao, Andreu Cabot, Erik M. J. Johansson, Gerrit Boschloo and Anders Hagfeldt. “Cobalt (II/III) Redox Electrolyte in ZnO Nanowire-Based Dye-Sensitized Solar Cells.” *ACS Appl. Mater. & Interfaces*. 2013, 5, 1902–1906.

3. **Jiandong Fan**, Cristian Fábrega, Reza Zamani, Alexey Shavel, Frank Güell, Alex Carrete, Teresa Andreu, Antonio M. López, Joan Ramón Morante, Jordi Arbiol, and Andreu Cabot, “Solution-Growth and Optoelectronic Properties of ZnO:Cl@ZnS Core-Shell Nanowires with Tunable Shell Thickness.” *J. Alloy. Compd.* 2013, 555, 213–218.
4. **Jiandong Fan**, Frank Güell, Cristian Fábrega, Andrew Fairbrother, Teresa Andreu, Antonio M. López, Joan Ramón Morante, and Andreu Cabot, “Visible Photoluminescence Components of Solution-Grown ZnO Nanowires: Influence of the Surface Depletion Layer.” *J. Phys. Chem. C.* 2012, 116, 19496–19502.
5. **Jiandong Fan**, Reza Zamani, Cristian Fábrega, Alexey Shavel, Cristina Flox, Maria Ibáñez, Teresa Andreu, Antonio M. López, Jordi Arbiol, Joan Ramón Morante and Andreu Cabot. “Solution-Growth and Optoelectronic Performance of ZnO:Cl/TiO₂ and ZnO:Cl/Zn_xTiO_y/TiO₂ Core-Shell Nanowires with Tunable Shell Thickness.” *J. Phys. D: Appl. Phys.* 2012, 45, 415301.
6. **Jiandong Fan**, Frank Güell, Cristian Fábrega, Alexey Shavel, Alex Carrete, Teresa Andreu, Joan Ramón Morante, and Andreu Cabot, “Enhancement of the photoelectrochemical properties of ZnO nanowires by tuning their coaxial doping profile.” *Appl. Phys. Lett.* 2011, 99, 262102.
7. **Jiandong Fan**, Alexey Shavel, R. Zamani, Cristian Fabrega, Jean Rousset, Servane Haller, Frank Güell, Alex Carrete, Teresa Andreu, Jordi Arbiol, Joan Ramon Morante, Andreu Cabot. “Control of the Doping Concentration, Morphology and Optoelectronic properties of vertically aligned chlorine-doped ZnO nanowires.” *Acta Materialia* 2011, 59, 6790-6800.
8. Maria Ibáñez, **Jiandong Fan**, Wenhua Li, Doris Cadavid, Raquel Nàfria and Andreu Cabot. “Means and Limits of Control of the Shell Parameters in Hollow Cadmium Chalcogenides obtained by the Kirkendall Effect.” *Chem. Mater.* 2011, 23, 3095–3104.
9. Li, Wenhua; Shavel, Alexey; Guzman, Roger; Rubio, Javier; Flox, Cristina; **Jiandong Fan**; Cadavid, Doris; Ibáñez, Maria; Arbiol, Jordi; Morante, Joan; Cabot, Andreu. “Morphology Evolution of Cu_{2-x}S Nanoparticles: From Spheres to Dodecahedrons.” *Chem. Commun.* 2011, 47, 10332–10334.
10. Jing Li, Guogang Xu, Shujuan Han, **Jiandong Fan**, Jiyang Wang, “Growth and optical properties of self-frequency-doubling laser crystal Yb:LuAl₃(BO₃)₄.” *J. Cryst. Growth* 2009, 11, 4251–4254.
11. H. J. Cong, H. J. Zhang, J. Y. Wang, W. T. Yu, **Jiandong Fan**, X. F. Cheng, S. Q. Sun, J. Zhang, Q. M. Lu, C. J. Jiang, and R. I. Boughton, “Structural and thermal properties of the monoclinic Lu₂SiO₅ single crystal: evaluation as a new laser matrix.” *J. Appl. Cryst.* 2009, 42(2), 284–294.

12. Jiandong Fan, Huaijin Zhang, Wentao Yu, Haohai Yu, Jiyang Wang and Minhua Jiang, “A Yb³⁺-doped NaY(WO₄)₂ crystal grown by the Czochralski technique”, *J. Appl. Cryst.* 2008, 41, 584-591.
13. Xiaojing Liu, Zeyan Wang, Guanghui Zhang, Guangwei Yu, Xinqiang Wang, Aidong Duan, Jiandong Fan, and Dong Xu, “Atomic Force Microscopy Studies on {101} Surfaces of L-arginine Trifluoroacetate Single Crystals.” *J. Phys. Chem. C* 2007, 111, 14165-14169.
14. Huaijin Zhang, Junhai Liu, Jiyang Wang, Jiandong Fan, Xutang Tao, Xavier Mateos, Valentin Petrov, and Minhua Jiang, “Spectroscopic properties and continuous-wave laser operation of a new disordered crystal:Yb-doped CNGG.” *Optics Express* 2007, 15, 9464-9469.
15. Jiandong Fan, H. J. Zhang, J. Y. Wang, M. H. Jiang, R. I. Boughton, D. G. Ran, S. Q. Sun, H. R. Xia, “Growth and thermal properties of SrWO₄ single crystal.” *J. Appl. Phys.* 2006, 100, 063513.
16. Jiandong Fan, Huaijin Zhang, Jiyang Wang, Zongcheng Ling, Hairui Xia, Xiufang Chen, Yonggui Yu, Qingming Lu, Minhua Jiang, “Growth, structure and thermal properties of Yb³⁺-doped NaGd(WO₄)₂ crystal”, *J. Phys. D: Appl. Phys.* 2006, 39, 1034–1041.
17. Z.C. Ling, H.R. Xia, D.G. Ran, F.Q. Liu, S.Q. Sun, Jiandong Fan, H.J. Zhang, J.Y. Wang, L.L. Yu. “Lattice vibration spectra and thermal properties of SrWO₄ single crystal.” *Chem. Phys. Lett.* 2006, 426, 85–90.

Conferences

1. Jiandong Fan, Yan Hao, Andreu Cabot, Erik M. J. Johansson, Gerrit Boschloo, and Anders Hagfeldt.. “Cobalt (II/III) Redox Electrolyte in ZnO Nanowires Dye-Sensitized Solar Cells”. EMRS spring conference, May 27-31, 2013, Strasbourg, France. **(Poster)**
2. Jiandong Fan, Frank Güell, Cristian Fábrega, Àlex Carreté, Alexey Shavel, Teresa Andreu, Joan Ramon Morante, Andreu Cabot. “Tuning the band-bending in core-shell nanowires to optimize the charge carrier transfer in photoelectrochemical water splitting”. 2011 MRS Fall Meeting. Nov.28.2011-Dec. 2.2011, Boston, United states. **(Oral presentation)**
3. Jiandong Fan, Wenhua Li, Alexey Shavel, Christian Fabregas, Teresa Andreu, Frank Güell, Joan Ramon Morante and Andreu Cabot. “Controlled synthesis and tunable optical and photoelectrochemical properties from ZnO nanorods to ZnO/ZnX (X=S,Se,Te) heterostructured nanotubes”. E-MRS Spring meeting. IUMRS ICAM & E-MRS/MRS Bilateral Energy Conferences, May 9-13, 2011, Nice, France. **(Oral presentation)**

Annex
